

# FRIB High Rigidity Spectrometer Preliminary Design Report

FRIB-M41800-AD-000531-R004

Issued 2 August 2021

Released by

8/2/2021

X



---

Remco Zegers  
HRS Scientific Spokesperson  
Signed by: zegers

Released by

8/2/2021

X



---

Richard York  
HRS Project Manager  
Signed by: york



## Revision History

Revision	Issued	Changes
R001	26 March 2019	Includes I-Yang Lee's comments.
R002	27 March 2019	Updated spokesperson's title. Updated section 3.5 and added an additional sentence.
R003	18 March 2020	Updated on the basis of the comments received during the Director's Review. The changes are detailed in <a href="#">a tracker document on Portal</a> .
R004	2 August 2021	Release as Preliminary Design Report.; Updated on basis of comments/recommendations received from external review April 2021.



# FRIB High Rigidity Spectrometer Preliminary Design Report

---

M41800-AD-000531-R004

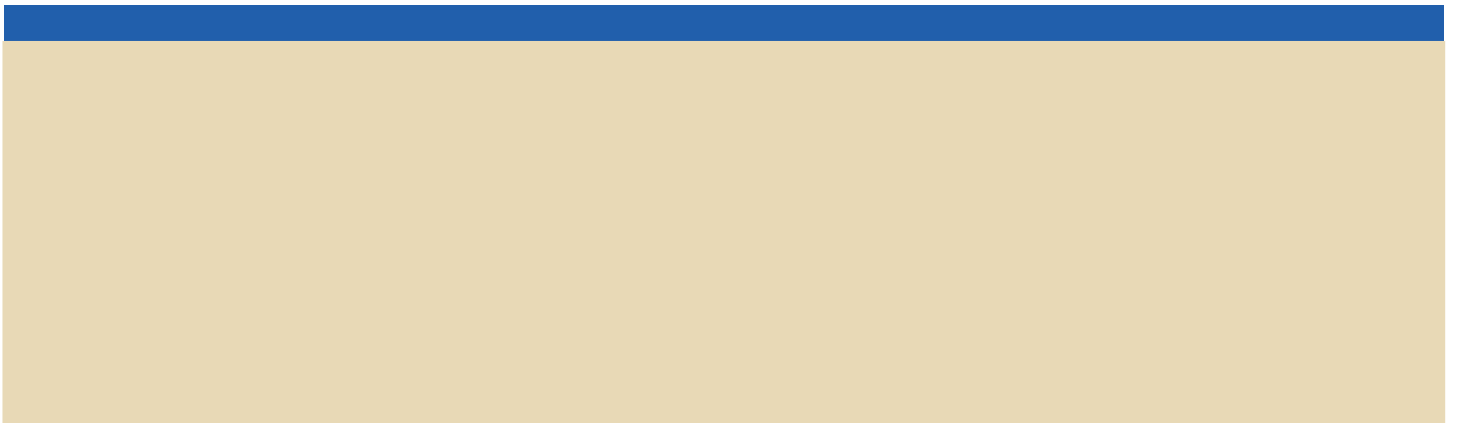


**MICHIGAN STATE**  
UNIVERSITY



U.S. DEPARTMENT OF  
**ENERGY**

Office of  
Science







## Contents

<b>1</b>	<b>Front Matter</b> .....	<b>6</b>
1.1	Contributors.....	6
1.2	Acronyms and abbreviations .....	8
1.3	List of figures .....	12
1.4	List of tables .....	21
<b>2</b>	<b>Executive summary</b> .....	<b>26</b>
2.1	Introduction .....	26
2.2	Scope .....	26
2.3	Capabilities.....	27
2.4	Cost and schedule.....	29
2.5	Acquisition strategy.....	29
2.6	References .....	29
<b>3</b>	<b>Project overview</b> .....	<b>30</b>
3.1	Introduction .....	30
3.2	Project organization.....	30
3.3	Work breakdown structure .....	31
3.4	Performance Parameters.....	33
3.5	Life Cycle Costs .....	34
3.6	Risk assessment.....	34
3.7	ESH and Quality Requirements and Plans .....	35
3.8	References .....	35
<b>4</b>	<b>Science enabled with the High Rigidity Spectrometer (HRS) at FRIB</b> .....	<b>37</b>
4.1	Introduction .....	37
4.2	Science with the HRS.....	39
4.2.1	How does visible matter organize itself.....	39
4.2.2	How does visible matter come into being and how does it evolve?.....	50
4.2.3	Probing fundamental symmetries through weak interaction studies.....	59
4.2.4	Applications – <b>Key example</b> : Improving models of nuclear fission .....	61
4.2.5	<b>Key example</b> – A game changer for nuclear reactions.....	61
4.2.6	<b>Key example</b> – Discovery science: The skin nuclei <sup>84</sup> Ni and <sup>140</sup> Sn .....	65
4.3	Science Specifications.....	67
4.3.1	Scientific Specifications for the Spectrometer Section: accommodating the diverse scientific program of the HRS user community .....	69
4.3.2	Scientific specifications for the HTBL: optimizing the luminosity for experiments at the HRS.....	84
4.4	References .....	102
<b>5</b>	<b>High Transmission Beam Line (HTBL) of the HRS</b> .....	<b>108</b>
5.1	Introduction and overview.....	109
5.2	Functional Requirements for the HTBL.....	111
5.3	Design approach and preferred alternative for the HTBL .....	112
5.3.1	Realization of achromatic and dispersive transport modes.....	112
5.3.2	Achromatic beam-transport mode.....	114
5.3.3	Dispersion-matching beam transport mode .....	115
5.3.4	Higher-order ion optics .....	118
5.4	End-to-end simulations.....	120
5.5	Angular and momentum resolutions .....	123



5.6 Angular and momentum acceptances ..... 125

5.7 Preferred HTBL alternative meets requirements ..... 128

5.8 Functional specifications for the HTBL ..... 128

    5.8.1 Magnetic elements ..... 128

    5.8.2 Diagnostics and detectors ..... 132

    5.8.3 Vacuum systems ..... 136

5.9 References ..... 136

**6 Spectrometer Section of the HRS.....138**

6.1 Introduction and overview ..... 138

6.2 Functional Requirements for the Spectrometer Section ..... 139

6.3 Design approach and preferred alternative for the Spectrometer Section ..... 140

    6.3.1 High-resolution mode ..... 140

    6.3.2 Neutron invariant-mass mode ..... 153

    6.3.3 ToF- $B\rho$  mass-measurement mode ..... 160

6.4 Preferred Spectrometer Section alternative meets requirements ..... 164

    6.4.1 High-resolution mode ..... 164

    6.4.2 Neutron invariant-mass mode ..... 165

    6.4.3 ToF- $B\rho$  mass-measurement mode ..... 166

    6.4.4 Switching between different Spectrometer Section Modes ..... 167

6.5 Functional specifications for the Spectrometer Section ..... 168

    6.5.1 Magnetic elements ..... 168

    6.5.2 Diagnostics and detectors ..... 180

    6.5.3 Vacuum systems ..... 183

6.6 References ..... 184

**7 Diagnostics and Detectors.....185**

7.1 Introduction and overview ..... 185

    7.1.1 The HTBL diagnostics and tracking systems ..... 186

    7.1.2 The Spectrometer Section diagnostics and detectors systems ..... 189

7.2 Requirements and performance ..... 191

    7.2.1 Requirements for the HTBL diagnostics and detector systems ..... 191

    7.2.2 Requirements for the Spectrometer Section diagnostics and detector systems ..... 194

7.3 The detector systems of the HRS ..... 196

    7.3.1 The focal planes of the HTBL ..... 196

    7.3.2 The focal planes of the Spectrometer Section ..... 201

    7.3.3 Data acquisition systems for the HRS ..... 211

    7.3.4 Ancillary detector and support ..... 213

    7.3.5 Alarms and interlocks for equipment protection ..... 213

7.4 References ..... 214

**8 Commissioning Plan.....217**

8.1 References ..... 218

**9 Magnets .....219**

9.1 Introduction and overview ..... 219

9.2 Requirements ..... 219

    9.2.1 High Transmission Beam Line (HTBL) magnets requirements ..... 219

    9.2.2 Spectrometer Section magnets requirements ..... 222

9.3 Design approach ..... 224

9.4 Preferred alternative ..... 225

    9.4.1 HTBL quadrupole magnets ..... 225



9.4.2	HTBL dipole magnets.....	227
9.4.3	HTBL steering magnets.....	230
9.4.4	Spectrometer Section quadrupoles.....	231
9.4.5	Spectrometer Section dipole magnets.....	235
9.5	Quench protection.....	243
9.6	References.....	244
<b>10</b>	<b>Power Supplies.....</b>	<b>245</b>
10.1	Introduction and overview.....	245
10.2	Requirements.....	245
10.3	Preliminary Design.....	249
10.3.1	Power supplies.....	251
10.3.2	Technical utilities and infrastructure.....	252
10.4	References.....	257
<b>11</b>	<b>Cryogenic Systems.....</b>	<b>258</b>
11.1	Introduction and overview.....	258
11.2	Requirements.....	258
11.3	Design approach.....	261
11.4	References.....	264
<b>12</b>	<b>Control Systems.....</b>	<b>265</b>
12.1	Introduction and overview.....	265
12.2	Requirements.....	266
12.2.1	Controls requirements.....	266
12.2.2	Protection systems requirements.....	269
12.2.3	Network and IT requirements.....	271
12.3	Design approach.....	271
12.3.1	Low-level control systems design approach.....	271
12.4	Design.....	273
12.4.1	Controls systems design.....	273
12.4.2	Protection systems design.....	275
12.4.3	Network and IT design.....	277
<b>13</b>	<b>Vacuum Systems.....</b>	<b>281</b>
13.1	Introduction and overview.....	281
13.2	Requirements.....	282
13.3	Preferred alternative.....	282
<b>14</b>	<b>Conventional Facilities.....</b>	<b>286</b>
14.1	Introduction.....	286
14.2	Radiation transport and safety.....	287
14.2.1	Requirements.....	287
14.2.2	Radiation transport analysis.....	287
14.2.3	Radiation analysis results.....	288
14.2.4	Magnet power-supply interlocks.....	290
14.2.5	Summary.....	291
14.3	References.....	291
<b>15</b>	<b>EHS and Quality assurance.....</b>	<b>292</b>
15.1	Introduction.....	292
15.2	Hazard analysis and controls.....	293
15.3	Hazard control implementation and management.....	293
15.4	Credited engineered controls with ESH impact.....	294



15.5	Non-credited controls with ESH impact.....	294
15.6	Selection of credited controls .....	294
15.7	Selection of non-credited controls .....	295
15.8	Management of controls .....	295
15.9	Management of credited controls .....	296
15.10	Compensatory measures .....	297
15.11	Management of non-credited controls .....	297
15.12	Control identification and maintenance .....	297
15.13	Quality assurance.....	298
15.14	References .....	298



# 1 Front Matter

## 1.1 Contributors

A basis for this preliminary design report was the 2014 whitepaper, titled “A high Rigidity Spectrometer for FRIB”, which was written by the HRS Working Group. The HRS Working Group presently consists of scientist from the following US institutions:

<b>US National Laboratories</b>	<b>US Universities &amp; Colleges</b>	
Argonne Nat'l Lab.	Augustana College	Ohio University
Lawrence Berkeley Nat'l Lab.	Bucknell University	Ohio Wesleyan University
Lawrence Livermore Nat'l Lab.	Central Michigan University	Rutgers University
Los Alamos Nat'l Lab.	Florida State University	Texas A&M University
Oak Ridge Nat'l Lab.	Davidson College	University of Tennessee
<b>Foreign Institutions</b>	Hope College	University of Notre Dame
GSI/FAIR (EU)	Indiana University	University of North Carolina/TUNL
RIBF/RIKEN (Japan)	Indiana Wesleyan University	Washington University St. Louis
TRIUMF (Canada)	Kalamazoo College	Ursinus College
University of Surrey (UK)	Michigan State University	Wabash College

Thirty-nine representative members from the Working Group have participated in regular meetings that were very beneficial for developing this report. These meetings were organized by S. Noji and R. Zegers and participants included: M. Amthor (Bucknell University), D. Bazin (MSU), T. Baumann (MSU), G. Berg (University of Notre Dame), J. Brown (Wabash College), Z. Chajeki (Western Michigan University), J. Cizewski (Rutgers University), M. Cortesi (MSU), M. Couder (University of Notre Dame), A. Couture (LANL), H. Crawford (LBLN), A. Estrade-Vaz (Central Michigan University), P. Fallon (LBNL), M. Famiano (Western Michigan University), N. Frank (Augustana College), A. Gade (MSU), H. Geissel (GSI), G. Grinyer (University of Regina), R. Grzywacz (University of Tennessee-Knoxville), P. Gueye (MSU), M. Hausmann (MSU), C. Hoffman (ANL), R. Janssens (The University of North Carolina at Chapel Hill), N. Kalantarians (Virginia Union University), T. Kubo (MSU), A. Macchiavelli (LBNL), W. Mittig (MSU), S. Mosby (LANL), S. Noji (MSU), P. Ostroumov (MSU), S. Pain (ORNL), J. Pereira (MSU), A. Plastun (MSU), M. Portillo (MSU), A. Rogers (University of Massachusetts Lowell), J. Silano (LLNL), G. Rogachev (Texas A&M), H. Sato (RIKEN), B. Sherrill (MSU), A. Stolz (MSU), O. Tarasov (MSU), A. Tonchev (LLNL), R. York (MSU), R. Zegers (MSU), A. Zeller (MSU).



In addition, nineteen members of the above group met in monthly meetings focused on the detector systems for the HRS. This meeting was organized by A. Estrade-Vaz from Central Michigan University and included: D. Bazin (MSU), T. Baumann (MSU), G. Berg (University of Notre Dame), Z. Chajecski (Western Michigan University), M. Cortesi (MSU), H. Crawford (LBLN), A. Estrade-Vaz (Central Michigan University), M. Famiano (Western Michigan University), G. Grinyer (University of Regina), R. Grzywacz (University of Tennessee-Knoxville), P. Gueye (MSU), M. Hausmann (MSU), C. Hoffman (ANL), K. Jones (University of Tennessee-Knoxville), N. Kalantarians (Virginia Union University), T. Kubo (MSU), M. Portillo (MSU), A. Rogers (University of Massachusetts Lowell), G. Rogachev (Texas A&M), O. Tarasov (MSU), R. Zegers (MSU)

Additional input from the FRIB User Community was received through Working Group meetings during the annual Low-Energy Community Meetings. The HRS Working Group closely coordinates with other FRIB Working Groups and the GRETA Project Team.

The HRS Working Group would like to thank J. Nolen (ANL), H. Simon (GSI), and M. Winkler (GSI) for their feedback on the ion-optical layout of the HRS during the Expert Meeting in May, 2017.

The following staff of the FRIB Laboratory contributed to the development and writing of this report: D. Bazin, T. Baumann, G. Berg, N. Bultman, E. Burkhardt, M. Cortesi, D. Crackel, K. Davidson, J. DeKamp, R. Fox, A. Gade, D. Georgobiani, P. Gibson, P. Grivins, K. Holland, M. Hausmann, A. Hussain, T. Kubo, D. Lawton, I. Malloch, P. Manwiller, S. Miller, S. Noji, P. Ostroumov, A. Plastun, M. Portillo, D. Ruddock, K. Schrock, B. Sherrill, A. Stolz, D. Stout, O. Tarasov, R. York, R. Zegers. The development of the preliminary design of the HRS was closely coordinated with the members of the FRIB CFID Division, in particular B. Bull and T. Elkin. The report was edited by A. Gade, R. York, and R. Zegers. J. Gabler, J. Rebenstock, and J. Lesniak assisted with referencing.

The work presented in this reported was supported by the U.S. Department of Energy Office of Science under Grant DE-SC0014554, ION-OPTICAL AND ASSOCIATED MAGNET FEASIBILITY STUDY OF A HIGH RIGIDITY SPECTROMETER (PI R. Zegers) and Grant DE-SC0000661, HRS PRE-CDR ACTIVITIES and HIGH RIGIDITY SPECTROMETER PROJECT – FY20 TO FY22 (PI R. York).

A fraction of Grant DE-SC0014554 was subawarded to the University of Notre Dame and provided support for G. Berg. He and S. Noji performed a large fraction of the ion-optical calculations for the HRS. Contributions from Hiromi Sato (RIKEN) on the design of the DS1 dipole magnet were very beneficial.



## 1.2 Acronyms and abbreviations

AC	Alternating Current
AHD	Activity Hazard Document
AI	Analog Input
ALARA	As Low As Reasonably Achievable
ALARP	As Low As Reasonably Practicable
ANL	Argonne National Laboratory
AO	Analog Output
ARIS	Advanced Rare Isotope Separator
AT-TPC	Active Target Time Projection Chamber
CAC	Credited Administrative Controls
CAESAR	CAESium iodide ARray
CCUSB	CAMAC Crate Universal Serial Bus
CD	Critical Decision
CDR	Conceptual Design Report
CEC	Credited Engineered Controls
CFF	ConFlat Flange
CREX	Calcium Radius Experiment
CTR	Cathode Ray Tube
Ctrl	Controls
DAQ	Data Acquisition
DC	Direct Current
DCC	Document Control Center
DDAS	Digital Data Acquisition System
DI	Digital Input
DO	Digital Output
DOE	Department of Energy
DOE-SC	Department of Energy Office of Science
DOM	Dispersive Optical Model
D-PPAC	Delay line Parallel-Plate Avalanche Counter
DRR	Device Readiness Review
EHS	Environment, Health, and Safety
EPICS	Experimental Physics and Industrial Control System
ESH&Q	Environment, Health, Safety, and Quality
FRIB	Facility for Rare isotope Beams
FWHM	Full Width at Half Maximum
FSQ	Fragment Separator Quadrupole
GDR	Giant Dipole Resonance





GET	General Electronics for TPC
GPM	Gallons per Minute
QQR	Giant Quadrupole Resonance
GRETA	Gamma-Ray Energy Tracking Array
GSI	GSI Helmholtz Centre for Heavy Ion Research
GT	Gamow-Teller
GTR	Gamow-Teller Resonance
HA	Hazard Analysis
HAGRID	Hybrid Array of Gamma Ray Detector
HiRA	High resolution Array
HRS	High Rigidity Spectrometer
HTBL	High Transmission Beam Line
HV	High Voltage
HVAC	Heating, ventilation, and air conditioning
IAS	Isobaric Analog State
IC	Ion Chamber
IEC	International Electrotechnical Commission
IFM	Interface Module
ISGMR	Isoscalar Giant Monopole Resonance
ISM	Integrated Safety Management
ISO	International Organization for Standardization
IT	Information Technology
JLAB	Jefferson Lab
JSA	Job Safety Analysis
KPP	Key Performance Parameters
LANL	Los Alamos National Laboratory
LBNL	Lawrence Berkeley National Laboratory
LCW	Low Conductivity Water
LENDA	Low Energy Neutron Detector Array
LIGO	Laser Interferometer Gravitational-Wave Observatory
LOTO	Lock-Out Tag-Out
LRP	Long Range Plan
MCP	Micro Channel Plate
MoNA-LISA	Modular Neutron Array - Large multi-Institutional Scintillator Array
MPS	Machine Protection System
MSU	Michigan State University
MTBF	Mean Time Between Failures
MTTR	Mean Time To Repair
NASA	National Aeronautics and Space Administration





NEC	National Electrical Code
NN	Nucleon-Nucleon
NRC	National Research Council
NSAC	Nuclear Science Advisory Committee
NSCL	National Superconducting Cyclotron Laboratory
ODH	Oxygen Deficiency Hazard
ODHCS	Oxygen Deficiency Hazard Control System
OHSAS	Occupational Health and Safety Assessment Series
OIC	Optical ion Chamber
ORNL	Oak Ridge National Laboratory
ORRUBA	Oak Ridge Rutgers University Barrel Array
PDR	Preliminary Design Report
PFGS	Prompt-Fission Gamma-ray Spectrum
PID	Particle Identification
PLC	Programmable Logic Controller
PMT	Photomultiplier Tube
PPAC	Parallel-Plate Avalanche Counter
PPEP	Preliminary Project Execution Plan
PPS	Personnel Protection System
pps	Particles per second
PREX	Lead Radius Experiment
PS	Power Supply
PW	Process Water
QA	Quality Assurance
QE	Quantum Efficiency
QPH	Quench Protection Heater
QWR	Quarter-Wave Resonator
ReA	Reaccelerator
RF	Radiofrequency
RFFS	Radiofrequency Fragment Separator
RIB	Rare Isotope Beam
RIBF	Radioactive Isotope Beam Factory
RIKEN	Rikagaku Kenkyusho (Institute of Physical and Chemical Research, Japan)
RR	Risk Reduction
RSS	Radiation Safety System
RT	Room Temperature
RTM	Room Temperature Magnet
SC	Superconducting
SCM	Superconducting Magnet



SCCM	Standard Cubic Centimeters per Minute
SeGA	Segmented Germanium Array
SIL	Safety Integrity Level
SOP	Standard Operation Procedure
S $\pi$ RIT-TPC	SAMURAI Pion-Reconstruction and Ion-Tracker Time Projection Chamber
TBD	To Be Determined
TEC	Total Estimated Cost
TF	Task Force
THGEM	Thick Gaseous Electron Multiplier
TKE	Total Kinetic Energy
TOF	Time of Flight
TPC	Total Project Cost
TPC	Time Projection Chamber
TTS	Transit Time Spread
UL	Underwriters Laboratories
UPS	Uninterruptible Power Supply
VAC	Voltage, Alternating Current
VANDLE	The Versatile Array of Neutron Detectors at Low Energy
VDC	Voltage, Direct Current
VMUSB	Versa Module Universal Serial Bus
WBS	Work Breakdown Structure
WFO	Work for others



### 1.3 List of figures

- Figure 2-1 Layout of the High Rigidity Spectrometer (HRS) at FRIB, consisting of the High-Transmission Beam Line (HTBL) and the Spectrometer Section. The conventional facilities that will house the HRS are as well as the Isotope Harvesting Laboratory were provided by MSU with beneficial occupancy February 2020. GRETA and MoNA-LISA are examples of ancillary detector systems that will be used in combination with the HRS. .... 28
- Figure 4-1 FRIB will allow users to answer the overarching questions from the NSAC 2007/15 Long Range Plan and the latest NRC Decadal Study, and thereby supporting the DOE Nuclear Physics Mission. The NSAC RIB TF developed 17 benchmarks to test facility capability to address these questions. Meeting these benchmarks has driven the technical scope and specifications for FRIB. The benchmarks also guide the equipment development necessary for the program. .... 38
- Figure 4-2: First ab-initio type Coupled Cluster calculations of  $2^+$  energies around the key nucleus  $^{78}\text{Ni}$  [HAG16]. In-beam  $\gamma$ -ray spectroscopy at a high rigidity spectrometer at FRIB will enable spectroscopy along magic chains to benchmark ab-initio calculations and explore the effects of many-body correlations in the regime of weak binding. .... 42
- Figure 4-3 Potential energy surface for  $^{78}\text{Ni}$ ,  $^{76}\text{Fe}$  and level schemes for the same nuclei as predicted by large-scale shell-model calculations [NOW16]. The dark blue minima indicate different deformations that the nucleus is predicted to assume at low excitation energies. Transition strength measurements at and around  $^{78}\text{Ni}$  will reveal band structures built on the different deformations and their interconnections. ... 43
- Figure 4-4 Simulation of the excitation energy spectrum of  $^{60}\text{Ca}$  as Doppler-reconstructed with GRETA following a direct one-proton knockout reaction from  $^{61}\text{Sc}$  at 200 MeV/u. The cross section was estimated based on [GAD14] with the  $2^+$  energy as predicted by large-scale shell model [LEN10] and full transmission of the  $^{61}\text{Sc}$  rare-isotope beam to the reaction target was assumed. Without the factor of 24 gain in luminosity from a High Rigidity Spectrometer, this experiment will not be possible (Figure from [FAL16]). .... 45
- Figure 4-5 Isotopes that FRIB will produce at intensities in between 0.0001/s and 1/s and that have neutron separation energy below 2 MeV and are of strong interest for invariant-mass spectroscopy. The limit of known nuclei on the neutron-rich side is indicated by the red line. Outlined isotopes provide an estimate of the limits of particle-bound isotopes from the KTUY model [KOU05]. For these very neutron-rich systems, such as around  $^{84}\text{Ni}$  and  $^{140}\text{Sn}$ , high luminosity is critical, which requires an experimental station that can operate at high rigidities. .... 46
- Figure 4-6 Overview of the main astrophysical processes superimposed on the chart of nuclei [AST17]. Often the most critical isotopes are farthest from stability and hence produced at low rates at FRIB. Sensitivity will be key to provide all the necessary astrophysical data [Figure from F. Timmes]. .... 51
- Figure 4-7 Sensitivity study for nuclear masses in an r process ensuing in a neutron star merger (Figure from [MUM16]). The darker the blue shading, the more important the nuclear mass for modeling the r process. .... 52
- Figure 4-8 Applicability of ToF-B $\rho$  mass measurement technique at FRIB. The reach for this technique is indicated by the red line, which indicates the RIB production rate of 1000 per week. At FRIB, a large fraction of the nuclei in the r-process path (orange) up to N~100 can be covered. Up to N~140, the less neutron-rich isotopes in the r-process path are covered and model extrapolations will be significantly improved. A large fraction of the nuclei of importance for neutron-star crustal processes (up to N~60) can



be measured at the HRS using the ToF-Bp technique. Mass resolutions of better than 150 keV (FWHM) for  $A=50$ , 300 keV for  $A=100$ , and 500 keV for  $A=170$  can be achieved..... 53

Figure 4-9 The 500 electron-capturing nuclei with the largest absolute change to the electron fraction  $|\Delta Y_e|$  up to neutrino trapping in the late stages of core-collapse supernovae [SUL16]. The most important region is in the neutron-rich region along the  $N=50$  line, which can be studied by using charge-exchange reactions at a high rigidity spectrometer. .... 54

Figure 4-10 (from Ref. [GOR13]) Final abundance distributions for ejecta produced in neutron-star (of 1.35 solar masses) mergers. The blue and red dots represent results based on different models for the fission process. The open circles represent solar abundances. .... 55

Figure 4-11 The symmetry energy  $S(\rho)$  as a function of baryon density. At sub-saturation density, the density dependence of the symmetry energy is reasonably constrained [HOR14], at supra-saturation density, the region important for neutron star and neutron star merger physics [LAT16], the measures from n-p flow and pion production differ widely and new constraints are needed that high-energy beams from FRIB can provide. .... 57

Figure 4-12 Example for the incident energy dependence of charged pion multiplicities in central collisions [IKE18]. With the HRS,  $^{132}\text{Sn}$  projectiles would be available for experiments at 170 MeV/u and higher while a 4Tm limit would restrict the  $^{132}\text{Sn}$  beam energy to 105 MeV/u. Experiments at high rigidity thus increase pion production by an order of magnitude and so significantly enhance the signal-to-noise in collision experiments with pion flow observables. .... 57

Figure 4-13 Systematics of the nuclear incompressibility,  $K_A$  (minus the Coulomb term), derived from measurement of the ISGMR in Sn isotopes, as a function of the asymmetry term  $(N-Z)/A$  [LI07]. The quadratic fit to the data leads to a value for the asymmetry term of nuclear incompressibility  $K_\tau = -550 \pm 100$  MeV. A measurement of the ISGMR in  $^{104}\text{Sn}$  and  $^{134}\text{Sn}$  to within  $\pm 0.2$  MeV would reduce the uncertainty in  $K_\tau$  to less than 50 MeV. .... 58

Figure 4-14 Sketch of the energy regions where certain reactions, accessing specific science topics or observables, would optimally be used at FRIB. For some of the key nuclei discussed throughout the science section, rigidities above 4 Tm are required already to achieve beam energies of 100 MeV/u. .... 62

Figure 4-15 Simulated momentum distribution of  $^{203}\text{Pt}$  following the knockout of a neutron from the  $2g_{9/2}$  orbital of  $^{204}\text{Pt}$ , fitted by theoretical distributions assuming either p, g, or i orbital angular momenta. The  $\chi^2$  values clearly indicate  $g_{9/2}$  as the best fit, in spite of the limited statistics. A momentum resolution for the  $^{203}\text{Pt}$  residue of better than 1 in 1300 is required to discriminate between the involved orbital angular momenta in this mass region..... 63

Figure 4-16 Illustration of the amount of space that must be kept available to place and operate GRETA at the reaction target. The radius of the frame holding the GRETA detectors is 63 cm, and the distance from the target to the end of a detector module is 108 cm. Additional space is required to insert a liquid-nitrogen bayonet, adding 37 cm to that distance. When projected onto the beam axis, this leads to a specification to leave at least 123 cm of space for GRETA. .... 72

Figure 4-17 Existing detector systems that will be placed around the target for experiments with the HRS: a) Gamma Ray Energy Tracking Array (GRETA) [GRE20]; b) LaBr(Ce)+CsI(Tl) array Apollo [COU15]; c) CAESium-iodide scintillator Array (CAESAR) [WEI10]; d) High-Resolution Detector Array (HiRA) [WAL07]; e) Segmented Germanium Array (SeGA) [SEG01]; f) NSCL- Köln Plunger [IWA16]; g) Hybrid Array of Gamma Ray Detector (HAGRiD) [SMI18]; h) Oak Ridge Rutgers University Barrel Array (ORRUBA) [PAI07]; i) Low-Energy Neutron Detector Array (LENDa) [PER12] and Versatile Array of



Neutron Detectors at Low Energy (VANDLE) [PET16]; j) The Active Target Time Projection Chamber (AT-TPC) [AYY17]; k) The S $\pi$ RIT-TPC [OTS16, JHA16], l) The Texas Active Target (TexAT) [KOS20].

..... 73

Figure 4-18 The geometrical efficiency as a function of excitation energy for neutrons emitted from an unbound system with mass number 40 at 180 MeV/u. A coverage of 90% is achieved up to an excitation energy of 2 MeV for a neutron solid angle coverage of 32 msr. .... 77

Figure 4-19 Simulation of the reaction plane reconstruction for heavy-ion collisions by using a TPC inserted in the sweeper magnet. The horizontal axis shows the difference in reaction plane angle for two subgroups of tracks in one event, as reconstructed in the TPC. If the difference is small, the reconstruction is of high quality. If the difference is large, the reconstruction is of poor quality. A substantial gain in efficiency and quality is achieved when increasing the sweeper magnet gap size from 48 cm to 60 cm. Further increasing to gap size comes with reduced additional gains [BRO20]. .... 78

Figure 4-20 Simulations of in-flight fission at 200 MeV/u in which both fission products are detected in the Spectrometer Section. In the top and bottom-left panels, the efficiency for detecting fission pairs is plotted as function of neutron (N) and proton number (Z). In the top-left panel the angular acceptances was set to  $\pm 60$  mrad (dispersive direction) by  $\pm 60$  mrad (non-dispersive direction); in the top-right panel the angular acceptances was set to  $\pm 50$  mrad (dispersive direction) by  $\pm 75$  mrad (non-dispersive direction); in the bottom-left panel the angular acceptances was set to  $\pm 50$  mrad (dispersive direction) by  $\pm 50$  mrad (non-dispersive direction). The bottom-right plot shows the averaged efficiency for the detection of both fission pairs as a function of mass number for each of the three angular acceptances. Correlations in the 2-D acceptance plots are caused by correlations between fission fragments that are produced and somewhat sensitive to fission model used to perform the simulations. .... 79

Figure 4-21 Overall efficiency for detecting both fission fragments as a function of solid angle for charged particles of the HRS. The saturation above 15 msr is due to limitations imposed by the momentum acceptance of the HRS. These calculations were performed with theoretical fission inputs using the CGMF code [TAL13] performed at LANL [LOV20]. .... 80

Figure 4-22 Schematic overview of ToF-B $\rho$  measurements. A cocktail of rare-isotope beams passes through ToF and tracking detectors in the fragment separator. The magnetic rigidity is measured at the target location of the Spectrometer Section. The time-of-flight stop signal comes from a detector placed in the focal plane of the Spectrometer Section, where tracking and  $\Delta E$ -E measurements are performed to do particle identification (PID). .... 81

Figure 4-23 Magnetic rigidities for which the rare-isotope production rate across the chart of nuclei is optimized for FRIB at 200 MeV/u (for FRIB at 400 MeV/u, see Section 4.3.2.6). This varies across the nuclear chart with the highest rigidities needed for the most neutron-rich species. .... 85

Figure 4-24 Gain in rare-isotope beam rate in the HRS compared to performing experiments with the existing S800 Spectrograph. These gains are estimated in end-to-end Monte-Carlo simulations as detailed in Section 5.4. The solid line indicates the trend of the gain in rate as a function of magnetic rigidity for rare isotopes produced by in-beam fragmentation. For rare isotopes produced via in-flight fission (here exemplified by  $^{84}\text{Ni}$ ) the gain is much higher than indicated by this trend line, due to the severe limitations imposed by the transmission to the S800 compared to the HRS. .... 87

Figure 4-25 Charge-state distributions after  $^{60}\text{Ca}$  (top row),  $^{140}\text{Sn}$  (middle row), and  $^{204}\text{Pt}$  (bottom row) beams pass through a  $^9\text{Be}$  target at equilibrium thickness (left column), a 130- $\mu\text{m}$  thick plastic scintillator





(middle column), and a set of tracking PPACs (right column). Orange, grey, yellow, and blue lines refer to final charge states of  $Z-Q=0, 1, 2,$  and  $3,$  respectively..... 89

Figure 4-26 (a) Illustration of the luminosity gain that can be achieved by performing experiments at rigidities for which the rare-isotope production rate is maximum. In the case of proton knockout from  $^{61}\text{Sc}$ , populating  $^{60}\text{Ca}$ , a 4 times thicker target can be used assuming that the change in velocity in the target does not exceed 5% in order to maintain a Doppler-reconstructed  $\gamma$ -ray energy resolution of better than 2%. (b) Luminosity gain factor due to the use of thicker reaction targets achieved by performing experiments up to 8 Tm by using the HRS compared to performing at 4 Tm by using the S800 magnetic spectrograph, as a function of proton number of the rare-isotope beam (y-axis) and rigidity used in the HRS (x-axis). ..... 90

Figure 4-27 Estimated luminosity gain factors that can be achieved by using the HRS compared to using the existing S800 Spectrometer across the chart of nuclei. The rare-isotope production rates are indicated by solid lines and the nuclei shown with white boundaries correspond to the path of the astrophysical r process. .... 92

Figure 4-28 Ratio of RIB yields for FRIB with 200 MeV/u capability and 400 MeV/u capability after an energy upgrade. The gain in beam intensity is a factor of 5-10 for the most neutron-rich isotopes, assuming that beams with a rigidity of up to 8-Tm can be transmitted to the target station of the HRS. The black squares designate primary beams used. .... 94

Figure 4-29 Estimated rigidities for which the production rates of rare isotope beams is optimized after a 400 MeV/u energy upgrade of FRIB. .... 95

Figure 4-30 Illustration of different beam transport modes: (a) achromatic beam transport, in which the momentum spread ( $\pm\Delta p/p$ ) in the beam contributes to the size of the image in the focal plane of the spectrometer; (b) lateral and angular dispersion-matched beam transport, in which the dispersion on target is additionally correlated with the angles of the incoming particles, such that the angular spreads of the beam particles associated with their differences in momenta are cancelled out in the spectrometer. The rays indicate particles with different momenta. Figure is adapted from [FUJ02]. .... 97

Figure 4-31 Conceptual design of a Double Quarter-Wave Resonator (QWR) cavity that serves as an RF Fragments Separator for the HRS. It operates at 20.125 MHz and provides an angular deflection of  $\pm 8.6$  mrad to achieve a contaminant suppression of a factor of about 300 for the case of  $^{100}\text{Sn}$ . The dimensions in the figure are in mm..... 99

Figure 4-32 LISE<sup>++</sup> Simulation of the operation of an RFFS placed in the HTBL for the purification of a  $^{100}\text{Sn}$  beam. In a) the operation at a frequency of 20.125 MHz is simulated. With a cut on the deflection position (y-axis) by using slit, it is possible to reduce the contamination from particle other than  $^{100}\text{Sn}$  particles by a large fraction. At a frequency of 40.25 MHz, shown in panel b), the RF bunches overlap and the ability to purify the  $^{100}\text{Sn}$  beam by using slits is strongly reduced compared to operation at 20.125 MHz. .... 100

Figure 5-1 Layout of the High-Transmission Beam Line (HTBL). .... 110

Figure 5-2 Naming convention of the components of the HTBL and Spectrometer Section of the HRS. 110

Figure 5-3 This figure schematically illustrates how the HTBL realizes both (a) achromatic and (b) dispersive beam-transport modes. See text for details. .... 113

Figure 5-4 Trajectory plots for the achromatic beam transport through the HTBL in the dispersive (top) and the non-dispersive (bottom) planes in first order. The dipole magnets are shown as orange boxes, with their heights representing the good-field regions ( $\pm 10$  cm) and vertical gaps ( $\pm 5$  cm). The quadrupoles are shown



as light-brown boxes, with their heights representing the warm-bore aperture sizes. The dark boxes on both ends extending to the pole-tip radii (15 cm), denote the cryostat vessels in which the sextupole and octupole coils are housed. The ensemble of rays correspond to the  $2\sigma$  values of the phase space of  $^{40}\text{Mg}$  coming out from the ARIS Fragment Separator with its optimal settings:  $\delta x_{\text{max}} = 1.2$  mm,  $\delta x'_{\text{max}} = 12.5$  mrad,  $\delta y_{\text{max}} = 3.4$  mm,  $\delta y'_{\text{max}} = 31.2$  mrad, and  $\delta p_{\text{max}}/p = 1.54\%$ . The different colors for the dispersive-plane trajectories correspond to the different momenta, which all coincide in the non-dispersive plane in this first-order plot. .... 115

Figure 5-5 Same as Figure 5-4, but for the dispersion-matched beam transport. The ensemble of rays correspond to the  $2\sigma$  values of the phase space of  $^{204}\text{Pt}$ :  $\delta x_{\text{max}} = 1.0$  mm,  $\delta x'_{\text{max}} = 3.2$  mrad,  $\delta y_{\text{max}} = 2.9$  mm,  $\delta y'_{\text{max}} = 8.0$  mrad, and  $\delta p_{\text{max}}/p = 0.25\%$ . .... 117

Figure 5-6 Same as in Figure 5-4 but in 5<sup>th</sup> order, a) with and b) without higher-order correctors. .... 119

Figure 5-7 Results of end-to-end simulations for  $^{40}\text{Mg}$  and  $^{84}\text{Ni}$  in LISE<sup>++</sup> in 3<sup>rd</sup> order. See text for details. .... 121

Figure 5-8 Angular and momentum resolutions in the achromatic mode calculated as the difference between the reconstructed and initial angle/momentum in trajectory-reconstruction simulations using COSY-calculated maps including up to 5<sup>th</sup> order. .... 123

Figure 5-9 Momentum and angular resolutions in the achromatic mode. Those achieved by a measurement at FB1 or FB3 alone are compared to the combination of those at FB1 and FB3. .... 124

Figure 5-10 Momentum resolution in the dispersion-matched mode. .... 124

Figure 5-11 Angular and momentum acceptances for the achromatic beam-transport modes of the HTBL as simulated in LISE<sup>++</sup> loaded with fifth-order transfer matrices obtained in COSY. The three 2D histograms show the angle-angle or angle-momentum correlations. The four 1D histograms are their slices around  $x'$  or  $y' = 0$  mrad or  $\Delta p/p = 0\%$  as indicated by the red lines. .... 126

Figure 5-12 Same as Figure 5-11, but for the dispersion-matched mode. .... 127

Figure 5-13 Schematic layout of the detector configuration of the diagnostic systems used at (a) FB1/FS0 and (b) FB3. .... 133

Figure 6-1 Layout of the Spectrometer Section of the HRS starting at FS0, showing dipoles DS1 and DS2, quadrupoles QS1A, QS2B, QS3B, QS4B, QS5A, and QS6A, focal planes FS1 and FS2, and possible locations for GRETA and MoNA-LISA. .... 139

Figure 6-2 The layout for the high-resolution mode of the Spectrometer Section. .... 141

Figure 6-3 Trajectory plots for the high-resolution mode of the Spectrometer Section in the dispersive (top) and the non-dispersive (bottom) planes in first order. The ensemble of trajectories correspond to those within the acceptance limits defined by the scientific requirements, i.e.,  $\delta x'_{\text{max}} = 50$  mrad,  $\delta y'_{\text{max}} = 75$  mrad, and  $\delta p_{\text{max}}/p = 2.5\%$ . Position divergences at FS0 of  $\delta x_{\text{max}} = \delta y_{\text{max}} = 3$  mm are used for visualization purposes. As in the previous figures, the heights of the orange and light-brown boxes represent aperture sizes of the dipole and quadrupole magnets, respectively. .... 143

Figure 6-4 Same as Figure 6-3 but in 5<sup>th</sup> order. Those with and without higher-order corrections are compared. .... 145

Figure 6-5 Angular and momentum resolutions in the high-resolution mode calculated as the difference between the reconstructed and initial angle/momentum in trajectory-reconstruction simulations using COSY-calculated maps including up to 5<sup>th</sup> order. .... 147



- Figure 6-6 Angular and momentum acceptances for the high-resolution mode represented in the same way as in Figure 5-11. .... 148
- Figure 6-7 Quadrupole components of the magnetic fields of the quadrupole magnets of the Spectrometer Section, (a) QSA and (b) QSB, calculated in Maxwell at the radii 160 mm and 320 mm, respectively (80% of the warm-bore radii). Different curves (40 each) correspond to different excitations covering the entire dynamic ranges of operation ..... 149
- Figure 6-8 Fifth-order ion-optical plots for the high-resolution mode of the Spectrometer Section at different magnetic rigidities, (a) 4 Tm, (b) 6 Tm, and (c) 8 Tm with corrections with sextupoles and octupoles. Trajectories are shown for  $\delta x = \pm 3.0$  mm,  $\delta x' = \pm 50$  mrad,  $\delta y = \pm 3.0$  mm,  $\delta y' = \pm 75$  mrad, and  $\delta p/p = -2.5, -1.25, 0, 1.25, 2.5\%$  denoted by different colors. The projections onto the dispersive (x) and non-dispersive (y) planes are shown in left and right columns, respectively. The yellow boxes denote the dipole magnets (DS1 and DS2), and the light-brown boxes the quadrupole magnets. .... 150
- Figure 6-9 Example of the images at FS2 of the unreacted beam and the reaction product for the one-neutron-knockout reaction from  $^{204}\text{Pt}$  at 100 MeV/u with a 100-mg/cm<sup>2</sup>-thick Be target. The top panels show the xy images (in 5<sup>th</sup> order) and the bottom panels show their x projections (in 1<sup>st</sup> order). The left panels are those with the HTBL in the dispersion-matched beam-transport mode, and the right panels are for the achromatic mode. The simulations were done in LISE<sup>++</sup> with the transfer matrices calculated in COSY included. .... 152
- Figure 6-10 Layout of the neutron invariant-mass mode of the Spectrometer Section. The target station FS0' is located between QS2B and DS1. .... 154
- Figure 6-11 Same as Figure 6-3, but for the neutron invariant-mass mode. The ensemble of trajectories correspond to those within the acceptance limits defined by the scientific requirements, i.e.,  $\delta x'_{\text{max}} = 70$  mrad,  $\delta y'_{\text{max}} = 36$  mrad, and  $\delta p_{\text{max}}/p = 5\%$ . Position divergences at FS0' of  $\delta x_{\text{max}} = \delta y_{\text{max}} = 3$  mm are used to depict the trajectories. .... 155
- Figure 6-12. Same as Figure 6-11 but in 5<sup>th</sup> order. Those with and without higher-order corrections are compared. .... 157
- Figure 6-13 Angular and momentum resolutions in the neutron invariant-mass mode. Those without (blue) and with (red) beam tracking are compared. .... 159
- Figure 6-14 Resolution (FWHM) that can be achieved in neutron invariant-mass spectroscopy as a function of excitation energy in the neutron-unbound system based on Monte-Carlo simulations. For two distances between the location of the target and the MoNA-LISA detector array (8 m and 15 m), resolutions are plotted for a perfect spectrometer, operation of the HRS with tracking detectors at FS0', and operation of the HRS with tracking detectors. The properties of the MONA-LISA array were kept fixed and a unbound system with A=40 was used. The results for an A=132 are very similar. .... 159
- Figure 6-15 Angular and momentum acceptances for the neutron invariant-mass mode. .... 160
- Figure 6-16 Layout of the HTBL and the Spectrometer Section of the HRS, together with the ARIS Fragment Separator for the ToF-B $\rho$  mass-measurement mode utilizing a 113-meter-long flight path. ... 162
- Figure 6-17 a) Trajectory plot for the high-resolution mode in the dispersive plane in first order. The spectrometer settings are the same as those in Figure 6-3, but the beam is momentum-dispersed at the entrance by the HTBL in the dispersion-matched mode. The trajectories in different colors correspond different momentum components. Only the transport in the dispersive plane is shown, since the transport



in the non-dispersive plane is identical to that of Figure 6.3. b) Same as a) but in fifth order without hardware corrections. c) Same as b) but with hardware corrections. ....	163
Figure 6-18 Stray field of DS1 at the maximum excitation. The box ( $\pm 3.5 \text{ m} \times 1.5 \text{ m} \times \pm 0.9 \text{ m}$ ) representing the footprint of GRETA placed at FS0' in the neutron invariant-mass mode. Only a quarter of DS1 is shown, where the other quarters were cut out of the model due to the symmetry. The stray fields in very close proximity of the coils are approximately 1800 Gauss, and at the locations of some of the digitizers they exceed the 600-Gauss limit set by GRETA. ....	172
Figure 6-19 Field distributions of DS1, QS1A, and QS2B at the maximum excitation along the beam direction. For the quadrupole fields (middle and bottom), the field strengths at a distance of 20 cm from the beam axis are shown. FS0, FS0', and the center of DS1 are denoted. The footprint of GRETA is shown by the light-brown boxes. The graphs are magnified as indicated for clarity. ....	173
Figure 6-20 Magnetic shielding plate as used downstream of the target location at the S800. A similar shielding plate will be adopted for FS0. Usage of the plate is optional. ....	174
Figure 6-21 Stray field of QS1A and QS2B at the maximum excitation in the high-resolution mode. The box at the origin ( $3.5 \text{ m} \times 1.5 \text{ m} \times \pm 1.25 \text{ m}$ ) represents the GRETA footprint. Only quarters of QS1A and QS2B are shown, where the other three quarters were cut out of the model due to the symmetry. The flux is normal to the yz and zx planes. ....	175
Figure 6-22 Stray field of QS1A and QS2B at the maximum excitation in the neutron invariant-mass mode. The box at the origin ( $3.5 \text{ m} \times 1.5 \text{ m} \times \pm 0.90 \text{ m}$ ) represents the GRETA footprint. Only quarters of QS1A and QS2B are shown, where the other three quarters were cut out of the model due to the symmetry. The flux is normal to the yz and zx planes. ....	176
Figure 6-23 Stray field of DS1 at the maximum excitation on the median plane plotted on top of the layout graphics. The 100-G and 10-G boundaries are denoted. GRETA are shown at FS0 (for the high-resolution mode) and at FS0' (for the neutron invariant-mass mode), and MoNA-LISA is shown at 12 meters from FS0'. ....	177
Figure 6-24 Stray field of QS1A and QS2B at the maximum excitation in the high-resolution mode on the median plane plotted on top of the layout graphics. GRETA is not shown in the interest of showing the field map. ....	178
Figure 6-25 Stray field of QS1A and QS2B at the maximum excitation in the neutron invariant-mass mode on the median plane plotted on top of the layout graphics. GRETA is not shown in the interest of showing the field map. MoNA-LISA is shown at a distance of 12 meters from FS0'. ....	179
Figure 6-26 Schematic layout of the detector configuration of the diagnostic systems used at FS1 and FS2. ....	181
Figure 7-1. Schematic layout of the diagnostics/detector systems for the HRS. Systems at FB1, FB2, FB3, FS0, and mobile systems (blue border) are part of WBS element TPC.T.3.01. Systems at FS1 and FS2 are part of WBS element TPC.T.3.02. ....	187
Figure 7-2. Schematic of the basic diagnostic systems configurations along the HTBL, used for the achromatic mode of operation (a) and for the dispersion-matched mode (b). ....	189
Figure 7-3 Schematic of the location of the diagnostic systems along the HRS, used for the neutron invariant-mass mode (top) and for the high-resolution mode (bottom). ....	191



Figure 7-4. Schematic layout of the detector configuration of the diagnostic systems used at FB1 and FS0. .... 197

Figure 7-5. Schematic layout of the detector configuration of the third diagnostics station (FB3), which include a tracking system (two D-PPACs), a PIN diode for energy-loss measurement for PID, a plastic scintillator, as well as a system of variable slits for beam tuning and other diagnostic purposes..... 197

Figure 7-6. a) Design of the Image box of the A1900 Fragment Separator, which serves as the model for the design of the HTBL diagnostics boxes FB1 and FB3. B) Design of a standard cross chamber used to insert viewers and other simple diagnostics and detector system, which serves as model for the box at FB2. .... 199

Figure 7-7. Schematic layout of the detector configuration of the focal planes of the Spectrometer Section. .... 202

Figure 7-8. Layout of the existing charged-particle detector chamber as presently used for experiments with the Sweeper Magnet at NSCL. The focal-plane detector chambers for the HRS have comparable layout, but are larger in size to accommodate the larger detector systems. .... 203

Figure 7-9. Schematic drawing of the tracking system of the spectrometer focal plane as it is presently used in the S800 Spectrograph at NSCL. The focal-plane tracking detectors of the HRS are upgraded versions of these detectors..... 205

Figure 7-10. Position-sensitive readout of the DC to be implemented for tracking at the spectrometer focal plane..... 205

Figure 7-11(a) Reconstructed pattern of a mask with holes and slits placed in front of a prototype drift chamber for the S800 spectrograph [COR20] that operates in the same manner as the drift chambers of the Spectrometer Section focal planes. (b)Projection in the dispersive direction of the reconstructed pattern from one of the holes in the mask. A position resolution of 0.25 mm ( $\sigma$ ; 0.6 mm FWHM) is deduced. . 206

Figure 7-12.Schematic layout of the OIC presently under construction for the S800 Spectrograph at FRIB. The detector volume is filled with Xenon gas and surrounded by an array of photodetectors. .... 207

Figure 7-13 Illustration of the Improvement in particle identification ( $\Delta E$  vs. ToF in arb. units) through increased  $\Delta E$  resolution ( $\sigma$ ) through LISE++ simulations – Top: Sn, In, Cd and Ag for a traditional (S800) ion chamber (left) and optical ion chamber (right) resolution. Bottom: Pb, Tl, Hg, Au at current (left) and improved resolution (right). Simulations were performed for one reaction residue per relevant Z line to illustrate the  $\Delta E$  separation in the particle identification for example one-neutron knockout experiments from  $^{108}\text{Sn}$  and  $^{212}\text{Pb}$  projectiles to  $^{107}\text{Sn}$  and  $^{211}\text{Pb}$ ..... 208

Figure 7-14. Schematic drawing of the scintillator detector used for timing at the S800 spectrograph focal plane. A similar design will be used at focal planes FS1 and FS2 of the Spectrometer Section. .... 209

Figure 7-15 Estimated timing resolution of a plastic scintillator detectors for the Spectrometer Section focal planes. Light is detected through 26 PMTs attached to the sides of the scintillators. The estimates are based on the response measured with a smaller-sized prototype. A resolution of  $\sim 120$  ps or better is achieved in all areas where particles will be detected in the focal plane. .... 210

Figure 7-16. Schematic drawing of the hodoscope detector for TKE measurements as presently used in the S800 Spectrograph. The hodoscope that will be used in the focal planes of the Spectrometer Section of the HRS will be similar, but the area covered will be larger to account for the larger beam envelope. .... 210



Figure 9-1 (Top) Overview of the magnetic elements of the HRS, with the nomenclature as shown on the left. The HTBL magnetic elements include triplets (TB <sub>x</sub> , x=1..8), dipoles (DB <sub>x</sub> , x=1..4), and steering magnets (SB1, SB2). The Spectrometer Section magnets include six single quadrupoles (type A = QS1A, QS5A, QS6A; type B = QS2B, QS3B, QS4B) and two dipoles (DS1, DS2). .....	220
Figure 9-2 a) Mechanical layout and b) picture of the Quadrupole Triplet used for TB <sub>x</sub> in the HTBL. The same quadrupole design is used in the NSCL A1900 Fragment Separator. ....	225
Figure 9-3 Mechanical design layout (left) and image (right) of an existing XPF 6-Tm dipole magnet used in the NSCL A1900 Fragment Separator. This magnet forms the basis of the dipole magnets used in the HTBL, which are scaled up to accommodate operation at rigidities of up to 8 Tm. ....	227
Figure 9-4 HTBL dipole magnet (DB1-DB4) layout with a length of 160 cm, a width of 280 cm, a height of 165 cm, a gap size of 10 cm, a gap width of 148 cm, necessary to accommodate a pole width of 118.4 cm. The magnet is shown next to an NSCL XFP dipole for comparison. ....	228
Figure 9-5 Magnetic field analysis of the DB <sub>x</sub> dipole magnets of the HTBL. (top) HTBL dipole field profile as a function of position along the central arc. (bottom) Analysis of the magnetic field outside of the steel, which is below the saturation level. This ensures that the fringe fields will not be excessive. ....	229
Figure 9-6 Stress (a and b) and deformation (c and d) calculations for the coil bobbin of the HTBL dipoles before (a and c) and after (b and d) the inclusion of an additional compression link. The displacement along the long straight section has been reduced from 1.76 mm to 0.95 mm. ....	230
Figure 9-7 (a) HTBL steerer (SB1-SB2) layout with a length of 26 cm, a width of 80 cm, a height of 89 cm, a gap of 21 cm, and a pole width of 44.5 cm. (b) SB <sub>x</sub> magnetic dipole field as a function of the position along the central arc, as calculated in MAXWELL. ....	231
Figure 9-8 Spectrometer warm iron quadrupoles section view and layout of QSA (smaller) and QSB with cryogenic service vessels as modeled in relative position before the DS1 spectrometer dipole. ....	233
Figure 9-9 Layout and magnetic-field analysis of the quadrupole magnet types of the Spectrometer Section. (a) Type A; (b) Type B. ....	234
Figure 9-10 Optimized DS1 magnet design vs. initial design. ....	237
Figure 9-11 Magnetic field on the outside of the yoke for the DS1 magnet. ....	237
Figure 9-12 Field profile of spectrometer section DS1 dipole at 3 different radii. ....	238
Figure 9-13 Steel support using three jacks at optimal locations. Upper steel weight applied as load on side yoke surfaces. Assumes frictionless slab to slab contact. Support areas below steel compensated in calculation to keep median plane level. ....	238
Figure 9-14 Bobbin stresses (a) and displacements (b) from helium pressure and Lorentz forces. ....	239
Figure 9-15 Spectrometer dipole DS1 assembly with coil cryostat and cryogenic service vessel. ....	240
Figure 9-16 DS2 dipole layout, including a cut-away view showing the pole-tip and coil details. The length of DS2 is 5.87 m, the width is 4.21 m, and the height is 2.40 m. ....	242
Figure 9-17 DS2 field non-uniformity as a function of the radial position. A non-uniformity ranging from +0.03% to -1.0% is achieved over the good field region in the preliminary design. Note that the ion-optical simulations have found this level of non-uniformity to be acceptable and close to a preliminary specification of 1% non-uniformity. ....	242
Figure 9-18 Circuit diagram for self-protecting magnets. ....	244

Figure 10-1 Typical rack row and device grounding block diagram ..... 249

Figure 10-2 Typical SCM PS block diagram..... 250

Figure 10-3 (top) Rack layout at the mezzanine level, providing space for 38 racks. (bottom) Rack layout at the ground floor level, providing space for 25 racks..... 254

Figure 10-4 Example of a Rack layout spreadsheet..... 254

Figure 10-5 Layout of conduits from equipment racks to the HTBL and Spectrometer Section of the HRS. .... 256

Figure 11-1 Cryogenic system layout preliminary design. .... 262

Figure 11-2 (a) NSCL Box 23 similar to proposed HRS Branch Box 2; (b) NSCL local valve box and transfer line section similar to proposed local HRS cryogenic boxes and transfer line..... 263

Figure 11-3 FRIB ESD-NSCL coupling and east-end distribution area. The HRS transfer line will supply the west-end distribution area. .... 264

Figure 12-1 a) PLC installed in rack; b) Commercial cable; c) Sample IFM; d) 19” racks installed at the Laboratory..... 274

Figure 12-2 Personnel Protection System Architecture ..... 276

Figure 12-3 Preliminary layout of the Personnel Protection Systems for the HRS. .... 277

Figure 12-4 MPS Fast Protection System architecture ..... 277

Figure 12-5 Controls Network Architecture ..... 279

Figure 12-6 Controls Network VLAN Segmentation ..... 279

Figure 13-1 Overview of the vacuum elements and pumping systems of the HRS..... 281

Figure 14-1 The location of the High Rigidity Spectrometer and Isotope Harvesting vault (indicated in red) within the FRIB complex on the campus of Michigan State University. .... 286

Figure 14-2 Layout of the High-Transmission Beam Line (HTBL) and the Spectrometer Section of the HRS ..... 287

Figure 14-3 HRS layout showing three possible beam loss locations (S1, S2, and S3), dipole failure locations (F1, F2, and F3) and radiation dose evaluation points (tallies) L3 (30 cm from door), L4 (30 cm from wall), L6 (60 cm cube at exit of 12” pipe), L7,L8, and L9 (30 cm from nearest walls). Labeled “Door”, the main vault entrance door consists of 18-inch thick steel backed by 6 inches of polyethylene. The closest public area is also shown. .... 288

## 1.4 List of tables

Table 3-1 Work Breakdown Structure for the High Rigidity Spectrometer ..... 32

Table 3-2 Performance Parameters for the HRS..... 34

Table 4-1 Summary of HRS science programs developed by the FRIB user community. The science programs are grouped by the primary overarching NRC Decadal and 2015 LRP science questions they address. For each program, the relevant NSAC 2007 RIB Task force Benchmarks are indicated. .... 41



Table 4-2 Specifications for the HRS for each of the scientific programs listed in Table 4-1. In the bottom three rows, the specifications are summarized by operational mode of the HRS, as described in Section 4.3.1.6. .... 68

Table 4-3 Overview of the three operational modes for the Spectrometer Section ..... 83

Table 4-4 Overview of the specifications of the Spectrometer Section, listed for the three main modes of operation: high-resolution, neutron invariant-mass, and ToF-B $\rho$  mass-measurement modes. .... 84

Table 4-5 Overview of six representative rare-isotope beams that were used to optimize the transmission efficiency of the beam line from the ARIS Fragment Separator to the Targets Station of the HRS. Transmission studies were performed in end-to-end Monte-Carlo simulations (from the production target at the ARIS Fragment Separator to the Target Station of the Spectrometer Section), including the placement of a wedge to optimize the purity of the beams. .... 86

Table 4-6 Luminosity gains for experiments at the HRS compared to performing experiments at the existing S800 Spectrometer for the six representative rare-isotope beams of Table 4-5. .... 91

Table 4-7 Scientific Specifications for the Beam Transport through the High Transmission Beam Line to the Spectrometer Section of the HRS. .... 101

Table 5-1 WBS for the HTBL beam physics. .... 108

Table 5-2 Requirements for the design of the HTBL. This table reproduces the specifications of Table 4-7. .... 111

Table 5-3 First-order matrix elements of the HTBL in the achromatic beam-transport mode and in the dispersion-matched beam-transport mode. Only the ten non-trivial matrix elements are listed. .... 117

Table 5-4 Rare-isotope beam phase spaces at the end of the ARIS Fragment Separator (FB0) obtained from Monte-Carlo Simulations in LISE<sup>++</sup>. The dimensions shown in the table are  $\pm 2\sigma$  values. .... 120

Table 5-5 Overview of the results from the end-to-end simulations performed in LISE<sup>++</sup>. The primary beam, production target, momentum acceptance in the Preseparator (prior to momentum compression), degrader, and rigidity used in the simulations are listed with the transmission efficiencies in the achromatic and dispersion-matched modes. .... 122

Table 5-6 Functional specifications of the quadrupole magnets for the HTBL. Each quadrupole has superimposed sextupole and octupole corrector coils. These quadrupoles are packaged in triplets (FSQB-FSQC-FSQB; FSQB repeats), which are labeled as TB1 through TB8 in Figure 5-1. .... 130

Table 5-7 Functional specifications of the dipole magnets for the HTBL. These dipoles are labeled as DB1 through DB4 in Figure 5-1. .... 131

Table 5-8 Functional specifications of the steerer dipole magnets for the HTBL. These steerer dipoles are labeled as SB1 and SB2 in Figure 5-1. .... 132

Table 5-9 General functional specifications for the diagnostics and detector systems for the HTBL. .... 135

Table 5-10 Functional specifications for the viewer systems for the HTBL. .... 135

Table 5-11 Functional specifications for the tracking and timing detectors for the HTBL. .... 135

Table 5-12 Functional specifications for the energy-loss detectors for the HTBL. .... 136

Table 6-1 WBS for the Spectrometer beam physics. .... 138





Table 6-2 Functional requirement for the three operational modes of the Spectrometer Section of the HRS (see also Table 4-4).	140
Table 6-3 First-order transfer-matrix elements for the high-resolution mode.	143
Table 6-4 Key first-order transfer-matrix elements at the final focus (FS2) of the Spectrometer Section for different magnetic rigidities. The last row shows the ratio of the dispersion to the magnification, the measure of the resolving power of the spectrometer. $\Delta_{\max}$ indicates the maximum deviation (in %) between the matrix elements for different rigidities.	149
Table 6-5 First-order transfer-matrix elements for the neutron invariant-mass mode.	155
Table 6-6 Comparison between the functional requirements for high-resolution mode and the capabilities achieved by the preferred alternative.	165
Table 6-7 Comparison between the functional requirements for neutron invariant-mass mode and the capabilities achieved by the preferred alternative.	166
Table 6-8 Comparison between the functional requirements for ToF-B $\rho$ mass-measurement mode and the capabilities achieved by the preferred alternative. For the calculations, $^{60}\text{Ca}$ at 6.43 Tm was assumed.	167
Table 6-9 Quadrupole magnet specifications for the Spectrometer Section.	170
Table 6-10 Dipole magnet specifications for the Spectrometer Section.	170
Table 6-11 General functional specifications for the diagnostics and detector systems of the Spectrometer Section.	182
Table 6-12 Functional specifications for the tracking and timing detectors for the Spectrometer Section.	182
Table 6-13 Functional specifications for the energy-loss detectors for the Spectrometer Section.	182
Table 7-1. Diagnostics and Detectors WBS.	185
Table 7-2 Overview of the detectors systems of the HRS, by location and purpose.	188
Table 7-3 General functional requirements for the diagnostics and detector systems for the HTBL.	192
Table 7-4 Functional requirements for the tracking and timing detectors for the HTBL, satisfied by D-PPAC and plastic scintillators, respectively.	192
Table 7-5 Functional requirements for the energy-loss detectors for the HTBL, satisfied by the usage of silicon PIN diode detectors.	193
Table 7-6 Functional requirements for the viewer systems for the HTBL.	193
Table 7-7 General functional requirements for the diagnostics and detector systems of the Spectrometer Section.	194
Table 7-8 Functional requirements for the tracking and timing detectors for the Spectrometer Section.	195
Table 7-9 Functional requirements for the energy-loss detectors for the Spectrometer Section.	196
Table 9-1. Magnet system WBS.	219
Table 9-2. High-Transmission Beam Line (HTBL) quadrupole magnet requirements for 8 triplets labeled TB1-TB8 in Figure 9-1. Each triplet has three quadrupole magnet elements: FSQB, FSQC, and FSQB. Each quadrupole segment includes sextupole and octupole windings.	221



Table 9-3 High-Transmission Beam Line (HTBL) dipole magnet requirements for dipoles labeled DBx in Figure 9-1 compared to extant NSCL XFP dipole magnets. .... 222

Table 9-4. High-Transmission Beam Line (HTBL) steerer dipole magnet requirements for steerers labeled SB1, SB2 in Figure 9-1. .... 222

Table 9-5 Quadrupole magnet requirements for the Spectrometer section of the HRS. .... 223

Table 9-6 Dipole magnet requirements for Spectrometer Section of the HRS. .... 224

Table 9-7 Design values for the quadrupole triplets that meet the requirements of Table 9-2 are provided. .... 226

Table 9-8 HTBL DBx dipole design values meeting the requirements of Table 9-3. .... 228

Table 9-9. HTBL SBx steerer design values that meet the requirements of Table 9-4. .... 231

Table 9-10 Spectrometer Section quadrupole design values that meet the requirements of Table 9-5. Note that the initial ion-optical simulations have found the integrated field non-uniformities to be acceptable. The non-uniformity values shown are the values calculated from the magnetostatic models and are similar to the preliminary estimates (1%). The field values from the MAXWELL model were found to achieve acceptable performance providing a sound basis for detailed design and optimization. .... 233

Table 9-11 Spectrometer Section sextupole and octupole design values that meet the requirements of Table 9-5. .... 235

Table 9-12 Spectrometer section DS1 dipole design values that meet the requirements of Table 9-6. .... 241

Table 9-13 Spectrometer section DS2 dipole design values that meet the requirements of Table 9-6. .... 243

Table 9-14 Quench protection methods used for each magnet and preliminary estimated quench results. .... 244

Table 10-1 Power Supply WBS ..... 245

Table 10-2 HTBL PS requirements. .... 251

Table 10-3 Spectrometer Section PS requirements. .... 252

Table 11-1. Work Breakdown Structure (WBS) for HRS cryogenic system. .... 258

Table 11-2. HTBL, Spectrometer Section, and distribution cryogenic loads at 4.5K. .... 260

Table 11-3 Cool-down parameters for each magnet type. .... 260

Table 11-4 Cryogenic load reduction from decommissioned coupled cyclotron elements. .... 261

Table 12-1 WBS for the control systems of the HRS ..... 265

Table 12-2 Signal list for the HTBL quadrupole triplets used to determine the controls I/O requirements. .... 267

Table 12-3 Device I/O Summary for the HTBL, separated into beamline, vacuum and cryoload control systems used to determine the controls I/O requirements. .... 268

Table 12-4 Device I/O Summary for the Spectrometer Section, separated into beamline and cryoload control systems used to determine I/O requirements. .... 269

Table 12-5 Radiation Safety System Hardware and I/O List used to determine I/O requirements ..... 270

Table 12-6 PLC hardware design summary for the HTBL. .... 272



Table 12-7 PLC hardware design summary for the Spectrometer Section..... 272

Table 13-1 WBS for the vacuum systems for the HRS ..... 281

Table 13-2 Vacuum elements of the HTBL..... 284

Table 13-3 Vacuum elements of the Spectrometer Section..... 285

Table 14-1. Beam intensities in particles per second (pps) that satisfy the 2 mrem/h requirement for 250 MeV/u <sup>18</sup>O, <sup>132</sup>Sn, and <sup>238</sup>U stopped at beam loss locations S1, S2, and S3 and tally locations L3, L4, L6, L7, L8, and L9. (see Figure 14-3)..... 290

Table 14-2 Beam intensities in particles per second (pps) that satisfy the 2 mrem/h requirement for 250 MeV/u <sup>18</sup>O, <sup>132</sup>Sn, and <sup>238</sup>U passing through dipole failure locations F1, F2, and F3 and tally locations L3, L4, L6, L7, L8, L9 (see Figure 14-3)..... 290





## 2 Executive summary

Note that this document represents the status of the High Rigidity Spectrometer (HRS) project in about the fourth quarter of FY2021 and includes updates resulting from external reviewer's comments and recommendations. The HRS design will continue to evolve in detail and be further optimized to provide best value while achieving the required performance within cost and on schedule. However, this document will not be further updated. The evolving HRS design parameters and engineering designs will be captured in parameter lists and other technical and engineering documentation. This document is based on a DCC document "FRIB High Rigidity Spectrometer (HRS) Parameters" FRIB-M41800-BL-000096-R002. Note that DCC documents may not be hyperlinked, but in most cases are available upon request.

The HRS project has achieved Critical Decision (CD) – 0 (mission need) in November 2018 and CD-1 (Alternate Selection and Cost Range) in September 2020.

### 2.1 Introduction

The Facility for rare Isotope Beams (FRIB) will be the world's premier rare-isotope beam facility producing a majority (~80%) of the isotopes predicted to exist. This unprecedented discovery potential can be realized by implementing state-of-the-art experimental equipment that can study these isotopes at the highest rates produced. The new High Rigidity Spectrometer (HRS) will substantially increase FRIB's scientific reach and productivity and address the overarching intellectual challenges from the 2015 NSAC Long Range Plan [LRP15] and the NRC Decadal Study [NRC13]. Eleven of the 17 NSAC RIB Taskforce benchmarks [NRC07], which were introduced to characterize the scientific research of a rare-isotope facility, require the use of fast beams at FRIB and benefit from the experimental program that will be performed at the HRS.

### 2.2 Scope

The HRS, shown in Figure 2-1, is proposed as the first major addition to the Facility for Rare Isotope Beams (FRIB) experimental facilities. The HRS consists of two segments: the High-Transmission Beam Line (HTBL) and the Spectrometer Section. The HTBL transports Rare Isotope Beams (RIBs) from the Advanced Rare Isotope Separator (ARIS) fragment separator [HAU13] focal plane (FB0) to the reaction target stationed at the entrance (FS0) of the Spectrometer Section, in which charged reaction products created at the target are analyzed. A wide variety of high-impact ancillary detector systems developed by the nuclear science community for experiments at FRIB will be used in combination with the HRS, such as the Gamma-Ray Energy Tracking Array (GRETA) [GRE20] and the Modular Neutron Array (MoNA-LISA) [BAU05]. The HRS project scope includes the design, procurement, installation, and



commissioning of the technical elements including the magnets and concomitant diagnostics, controls, power supplies, and cryogenic ancillary systems. The conventional facilities were provided by Michigan State University (~\$23M) with beneficial occupancy in February 2020.

## 2.3 Capabilities

The key characteristic of the proposed HRS is its ability to accommodate rare-isotope beams up to magnetic rigidities of 8 Tm, matching the rigidities at which the rare-isotope production in the ARIS fragment separator is optimized for isotopes across the chart of nuclei, even with an envisioned FRIB upgrade to 400 MeV/u. Consequently, experiments with the HRS greatly increase the sensitivity of the scientific program at FRIB, in particular for experiments with the most neutron-rich isotopes that have the highest potential for discovery. In combination with the ability to use thicker reaction targets at the higher magnetic rigidities, gain factors in luminosity of 2 to 100 will be achieved for over 90% of experiments with neutron-rich isotopes. These gains are over what will be possible with existing spectrometers at the National Superconducting Cyclotron Laboratory (S800 and Sweeper) that have a maximum magnetic rigidity of 4 Tm. The largest luminosity gains are achieved for the most neutron-rich species, including many of the nuclei that in the path of the astrophysical *r* process.



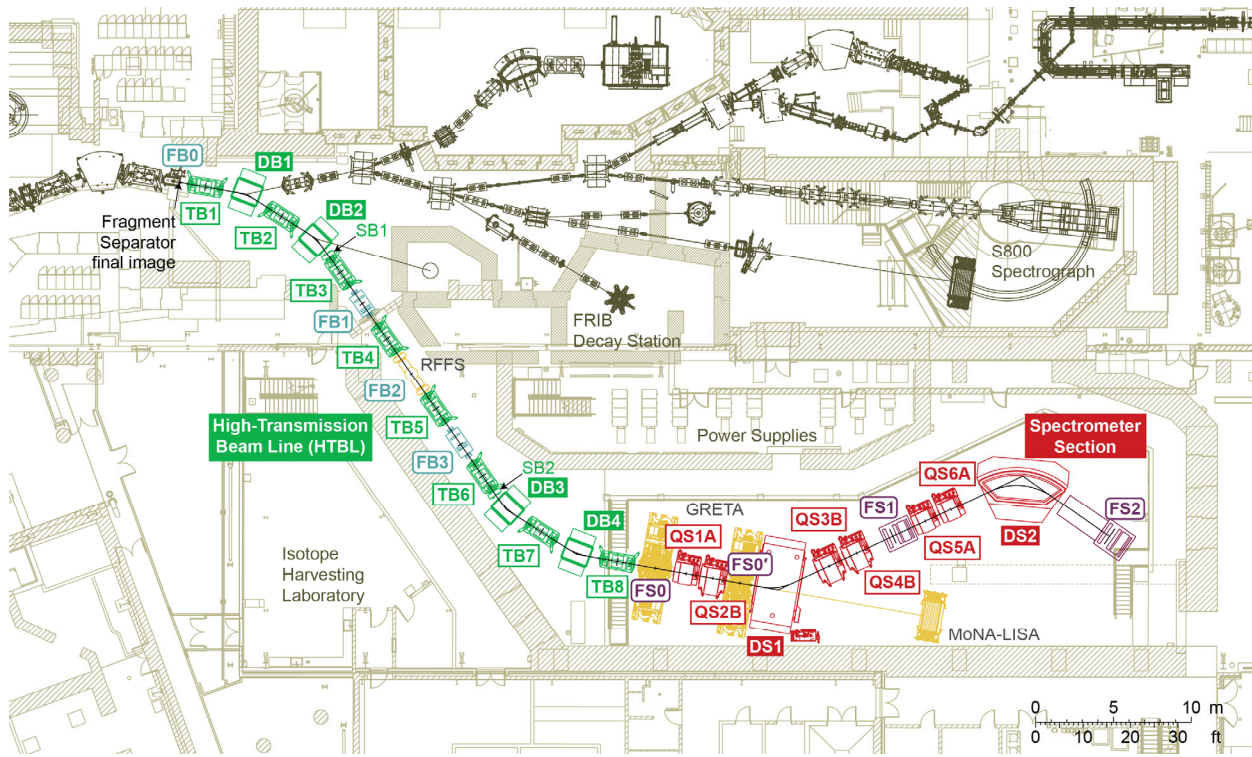


Figure 2-1 Layout of the High Rigidity Spectrometer (HRS) at FRIB, consisting of the High-Transmission Beam Line (HTBL) and the Spectrometer Section. The conventional facilities that will house the HRS are as well as the Isotope Harvesting Laboratory were provided by MSU with beneficial occupancy February 2020. GRETA and MoNA-LISA are examples of ancillary detector systems that will be used in combination with the HRS.

## 2.4 Cost and schedule

A preliminary cost and schedule estimate have been made for the HRS project. The preliminary Total Project Cost (TPC) is about \$96.5M in then-year dollars including a contingency of approximately 40.6% from a bottom-up element-by-element analysis. Depending on funding, the project is estimated to take approximately eight years to complete.

## 2.5 Acquisition strategy

Michigan State University designs and establishes the HRS project with financial assistance from DOE and additional contributions provided by MSU. MSU will own the HRS, operate the HRS for DOE, and MSU will be responsible for decommissioning of the HRS. The Cooperative Agreement between MSU and DOE-SC outlines the roles and responsibilities between MSU and DOE-SC. The design, fabrication, testing, assembly, installation and commissioning of the HRS project will be mainly performed by MSU staff. Some work may be performed by national laboratories or universities under work for others (WFO) agreements or similar. Much of the subcontracted work to be performed for the HRS project consists of hardware fabrication. Consistent with the acquisition strategy which provides financial assistance to MSU and with DOE Contracting Officer direction, the HRS project will be regulated external to DOE through the existing regulators who regulate activities at MSU.

## 2.6 References

- [BAU05] T. Baumann et al., *Nucl. Instr. and Meth. A*543, 517 (2005)
- [GRE20] GRETA Final Design Report
- [HAU13] M. Hausmann *et al.*, Design of the Advanced Rare Isotope Separator ARIS at FRIB, *Nucl. Instrum. Methods Phys. Res., Sect. B* 317, 349 (2013)
- [LRP07] The Frontiers of Nuclear Science, A Long Range Plan, Nuclear Science Advisory Committee (2007)
- [NRC07] Scientific Opportunities with a Rare-Isotope Facility in the United States, National Research Council; Division on Engineering and Physical Sciences; Board on Physics and Astronomy; Rare-Isotope Science Assessment Committee (2007)
- [NRC13] National Research Council. *Nuclear Physics: Exploring the Heart of Matter*. Washington, DC: The National Academies Press, 2013



## 3 Project overview

### 3.1 Introduction

The Facility for rare Isotope Beams (FRIB) will be the world's premier rare-isotope beam facility producing a majority (~80%) of the isotopes predicted to exist. This unprecedented discovery potential can be realized by implementing state-of-the-art experimental equipment that can study these isotopes at the highest rates produced. Eleven of the 17 NSAC RIB Taskforce benchmarks [NRC07], which were introduced to characterize the scientific research of a rare-isotope facility, require the use of fast beams at FRIB. All of these programs require a magnetic spectrograph of the type described in this document. A new High Rigidity Spectrometer (HRS) will substantially increase FRIB's scientific reach and productivity and addresses the overarching intellectual challenges from the 2015 NSAC Long Range Plan [LRP15] and the NRC Decadal Study [NRC13]. The scientific reach of the HRS is discussed in detail in Section 4. The HRS, shown in Figure 2-1, is proposed as the first major addition to the FRIB experimental facilities.

The 8 Tm bending power of the proposed HRS matches the rigidities at which rare isotopes will be produced at FRIB, even with the envisioned FRIB upgrade to 400 MeV/u. This will enable the most sensitive experiments across the entire chart of nuclei, thereby enabling experiments with the most neutron-rich nuclei available at FRIB. In combination with the ability to use thicker reaction targets at the higher rigidity, gain factors in luminosity of 2 to 100 will be achieved for over 90% of experiments with neutron-rich isotopes. These gains are over what will be possible with existing spectrometers at NSCL (S800 and Sweeper) that have a maximum rigidity of 4 Tm. The largest luminosity gains are achieved for the most neutron-rich species.

### 3.2 Project organization

The High Rigidity Spectrometer (HRS) Project will deliver the scope funded by the Total Project Cost. The HRS Project has been established within the FRIB Laboratory, which is a unit within Michigan State University (MSU). The HRS Project will be managed by utilizing the expertise and processes implemented at the Laboratory for the execution of the FRIB Project. This ensures the complete integration of the HRS into FRIB to provide the full benefit of the opportunities for FRIB Users. Priorities between different activities at the FRIB Laboratory are set to maximize the FRIB scientific program.

MSU will design, build, and commission the HRS Project with financial assistance from DOE and contributions from MSU. While DOE Order 413.3B [DOE4133B] does not apply to financial assistance transactions, the project will follow best project management practices.





### 3.3 Work breakdown structure

The HRS Project has organized the scope of work into a Work Breakdown Structure (WBS). The WBS contains the complete definition of the HRS Project at Michigan State University and forms the basis for all phases of the project: planning, execution, control, and oversight of contracts. The HRS WBS [M41800-BL-000090] is shown in Table 3-1.

The WBS elements are defined as specific systems, management, research and development, or pre-operations. The WBS elements are discrete items of project work and are consistent with execution methods. Note the facility infrastructure was designed to specifications provided by HRS personnel, paid for by MSU, and completed February 2020. As a consequence, facility infrastructure is not part of the HRS DOE project scope.

WBS elements HRS.1, HRS.3, and HRS.4 are the full scope included in the Total Project Cost (TPC) and will be delivered by the HRS Project. Level 2 elements of the FRIB Project WBS are:

- HRS.1 Management and Support – Project office administrative and management activities that integrate over the entire project
- HRS.3 Experimental Systems-High Rigidity Spectrometer – All phases of design, procurement, installation, and commissioning of the experimental systems
- HRS.4 Pre-operations - integrated testing and commissioning to achieve CD-4

The performance baseline will be formulated against WBS level 3.



Table 3-1 Work Breakdown Structure for the High Rigidity Spectrometer

WBS Element		WBS Element		WBS Element	
Description	Element	Description	WBS Element	Description	Element
<b>Management &amp; Support</b> HRS.1.01	HRS.1	<b>Experimental Systems - High Rigidity Spectrometer</b> HRS.3	HRS.3	<b>Preoperations</b> HRS.4	HRS.4
Project Management HRS.1.01.01	1	High Transmission Beamline (HTBL) HRS.3.01	HRS.3.01	Integrated Testing and Systems Commissioning HRS.4.01	HRS.4.01
Travel HRS.1.01.02	2	High Transmission Beamline Beam Physics HRS.3.01.01	HRS.3.01.01	Integrated Testing HRS.4.01.01	HRS.4.01.01
Business Management HRS.1.02	3	High Transmission Beamline Diagnostics and Tracking HRS.3.01.02	HRS.3.01.02	Commissioning HRS.4.01.02	HRS.4.01.02
Project Controls HRS.1.02.01	4	HTBL Diagnostic Devices HRS.3.01.02.01	HRS.3.01.02.01	Performance Parameters and Completion Criteria HRS.4.01.03	HRS.4.01.03
Procurement Support HRS.1.02.02	5	HTBL Tracking Detectors HRS.3.01.02.02	HRS.3.01.02.02		
Material Handling HRS.1.02.03		High Transmission Beamline Magnets HRS.3.01.03	HRS.3.01.03		
Supplies and Services HRS.1.02.04		HTBL Dipole Magnets HRS.3.01.03.01	HRS.3.01.03.01		
<b>Environmental Safety, Health and Quality (ESH&amp;Q)</b> HRS.1.03		HTBL Quadrupole & Multipole Magnets HRS.3.01.03.02	HRS.3.01.03.02		
Quality Assurance HRS.1.03.01		HTBL Installation, Testing and Magnet Mapping HRS.3.01.03.03	HRS.3.01.03.03		
ES&H HRS.1.03.02		High Transmission Beamline Vacuum HRS.3.01.04	HRS.3.01.04		
Systems Engineering & Integration HRS.1.04		High Transmission Beamline Power Supplies HRS.3.01.05	HRS.3.01.05		
Systems Engineering HRS.1.04.01		High Transmission Beamline Cryogenics HRS.3.01.06	HRS.3.01.06		
Documentation HRS.1.04.02		High Transmission Beamline Low Level Controls HRS.3.01.07	HRS.3.01.07		
Integrated Design HRS.1.04.03		High Transmission Beamline Alignment HRS.3.01.08	HRS.3.01.08		
		Spectrometer HRS.3.02	HRS.3.02		
		Spectrometer Beam Physics HRS.3.02.01	HRS.3.02.01		
		Spectrometer Magnets HRS.3.02.03	HRS.3.02.03		
		Spectrometer Dipole Magnets HRS.3.02.03.01	HRS.3.02.03.01		
		Spectrometer Quadrupole & Multipole Magnets HRS.3.02.03.02	HRS.3.02.03.02		
		Spectrometer Installation, Testing and Magnet Mapping HRS.3.02.03.03	HRS.3.02.03.03		
		Spectrometer Structural Support and Access to Detector Systems HRS.3.02.04	HRS.3.02.04		
		Spectrometer Detector Support and Access to Reaction Target HRS.3.02.04.01	HRS.3.02.04.01		
		Spectrometer Detector Support for MoNA-LISA Detector System HRS.3.02.04.02	HRS.3.02.04.02		
		Spectrometer Detector Access Platforms HRS.3.02.04.03	HRS.3.02.04.03		
		Spectrometer Focal Plane Detector Systems HRS.3.02.05	HRS.3.02.05		
		Spectrometer High Resolution Mode Focal Plane Detector Systems HRS.3.02.05.01	HRS.3.02.05.01		
		Spectrometer Invariant Mass Mode Focal Plane Detector Systems HRS.3.02.05.02	HRS.3.02.05.02		
		Spectrometer Vacuum HRS.3.02.06	HRS.3.02.06		
		Spectrometer Power Supplies HRS.3.02.07	HRS.3.02.07		
		Spectrometer Cryogenics HRS.3.02.08	HRS.3.02.08		
		Spectrometer Low Level Controls HRS.3.02.09	HRS.3.02.09		
		Spectrometer Alignment HRS.3.02.10	HRS.3.02.10		
		Central Systems HRS.3.03	HRS.3.03		
		Protection Systems HRS.3.03.01	HRS.3.03.01		
		Personnel Protection Systems HRS.3.03.01.01	HRS.3.03.01.01		
		Machine Protection Systems HRS.3.03.01.02	HRS.3.03.01.02		
		Network & IT HRS.3.03.02	HRS.3.03.02		
		High Level Controls HRS.3.03.03	HRS.3.03.03		
		Technical Utilities and Infrastructure HRS.3.03.04	HRS.3.03.04		

WBS LEVEL KEY	Level
Example	1
HRS.1	2
HRS.1.01	3
HRS.1.01.01	4
HRS.1.01.01.01	5



### 3.4 Performance Parameters

The Threshold Key Performance Parameters, Objective Key Performance Parameters, and Ultimate Performance Parameters have been defined in the Preliminary Project Execution Plan (PPEP) [FRIB-M41800-AD-000585] and are based on the specifications discussed in Section 4.3.

The Threshold and Objective Key Performance Parameters (KPPs), and Ultimate Performance Parameters (UPPs) for the HRS are provided in Table 3-2. All sets of performance parameters will be demonstrated with beams delivered from FRIB. The Threshold KPPs define the minimum acceptable performance required to satisfy mission need and CD-4 project completion. These Threshold KPPs demonstrate the successful completion of technical construction, and minimal commissioning resulting in transport of an isotope beam through the HTBL and the detection, identification, and momentum analysis in the Spectrometer Section through the measurement of the momentum distribution of the residual nucleus from single-nucleon knockout from an  $^{40}\text{Ar}$  or similar-mass isotope beam.

The Objective Key Performance Parameters (Objective KPPs) deliver the baseline and ensure that a large majority of the science program of the HRS can be performed for rare-isotope beams with masses of up to  $A=132$ . Experiments with beams with  $A>132$  are feasible, but resolutions do not meet the full set of specifications for the HRS.

The Ultimate Performance Parameters (UPPs) are achieved, after CD-4 after gaining operational experience using the HRS with a variety of beams and in multiple operational modes. The full science program of the HRS can be performed and the mission goals for the HTBL and Spectrometer Section can be achieved with UPP performance.





Table 3-2 Performance Parameters for the HRS

	Threshold Key Performance Parameters	Objective Key Performance Parameters	Ultimate Performance Parameters
Magnetic rigidity	7 Tm	7 Tm	8 Tm
Momentum resolving power $p/\Delta p$ (FWHM)	750	1000	1500
Mass resolving power $M/\Delta M$ (FWHM)	100	220	400
Charge resolving power $Z/\Delta Z$ (FWHM)	34	85	156
Beam-transport modes	Achromatic	Achromatic and dispersion-matched	Achromatic and dispersion-matched
Angular resolution: tracking in HTBL and in Spectrometer Section	15 mrad	10 mrad	5 mrad
Rare-isotope beam transmission in achromatic mode	50%	75%	95%
Momentum acceptance and solid angle Spectrometer Section (High resolution mode)	$\pm 2.0\%$ / 10 msr	$\pm 2.0\%$ / 10 msr	$\pm 2.5\%$ / 15 msr

### 3.5 Life Cycle Costs

The Life Cycle Costs include cost of implementation, operation, and decommissioning.

The HRS components can have an operational life of at least 20 years. The cost of HRS operation will be supported by FRIB operations. HRS operations cost is estimated to be \$1.125M annually (FY19 \$). Operations is estimated to begin in 2028 with operations until 2048 (20 years). Escalating costs to mid-point (2038 = 19 years) and assuming inflation of 2.3% equals about \$1.125M x (1.54 = escalation) x 20 years ~\$35M.

The decommissioning costs are not included here since from the FRIB Cooperative Agreement, MSU is responsible for decommissioning costs.

The estimated life-cycle cost to government is about \$96.5M (construction) + \$35M (20 years operation paid from FRIB operational budget) + ~\$0M (MSU decommissioning) equals ~\$131M.

### 3.6 Risk assessment

The HRS Project has a risk registry to catalog, assess, track and develop management actions for discrete (“known” or forecasted) risk events and their associated potential impacts to the HRS project cost, schedule, or technical baselines. Since the HRS Project has ion optics based on



simulations benchmarked by decades of MSU Rare Isotope Beam (RIB) experience and since the required hardware is similarly based upon decades of MSU utilizing superconducting driven, iron-dominated magnetic elements, as well as power-supply, controls, diagnostics, and detector technology, there will be no R&D program required.

Following the HRS Project Risk Management Plan [FRIB-M41800-PL-000358], control Account Managers have first-line responsibility for the bottom-up estimate of potential contingency as well as discrete risk identification, assessment, reporting, and development of mitigation plans and strategies as inputs to the risk register. The risk register is reviewed periodically by HRS project management to ensure risks are appropriately classified, that mitigation plans are developed and implemented where needed, and to ensure resources are allocated consistent with management priorities to reduce risk. The current risk registry [FRIB-M41800-PG-000010] entries amount to a 6% contingency.

The preliminary Total Project Cost (TPC) is about \$96.5M in then-year dollars including a contingency from item-by-item, bottom-up analysis of approximately 40.6%. Depending on funding, the project is estimated to take approximately eight years to complete. At the current state of the design, HRS project management has determined that this level of contingency in light of the risks identified is adequate to avoid undue overall risk to the proposed project.

### 3.7 ESH and Quality Requirements and Plans

The various regulatory agencies both establish requirements for HRS design, establishment, and operation and provide oversight and inspection of the project's implementation of the requirements. The applicable HRS project regulatory requirements are documented in the Regulatory Requirements document [FRIB-T10400-TD-000363]. Regulating agencies include (but are not limited to) the U.S. Nuclear Regulatory Commission, the U.S. Department of Transportation, various State of Michigan agencies and Michigan State University.

The HRS Project team has committed to maintaining ISO 45001, ISO 14001, and ISO 9001, registered programs. These self-imposed and third-party registered management systems assure that FRIB maintains the current high standards for Occupational Health and Safety, Environmental Management, and Quality Management required to maintain these certifications.

### 3.8 References

[DOE4133B] <https://www.directives.doe.gov/directives-documents/400-series/0413.3-BOrder-B-chg5-minchg>

[FRIB-T10400-TD-000363] FRIB Regulatory Requirements with ESH&Q inputs

[FRIB-T10102-PL-000213] FRIB Project Risk Management Plan



[FRIB-M41800-AD-000585] Preliminary Project Execution Plan for the High Rigidity Spectrometer

[FRIB-M41800-PL-000358] High Rigidity Spectrometer (HRS) Risk Management Plan

[FRIB-M41800-PG-000010] HRS Risk Register

[LRP07] [The Frontiers of Nuclear Science, A Long Range Plan, Nuclear Science Advisory Committee \(2007\)](#)

[NRC07] [Scientific Opportunities with a Rare-Isotope Facility in the United States, National Research Council; Division on Engineering and Physical Sciences; Board on Physics and Astronomy; Rare-Isotope Science Assessment Committee \(2007\)](#)

[NRC13] National Research Council. *Nuclear Physics: Exploring the Heart of Matter*. Washington, DC: The National Academies Press, 2013



## 4 Science enabled with the High Rigidity Spectrometer (HRS) at FRIB

### 4.1 Introduction

The Facility for Rare Isotope Beams (FRIB) will be the world’s premier rare-isotope beam facility, producing a majority (~80%) of the isotopes predicted to exist [ERL12, AFA13]. The scientific community envisions to make full use of this vast, new access to the nuclear landscape through experimental programs that have the furthest reach into “terra incognita” on the nuclear chart. The unprecedented access to new isotopes makes FRIB a critical component of the DOE mission to understand the fundamental forces and particles of nature as manifested in nuclear matter and will provide the necessary expertise and tools from nuclear science to meet national needs. The DOE Nuclear Physics mission, its relation to the FRIB science drivers, their reflection in the NRC decadal study “Nuclear physics: Exploring the Heart of Matter” [NRC13], the NSAC 2007 and 2015 LRP key questions [LRP07, LRP15], and the NSAC Rare Isotope Beam Taskforce 17 benchmarks [NRC07] are illustrated in Figure 4-1. The figure illustrates how the scientific goals of the field, addressing the challenges posed by the NRC Decadal Study and reiterated in the 2015 LRP, drive FRIB capabilities. The FRIB project has used the benchmarks to evaluate the facility’s ability to deliver on its scientific promise. The bottom of the figure illustrates the tools required for each of the benchmarks. To achieve the goals, the need for a broad-approach technical scope was recognized that provides fast, stopped, and reaccelerated beams of rare isotopes. Of the 17 benchmarks, 11 require the use of fast beams (indicated in red in Figure 4-1) and strongly benefit from the use of a magnetic spectrograph.

**Impact of a high rigidity spectrometer:** The scientific impact of the FRIB fast beam science program will be substantially enhanced (by luminosity gain factors of between two and one hundred for neutron-rich isotopes, with the largest gains for the most neutron-rich species) by construction of a high-performance magnetic spectrograph. The High Rigidity Spectrometer (HRS), consisting of the High-Transmission Beam Line (HTBL) and the Spectrometer Section, will allow experiments with beams of rare isotopes at magnetic rigidities for which the maximum production rates for fragmentation or in-flight fission are achieved. This enhancement in experimental sensitivity provides access to critical isotopes not available otherwise. The scientific benefit of this additional sensitivity is discussed below. The scientific reach of the experimental program at FRIB is also enhanced by opportunities to perform experiments at beam energies in the 100-250 MeV/*u* range. The key spectrometer feature needed to reach the sensitivity limits of FRIB and access additional forefront science above 100 MeV/*u* is operation at rigidities of up to 8 Tm, appropriate even with the envisioned FRIB upgrade to 400 MeV/*u*. The current laboratory spectrometers are limited to 4 Tm.



<p><b>U.S. Department of Energy Office of Science Office of Nuclear Physics mission is to understand the fundamental forces and particles of nature as manifested in nuclear matter, and provide the necessary expertise and tools from nuclear science to meet national needs</b></p>			
<p><b>DOE-SC Nuclear Physics mission is accomplished by supporting scientists who answer overarching questions in major scientific thrusts of basic nuclear physics research</b></p>			
<p>Intellectual challenges from National Research Council Decadal Study and the Nuclear Science Advisory Committee (NSAC) 2015 Long Range Plan (LRP)</p>			
Nuclear Structure	Nuclear Astrophysics	Tests of Fundamental Symmetries	Applications of Isotopes
How does subatomic matter organize itself and what phenomena emerge?	How did visible matter come into being and how does it evolve?	Are fundamental interactions that are basic to the structure of matter fully understood?	How can the knowledge and technological progress provided by nuclear physics best be used to benefit society?
<p><b>Overarching Questions from NSAC 2007 LRP</b></p>			
What is the nature of the nuclear force that binds protons and neutrons into stable nuclei and rare isotopes?  What is the origin of simple patterns in complex nuclei?	What is the nature of neutron stars and dense nuclear matter?  What is the origin of the elements in the cosmos?  What are the nuclear reactions that drive stars and stellar explosions?	Why is there now more matter than antimatter in the universe?	What are new applications of isotopes to meet the needs of society?
<p><b>Overarching questions are answered by rare-isotope research</b></p>			
<p>17 Benchmarks from NSAC Rare Isotope Beam Task Force measure capability to perform rare-isotope research</p>			
<p>1. Shell structure 2. Superheavies 3. Skins 4. Pairing 5. Symmetries 13. Limits of stability 14. Weakly bound nuclei 15. Mass surface</p>	<p>6. Equation of state (EOS) 7. r process 8. <sup>15</sup>O(α,γ) 9. <sup>59</sup>Fe supernovae 13. Limits of stability 15. Mass surface 16. rp process 17. Weak interactions</p>	<p>12. Atomic electric dipole moment 15. Mass surface 17. Weak interactions</p>	<p>10. Medical 11. Stewardship</p> <p><b>(HRS contributes)</b></p>
<p><b>MSU proposed technical scope is sufficient to meet all benchmarks</b></p>			

Figure 4-1 FRIB will allow users to answer the overarching questions from the NSAC 2007/15 Long Range Plan and the latest NRC Decadal Study, and thereby supporting the DOE Nuclear Physics Mission. The NSAC RIB TF developed 17 benchmarks to test facility capability to address these questions. Meeting these benchmarks has driven the technical scope and specifications for FRIB. The benchmarks also guide the equipment development necessary for the program.





The 2015 NSAC LRP recognized that the “HRS...will be essential to realize the scientific reach of FRIB” and that “Another key addition to FRIB is the proposed High-Rigidity Spectrometer, which would enable in-flight reaction experiments with the most neutron-rich nuclei available from FRIB.” The strong community support was reiterated in the 2018 Low-Energy Community meeting, at which the following resolution was unanimously adopted: “The community endorses the prompt initiation and timely completion of the High Rigidity Spectrometer (HRS) construction project, an essential instrument for fast-beam experiments at FRIB.”

## 4.2 Science with the HRS

The following sections summarize, for each of the four challenges posed by the NRC Decadal Study and reiterated in the 2015 LRP, example research programs that will be enabled when the fast rare-isotope beams produced at FRIB can be used at the optimum magnetic rigidities. The last two sections outline the opportunities afforded by a high rigidity spectrometer for nuclear reactions and discovery science at FRIB. Throughout this science section, high-impact key examples are highlighted that – once enabled – allow for broad research programs addressing the 11 benchmarks associated with fast beams, all using similar experimental approaches. In Table 4-1, an overview of the science programs afforded by the HRS is provided and linked to the relevant benchmarks. In Section 4.3, scientific specifications are determined for each of these programs, which serve as input for the preliminary design of the HRS.

### 4.2.1 How does visible matter organize itself

One of the key challenges identified for the field of nuclear science in the National Academies Decadal Study is: “How does subatomic matter organize itself and what phenomena emerge?” [NRC13]. Answers to this compelling question require a predictive model of atomic nuclei that is based on the fundamental interactions at play between its constituents. On the quest for this comprehensive description of nuclei and their reactions, the properties of rare isotopes have emerged as the critical constraints for improving our understanding of poorly known but essential many-body forces [FOR13]. The shortest-lived, weakly bound isotopes near the nucleon driplines also uniquely quantify the role of the particle continuum that contributes to all nuclear systems including neutron stars.

The following five subsections outline a research program focused on crucial aspects of nuclear structure research, including the study of shell structure, collectivity, and shapes; spectroscopy in the particle continuum; the exploration of the proton-neutron degree of freedom; and point out the opportunity of commensal decay spectroscopy following reactions. The key examples of this section are the spectroscopy of bound states in the most neutron-rich Ca isotopes and the spectroscopy of neutron-unbound states in the region around  $^{40}\text{Mg}$ .





#### 4.2.1.1 Evolution of shell structure, collectivity, and shape

The often surprising properties of nuclei beyond the valley of  $\beta$  stability have prompted extensive experimental and theoretical studies aimed at identifying the multiple driving forces behind the dramatic changes in nuclear shell structure that are encountered in rare isotopes. A multitude of observables are needed for a comprehensive picture of structural evolution in the quest for a predictive model. These include excitation energies, spins, parities, and transition matrix elements. Often, long semi-magic isotopic chains emerge as critical since they allow tracking shell evolution from the proton to the neutron dripline, with several doubly magic systems along the way. Complementary information is sought in regions of rapid changes in shape or collective behavior where certain drivers of structural change can be isolated. Outlined in the following are example research programs that will be enabled by a high rigidity spectrometer.



Table 4-1 Summary of HRS science programs developed by the FRIB user community. The science programs are grouped by the primary overarching NRC Decadal and 2015 LRP science questions they address. For each program, the relevant NSAC 2007 RIB Task force Benchmarks are indicated.

	HRS Science Program	NSAC 2007 RIB Task force Benchmark										
		1. Shell structure	3. Skins	5. Symmetries	6. Equation of State	7. R-process	11. Stewardship	13. Limits of Stability	14. Weakly-bound nuclei	15. Mass Surface	16. RP-process	17. Weak interactions
<b>Nuclear Structure</b>	At the limits of the nuclear chart: at and beyond the neutron dripline	x	x		x			x	x			
	Single-particle structure and collectivity from prompt in-beam gamma-ray spectroscopy	x				x		x				
	Fingerprints of shell evolution with isomer studies	x				x					x	
	Excited-state lifetimes as indicators of shell-evolution	x										
	Inelastic proton scattering as a probe of the pn degree of freedom	x										
	Physics along the N=Z line	x		x		x		x			x	
	Commensal decay spectroscopy following reactions	x										x
	Knock-out reactions	x										
	Quasifree scattering				x							
	Elastic scattering		x		x							
	Total reaction/interaction measurements		x		x				x			
<b>Nuclear Astrophysics</b>	Heavy-ion collisions				x							
	Heavy-ion EM excitations				x	x						
	Isoscalar giant resonances		x		x							
	Isvector giant resonances		x		x							x
	Time-of-flight mass measurements	x				x				x	x	
	Projectile fragmentation and in-flight fission of neutron-rich nuclei					x		x				
	Weak Reaction rates for astrophysics					x					x	x
<b>Fundamental Symmetries</b>	Gamow-Teller strengths, neutrinos, and the quenching of $g_A$	x										x
<b>Applications</b>	Improving nuclear structure inputs to fission models	x						x				



**Exploring shell structure in isotopic chains with prompt in-beam  $\gamma$ -ray spectroscopy following reactions** – In-beam  $\gamma$ -ray spectroscopy with fast beams is often used as a sensitive tool to tag an inelastic excitation or to identify and quantify the final states populated in reactions, ultimately providing cross sections for reactions to specific final states [GAD08a]. Single-particle properties tracked across long isotopic chains towards the extremes of isospin provide an opportunity to isolate specific drivers of shell evolution as function of neutron-richness and weak binding.

A high rigidity spectrometer coupled to a  $\gamma$ -ray detection array such as GRETA will enable the detailed prompt  $\gamma$ -ray spectroscopy at the very limits of FRIB reach, and the combination of the two devices will be a cornerstone of experimental equipment for discovery science at FRIB. Such programs will extend to all proton-magic isotopic chains and their vicinity, with the  $Z=28$  Ni isotopes next in reach for ab-initio Coupled-Cluster calculations [HAG16], see for example Figure 4-2 for predictions of  $2^+_1$  state energies in even-even Ni isotopes out to  $A=80$ . This is only possible for the most relevant nuclei furthest away from stability when projectile beams can be used at the rigidities where their production is optimum.

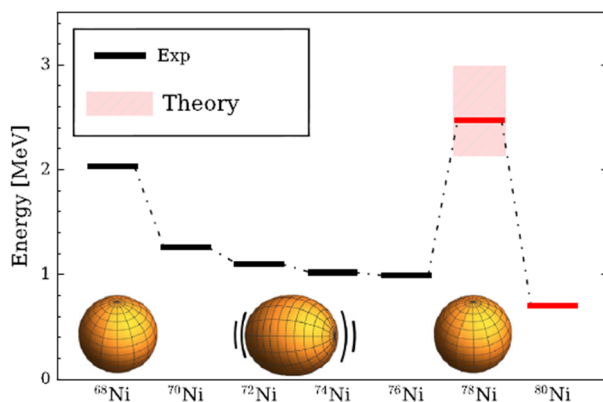


Figure 4-2: First ab-initio type Coupled Cluster calculations of  $2^+$  energies around the key nucleus  $^{78}\text{Ni}$  [HAG16]. In-beam  $\gamma$ -ray spectroscopy at a high rigidity spectrometer at FRIB will enable spectroscopy along magic chains to benchmark ab-initio calculations and explore the effects of many-body correlations in the regime of weak binding.

**Excited-state lifetimes as indicators of shell evolution** – Excited-state lifetime measurements provide a model-independent approach to obtain transition matrix elements which quantify and characterize collective phenomena. Using a system comprised of a target and degrader foils (plunger device),  $\gamma$  rays emitted behind each foil will have different Doppler shifts and the lifetime of the state emitting the  $\gamma$ -ray transition can then be determined using relative  $\gamma$ -ray yields measured at different foil separations [IWA16]. This approach is applicable to different transition modes such as E1, M1 and E2 excitations if the level lifetimes are within measurable ranges of about one picosecond to one nanosecond. At a high rigidity spectrometer, such excited-state lifetime measurements will be performed using GRETA placed around a plunger device at the target position. The higher beam energies possible, afforded by a high rigidity spectrometer, will

not only give access to new regions of the nuclear chart but also increase the reach of such recoil-distance measurements that are based on a multi-foil plunger scheme.

Rapid changes in the collectivity and shape coexistence phenomena induced by shell evolution far from stability are of great interest in the pursuit of a comprehensive understanding of nuclei [HEY11,GAD16]. A new region of interest only accessible at FRIB is the ‘fifth island of inversion’ around  $^{78}\text{Ni}$  [NOW16], where so-called normal-order and shell-breaking intruder configurations compete, which results in the appearance of two or more different intrinsic shapes and associated band structures even at low excitation energies (see Figure 4-3).

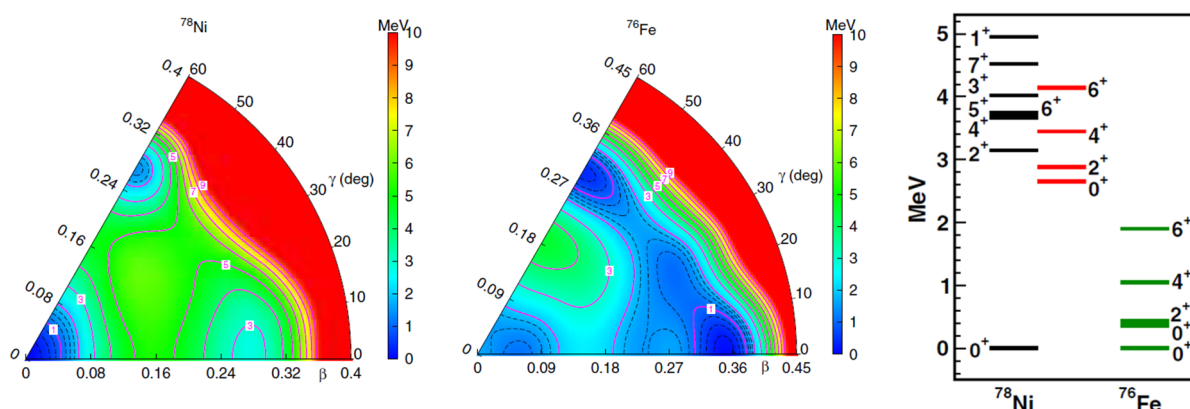


Figure 4-3 Potential energy surface for  $^{78}\text{Ni}$ ,  $^{76}\text{Fe}$  and level schemes for the same nuclei as predicted by large-scale shell-model calculations [NOW16]. The dark blue minima indicate different deformations that the nucleus is predicted to assume at low excitation energies. Transition strength measurements at and around  $^{78}\text{Ni}$  will reveal band structures built on the different deformations and their interconnections.

Critical excited-state lifetime measurements for the  $2^+$  and  $4^+$  states in such neutron-rich nuclei can be performed at FRIB by combining GRETA and a high rigidity spectrometer to enable measurements at optimum production yields and with the highest  $\gamma$ -ray energy yield. Through the measurement of transition rates for higher-lying states, the excited band character as well as associated shell configurations can be experimentally investigated for the first time in many critical regions of the nuclear chart. In this way, modification of the shell structure will be probed as a function of spin, isospin, and excitation energy, paving the way for a complete understanding of the shell evolution in rare isotopes.

**Fingerprints of shell evolution with isomer studies** – An experimental challenge for the powerful reaction studies proposed for medium-heavy to heavy nuclei is the occurrence of long-lived isomeric states in the reaction products as well as in the incoming projectile beam. Such

isomers may be yrast traps, signal symmetries (K isomers), or connect to the particle continuum (particle-emitting isomer). In fact, these isomeric states are often direct fingerprints of shell evolution: Excited states that cross a shell gap to intrude the normal-order single-particle structure may become isomeric through their hindered decays [GAD15].

In order to identify and characterize the tell-tale important isomeric states, a new approach of tagging and identifying the population of isomeric states in the reaction products has been developed recently and applied at the S800 spectrograph at NSCL [ME111, WIM14]. The decays of isomeric states with lifetimes between  $\sim 100$  ns and several ms have been observed and event-by-event linked to the implantation event. In certain regions, such as the neutron-rich isotopes around  $^{78}\text{Ni}$ , in-beam experiments at a high rigidity spectrometer will benefit from such detection of delayed  $\gamma$ -ray or conversion electrons in the focal plane to identify and characterize the isomeric states populated.

#### 4.2.1.2 Key example – Spectroscopy the most neutron-rich Ca isotopes

The proton-magic calcium isotopes with  $Z=20$  present a unique laboratory for studying the evolution of nuclear structure with increased neutron number. Within this single isotopic chain are some of the clearest examples to date of changing single-particle energies as a result of the spin-isospin component of the nucleon-nucleon interaction, namely the appearance of new sub-shell gaps at  $N=32$  and  $34$  [HUC85, STE13]. In addition, recent microscopic and ab-initio calculations [HOL12, HAG12, HER14, HOL14] have highlighted the Ca isotopes as a region critical for testing the role of many-body forces and the particle continuum.

FRIB will provide access along the  $^{20}\text{Ca}$  isotopic chain with unparalleled reach, allowing for detailed spectroscopy as far as  $N=36$ , and first spectroscopy out to  $^{60}\text{Ca}$ . Benchmark tests of microscopic and ab-initio theory will be possible using direct nucleon knockout reactions. Figure 4.4 shows a simulated Doppler reconstructed spectrum of  $^{60}\text{Ca}$  as it may be observed following a  $^9\text{Be}(^{61}\text{Sc}, ^{60}\text{Ca}+\gamma)$  one-proton knockout reaction performed at a high rigidity spectrometer with  $\gamma$ -ray detection using GRETA (150 hours of beam on a  $500\text{ mg/cm}^2$  thick target). Fast beams of neutron-rich Ca isotopes will have magnetic rigidities approaching 6 Tm and a high rigidity spectrometer will be critical to enable such nucleon knockout experiments at the optimum projectile production yields. This is demonstrated with Figure 4-4: If the same experiment was performed at the S800 [BAZ03] (with a maximum rigidity of 4 Tm), the yield would drop by a factor of 24 for the same run time, rendering the measurement essentially impossible.



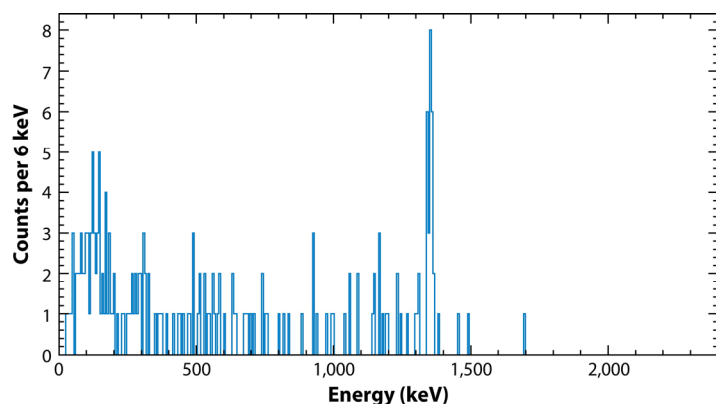


Figure 4-4 Simulation of the excitation energy spectrum of  $^{60}\text{Ca}$  as Doppler-reconstructed with GRETA following a direct one-proton knockout reaction from  $^{61}\text{Sc}$  at 200 MeV/u. The cross section was estimated based on [GAD14] with the  $2^+$  energy as predicted by large-scale shell model [LEN10] and full transmission of the  $^{61}\text{Sc}$  rare-isotope beam to the reaction target was assumed. Without the factor of 24 gain in luminosity from a High Rigidity Spectrometer, this experiment will not be possible (Figure from [FAL16]).

Such in-beam  $\gamma$ -ray spectroscopy experiments at the limits of the nuclear chart are enabled by the increased luminosity from the use of thick reaction targets. The combined gains of projectile beam delivery at a rigidity that optimizes the rare-isotope beam production and increased luminosity through the use of thick secondary targets are often 1-2 orders in magnitude.

#### 4.2.1.3 Key example – Nuclear structure in the particle continuum around $^{40}\text{Mg}$

Unique opportunities for nuclear structure physics arise in various regions of the nuclear chart. Approaching the particle continuum, for example, near and beyond the neutron dripline, structural change is driven by weak binding and modified many-body correlations [DOB07]. New phenomena, such as two-neutron radioactivity or ground-state di-neutron emission, discovered at NSCL [KOH13,SPY12], emerge as unique messengers of the nuclear interior.

The structure of these neutron-unbound nuclei, populated by different reactions from fast rare-isotope beams impinging on a reaction target at the target position of a high rigidity spectrometer, will be determined from the reconstructed decay energy. This is accomplished by measuring the full 4-momenta of the neutron(s) and the projectile-like charged residue. Using invariant mass spectroscopy, the MoNA-LISA/Sweeper [BAU05,MRI09] setup at NSCL has been pioneering in the exploration of the most neutron-rich nuclei. In such experiments, typically, a one- or two-proton knockout reaction from a rare-isotope beam is used to populate an unbound state or nucleus which then immediately, within  $\sim 10^{-21}$  seconds, decays into the projectile-like decay daughter and one or more neutrons. The charged remnant is deflected into a suite of detectors by the Sweeper magnet while the neutrons, unaffected by the magnetic field, travel forward into the MoNA and LISA neutron arrays. Since the momentum, angle, and mass of each particle in the decay process are measured, the momentum 4-vectors are known and the invariant mass or decay energy of the system can be reconstructed [BAU12].





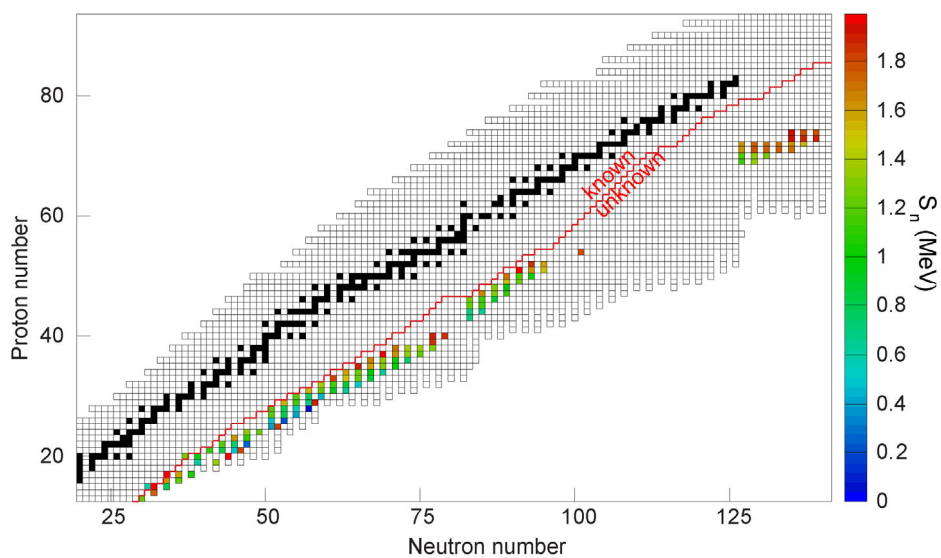


Figure 4-5 Isotopes that FRIB will produce at intensities in between  $0.0001/s$  and  $1/s$  and that have neutron separation energy below 2 MeV and are of strong interest for invariant-mass spectroscopy. The limit of known nuclei on the neutron-rich side is indicated by the red line. Outlined isotopes provide an estimate of the limits of particle-bound isotopes from the KTUY model [KOU05]. For these very neutron-rich systems, such as around  $^{84}\text{Ni}$  and  $^{140}\text{Sn}$ , high luminosity is critical, which requires an experimental station that can operate at high rigidities.

As illustrated in Figure 4-5, by combining  $\gamma$ -ray spectroscopy with neutron invariant-mass spectroscopy, a large number of very neutron-rich systems that have low neutron-separation energies can be investigated, ranging from light to heavy nuclei. Such studies will venture deep into terra incognita and require the highest beam luminosities, and therefore, a spectrometer that operates at high rigidities.

One region of interest is the group of weakly bound nuclei around  $^{40}\text{Mg}$ , where the  $N=28$  shell closure is suspected to break down. Invariant mass spectroscopy of neutron-unbound states is critical to understand the impact of the neutron continuum on shell evolution. A recent frontier has been the study of multi-neutron correlations in the break-up of systems unbound with respect to two or more neutrons. In this region,  $^{38}\text{Na}$  and  $^{44}\text{Mg}$ , for example, are predicted to be unbound to the emission of four neutrons [MOE95] and their investigation is of great interest for understanding multi-neutron correlations in the continuum.

In the  $^{40}\text{Mg}$  region, the combined gains, from accepting beams at the rigidity that optimizes their production and the luminosity afforded by a thick reaction target, over performing the experiment at 4 Tm exceed a factor of 100.



#### 4.2.1.4 The proton-neutron degree of freedom

The proton-neutron degree of freedom and its impact on nuclear observables is among the central aspects in nuclear structure physics. Throughout physics, symmetries play a fundamental role in our basic understanding and theoretical description of nature. In nuclei, the similarity of neutrons and protons combined with the charge independence of the nuclear force is contained in the concept of isospin symmetry. Complementary approaches have been developed that probe the proton-neutron degree of freedom in the most exotic nuclei.

The following briefly outlines example programs envisioned at FRIB where inelastic proton scattering, spectroscopy along the  $N=Z$  line, and the investigation of spin-isospin degrees of freedom are enabled at a high rigidity spectrometer, exploring the proton-neutron degree of freedom far from stability.

**Inelastic proton scattering as a probe of the proton-neutron degree of freedom** – Inelastic proton scattering has been proven to be a powerful tool in the investigation of the proton–neutron degree of freedom in nuclear structure physics [ALA96]. In the proximity of a closed neutron or proton shell, the quantification of proton and neutron contributions to a transition rate provides crucial information on the relative importance of valence nucleons and the core. In inelastic proton scattering, collective modes are preferentially excited. In even–even nuclei these are most often the lowest-lying  $2^+$  and  $3^-$  excited states. Hadronic scattering is complementary to Coulomb excitation, for example, since the electromagnetic (Coulomb) excitation interrogates the proton transition matrix element,  $M_p$ , only, while inelastic proton scattering probes both proton and neutron matrix elements. Deformation lengths deduced for excited states populated in proton scattering can be combined with electromagnetic reduced transition probabilities,  $B(E2)$ , from Coulomb excitation or excited-state lifetime measurements, to determine the ratio of neutron to proton transition matrix elements  $M_n/M_p$  [BER83]. This ratio, for collective  $2^+$  states in even-even nuclei, is a sensitive indicator of a shell closure.

An inverse-kinematics proton scattering program using a liquid-hydrogen target and GRETA for  $\gamma$ -ray tagging would focus on key the nuclei  $^{100}\text{Sn}$  and  $^{132}\text{Sn}$  at  $Z = 50$ , the  $N = 82$  nucleus  $^{128}\text{Pd}$ ,  $^{50}\text{Ni}$  and  $^{78}\text{Ni}$  at  $Z = 28$ ,  $^{58}\text{Ca}$  at  $Z = 20$ , and the  $N = 28$  nucleus  $^{40}\text{Mg}$ , for example. Such studies will only succeed if the optimum production yields can be used at the rigidities enabled by a high rigidity spectrometer.

Similarly, proton-tagged scattering measurements using an active-target time projection chamber currently under development would be used at a high rigidity spectrometer to constrain optical model parameters for exotic nuclei through proton angular distribution measurements.



**Physics along the  $N=Z$  line** – The consequences of isospin symmetry are most clearly revealed in nuclei containing equal or nearly equal numbers of protons and neutrons ( $N \cong Z$ ) [WAR06]. With increasing mass, the proton dripline moves closer to isotopes along the  $N=Z$  line, and neutron-deficient nuclei beyond  $N=Z$  are unbound, including one of the  $T=1/2$  mirror partners. A high rigidity spectrometer will allow access to these isotopes and enable science related to isospin symmetry breaking, pairing interactions in nuclei, defining the boundaries of the proton dripline, spectroscopy and mass measurements of unbound nuclei and the physics in the vicinity of  $N=Z=50$   $^{100}\text{Sn}$ .

In recent years, studies of mirror nuclei in the  $f_{7/2}$  shell have provided information on Coulomb energy difference (CEDs) up to high spin [BEN07]. Many of these experiments have increased their reach in both spin and isospin degrees of freedom through the use of modern advanced  $\gamma$ -ray detector systems coupled to fast-beam spectrographs [MIL16a, MIL16b]. These types of experiments, when performed at FRIB with GRETA at a high rigidity spectrometer, will allow to push further into the  $fp$  shell and out to the most neutron-deficient members of an isobaric multiplet. In particular, measurements of the  $T=1/2$  mirror pairs beyond  $^{70}\text{Kr}$  and approaching  $^{100}\text{Sn}$  will be possible to study in detail, yielding the most complete data yet at the most extreme limits along the  $N=Z$  line.

Little information exists on many short-lived unbound nuclei beyond the proton dripline. While some proton-unbound nuclei can and have been studied through beta-delayed proton emission [BLA07], many are only accessible using in-flight decay methods. Experiments which utilize techniques similar to those recently employed for  $^{69}\text{Br}$  [ROG11] require a spectrometer capable of identifying and measuring the heavy decay residue. A high rigidity spectrometer would be the high-resolution tool for such proton resonance spectroscopy of dripline nuclei which lie along the  $N=Z$  line between rubidium and tin, with their properties nearly completely unknown. A spectrometer setup with an open geometry and ample opportunity for charged-particle detection would be needed.

For such experiments, the higher beam energy afforded by a high rigidity spectrometer will not only help to maximize the projectile rate but also increase beam purity, which is notorious on the proton-rich side of the nuclear chart at lower beam energies.

**The spin-isospin degree of freedom from Gamow Teller strength** – The extraction of Gamow-Teller strength distributions from intermediate-energy charge-exchange reactions provides an important tool for testing theoretical models. Gamow-Teller strength distributions are very sensitive to the evolution of nuclear shells in asymmetric systems. Since Gamow-Teller transitions are associated with spin and isospin transfer, experiments provide a rather direct window into the spin-isospin components of the nucleon-nucleon interaction [OST92, HAR01]. Rare-isotope production rates at FRIB peak at around 170-200 MeV/u which is near ideal for ensuring a clean



one-step reaction mechanism [LOV81, OST92] and a near model-independent extraction of Gamow-Teller strengths.

A unique way of testing the goodness of a core – defining a model space in nuclear theory – uses Pauli blocking effects in charge-exchange reactions. If  $N=50$  was a good neutron core on the neutron-rich side of the nuclear chart, charge-exchange reactions in the  $(n,p)$  direction would proceed with little cross section and suppressed Gamow Teller strength since the transition is blocked. For example, the rare-isotope production rates at FRIB and the very efficient transmission to the HRS will allow for such experiments along  $N=50$  from stable  $^{86}\text{Kr}$  to neutron-rich  $^{80}\text{Zn}$ . Gamow-Teller transitions strengths in unstable nuclei are also sensitive probes of shell-mixing [ZEG10,MEH12] and will be used across the chart of nuclei as complementary tools to other probes for mapping shell evolution.

For charge-exchange reactions in inverse kinematics, a high rigidity spectrometer will be used to detect and characterize the heavy-ion reaction products. For the  $(p,n)$  charge-exchange probe in inverse kinematics [SAS11,SAS12], existing low-energy neutron detector arrays can be used to detect recoil neutrons, in combination with the Ursinus Liquid Hydrogen target. For the  $(^7\text{Li},^7\text{Be})$  reaction, GRETA will be used to detect both the 430-keV  $\gamma$  ray from the first excited state in  $^7\text{Be}$ , tagging spin-transfer, as well as  $\gamma$  rays emitted in-flight from the excited nucleus produced in the charge exchange. In addition, decay particles (neutrons and/or protons) emitted from reaction residues when excited above the particle-decay threshold will be detected with neutron and charged-particle detectors placed downstream from the reaction target. By employing invariant-mass spectroscopy, the excitation energy can then be determined. Below the particle decay threshold, the excitation energy can be extracted directly from the heavy ion detected in the spectrometer. An alternative to the  $(^7\text{Li},^7\text{Be})$  reaction is the  $(d,^2\text{He})$  reaction in inverse kinematics. A time projection chamber will be used to reconstruct the momentum of the unbound  $^2\text{He}$ -particle from the accurate measurement of the momentum of the two decay protons, while the projectile-like reaction residues will be detected and characterized in the HRS. From the reconstructed  $^2\text{He}$  momentum, the excitation energy and scattering angle can be determined.

#### 4.2.1.5 Opportunities with commensal decay spectroscopy following reactions

In typical fragmentation or nucleon removal experiments, a large number of very exotic nuclei can be produced and transmitted to the focal plane of a spectrometer. Downstream of particle identification detectors in the focal plane, reaction products could be implanted into an active stopper such as a Si detector array, which would act as a total-kinetic energy detector, but would also be sensitive to the signals from the subsequent  $\alpha$  or  $\beta$  decays of rare reaction products. A scintillator array immediately downstream of the implantation station would be sensitive to



isomeric  $\gamma$  rays, such as the current S800 hodoscope [MEI11,WIM14], but also to delayed  $\gamma$  rays in the  $\alpha$  or  $\beta$  decay daughters.

Such a focal-plane detector arrangement would provide a unique opportunity to take advantage of the cocktails of rare isotopes produced in a variety of reactions delivered to the focal plane of the spectrometer in a standard experiment. These isotopes will likely be among the most exotic produced at FRIB, and innately of physics interest. Optimization of the high rigidity spectrometer focal plane will allow optimal use of FRIB beams, with decay information obtained simultaneously with the (primary) physics goals of the in-flight experiment.

#### 4.2.2 How does visible matter come into being and how does it evolve?

Reaction and decay networks in stars, stellar explosions, and binary mergers are responsible for the ongoing nucleosynthesis in the Universe (see Figure 4-6). They power astrophysical phenomena, such as novae, supernovae, nucleosynthesis in neutron-star collisions, and X-ray bursts. Nuclear properties determine the light curves of many objects, the elemental abundances or in the composition of meteorites and pre-solar grains. Neutron stars, the remnants of supernova explosions of massive stars, are among the most compact objects with a crust that may contain some of the most neutron-rich nuclei possible in the crust surrounding a core of unknown composition. The nuclear equation of state, electron capture rates, and the location of the neutron dripline are most important to understand these extreme objects.

One of the challenges in the field is an understanding of the  $r$  process thought responsible for the origin of the heavy elements in the Universe. The possible sites of the  $r$  process and consequently its conditions and reaction and decay sequences have remained elusive until 2017 where one  $r$ -process site was reported from a spectacular multi-messenger astronomy campaign following the first LIGO/Virgo observation of the gravitational wave signal, GW170817, from a neutron-star merger [ABB17]. In addition to the gravitational-wave signal originating from two neutron stars spiraling into each other, a kilonova, powered by the radioactive decay of the synthesized neutron-rich nuclear matter, was left behind, observed and characterized across the electromagnetic spectrum [KAS17]. An understanding of the radioactive decays of the rare isotopes produced during the merger is crucial to interpret the kilonova signal and connect it to elemental abundances attributed to an  $r$  process. The gravitational-wave signal from GW170817 also provided unprecedented information on the size, mass, and deformability of neutron stars, which directly inform the fundamental properties of dense nuclear matter – in turn, knowledge on the nuclear equation of state is crucial to deduce the energy radiated by the gravitational waves and understand the amount of neutron-rich matter released.





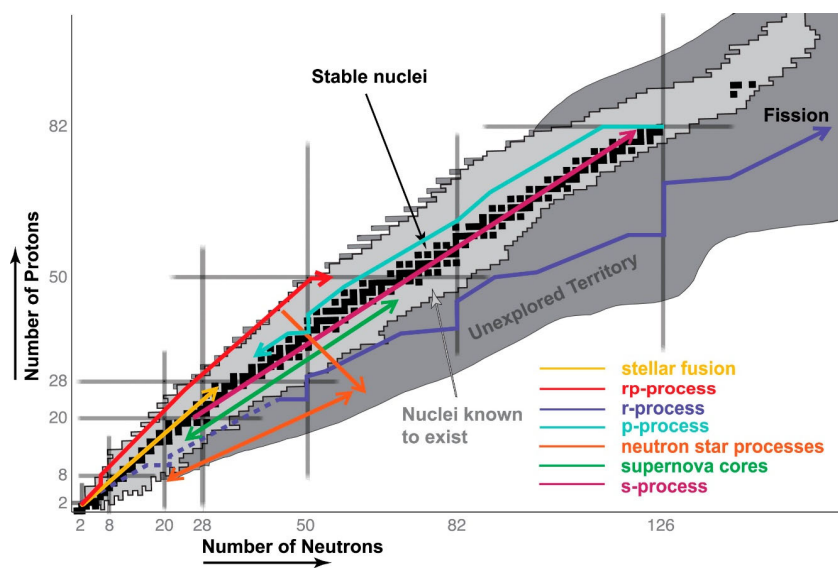


Figure 4-6 Overview of the main astrophysical processes superimposed on the chart of nuclei [AST17]. Often the most critical isotopes are farthest from stability and hence produced at low rates at FRIB. Sensitivity will be key to provide all the necessary astrophysical data [Figure from F. Timmes].

At a high rigidity spectrometer at FRIB, heavy-ion reactions can be used to constrain the nuclear equation of state, nuclear masses, needed to determine Q values in all nucleosynthesis process, including the  $r$  process, can be determined very far from stability through time-of-flight mass measurements, and electron capture rates and nuclear fission can be characterized to constrain nucleosynthesis in the  $r$  process. This is outlined in the following sections.

#### 4.2.2.1 Key example – Access nuclear masses closest to the dripline

Most nucleosynthesis processes involve rare isotopes far from stability, in particular, the  $r$  process and processes in the crust of neutron stars proceed along very neutron-rich nuclei. Nuclear masses are needed to understand the reaction and decay paths since they set the Q values.

Predictions from models [ERL12] agree quite well for known masses, but the divergence between different model predictions grows steadily (to several MeVs) when extrapolating into unexplored regions, in particular on the neutron-rich side. For astrophysical purposes, the present theoretical mass uncertainties need to be improved with measurement far out to anchor extrapolations. Typically, measurements of mass excesses of nuclei far from stability with a precision of 0.1-0.5 MeV are required. For the  $r$  process in neutron star mergers, data on a large number of very neutron-rich nuclei are needed to reveal relevant systematic trends in the mass surface (see Figure 4-7).



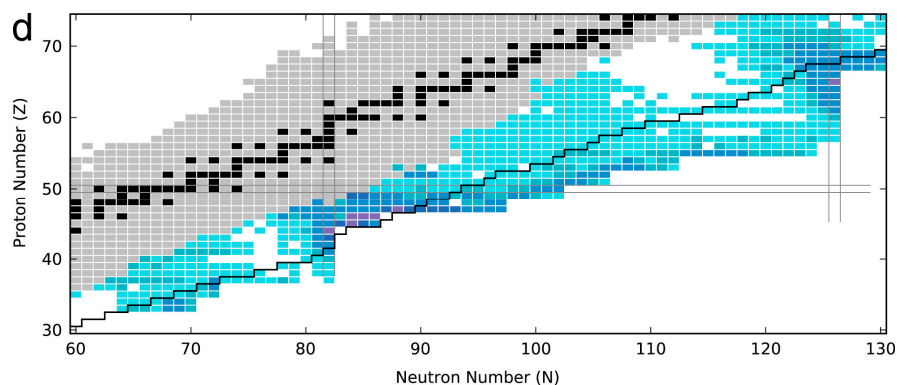


Figure 4-7 Sensitivity study for nuclear masses in an  $r$  process ensuing in a neutron star merger (Figure from [MUM16]). The darker the blue shading, the more important the nuclear mass for modeling the  $r$  process.

Far from stability, masses can be deduced efficiently from the simultaneous measurement of an ion's time-of-flight (ToF), charge, and magnetic rigidity through a magnetic system of a known flight path. ToF mass measurements can reach a significant fraction of the nuclei relevant for the  $r$  process and neutron star crust physics. Tens of masses can be measured in one experiment, including of shortest-lived ones closest to the neutron dripline (see [EST11, MEI13, MEI15] for the reach using NSCL's S800 analysis and spectrograph beam lines for ToF mass measurements). The flight path at a high rigidity spectrometer at FRIB would comprise the transmission and spectrometer beam lines, as well as part of the ARIS Fragment Separator.

Figure 4-8 shows that at FRIB, at the rigidities that optimize rare-isotope production, a large fraction of the nuclei on the  $r$ -process path (orange) up to  $N \sim 100$  can be reached with such measurements. Up to  $N \sim 140$ , the less neutron-rich isotopes in the  $r$ -process path can be accessed and model extrapolations will be significantly improved. A large fraction of the nuclei of importance for neutron-star crustal processes (up to  $N \sim 60$ ) can be measured at a high rigidity spectrometer using the ToF- $B\rho$  technique. Mass resolutions of better than 150 keV (FWHM) for  $A=50$ , 300 keV for  $A=100$ , and 500 keV for  $A=170$  are achievable. The reach assumed for the above-mentioned opportunities assumed 1000 particles per week accumulated.

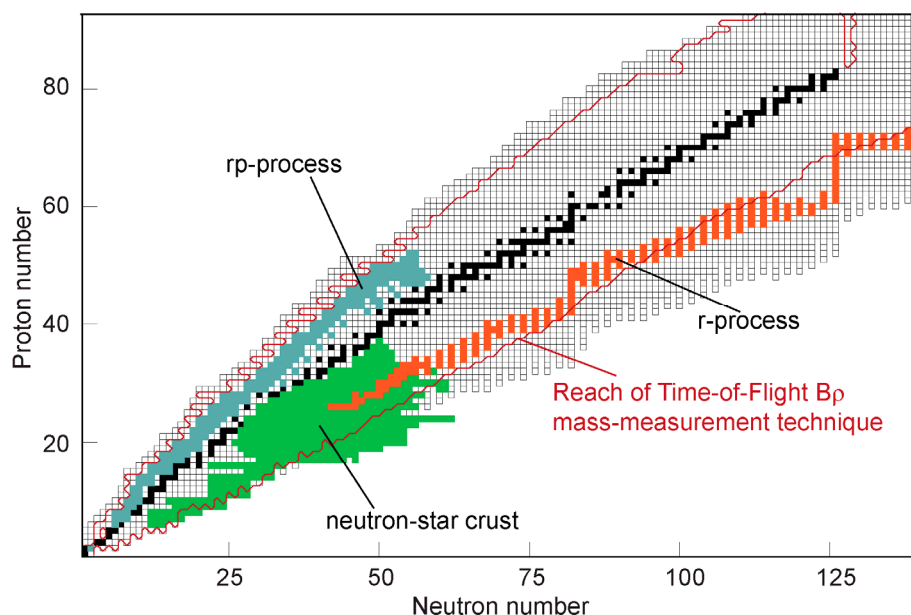


Figure 4-8 Applicability of ToF-Bp mass measurement technique at FRIB. The reach for this technique is indicated by the red line, which indicates the RIB production rate of 1000 per week. At FRIB, a large fraction of the nuclei in the r-process path (orange) up to  $N \sim 100$  can be covered. Up to  $N \sim 140$ , the less neutron-rich isotopes in the r-process path are covered and model extrapolations will be significantly improved. A large fraction of the nuclei of importance for neutron-star crustal processes (up to  $N \sim 60$ ) can be measured at the HRS using the ToF-Bp technique. Mass resolutions of better than 150 keV (FWHM) for  $A=50$ , 300 keV for  $A=100$ , and 500 keV for  $A=170$  can be achieved.

#### 4.2.2.2 Weak reaction rates in nuclear astrophysics

Weak reactions involving unstable nuclei play key roles in pre-[HEG01] and late evolution of core-collapse supernovae [BET79,HIX03,LAN03,JAN07,SUL16,RIC17], thermonuclear supernovae [BRA00,IWA99,ZEG08], neutron stars and their crusts [GUP07,SCH13] and neutron-star mergers [GOR15]. For the astrophysical applications listed above, details of the Gamow-Teller strength distribution in the electron-capture/ $\beta^+$  direction are most important, but transition in the  $\beta^-$  direction must be known with reasonable precision as well. Weak rates on rare isotopes are critical, as shown in Figure 4-9 for the example of electron captures in the late stages of core-collapse supernovae.

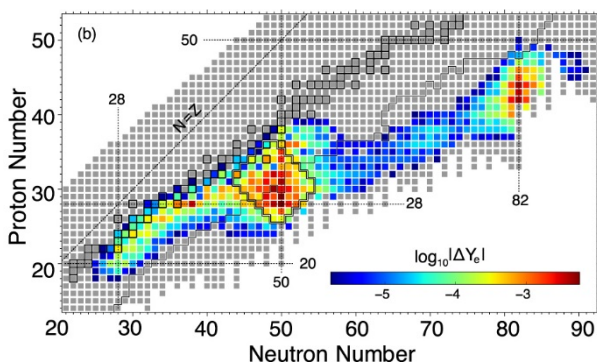


Figure 4-9 The 500 electron-capturing nuclei with the largest absolute change to the electron fraction  $|\Delta Y_e|$  up to neutrino trapping in the late stages of core-collapse supernovae [SUL16]. The most important region is in the neutron-rich region along the  $N=50$  line, which can be studied by using charge-exchange reactions at a high rigidity spectrometer.

Many of the sensitive nuclei are far from stability, for example in the region around  $^{78}\text{Ni}$ , and it will be critical to be able to perform the charge-exchange measurements at the rigidities where the rare-isotope production is optimized. It will be impossible to measure all the relevant Gamow-Teller strength distributions and accurate theoretical models are required to estimate the weak rates of interest for all astrophysical applications. Weak interaction rates measured for such key nuclei will serve as nuclear theory benchmarks for extrapolating into the regions out of reach experimentally.

The complete arsenal of charge-exchange probes, such as  $(p,n)$ ,  $(d,^2\text{He})$  and  $(^7\text{Li},^7\text{Be})$  in inverse kinematics, will be employed for the weak-rate measurements. The advantage of combining charge-exchange experiments with high-resolution  $\gamma$ -ray spectroscopy has been demonstrated [NOJ14,NOJ15,ZAM19,TIT19] and is envisioned with GRETA at a high rigidity spectrometer. As shown in Figure 4-9, the region around  $^{78}\text{Ni}$  is critical for constraining electron-capture rates in core-collapse supernovae and is mostly accessible for charge-exchange experiments at the HRS. Neutron-rich isotopes with proton numbers between 10 and 50 are important for heating and cooling processes in neutron-star crusts and most of the important cases [SCH13] can be reached in experiments with the HRS.

#### 4.2.2.3 Projectile fragmentation and in-flight fission of neutron-rich nuclei

Fission properties of neutron-rich isotopes are an important input for astrophysical models of nucleosynthesis during the  $r$ -process. As the sequence of neutron captures and  $\beta$  decays that drives the  $r$ -process takes the matter flow towards very heavy isotopes, different fission modes (spontaneous, induced and  $\beta$ -delayed fission) will become the dominant reaction types [PAN05] and will impact the end-point for the  $r$  process. Therefore, fission stalls the reaction flow to the heavier masses and determines the heaviest elements that can be synthesized. Fission also affects the final abundances of the produced heavy elements. For example, when nuclei decay towards stability at the end of the neutron-capture stage,  $\beta$ -delayed fission will reduce the amount of cosmochronometer isotopes, such as Uranium and Thorium, that are synthesized in the  $r$ -process

[THI83, SCH02]. Fission also has an important global effect on the abundance patterns of  $r$ -process isotopes in the mass region of fission fragments.

Reliable data on the isotopic distribution of fission fragments is necessary to understand this effect, in particular for an  $r$ -process scenario at sites with very high neutron density, such as mergers of binary neutron-star systems. In such neutron-rich scenarios, the reaction flow will go through several cycles of synthesis up to heavy masses, followed by fission-recycling back to intermediate mass region [KOR12, GOR13]. The distribution of fission fragments then leaves a strong imprint on the resulting  $r$ -process abundances, and can contribute to a robust abundance pattern of individual  $r$ -process events, as illustrated in Figure 4-10.

Recent progress on fission measurements [SCH01, ERL12a, CAA13, PEL13, AND10] shows the potential for having appropriate data to improve our understanding of this very complex many-body process. The ability to produce very neutron-rich heavy beams at FRIB, coupled with the high transmission to a high rigidity spectrometer and the potential for measuring fission fragments in coincidence, allows for detailed measurements of fission-fragment distributions in unexplored regions of the nuclear chart, thereby providing critical data for understanding of the physics of nuclear fission in  $r$ -process calculations.

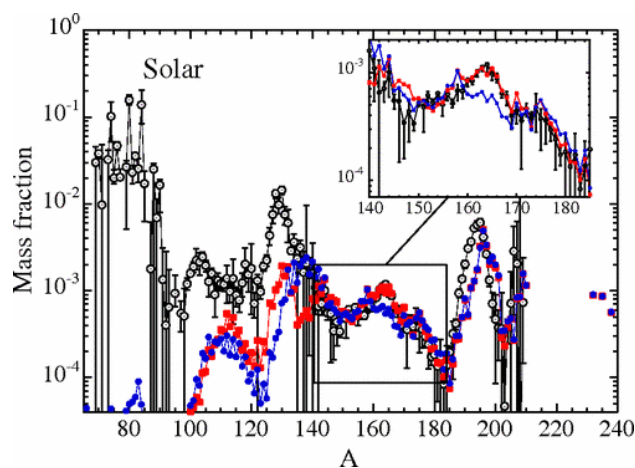


Figure 4-10 (from Ref. [GOR13]) Final abundance distributions for ejecta produced in neutron-star (of 1.35 solar masses) mergers. The blue and red dots represent results based on different models for the fission process. The open circles represent solar abundances.

#### 4.2.2.4 Key example – The nuclear Equation of State from heavy ion collisions

The nuclear equation of state (EoS), particularly for neutron-rich matter, plays a significant role in supernovae and neutron-star mergers [DAN02]. The EoS describes relationships between energy, pressure, temperature, density and isospin asymmetry in a nuclear system. At low temperature, the EoS can be separated into a symmetric matter contribution that is independent of the isospin asymmetry and a poorly constrained symmetry-energy term, proportional to the square of the asymmetry [LI08]. This feature of the nuclear interaction also determines the nature and size of

neutron stars and the thickness of neutron skins of nuclei [LAT01,LAT04,LAT13,LAT15]. Uncertainties in the density dependence of the symmetry energy are large [HEB10, GAN12,LAT13].

Macroscopic quantities of asymmetric nuclear matter exist in neutron stars and in type II supernovae over a wide range of densities [LAT01]. Constraints on the EoS and the symmetry energy at sub-saturation and supra-saturation densities are critical for an understanding of neutron-star properties such as stellar radii and moments of inertia, crustal vibration frequencies [LAT04,VIL04], neutron-star cooling rates [LAT04,STE05], and most recently, the interpretation of the gravitational wave signal and electromagnetic emissions from the GW170817 neutron star merger event detected by LIGO/Virgo [ABB17, RAD18].

Several consistent laboratory constraints for the density dependence of the symmetry energy exist at sub-saturation densities [TSA12, LAT13, HOR14], see Figure 4-11, while the constraints above saturation density are inconsistent [XIA08, RUS11]. The region above  $\rho/\rho_0$  is particularly important for the interpretation of neutron star and neutron star merger properties.

At FRIB, heavy-ion collisions [LI08] will be performed to constraining the EoS, especially at supra-saturation densities, where the uncertainties are largest. The symmetry energy at high densities can be probed in heavy-ion reactions by comparing the relative emission of members of isospin multiplets, e.g.  $\pi^-$  vs.  $\pi^+$ ,  $n$  vs.  $p$ ,  $t$  vs.  ${}^3\text{He}$ , etc., which experience symmetry potentials and symmetry forces of opposite sign [FAM06, LI05, LI05b,DIT10, XIA08].

The beam energies of 170-200 MeV/u available at FRIB allow for studies of the symmetry energy at both sub- and supra-saturation density. To reach the highest densities, heavy-ion experiments, such as for example a 175 MeV/u  ${}^{132}\text{Sn}$  beam impinging on a  ${}^{124}\text{Sn}$  target, require a high rigidity spectrometer to transport the 5.25 Tm  ${}^{132}\text{Sn}$  beam [LI02]. For example, at 200 MeV/u  ${}^{132}\text{Sn}$  beam energy,  $\sim 1.75 \rho/\rho_0$  supra saturation density is probed [LI02]. In general, experiments would simultaneously measure ratios of charged pions, neutrons/protons, light charged particles, and projectile-like fragments from heavy-ion collisions induced by neutron- and proton-rich rare-isotope beams, using among other detection systems a time projection chamber in front of the high rigidity spectrometer or inside the first dipole of the spectrometer section to track light charged particles, similar to work performed with the S $\pi$ RIT-TPC at RIBF [OTS16, JHA16]. At a high rigidity spectrometer, neutrons would be detected in MoNA-LISA and heavy charged particles would be identified and analyzed in the spectrometer section. At the beam energies enabled by a high-rigidity beam transport system, 200 MeV/u vs. 105 MeV/u for the example of a  ${}^{132}\text{Sn}$  beam, charged pion production increases by more than an order of magnitude, enabling the use of pion flow to probe the nuclear equation of state (see Figure 4-12). It is noted that an upgrade of FRIB





to 400 MeV/u (see Section 4.3.2.6) would increase the cross sections for pion production by at least one more order of magnitude with the  $NN$  pion production threshold well exceeded.

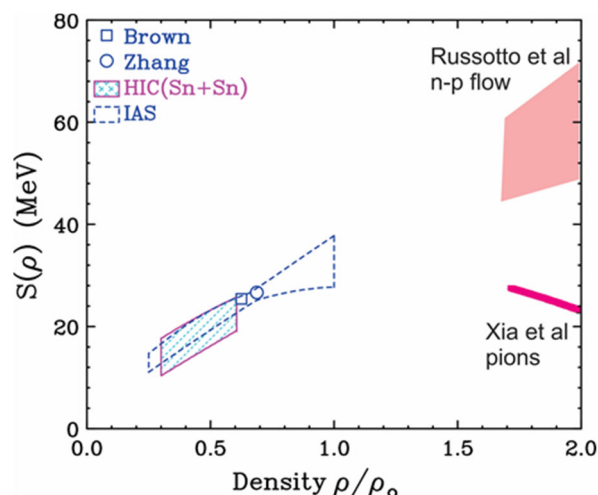


Figure 4-11 The symmetry energy  $S(\rho)$  as a function of baryon density. At sub-saturation density, the density dependence of the symmetry energy is reasonably constrained [HOR14], at supra-saturation density, the region important for neutron star and neutron star merger physics [LAT16], the measures from n-p flow and pion production differ widely and new constraints are needed that high-energy beams from FRIB can provide.

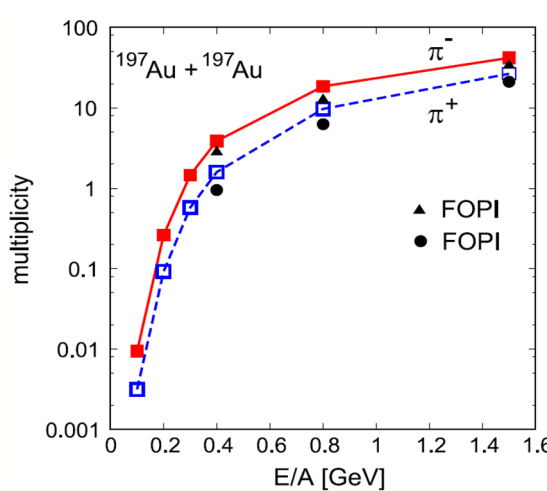


Figure 4-12 Example for the incident energy dependence of charged pion multiplicities in central collisions [IKE18]. With the HRS,  $^{132}\text{Sn}$  projectiles would be available for experiments at 170 MeV/u and higher while a 4Tm limit would restrict the  $^{132}\text{Sn}$  beam energy to 105 MeV/u. Experiments at high rigidity thus increase pion production by an order of magnitude and so significantly enhance the signal-to-noise in collision experiments with pion flow observables.

#### 4.2.2.5 Properties of nuclear matter from the study of resonances

Giant resonances provide complementary constraints on the properties of nuclear matter at sub-saturation density. Below, it is briefly outlined how isoscalar and isovector giant resonances add to the effort of constraining the nuclear equation of state by probing incompressibility or neutron-skin thicknesses.

**Isoscalar Giant Resonances** – The energy of the isoscalar giant monopole resonance (ISGMR) or the nuclear “breathing mode” is directly related to the nuclear incompressibility, a critical component of the nuclear equation of state. In recent years, measurements of ISGMR over series of Sn and Cd isotopes [LI07,PAT12] have provided an “experimental” value for the asymmetry term of nuclear incompressibility,  $K_\tau$  ( $K_\tau = -550 \pm 100$  MeV), which is derived from studying the nuclear compressibility  $K_A$  as a function of  $(N-Z)/A$ , as shown in Figure 4-13. This term is governed by the first and second derivatives (as a function of density) of the symmetry energy at sub-



saturation densities [COL14] and, as discussed above, is important in the study of, among other objects, neutron stars. Extending these measurements to very neutron-rich isotopes is important to more precisely determine the value of this asymmetry term. Another important issue that would be addressed by ISGMR measurements in very neutron-rich nuclei is that of the “soft” monopole resonance resulting from the vibrations of the neutron skin; one would then have an incompressibility of the core and another one of the skin. This would result in ISGMR strengths at low energies—this low-lying monopole strengths is akin to low-lying dipole strength observed in many nuclei [SAV13] and has drawn strong interest [PAA07,KHA11,KHA13,HAM14].

Successful measurements of the ISGMR have been performed on  $^{56}\text{Ni}$  [MON08] and  $^{68}\text{Ni}$  [VAN14]. Similar to the latter experiment, at a high rigidity spectrometer at FRIB, measurements can be performed by placing an Active Target TPC (AT-TPC) filled with helium at the target station. The TPC would be used to detect the recoil particle (either the deuteron or  $\alpha$ -particle) and the spectrometer would detect the heavy nucleus to provide a clean trigger. For example, the ISGMR could be studied in Sn isotopes with mass numbers ranging from 104 to 134 for which intensities of  $\sim 10^4$  pps are available for in-beam experiments when transported through the high transmission beam line from the ARIS Fragment Separator to the high rigidity spectrometer. Such measurements have the potential to reduce the uncertainty in  $K_\tau$  by more than a factor of 2 (see Figure 4-13).

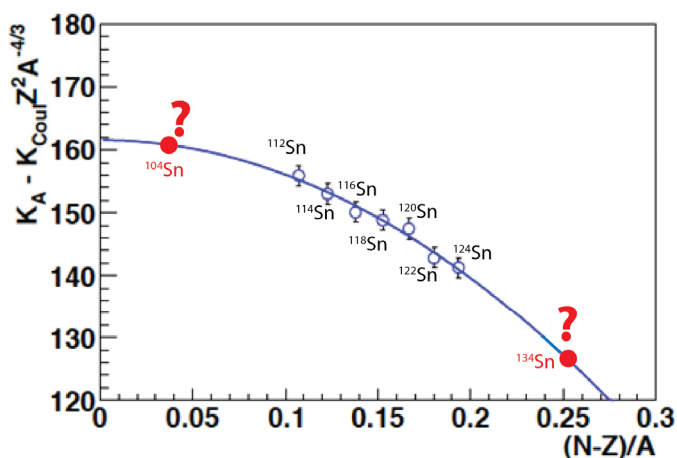


Figure 4-13 Systematics of the nuclear incompressibility,  $K_A$  (minus the Coulomb term), derived from measurement of the ISGMR in Sn isotopes, as a function of the asymmetry term  $(N-Z)/A$  [LI07]. The quadratic fit to the data leads to a value for the asymmetry term of nuclear incompressibility  $K_\tau = -550 \pm 100$  MeV. A measurement of the ISGMR in  $^{104}\text{Sn}$  and  $^{134}\text{Sn}$  to within  $\pm 0.2$  MeV would reduce the uncertainty in  $K_\tau$  to less than 50 MeV.

**Isovector Giant Resonances** – Isovector giant resonances are associated with out-of-phase density oscillations of protons and neutrons in nuclei [HAR01,PAA07]. Their study, through charge-exchange reactions at intermediate energies, provides access to macroscopic nuclear matter properties associated with the difference between the two Fermi fluids such as the symmetry potential and the neutron-skin thickness [DAN03]. By varying the neutron-to-proton ratio along an isotopic chain, sensitivity is gained to these properties [PAA07]. Another degree of freedom arises from spin oscillations of the nucleons, leading to the isovector “spin-flip” giant resonances.

The study of these resonances are thus excellent probes of isovector spin-isospin sector of the nucleon-nucleon effective interaction [FRA05], and are desirable for improving the reliability of calculations.

The two simplest isovector giant resonances are the Isobaric Analog State (IAS) and the Gamow-Teller Resonance (GTR). The energy splitting between the IAS and the centroid of the Gamow-Teller resonance provides a model-dependent measure of the neutron-skin thickness [VRE03]. The analysis of the IAS [LOC14,DAN17,LOC17] and of the Isovector Giant Dipole Resonance [KRA99,YAK06] has also been used study neutron skins. For both of these approaches, experiments with nuclei that have large neutron-to-proton asymmetries are critical to reduce the uncertainties [SAG07]. The nuclear size and density distribution are important properties of nuclei that determine the nuclear potential, single-particle orbitals and wave functions. Determination of the neutron skin thickness are critical for understanding the bulk properties of nuclei. The neutron-skin thickness is also closely related to the symmetry energy [BRO00,DAN03,SAG07, BRO13,LAT13,NAZ14], which determines, for example, the radii of neutron stars [STE05,LAT16]. The increased thickness of neutron skins in unstable neutron-rich isotopes forms a key motivation for performing such studies at FRIB.

In experiments that explore isovector giant resonances in rare isotopes, the measurement of the light recoil particle will be facilitated in a detector near the reaction target to determine the excitation energy and center-of-mass scattering angle, while the spectrometer serves to analyze the projectile-like ejectile and isolate the charge-exchange reaction (see also 4.2.1.1).

Rare isotope beams can also be employed as a probe for specific spin-isospin excitations. For example, the ( $^{10}\text{Be}, ^{10}\text{B}+\gamma$ ) [SCO17] and ( $^{12}\text{N}, ^{12}\text{C}+\gamma$ ) [NOJ18] reactions in forward kinematics have been developed to isolate the illusive isovector giant monopole resonance and isovector spin giant monopole resonance, respectively. Measuring the properties of these giant resonances is important for constraining bulk properties of nuclear matter such as the surface and volume symmetry energy coefficients. To extend these pioneering studies to heavy nuclei, FRIB beam intensities are required. The experimental will also strongly benefit from the coupling of the HRS and GRETA.

### 4.2.3 Probing fundamental symmetries through weak interaction studies

The properties of rare isotopes provide a window into the fundamental symmetries of nature, and offer the possibility to explore physics beyond the standard model of particle physics on energy scales that rival high-energy collider physics.



#### 4.2.3.1 Key example – The quenching of $g_A$ : Charge exchange reactions in $^{100}\text{Sn}$ and asymmetric systems

A fundamental weak coupling, characterized through the axial vector constant  $g_A$ , can be uniquely explored with fast-beam charge-exchange reactions. The hypothesis that the weak vector current  $g_V$  is conserved, or not renormalized by the strong interaction [FEY58], has been tested experimentally to the level of  $1.2 \times 10^{-4}$  [HAR14]. The axial vector constant, however, appears to be renormalized or “quenched” by the strong interaction. This quenching of  $g_A$  is apparent in the over-prediction of  $\beta$ -decay and two-neutrino double  $\beta$  decay matrix elements when using the bare value of  $g_A$ . Similarly, in charge-exchange experiments only about 50-60% of the Gamow-Teller sum-rule strength is observed at excitation energies up to the giant-resonance region (below  $\sim 20$  MeV) [GAA81,GAA85]. The poorly understood mechanism of the quenching is a long-standing issue that has important implications for neutrino physics and astrophysics. An important additional question is: does whatever is responsible for this renormalization of  $g_A$  also quench neutrino-less double- $\beta$  decay? An answer to this question is important for accurately estimating neutrino-less double  $\beta$  decay matrix elements and resulting decay rates (these may scale approximately with  $g_A^4$ ) [SUH17] in the planning for ton-scale discovery experiments [NDB14].

Three mechanisms are thought to contribute to the quenching of the sum-rule strength [BRO88]: 1) mixing between 1p-1h GT states and 2p-2h configurations via the strong tensor interaction moves GT strength to excitation energy beyond the GT giant resonance [HYU80,ARI99]; 2) coupling to the  $\Delta(1232)$ -isobar nucleon-hole state [ERI73]; 3) meson-exchange currents. Evidence for the first mechanism, which is thought to be the strongest [BRO88], has been found [YAK05] in the analysis of  $(p,n)$  [WAK97] and  $(n,p)$  reaction data [YAK05] of  $^{90}\text{Zr}$ . However, recent results from a  $(p,n)$  experiment in inverse kinematics on unstable  $^{16}\text{C}$  [LIP18] indicate that the first quenching mechanism can be well studied in light neutron-rich isotopes, since the transition strength in the  $\beta^+$  direction is Pauli blocked and the Gamow-Teller excitations strongly dominate the measured spectra, thereby simplifying the analysis and observation of the Gamow-Teller strength at excitation energies above the giant resonance region. Hence,  $(p,n)$  experiments at the HRS on very neutron-rich systems provide one way to better understand the quenching mechanism.

A second opportunity to study the renormalization of the axial-vector coupling constant  $g_A$  is by measuring charge-exchange reactions from doubly magic  $^{100}\text{Sn}$  and investigating the Gamow-Teller strength distribution in combination with results from  $\beta$ -decay data [HIN12]. By studying the details of the Gamow-Teller strength distribution and its direct decay properties insight into the microscopic origin can be achieved. Such a measurement is even challenging at FRIB and the  $^{100}\text{Sn}$  beam would be needed at optimum production rigidity and be transported with minimal losses to a thick Hydrogen target for performing a  $^{100}\text{Sn}(p,n)$  experiment in inverse kinematics. Experimental sensitivity will be critical to enable measurement of this and similar charge-



exchange reactions. In addition, an open geometry at forward scattering angles for the detection of decay protons is necessary to elucidate the microscopic structure of the Gamow-Teller strength distribution.

#### 4.2.4 Applications – **Key example:** Improving models of nuclear fission

Nuclear fission represents a challenging and complex many-body process with significant impact on derivative nuclear technologies in the fields of nuclear energy, defense, and homeland security. Driven by the importance of fission, the evolution of this sub-field is ongoing, with significant advances taking place on both experimental and theoretical/computational fronts.

Recent theoretical work has investigated the sensitivity of fission model parameters to the prompt fission  $\gamma$ -ray spectrum (PFGS) [TAL12, STE13a], and is complemented by next generation PFGS measurements on the major actinides [JAN13,ULL14,OBS13]. The model uses a Monte-Carlo Hauser-Feshbach approach to calculate the spectrum and correlations between neutrons and  $\gamma$  rays emitted from fission fragments, and the predictive capability is ultimately limited by incomplete knowledge of the nuclear structure of the neutron-rich fission fragments involved.

The broad range of intense neutron-rich beams available at FRIB can be exploited to improve the nuclear structure underpinning these calculations. In particular,  $\gamma$ -ray spectroscopy following fragmentation reactions could inform these calculations directly through the measurement of discrete, low-lying states. A sensitive, high rigidity spectrometer with a large momentum and angle acceptance, combined with the efficiency and resolution of GRETA would allow surveys across large sections of the nuclear landscape for neutron-rich nuclei between mass numbers of 80 and 140. The fission process of heavy nuclei, excited by surrogate reactions to simulate neutron-capture, can be studied provided sufficient sensitivity and rigidity is available. To study the correlations between fission fragments, the ability to detect and analyze both fission fragments simultaneously would be a game changer. For this purpose, it is advantageous that experiments are performed at high rigidities, as the kinematic focusing of the fission fragments towards forward scattering angles in the laboratory frame increases, which reduces the requirement for the acceptance of a spectrometer and makes such unique measurements feasible.

#### 4.2.5 **Key example** – A game changer for nuclear reactions

FRIB's beam energy range for rare isotopes – from keV/u to 200 MeV/u – will enable a broad arsenal of direct, compound, and heavy-ion nuclear reaction mechanisms to be applied for the extraction of key nuclear properties, while also providing benchmarks in the quest for a needed unified description of nuclear structure and nuclear reactions [NAV16]. Nuclear reactions are among the prime experimental tools used to address the science thrusts of the field, including nuclear structure physics, nuclear astrophysics, the study of fundamental symmetries, and the



application of isotopes. At the highest energy range, for which measurements can only be realized at a high rigidity spectrometer, certain classes of direct reactions can be optimally used to probe the structure of the nucleus and nuclear matter.

Figure 4-14 sketches the energy regions that will be used at FRIB for certain reactions together with the broad science topics or observables that are addressed. Already at 100 MeV/u, the rigidities of <sup>40</sup>Mg and <sup>84</sup>Ni exceed 4 Tm. For <sup>40</sup>Mg and <sup>60</sup>Ca, rigidities exceeding 6.1 and 5.5 Tm, respectively, are needed to accommodate reactions beyond 150 MeV/u. The rigidities that would optimally be used to probe skin nuclei in a regime where the conditions for required theoretical approximations to the reaction mechanisms are met exceed 6 Tm for <sup>84</sup>Ni and <sup>140</sup>Sn.

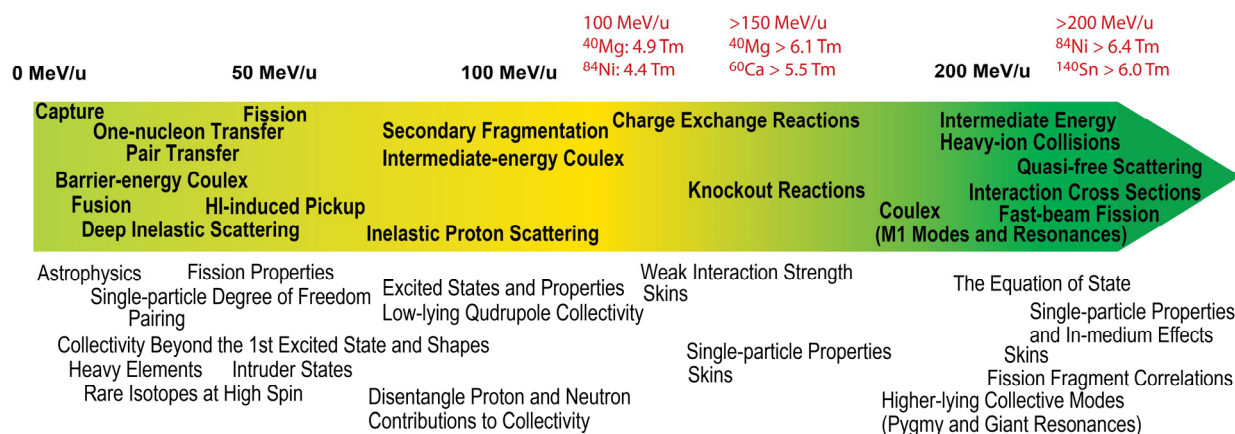


Figure 4-14 Sketch of the energy regions where certain reactions, accessing specific science topics or observables, would optimally be used at FRIB. For some of the key nuclei discussed throughout the science section, rigidities above 4 Tm are required already to achieve beam energies of 100 MeV/u.

Below, the advantages of achieving the high beam energies afforded by a high rigidity spectrometer at FRIB are discussed for some of the reactions mentioned throughout the science section.

**Knockout reactions** – Direct one-nucleon knockout reactions from fast exotic beams have been developed into a powerful technique, extending the detailed study of the nuclear wave function to short-lived rare isotopes [HAN03, GAD08b]. Heavy-ion, e.g. <sup>9</sup>Be or <sup>12</sup>C, induced one-nucleon knockout reactions at intermediate beam energies have been successfully applied at rates of less than 1 particle/s. The shape of the longitudinal momentum distribution of the projectile-like residue carries the information on the orbital angular momentum (*l*-value) of the knocked-out nucleon. Gamma-ray spectroscopy in coincidence with the heavy knockout residue provides the identification of the final state [GAD08a]. In comparison to reaction theory, spectroscopic factors, which relate to the occupation number of single-particle orbitals, can be derived from measured partial cross sections to individual final states of the residue. One-nucleon knockout reactions thus





provide an identification of single-particle components in the ground-state wave function of the rare-isotope projectile and a measure of the relative separation and occupation of single-particle levels.

Figure 4-15 illustrates the momentum resolution requirements for one-neutron knockout from  $^{204}\text{Pt}$ . This reaction would provide single-neutron structure at the key  $N=126$  neutron shell closure which is not only interesting from a nuclear structure point of view but also is relevant for the  $r$  process. The theoretical cross sections that enter all knockout work use a reaction theory description [TOS99, TOS01] in the framework of straight-line trajectories (eikonal approach) and sudden approximation. Both approximations, sudden and eikonal, become increasingly more accurate at the higher projectile energies that are afforded by FRIB together with a high rigidity spectrometer. These energies together with the identification of the removed proton or neutron with charged-particle or neutron detectors will enable the use of the reaction framework in the optimum energy regime, without kinematic limits for the removal of the most deeply-bound nucleons [FLA12], and with a direct probe of knockout mechanism via light-particle detection [BAZ09]. For the extraction of  $l$ -values in the studies of nuclear shell structure, symmetric longitudinal momentum distributions of the knockout residues are observed at RIBF beam energies of around 200 MeV/ $u$ , see for example [KOB12], while at the lower NSCL energies of about 70-90 MeV/ $u$ , pronounced tails are encountered [GAD05]. With the high beam energies possible at a high rigidity spectrometer, orbital angular momenta can be assigned unambiguously from symmetric longitudinal momentum distributions of the residue, allowing to track the evolution of nuclear structure with unprecedented clarity.

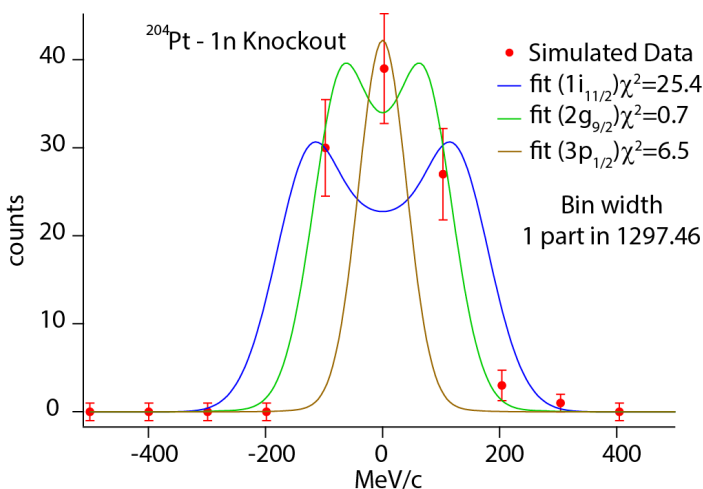


Figure 4-15 Simulated momentum distribution of  $^{203}\text{Pt}$  following the knockout of a neutron from the  $2g_{9/2}$  orbital of  $^{204}\text{Pt}$ , fitted by theoretical distributions assuming either  $p$ ,  $g$ , or  $i$  orbital angular momenta. The  $\chi^2$  values clearly indicate  $g_{9/2}$  as the best fit, in spite of the limited statistics. A momentum resolution for the  $^{203}\text{Pt}$  residue of better than 1 in 1300 is required to discriminate between the involved orbital angular momenta in this mass region.

**Quasifree scattering** – As discussed above, knockout reactions are powerful tools for extracting information on the nuclear wave function. The relatively strong absorption makes the reaction probability peak near the surface of the nucleus. Similar arguments hold for transfer and Coulomb break-up reactions. To probe deeper into the nucleus, nucleon knockout reactions using protons as



the probe, i.e.  $(p,2p)$  and  $(p,pn)$ , have been used. Spectral functions of protons and neutrons in the wide range from valence nucleons to the deeply bound core states can be investigated. In addition, by studying cluster knockout reactions, such as  $(p,pd)$  or  $(p,p\alpha)$ , nucleon-nucleon correlations and cluster structures in nuclei can be probed. As a consequence of being deeply bound, nucleons become sensitive to in-medium modifications [KRE95], which will affect the observables measured in these quasifree reactions.

At FRIB, the energy of rare-isotope beams will be below the optimum regime for spectroscopic use of quasifree knockout studies since distortions and in-medium effects in general will play an important role at 100 MeV/ $u$  in the  $(p,2p)$  equal-sharing scenario. However, this in turn provides the interesting opportunity, if spectroscopic information is known, to probe the elusive in-medium modifications, providing a unique window into the role of in-medium effects in very asymmetric nuclear matter [LI93, LI94, CHE03, LI05, SAM06, JIA07]. The optimum condition for using quasifree scattering as a spectroscopic tool to access spectral functions is an incoming beam energy of about 400 MeV/ $u$ . In that case, the energies of the outgoing nucleons still fall mostly in the energy window with minimum distortions [FRA95] (200 MeV/ $u$  in the exit channel for the equal sharing scenario). This optimum projectile beam energy regime may become available at FRIB following an energy upgrade to 400 MeV/ $u$  (See also Section 4.3.2.6).

**Heavy-ion electromagnetic excitations** – Electromagnetic excitations induced by heavy ions (Coulomb excitation) at intermediate and relativistic beam energies have long been used to provide detailed information about collective degrees of freedom in nuclei [BER88, GLA98]. Excitations of rare isotopes can be studied by scattering these particles of a stable high- $Z$  target. The exchange of virtual photons, when the rare-isotope beam passes through the Coulomb field of the high- $Z$  target, results in high cross sections for collective excitations. Contributions from interactions mediated by the strong nuclear force are reduced at very forward scattering angles. For a given secondary beam and target, the sensitivity for exciting a particular collective state strongly depends on the choice of the beam energy [GLA98]. Below 100 MeV/ $u$ , the first excited  $2^+$  state is most strongly excited. Above 200 MeV/ $u$ , the excitation probability for the higher-lying Giant Dipole Resonance (GDR) and Giant Quadrupole Resonance (GQR) increases steeply.

To efficiently study the GDR and GQR at FRIB, experiments should be performed close to the beam energies at which the rare-isotope production rates are maximum (170-200 MeV/ $u$ ). Especially the excitation of the GDR is of great interest, since its properties provide a probe of the charge distributions in nuclei. A fragmentation and a shift of the GDR strength towards lower excitation energies was predicted for heavier nuclei as the neutron dripline is approached [SUZ90]. This redistribution of strength is due to changes in the nuclear mean field as a function of  $N/Z$  combined with the proximity of the continuum for all particle-hole excitations [ZEL06]. Such a redistribution of strength towards lower energies was, for example, observed in studies of the GDR in  $^{130,132}\text{Sn}$  [ADR05]. Exploration of the existence and low-lying dipole strength in neutron-rich



nuclei is not only of importance for understanding collective motions in asymmetric nuclei, they are also important for understanding the relative abundances produced in the astrophysical  $r$  process [SAV13]. Although during much of the  $r$  process, photodisintegration and radiative capture are in equilibrium, near the end of the process, nucleosynthesis depends on the absolute rates of the  $(n,\gamma)$  and  $(\gamma,n)$  processes and the latter will be affected by the low-lying dipole strength. For example, in the region near the above-mentioned cases of  $^{130,132}\text{Sn}$ , several waiting points in the  $r$ -process path are nearby and could be affected.

Measurements require projectile beam energies that exceed the 4 Tm limit for neutron-rich nuclei and the detection of the heavy fragment, as well as photons and neutrons emitted in the decay of the excited nucleus. At a high rigidity spectrometer, MoNA-LISA and GRETA would be well suited for coincident neutron and  $\gamma$ -ray spectroscopy.

#### 4.2.6 Key example – Discovery science: The skin nuclei $^{84}\text{Ni}$ and $^{140}\text{Sn}$

New opportunities and surprises are expected from access to unusual nuclear systems at the extremes of isospin. FRIB will produce nuclei with the most extreme  $N/Z$  ratios, including very neutron-rich systems in which the excess neutrons will arrange to form a skin.  $^{84}\text{Ni}$  and  $^{140}\text{Sn}$  are examples of such nuclei that are expected to have significant neutron skin thicknesses, 0.51 fm and 0.36 fm, respectively [ERL12], as compared to stable isotopes that have skins closer to 0.1 fm thickness. Aside from the importance of the neutron skin thickness for the nuclear equation of state, outlined in Sections 4.2.2.4 and 4.2.2.5, reactions induced by nuclei with extreme neutron skins may be the only way to study neutron matter in the laboratory. For the two examples given above, the total luminosity gains of performing reactions at a high rigidity spectrometer over existing spectrographs limited to 4 Tm are 79-fold and 5.5-fold for  $^{84}\text{Ni}$  and  $^{140}\text{Sn}$ , respectively. For both the Ni and Sn proton magic chain, the skin thicknesses can be characterized along isotopic chains with a variety of methods of which interaction cross section and proton scattering measurements potentially have the furthest reach. These two techniques as performed at a high rigidity spectrometer at FRIB are briefly outlined below.

**Elastic scattering** – Whereas charge radii can be determined by through electron scattering, muonic atoms, and laser spectroscopy via isotopic shift measurements, matter radii, which are needed to deduce the neutron radii, can be probed in hadronic scattering. Elastic proton scattering has already been applied to, for example, the cases of  $^4\text{He}$ ,  $^6\text{He}$  and  $^8\text{He}$  [ALK97],  $^{40}\text{Ca}$ ,  $^{48}\text{Ca}$  [CLA03] and  $^{208}\text{Pb}$  [KAR02, CLA03]. Such studies are complementary to the reaction/interaction cross section measurements outlined below since they carry different systematic uncertainties. They also complement the more model-independent extraction of neutron skin thicknesses from parity-violating electron scattering experiments at JLAB [ABR12,PAS11,MAM13], which is confined to stable nuclei at present. Systematic studies over isotopic chains extending to very



neutron-rich nuclei will provide additional constraints on the equation of state as the increase in skin is mapped as function of the isospin.

The key to ensuring that proton elastic scattering data provide accurate information on density distributions and matter radii is the confirmation that the extracted parameters are beam-energy independent [CLA03,KAR02]. This can be done by analyzing the elastic differential cross section within a consistent theoretical framework over a wide range of momentum transfers (i.e. up to large scattering angles) for a variety of beam energies. With a high rigidity spectrometer at FRIB, it will be possible to pursue such experiments for very neutron-rich systems up to high beam energies. Sufficient statistics could be acquired using thick Hydrogen targets or active-target time-projection chambers. Elastic scattering experiments in inverse kinematics off the proton are also motivated by recent advances made in the framework of the dispersive optical model (DOM) to quantify the spectral strength in the continuum orbits that are filled in the independent particle model [MUE11,MAH14]. The key breakthrough in the DOM analysis is that it links structure information directly with continuum physics and produces a paradigm shift in which nuclear reactions and structure can be analysed as different aspects of the same underlying science.

**Total reaction/interaction measurements** – Absorption measurements are complementary to elastic proton scattering. They can also provide information about the matter radii of isotopes [OZA01]. Traditionally, two types of measurements have been used. In reaction cross section ( $\sigma_R$ ) measurements the total probability of interactions between a nucleus and a target is determined from a measurement of the particles transmitted through a target without any interaction. In interaction cross section ( $\sigma_I$ ) measurements, the total probability of a reaction between a nucleus and a target is measured for which the nucleus changed proton and/or neutron number. The difference between  $\sigma_R$  and  $\sigma_I$  are inelastic-scattering events, i.e. events in which energy and momentum are transferred between projectile and target but the neutron and/or proton number does not change:  $\sigma_R = \sigma_I + \sigma_{inelastic}$ . More recently, charge-changing cross sections ( $\sigma_{CC}$ ) have been developed for probing the point-proton distribution rms radii (usually referred to as the proton rms radii) of nuclei [BLA92]. Combining  $\sigma_R$  or  $\sigma_I$  and  $\sigma_{CC}$  (or the proton rms radii obtained from other probes) provide a way to determine the neutron rms radii. Such a technique has been applied on neutron-rich nuclei at incident beam energies of  $\sim 200$  MeV/ $u$  and higher [TER14, EST14, YAM11].

These analyses are model-dependent and rely on the application of Glauber models in the optical limit, which are optimally applied at several 100s of MeV/ $u$ . Amos et al. [AMO06] also studied the prospect of using the reaction cross sections on protons as a tool to measure the spatial distribution of neutrons in exotic nuclei. They showed that by folding nuclear structure densities with effective in-medium nucleon-nucleon interactions, good descriptions of the reaction cross section data can be achieved at energies from 65-200 MeV/ $u$ . These results have paved the way



for studies of reaction cross sections at FRIB. At lower beam energies, the separation between inelastic and elastic channels is feasible without  $\gamma$ -ray spectroscopy even for relatively massive nuclei. With a high rigidity spectrometer, studies can be performed over a wide beam-energy range, reaching the ones where Glauber model approaches are increasingly reliable, which will help to constrain systematic uncertainties. In addition, being able to achieve the highest rare-isotope beam intensities for the most neutron-rich nuclei is critical and can only be accomplished if the beams can be used at the rigidities that optimize their production.

### 4.3 Science Specifications

In Table 4-2 the scientific requirements for the HRS based on the envisioned science program described in section 4.2 and Table 4-1 are summarized and sorted by the key scientific questions of the NRC Decadal study [NRC13] and the 2015 NSAC Long-Range Plan [LRP15]. These scientific specifications have been established by the members of the HRS working group based on the 2014 HRS whitepaper [HRS14] and additional and more detailed studies of the scientific program. For this purpose, 35 representative members of the working group met in biweekly meetings. In addition, the full working group met during the low-energy community meetings and organized workshops to collect broad input from the FRIB user community.

Because of the wide variety of experiments that will be run with the HRS, it is important to establish clear specifications imposed by the broad scientific program. In practice, many of the experiments have overlapping specifications. Therefore, in establishing a summarized list of scientific specifications, a set of “prototypical” experiments was chosen that encompass the specifications of other experiments.

The scientific specifications for the HRS can be divided into two groups. The first set of specifications pertain to the Spectrometer Section and is motivated by the detailed conditions for optimizing each of the scientific programs. These specifications include the need to place and interface with ancillary detector systems that are necessary to perform the experiments foreseen by the user community. The specifications that pertain to the Spectrometer Section are detailed in Section 4.3.1.

The second set of specifications is mandated by the goal to perform experiments with nuclei that have the most extreme neutron-to-proton ratios and are produced at the lowest rates at FRIB. Consequently, optimization of the luminosity of experiments performed at the HRS is key to meeting the needs of the FRIB user’s community. This is important for all scientific programs listed in Table 4-1 and primarily sets specifications for the High-Transmission Beam Line (HTBL) that transports beams from the ARIS Fragment Separator to the reaction target of the HRS. The specifications that impact the luminosity are described in Section 4.3.2.



Table 4-2 Specifications for the HRS for each of the scientific programs listed in Table 4-1. In the bottom three rows, the specifications are summarized by operational mode of the HRS, as described in Section 4.3.1.6.

HRS Science Program		Specification															
		Maximum mass number	Minimum mass resolving power	Minimum charge resolving power	Time of flight resolution (ps)	Minimum flightpath charged particles (m)	Minimum momentum resolving power	Minimum spectrometer solid angle (msr)	Angular resolution (mrad)	Minimum space around target (cm)	Minimum momentum acceptance (dp/p in %)	Maximum neutron flight path (m)	Minimum neutron solid angle (msr)	Gapsize for Time Projection Chamber (cm)	Unreacted beam rejection	Maximum rigidity (Tm)	Mode: (H)High Resolution, (I)Invariant Mass, (M)mass measurement
Nuclear Structure	At the limits of the nuclear chart: at and beyond the neutron dripline	132	220	85	150	11	290	10	5	90	±5	15	32		y	8	I
	Single-particle structure and collectivity from prompt in-beam gamma-ray spectroscopy	238	400	156	150	25	1500	10	10	123	±2.5		-		y	8	H
	Fingerprints of shell evolution with isomer studies	238	400	156	150	25	1500	10	10	123	±2.5		-		y	7	H
	Excited-state lifetimes as indicators of shell-evolution	238	400	156	150	25	1500	10	10	123	±2.5		-		y	8	H
	Inelastic proton scattering as a probe of the pn degree of freedom	238	400	156	150	25	>400	5	10	123	±2.5		-		y	8	H
	Physics along the N=Z line	100	170	156	150	11	1500	10	10	-	±2.5		-		y	5	H
	Commensal decay spectroscopy following reactions	238	400	156	150	25	>400	10	10	-	±2.5		-		-	8	H
	Knock-out reactions	238	400	156	150	25	1500	10	10	123	±2.5		-		y	8	H
	Quasifree scattering	238	400	156	150	25	1500	5	10	123	±2.5		-		y	8	H
	Elastic scattering	238	400	156	150	25	1000	10	10	123	±2.5		-		y	7	H
Total reaction/interaction measurements	238	400	156	150	25	1000	10	10	123	±2.5		-		y	8	H	
Nuclear Astrophysics	Heavy-ion collisions	-	-	-	-	-	-	-	-	-	-	(15)	(32)	60	-	8	I
	Heavy-ion electro-magnetic excitations	238	400	156	150	25	1000	10	5	123	±2.5		-		-	8	H
	Isoscalar giant resonances	238	400	156	150	25	>400	10	10	100	±2.5		-		-	6	H
	Isovector giant resonances	238	400	156	150	25	1500	10	5	123	±2.5		-		y	6	H
	Time-of-flight mass measurements	238	10000	156	30	90	>10000	<10	-	-	±0.5		-		-	7	M
	Projectile fragmentation and in-flight fission of neutron-rich nuclei	238	400	156	150	25	1000	15	10	123	±2.5		-		y	6	H
	Weak reaction rates for astrophysics	238	400	156	150	25	1000	10	5	123	±2.5		-		y	6	H
Fundamental Symmetries	Gamow-Teller strengths, neutrinos, and the quenching of $g_A$	238	400	156	150	25	1500	5	10	123	±2.5		-		y	7	H
Applications	Improving nuclear structure inputs to fission models	238	400	156	150	25	1000	15	10	123	±2.5		-		y	6	H
<b>Specifications Summary by Mode</b>																	
High resolution		238	400	156	150	25	1500	15	5	123	±2.5		-		y	8	H
Invariant mass		132	220	85	150	11	290	10	5	90	±5	15	32	60	y	8	I
Mass measurement		238	10000	156	30	90	>10000	<10	-	-	±0.5		-		-	7	M





### 4.3.1 Scientific Specifications for the Spectrometer Section: accommodating the diverse scientific program of the HRS user community

To meet the objectives of the FRIB Scientific User Committee of FRIB, the Spectrometer Section must accommodate a broad spectrum of experiment types. Each of these experiment types have their own specifications. In Table 4-2, the specifications for each experimental program that affect the scope and properties of the Spectrometer Section are specified as:

- Maximum mass number
- Minimum mass resolving power
- Minimum charge resolving power
- Time of flight resolution
- Minimum flightpath for charged particles
- Minimum momentum resolving power
- Minimum spectrometer solid angle
- Angular resolution
- Minimum space around target for the placement of ancillary detector systems
- Minimum momentum acceptance
- Maximum neutron flight path for programs that involve the detection of in-flight neutrons
- Minimum neutron solid angle for programs that involve the detection of in-flight neutrons
- Whether the program requires unreacted beam rejection in the focal plane of the spectrometer
- Maximum Rigidity

Some of the specifications, such as for the momentum and mass resolving powers, depend on the exact beam energy. For the purpose of the values in Table 4-2, a beam energy of 160 MeV/u has been used in the determination of the specifications. In the following, prototypical experiments that were used to set these specifications are described.

#### 4.3.1.1 Prototypical experiment I: Single-particle structure and collectivity from prompt in-beam $\gamma$ -ray spectroscopy

As described in Section 4.2.1.1, experiments aimed at elucidating the evolution of shell structure and properties of nuclei far away from the valley of stability by using in-beam  $\gamma$ -ray spectroscopy are an important motivation for the construction of the HRS. By combining the Gamma-Ray Energy Tracking Array (GRETA) [GRE20] with the HRS, the world's most sensitive in-beam  $\gamma$ -ray spectroscopy facility will be created, which is necessary to perform experiments such as those aimed at investigating spectroscopy of the most neutron-rich calcium isotopes (see Section 4.2.1.2). It is important that experiments can be carried out at magnetic rigidities for which the





rare-isotope production rates are maximized. For the very neutron-rich isotopes, this requires that the spectrometer can operate up to a rigidity of 8 Tm (See Section 4.3.2.1). The optimization of the luminosity for experiments with rare isotopes at the HRS will be discussed in detail in Section 4.3.2.

Experiments that combine the HRS and GRETA will be carried out with rare-isotope beams across the chart of nuclei, requiring that particles can be identified and resolved up to high mass numbers ( $A \sim 238$ ). A mass resolving power ( $R_m = m/\Delta m$ , where  $\Delta m$  is the width in Full Width at Half Maximum (FWHM)) of 400 is required to achieve a separation of four standard deviations between neighboring mass units. Hence, by making a  $\pm 2\sigma$  mass cut, only 5% of the events are lost, which is equal to the maximum loss in transmission through the HTBL to the Spectrometer Section Target (see Section 4.3.2). It is not uncommon that the mass of the particles of interest differ by one unit from a contaminant peak that is much stronger. At a separation of four standard deviations, a signal-to-background ratio of about four can be achieved if the production of the neighboring contaminant is 100 times stronger than the production of the particle of interest and an asymmetric cut of  $-\sigma$  to  $+2\sigma$  is made around the peak of interest. This scenario can be considered an extreme case and the signal-to-noise ratio of 4 is sufficient to carry out the program summarized in Section 4. The mass resolving power is defined through the following:

$$\frac{1}{R_m} = \delta \frac{\Delta m}{m} = \frac{\delta x_f \oplus M_x \delta x_i}{D_x} \oplus \gamma^2 \frac{\delta \text{ToF}}{\text{ToF}},$$

in which  $\delta \frac{\Delta m}{m}$  is the uncertainty in the relative mass difference,  $M_x$  and  $D_x$  are the horizontal magnification and dispersion of the spectrometer, respectively;  $x_i$  and  $x_f$  are the positions of the trajectories relative to the central trajectory in the initial (achromatic) object and final (dispersive focus) locations;  $\gamma$  is the Lorentz factor, and ToF is the time of flight. The  $\oplus$  operator denotes the addition in quadrature of independent quantities<sup>1</sup>, and  $\delta$  indicates the uncertainty (in FWHM) for a parameter. Hence, the specification for the mass resolving power imposes constraints on the detector system used for tracking and identifying particles: the resolution of the focal-plane detector ( $\delta x_f$ ) of the Spectrometer Section must at least be 1 mm, and a time-of-flight ( $\delta \text{ToF}$ ) resolution of 150 ps (FWHM) must be achieved. By using these parameters, and using a typical beam image spot size ( $\delta x_i$ ) at the target of 5 mm, the specification to achieve a mass resolving power of 400 requires a flight-path length from the reaction target to the focal-plane detectors of the Spectrometer Section of at least 25 m.

To select the isotopes of interest, it is also necessary to identify the charge number. Similar to the requirement for the mass resolving power, a  $4\sigma$  separation between isotopes with a difference in

---

<sup>1</sup>  $\delta a \oplus \delta b = \sqrt{(\delta a)^2 + (\delta b)^2}$

charge number by one is needed to limit the loss in events by a  $\pm 2\sigma$  cut to 5%. This requirement corresponds to a charge resolving power ( $R_Z=Z/\Delta Z$ ) of 156 for  $Z=92$ , where  $\Delta Z$  is the resolution (FWHM). This requirement results into a requirement for the resolution of the energy-loss detectors for the HRS, as  $\sigma_Z/Z=\sigma_{\Delta E}/(2\Delta E)$ , where  $\Delta E$  is the measured energy loss in an energy-loss detector.

An advantage of performing in-beam  $\gamma$ -ray spectroscopy experiments with fast beams is that the reaction products that are detected in the Spectrometer Section in coincidence with  $\gamma$ -rays in GRETA, are strongly forward boosted. A spectrometer acceptance of 10 msr ( $\pm 50$  mrad in the dispersive and non-dispersive directions) is sufficient to collect the reaction products. Based on the experience experiments with the S800 [BAZ03] spectrograph, a momentum acceptance ( $\delta p/p$ ) of  $\pm 2.5\%$  is required to carry out experiments efficiently. With such a momentum acceptance, the momentum distribution of the recoiling particle after interacting with the target can be measured in a single rigidity setting of the spectrometer for experiments with nuclei with mass greater than approximately 30. This is important for reducing the beam-time required to measure the full momentum distribution.

As the largest detector array that will be placed at the target station of the Spectrometer Section, GRETA imposes a constraint on the area around the target that must be available in general for the placement of a wide variety of detector systems. Therefore, the HRS working group closely coordinates with the GRETA project team and established that at least 123 cm must be kept free upstream and downstream of the reaction target, as illustrated in Figure 4-16.

Besides GRETA, there are a wide variety of other devices that will be placed around the target for specific experiments. A sample of these detector systems is shown in Figure 4-17 and include detectors systems for  $\gamma$ -rays, charged particles, and neutrons.



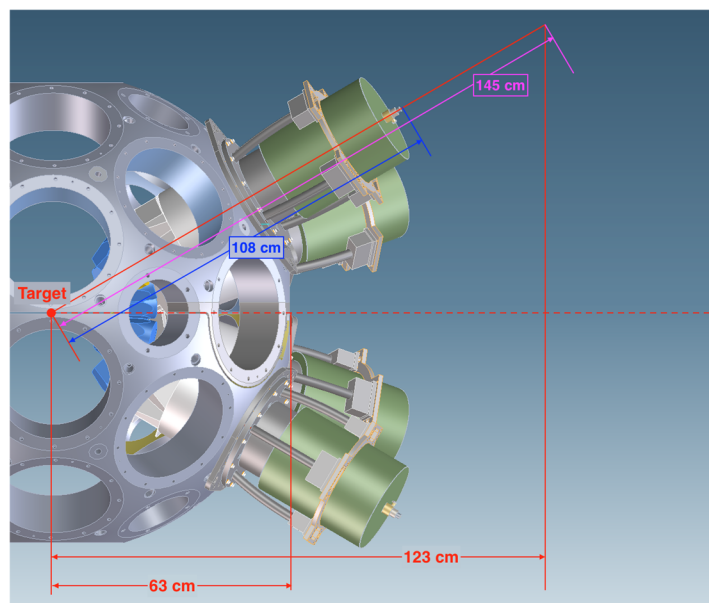


Figure 4-16 Illustration of the amount of space that must be kept available to place and operate GRETA at the reaction target. The radius of the frame holding the GRETA detectors is 63 cm, and the distance from the target to the end of a detector module is 108 cm. Additional space is required to insert a liquid-nitrogen bayonet, adding 37 cm to that distance. When projected onto the beam axis, this leads to a specification to leave at least 123 cm of space for GRETA.

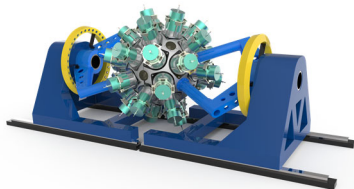
#### 4.3.1.2 Prototypical experiment II: Knock-out reactions

As described in Section 4.2.5, direct and heavy-ion nuclear reaction studies at the HRS will be crucial for understanding key nuclear properties and the mechanisms in which nuclei interact. Integral to such studies is the ability to accurately reconstruct the momenta of the charged particles in the Spectrometer Section. Knockout experiments from heavy nuclei (see the case of neutron knockout in Figure 4-15) provide a strong constraint on the momentum resolving power ( $R_p$ ) that needs to be achieved. The momentum resolving power is determined by:

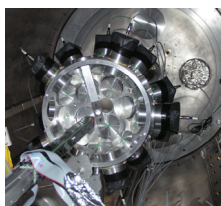
$$R_p = \frac{p}{\delta p} = \frac{D_x}{\delta x_f \oplus M_x \delta x_i}$$

In order to detect identify the angular momentum carried by the knocked-out neutron from  $^{204}\text{Pt}$ , the momentum resolving power must be at least 1300 with a beam-spot image size of 5 mm (FWHM) and a focal-plane detector resolution of 1 mm (FWHM). To perform similar experiments up the highest mass number (238), a momentum resolving power of 1500 is specified.

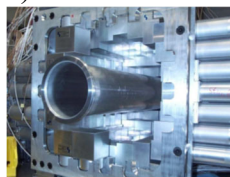
a) GRETA



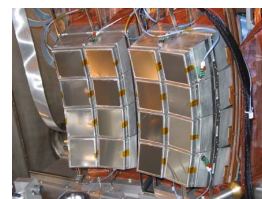
b) LANL-Apollo



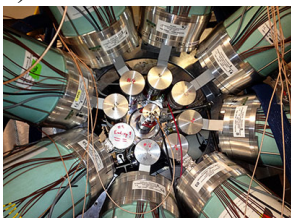
c) CAESAR



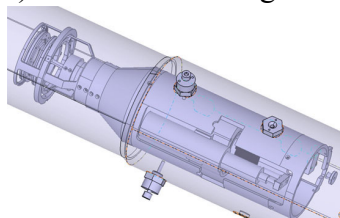
d) HiRA



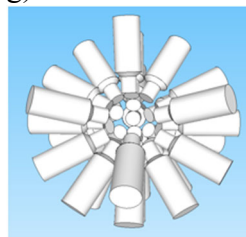
e) SeGA



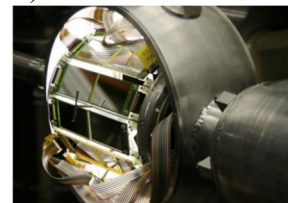
f) NSCL-Köln Plunger



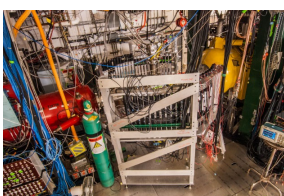
g) HAGRiD



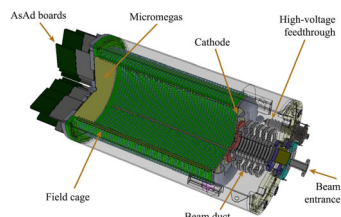
h) ORRUBA



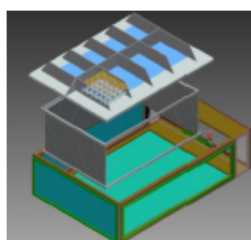
i) LENDA & VANDLE



j) AT-TPC



k)  $S\pi$ RIT-TPC



l) TexAT

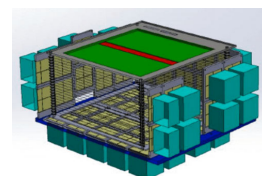


Figure 4-17 Existing detector systems that will be placed around the target for experiments with the HRS: a) Gamma Ray Energy Tracking Array (GRETA) [GRE20]; b) LaBr(Ce)+CsI(Tl) array Apollo [COU15]; c) CAESium-iodide scintillator Array (CAESAR) [WEI10]; d) High-Resolution Detector Array (HiRA) [WAL07]; e) Segmented Germanium Array (SeGA) [SEG01]; f) NSCL- Köln Plunger [IWA16]; g) Hybrid Array of Gamma Ray Detector (HAGRiD) [SMI18]; h) Oak Ridge Rutgers University Barrel Array (ORRUBA) [PAI07]; i) Low-Energy Neutron Detector Array (LEND) [PER12] and Versatile Array of Neutron Detectors at Low Energy (VANDLE) [PET16]; j) The Active Target Time Projection Chamber (AT-TPC) [AYY17]; k) The  $S\pi$ RIT-TPC [OTS16, JHA16], l) The Texas Active Target (TexAT) [KOS20].

In addition to being able to accurately measure the momenta of the charged particles in the HRS, it is important for some experiments that unreacted beam particles can be blocked prior to entering the spectrometer focal plane detectors and possibly limiting the intensity with which the experiment can be performed. This is particularly important for experiments at the Spectrometer Section, since the likelihood that unreacted beam particles are within the momentum acceptance of the spectrometer becomes higher for heavier beams because the magnetic rigidities of the unreacted beam particles and desired reaction products are often close. The necessary unreacted-beam rejection factor varies strongly from one experiment to another. In experiments with unreacted beam rates that are far below the rate capabilities of the focal plane detectors or where



the unreacted beam has a rigidity very different from the particles of interest and does not enter the focal plane, no rejection is required. In the worst case, a high-intensity ( $10^6$  pps) beam must be rejected with at least 99% efficiency to prevent the rate in the focal plane detectors to exceed the capabilities of the detectors. In cases where unreacted beam rejection is needed, it is important to have a focus at a location prior to the tracking detectors, so that unreacted beam particles can be intercepted by using beam blockers, while minimizing the interference with the measurement of the particles of interest. To achieve good momentum resolving power and to create the possibility to block unreacted beams, it will be necessary to use the dispersion-matching technique, as discussed in section 4.3.2.7.1.

#### 4.3.1.3 Prototypical experiment III: Invariant-mass spectroscopy at and beyond the neutron dripline

As discussed in Section 4.2.1.3, unique opportunities arise at FRIB by being able to study weakly and neutron-unbound systems, in which new and exotic phenomena associated with very large neutron-to-proton asymmetry are expected. Such experiments require invariant-mass spectroscopy in which the momentum vectors of one or more neutrons that are emitted in flight from the neutron-unbound system and the charged residual nucleus are used to reconstruct the unbound system. For that purpose, the MoNA-LISA plastic-scintillator neutron detector array [BAU05,MRI09] is used. To achieve sufficient resolution in the reconstructed neutron momentum vectors, the detector must be placed sufficiently far away from the target. Invariant-mass spectroscopy experiments with neutrons benefit from being able to use the fast beams made available by the HRS as the neutrons are strongly forward boosted and can be detected with good efficiency even when placed far away. By placing the detectors further, the neutron velocity measurement gains accuracy as the relative uncertainty in the time-of-flight is reduced. Experiments with MoNA-LISA placed up to 15 m from the target are envisioned, which imposes a constraint on the layout of the HRS within the experimental hall.

The ability to measure neutrons at forward angles sets a stringent requirement on the ion-optical elements of the Spectrometer Section placed immediately after the target: they cannot block the path of the neutrons towards MoNA-LISA. A sweeper magnet with a large gap is thus required to sweep the charge particles away from the beam axis. The location of the target and the depth and the gap sizes of the sweeper magnet set the vertical acceptance for the neutrons emitted in flight.

At least 90% geometrical coverage for neutrons emitted in flight from an  $A=40$  system with an excitation energy of less than 2 MeV at 180 MeV/ $u$  (see Section 4.2.1.3) must be achievable for a distance of 8 m between the target and the MoNA-LISA array, which corresponds to a solid-angle coverage of 32 msr, as shown in Figure 4-18. In practice, it is the angular acceptance for neutrons in the vertical direction ( $\pm 90$  mrad) which is the primary constraint as it sets the gap height of the sweeper magnet. Up to vertical angular acceptances of  $\pm 90$  mrad, the gain in geometrical efficiency



for the neutron detection increases linearly with increased angular acceptance. At larger vertical angular acceptances, the gain in geometrical acceptance saturates because it is constrained by the size of the MoNA-LISA neutron array, rather than the acceptance of the neutrons passing through the sweeper magnet. For larger distances between the target and the MoNA-LISA array, the gain in geometrical acceptance achieved by increasing the vertical angular acceptance of the neutrons saturate more quickly. Hence, a vertical angular acceptance of  $\pm 90$  mrad is an appropriate choice. To optimize the vertical acceptance for the neutrons, it is preferable to place the target close to the sweeper magnet. Keeping in mind that some infrastructure is needed around that target, a minimum distance of 50 cm between the location of the target and the entrance of the sweeper magnet was selected. We note that the requirement of a  $\pm 90$  mrad angular acceptance in the vertical direction translates to a dipole gap size of just below 60 cm for the sweeper magnet presented in Section 6.

If larger detectors must be placed around the target, a larger distance between the dipole magnet and the target location might be necessary. For example, a distance between the target and the edge of the sweeper magnet of at least 90 cm would allow for the placement of GRETA with its forward ring of detector removed, which is beneficial for experiments in which  $\gamma$ -ray and neutron invariant-mass spectroscopy are performed simultaneously (see Figure 4-5). The use of GRETA requires that the magnetic field at the location of its detectors is less than  $\sim 600$  Gauss (although for elements that are very near DS1 levels of 700-900 Gauss can be tolerated) [ROD21], which is an important consideration when it is placed near the Sweeper magnet. The use of detectors that use photomultiplier tubes (PMTs) near the sweeper magnet is likely not feasible due to stray fields as a requirement that the fields stay below levels that can be mitigated by local shielding ( $\sim 25$  Gauss, based on experience at the S800 spectrograph and at the SAMURAI magnet [SAS21]) is probably not realistic. Alternatively, detectors that use Silicon Photo Multipliers (SiPMs) instead of PMTs, such as the Apollo Array [COU15], could be used. Since the MoNA-LISA array employs PMTs, it is also important that the fields have dropped to levels below 25 Gauss near the array when placed at 8 m from the target location in front of the sweeper magnet, which corresponds to the closest distance of MoNA-LISA to the sweeper magnet.

Invariant-mass spectroscopy will be mostly carried out in experiments with neutron-rich rare isotopes of mass number below 132 and charge number below 50, requiring a magnetic rigidity of 8 Tm (See Section 4.3.2.1). The specifications for the mass and charge resolving power of the charged residual nucleus in the Spectrometer Section for such experiments are not as stringent as for other types of experiments and  $R_m=220$  and  $R_Z=85$  are sufficient to achieve sufficient mass and charge separation (four standard deviations) as for the types of experiments performed with heavier systems. To achieve this mass resolving power a flight path for the time-of-flight measurement of 11 m is necessary. For invariant-mass spectroscopy beyond mass 132, a higher resolving power and thus a longer flightpath is required. The specifications for the momentum resolving power of the Spectrometer Section are less stringent ( $R_p=290$ ) than for most other experiments, as the





accuracy of the invariant-mass reconstruction is dominated by the measurement of the neutron momentum vector. At the momentum resolving power of 290, the loss in invariant mass resolution for the  $A=40$  system compared to a perfect momentum determination is only 10% if MoNA-LISA is placed at 15 m from the target (for which the best neutron time-of-flight resolutions are achieved). For similar reasons, the angle of the charge particle must be determined with a resolution (FWHM) of 5 mrad. At this resolution, the loss in invariant-mass resolution is only 10% compared to a measurement in which a perfect angular measurement is achieved. If MoNA-LISA is placed closer to the target, the benefits of a better momentum and angular resolution for the charged particle become smaller. It is further noted that the gain in invariant-mass resolution by placing MoNA-LISA 2 meters further downstream (17 m instead of 15 m) is about 10% as well, so that the contributions from the tracking of the charged particles and neutrons are balanced under these circumstances.

It is important that the momentum acceptance of the Spectrometer Section is larger than necessary for most other experiment types. A momentum acceptance ( $\delta p/p$ ) of  $\pm 5\%$  is required to perform invariant-mass spectroscopy of the light neutron-rich systems as the momentum kicks induced by the decaying neutrons become significant. The solid-angle covered by the spectrometer must be similar (10 msr) to that of other experiment with fast rare-isotope beams in inverse kinematics, in order to capture the charged particles that decayed in flight. For the case of relatively light nuclei such as the  $A=40$  system described above, the scattering angle of the charged particle after the emission of a single neutron is less than 15 mrad, even at high excitation energies. Consequently, even if several neutrons are emitted in flight, the charged particle will still be detected if angular ranges of  $\pm 50$  mrad are covered in the dispersive and non-dispersive directions.

Although the focus in this section is on the kinematics reconstruction of unbound states that emit neutrons, it is important to point out that several other types of experiments also rely on the detailed reconstruction of momentum vectors to reconstruct excitation energies and scattering angles that are necessary for the interpretation of the data. Examples include the ( ${}^7\text{Li}, {}^7\text{Be}$ ) reaction in inverse kinematics (see Section 4.2.1.4), the ( ${}^{10}\text{Be}, {}^{10}\text{B}$ ) and ( ${}^{12}\text{N}, {}^{12}\text{C}$ ) reactions in forward kinematics (see Section 4.2.2.5), and quasifree scattering experiments (see Section 4.2.5). These experiments therefore also require the good angular resolution of 5 mrad for the charged particle track. In addition, having such a good angular resolution is also important for heavy-ion Coulomb excitation experiments (See Section 4.2.5), where angular cuts are necessary to constrain the impact parameter of the reaction, and for elastic scattering experiments, for which the angular distribution has to be measured for constraining matter radii and density distributions (see Section 4.2.6).



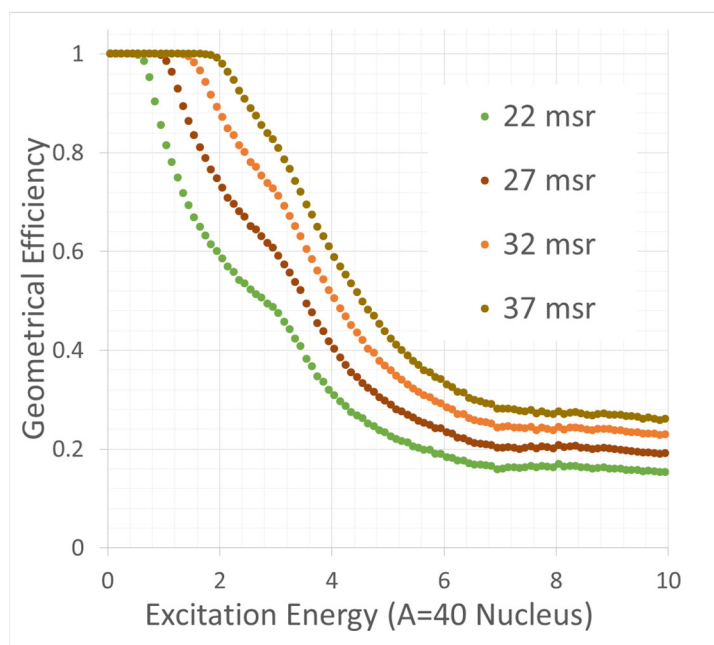


Figure 4-18 The geometrical efficiency as a function of excitation energy for neutrons emitted from an unbound system with mass number 40 at 180 MeV/u. A coverage of 90% is achieved up to an excitation energy of 2 MeV for a neutron solid angle coverage of 32 msr.

Finally, we note that the gap size of the sweeper magnet is also constrained by the need to insert a time-projection chamber (TPC) for the purpose of heavy-ion collision experiments, as discussed in 4.2.2.4. To study this constraint, simulations in combination with available data from measurements with the Spirit-TPC developed for use for experiments with the SAMURAI magnet at RIBF/RIKEN [OTS16, JHA16]. Based on these studies, it was found that a gap size of 60 cm is required to optimize the reconstruction efficiency and the quality of reconstruction of the reaction plan [BRO20]. As shown in Figure 4-19, an additional increase in the gap size results in relatively small gains in efficiency and quality.

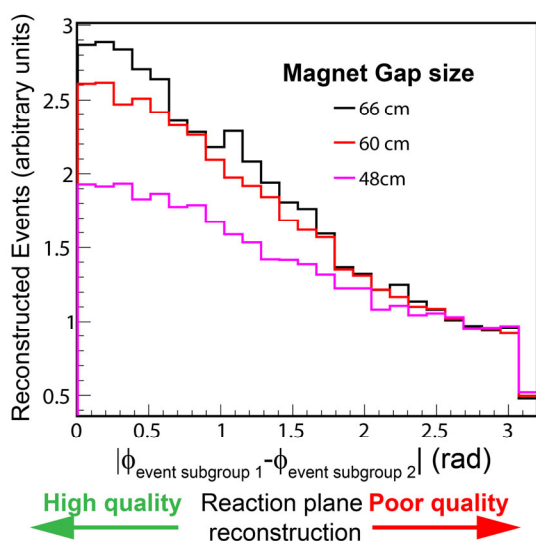


Figure 4-19 Simulation of the reaction plane reconstruction for heavy-ion collisions by using a TPC inserted in the sweeper magnet. The horizontal axis shows the difference in reaction plane angle for two subgroups of tracks in one event, as reconstructed in the TPC. If the difference is small, the reconstruction is of high quality. If the difference is large, the reconstruction is of poor quality. A substantial gain in efficiency and quality is achieved when increasing the sweeper magnet gap size from 48 cm to 60 cm. Further increasing to gap size comes with reduced additional gains [BRO20].

#### 4.3.1.4 Prototypical experiment IV: In-flight fission

As discussed in Section 4.2.4, in-flight fission experiments with fast beams enable the measurement of both fission fragments simultaneously, which provides a unique opportunity to study the correlations between the fission fragments and to gain a better understanding of the fission mechanism. In-flight fission experiments in which both fission fragments must be detected in the Spectrometer Section pose a constraint on the angular acceptance, as a large fraction of the fission cone must be within the acceptance. This is demonstrated in Figure 4-20, in which the efficiency of detection of fission pairs for different angular acceptances of the Spectrometer Section are shown for in-flight fission of at 200 MeV/u. The excitation energy was set at 20 MeV. The simulation was performed in LISE<sup>++</sup>, taking into account the angular acceptances of the Spectrometer Section. Three different angular acceptances are shown in combination with a momentum acceptance of 3%. For angular acceptances of  $\pm 60$  mrad (dispersive direction) by  $\pm 60$  mrad (non-dispersive direction) and  $\pm 50$  mrad (dispersive) by  $\pm 75$  mrad (non-dispersive), the averaged efficiencies for the detection of both fission fragments are comparable and around 10%, sufficient for performing in-flight fission studies. For smaller angular acceptances, such as  $\pm 50$  mrad (dispersive) by  $\pm 50$  mrad (non-dispersive) as shown in Figure 4-20 as well, the efficiency is much less than 10% on average, and close to 0 for certain mass numbers. The latter would be very detrimental for detailed studies of fission. Therefore, a minimum solid angle of 15 msr is determined as the minimum requirement for in-flight fission studies. It is noted that for the asymmetric acceptance of  $\pm 50$  mrad (dispersive) by  $\pm 75$  mrad (non-dispersive), the efficiency is relatively flat as a function of mass number. For the symmetric acceptance of  $\pm 60$  mrad (dispersive) by  $\pm 60$  mrad (non-dispersive), the efficiency is higher around the central mass number, and lower for asymmetric fission pairs.

The above calculations were repeated with theoretical fission calculations for  $^{240}\text{Pu}$  from the CGMF code [TAL13] performed at Los Alamos National Laboratory [LOV20]. Although the details of the fission fragment distributions are different than those used in the LISE<sup>++</sup> calculations, the outcome in terms of the requirement for the solid angle coverage is the same [ZEG20]. It was also shown that the increase in the efficiency for detecting both fission fragments saturates if the solid angle coverage is increased further, as the momentum acceptance for measuring both fission fragments becomes the constraining factor, as is shown in Figure 4-21.

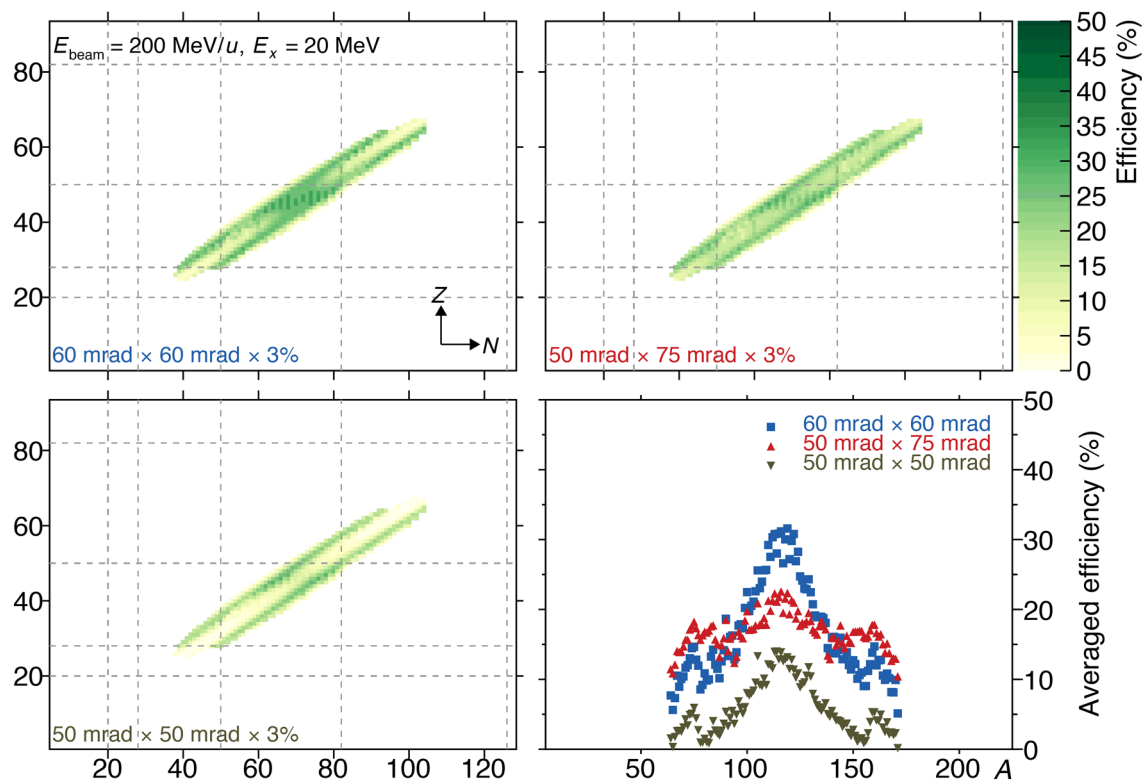


Figure 4-20 Simulations of in-flight fission at 200 MeV/u in which both fission products are detected in the Spectrometer Section. In the top and bottom-left panels, the efficiency for detecting fission pairs is plotted as function of neutron ( $N$ ) and proton number ( $Z$ ). In the top-left panel the angular acceptances was set to  $\pm 60$  mrad (dispersive direction) by  $\pm 60$  mrad (non-dispersive direction); in the top-right panel the angular acceptances was set to  $\pm 50$  mrad (dispersive direction) by  $\pm 75$  mrad (non-dispersive direction); in the bottom-left panel the angular acceptances was set to  $\pm 50$  mrad (dispersive direction) by  $\pm 50$  mrad (non-dispersive direction). The bottom-right plot shows the averaged efficiency for the detection of both fission pairs as a function of mass number for each of the three angular acceptances. Correlations in the 2-D acceptance plots are caused by correlations between fission fragments that are produced and somewhat sensitive to fission model used to perform the simulations.

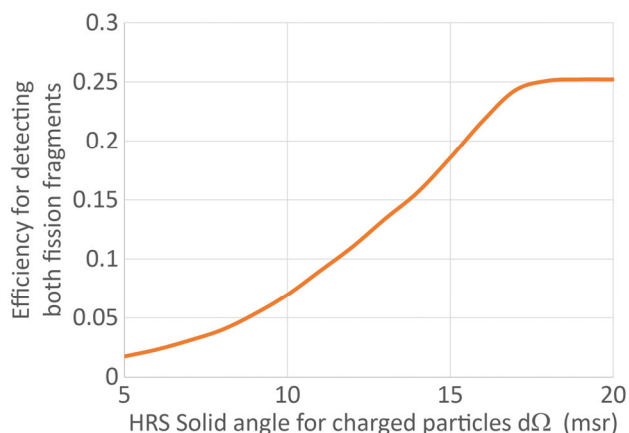


Figure 4-21 Overall efficiency for detecting both fission fragments as a function of solid angle for charged particles of the HRS. The saturation above 15 msr is due to limitations imposed by the momentum acceptance of the HRS. These calculations were performed with theoretical fission inputs using the CGMF code [TAL13] performed at LANL [LOV20].

#### 4.3.1.5 Prototypical experiment V: Time-of-flight magnetic-rigidity mass measurements

As discussed in Section 4.2.2.1, time-of-flight magnetic rigidity (ToF- $B\rho$ ) mass measurements provide a unique opportunity to simultaneously measure a large number of nuclear masses that define the mass surface far from the valley of stability and constrain theoretical models. Such data are important for astrophysical modeling, in particular the  $r$  process. ToF- $B\rho$  measurements are different than all other experiments foreseen with the HRS and, therefore, pose different constraints. A schematic overview of ToF- $B\rho$  measurements as foreseen is shown in Figure 4-22. This scheme is based on successful experiments performed at NSCL with the S800 [EST11,MEI13,MEI15]. A cocktail beam of rare-isotopes passed through a time-of-flight start detector and tracking detector which are placed in the fragment separator. By operating the HTBL in dispersion-matched mode (see Section 4.3.2.7.1), the rigidity of the beam can be measured at the target station of the HRS by measuring the position in the dispersive direction. Unlike other experiments at the HRS, the spectrometer is used to analyze the beam particles rather than the reaction products: all nuclei will be detected at the same position in the focal plane of the Spectrometer Section, where a time-of-flight stop detector and energy loss detectors for particle identification must be placed. To achieve the desired mass resolution of  $10^{-4}$ , a time-of-flight resolution of better than 30 ps must be achieved. In addition, dedicated detectors for tracking at the Fragment Separator and the target position at the entrance of the Spectrometer Section are required that achieve  $\sim 0.3$ -mm (FWHM) position resolution. In order to achieve a mass resolving power of 10000, the momentum resolving power ( $R_p$ ) must be better than 10000 for the ToF- $B\rho$  measurements. The acceptance requirements for the Spectrometer Section (less than 10 msr solid angle and  $\pm 0.5\%$  in momentum) are less stringent as for other experiments, as no reaction takes places at the target in front of the Spectrometer Section.



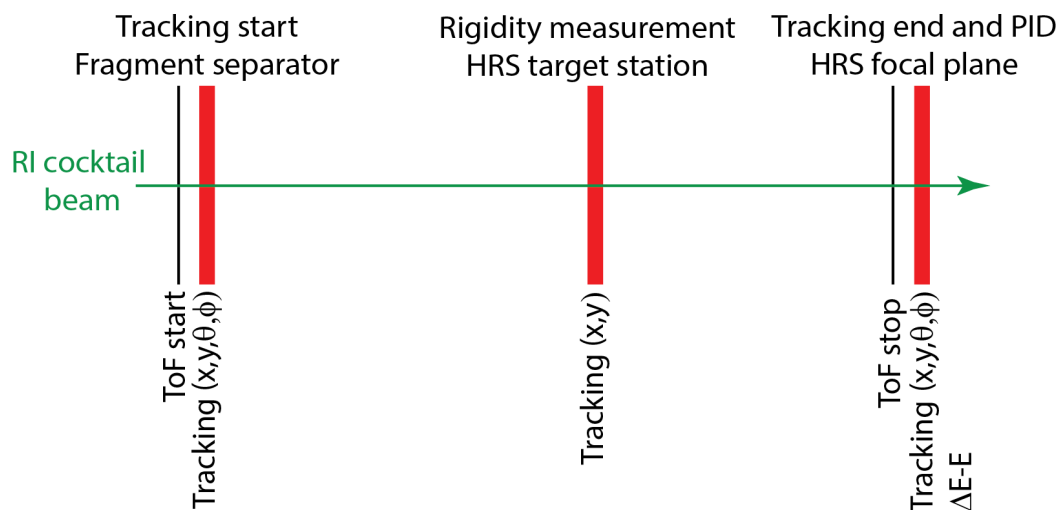


Figure 4-22 Schematic overview of ToF- $B\rho$  measurements. A cocktail of rare-isotope beams passes through ToF and tracking detectors in the fragment separator. The magnetic rigidity is measured at the target location of the Spectrometer Section. The time-of-flight stop signal comes from a detector placed in the focal plane of the Spectrometer Section, where tracking and  $\Delta E-E$  measurements are performed to do particle identification (PID).

#### 4.3.1.6 Overview of specifications for the Spectrometer Section of the HRS: three basic modes of operation

Based on the specifications for the experimental programs in Table 4-2, three basic modes of operation were identified, that have very different sets of specifications: a high-resolution mode, an invariant-mass mode, and a time-of-flight mass-measurement mode, which are briefly described below. An overview of the basic functionalities of these three modes is provided in Table 4-3.

**High-resolution mode:** This mode is necessary for a large fraction of the experimental types listed in Table 4-1 and the science program described in Section 4. It allows for the particle identification of the heaviest nuclei ( $A=238$ ), which requires a flight path of 25 m in the Spectrometer Section to achieve a mass resolving power of at least 400, with a time-of-flight resolution of 150 ps. In this mode, a relatively high momentum resolving power of 1500 with a beam spot size of 5 mm (FWHM) must be achieved with achromatic beam transport (See Section 4.3.2.7.1) even without tracking the incoming beam. The specifications for the momentum acceptance ( $\pm 2.5\%$ ) and solid angle coverage (15 msr) are sufficient for a large fraction of the experimental programs, including in-flight fission experiments that require a solid-angle coverage of 14.4 msr. The space around the target station is sufficient for the placement of all ancillary detector systems, including GRETA. In this mode, there is no strict specification on the solid angle coverage of neutrons at forward scattering angles. The rigidity requirement is 8 Tm. As an option, tracking detectors in the HTBL (See Section 4.3.2.7.2) can be utilized to achieve a higher momentum resolution through the



determination of the momentum of the incoming beam. Similarly, tracking detectors in the HTBL can be used to determine the angle of the beam particles on target and to improve the angular resolution of the reconstructed scattering angle. As discussed in Section 4.3.2.3, the use of tracking detectors in the beam line introduces the production of charge-states of the beam particles, in particular for beams with a high atomic number. This reduces the beam intensity (as beam particles in a charge-state other than preferred have different magnetic rigidity and will not be transported to the target) and potentially introduces contaminations. Therefore, as an alternative, one can operate the HTBL in dispersion-matched beam transport mode (See Section 4.3.2.7.1), in which the momentum spreads and the angular spreads associated with the different momenta are cancelled out. In that case, tracking detectors are not needed to achieve a resolution better than the momentum and angular spreads in the beam, but at the cost of beam intensity. Similar to the experiments presently carried out with the existing S800 Spectrometer, the choices related to the use of tracking detectors and beam transport modes depends strongly on the goals and constraints for particular experiments.

A variety of detectors will be used around the target and some are sensitive to magnetic fields. In particular detector systems that use photomultiplier tubes (PMTs) must be shielded against stray magnetic field. It is possible to shield PMTs locally for magnetic stray fields that are  $\sim 25$  Gauss. Therefore, magnetic fields around the target area must stay below such levels.

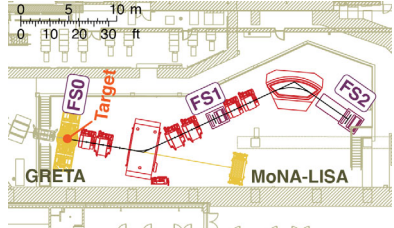
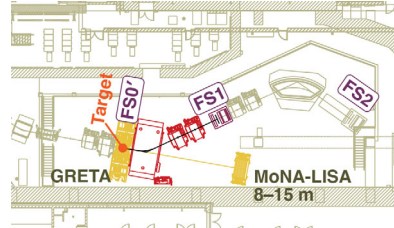
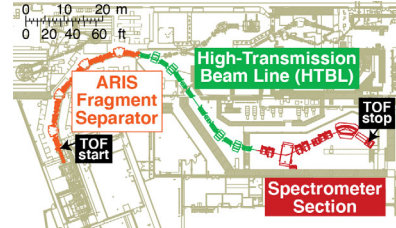
**Neutron invariant-mass mode:** This mode is necessary for experiments in which fast neutrons must be detected with a large solid angle coverage (32 msr) at forward angles, which is necessary for the neutron invariant-mass spectroscopy experiments (see Section 4.2.1.3), as well as heavy-ion collision experiment aimed at elucidating the Equation of State (see Section 4.2.2.4). In this mode, the specifications for mass and momentum resolving power of the Spectrometer Section of the HRS are less stringent than for the high-resolution mode ( $R_p=290$  and  $R_m=220$ , respectively), but the momentum acceptance specification is larger ( $\pm 5\%$ ). A key specification for this mode is the 32-msr solid-angle coverage for the neutrons at forward angles. A neutron flight-path length of up to 15 m must be accommodated. Less space for the placement of ancillary detectors is needed, but the use of GRETA with its most forward detector ring removed should be possible (at least 90 cm space up- and downstream of the target). Because the constraints on the momentum and mass resolving power are less stringent than for the high-resolution mode, experiment in the neutron invariant mass mode will predominantly be performed with achromatic beam transport through the HTBL (See Section 4.3.2.7.1). The large size of the beam spot associated with operating in dispersion-matched beam transport mode through the HTBL is detrimental to resolution of the neutron angular measurement, which must be avoided to achieve good resolutions in the reconstructed invariant-mass spectra.

As discussed in Section 4.3.1.3, the high fields associated with a large sweeper magnet make it difficult to reduce stray field to levels necessary for installing detectors that utilize PMTs near the



target location. The placement of GRETA at this location requires fields generally below 600 G, although for elements that are very near DS1 levels of 700-900 Gauss can be tolerated [ROD21]. Near the MoNA-LISA detector array, which utilizes PMTs, magnetic fields should be below 25G.

Table 4-3 Overview of the three operational modes for the Spectrometer Section

High Resolution Mode	Neutron Invariant-Mass Mode	ToF- $B\rho$ Mass Measurement Mode
Provides the full capabilities of the HRS and meets the specifications for majority of the science program	Meets the specifications for invariant-mass spectroscopy experiments in which neutrons are detected in the MoNA-LISA array	Achieves a long flight path from the beginning of the ARIS Reconfigured A1900 to the Focal Plane of the HRS required for ToF- $B\rho$ mass measurements
		

**ToF- $B\rho$  mass measurement mode:** This mode is specific for the ToF- $B\rho$  mass measurements (see Section 4.2.2.1). The Reconfigured A1900 of the ARIS Fragment Separator [HAU13], the HTBL, and the Spectrometer Section of the HRS must serve to create a very long flight path of at least 90 m. From the ion-optical point of view, the Spectrometer Section is operated in the same way as in the high-resolution mode, whereas the HTBL is operated such that these two are dispersion-matched and the entire system is doubly achromatic. By using dedicated detector systems for the ToF measurements, resolutions of better than 30 ps must be achieved to perform mass measurements with a mass resolving power of  $10^4$ . A momentum resolving power of better than  $10^4$  is required, but since there are no reactions that are being studied there are no stringent specifications on the momentum and angular acceptance of the Spectrometer Section.

Each of the experimental programs is categorized in one of the operational modes in the most right-hand side column of Table 4-2. Then, the specifications for each of the modes was determined by considering all the relevant experimental programs and taking the most constraining value for each of the specified values. These summarized specifications are shown at the bottom of Table 4-2. For convenience, these summarized specifications are shown in a separate table in Table 4-4. This table served as input for the ion-optical and detector designs.

Table 4-4 Overview of the specifications of the Spectrometer Section, listed for the three main modes of operation: high-resolution, neutron invariant-mass, and ToF-B $\rho$  mass-measurement modes.

Mode	High-resolution	Neutron invariant-mass	ToF-B $\rho$ mass-measurement
<b>Specification for</b>			
Maximum mass number	238	132	238
Mass resolving power	400	220	10000
Charge resolving power	156	85	156
Time-of-flight resolution (ps)	150	150	30
Flight path for charged particles (m)	25	11	90
Momentum resolving power	1500	290	>10000
Spectrometer solid angle (msr)	15	10	3
Angular resolution (mrad)	5	5	-
Space around target (cm)	123	90	-
Momentum acceptance ( $\delta p/p$ in %)	$\pm 2.5$	$\pm 5$	$\pm 0.5$
Neutron solid angle (msr)	-	32	-
Neutron flight-path length (m)	-	15	-
Gap for Time Projection Chamber (cm)	-	60	-
Unreacted beam rejection	yes	yes	-
Maximum magnetic rigidity (Tm)	8	8	7

#### 4.3.2 Scientific specifications for the HTBL: optimizing the luminosity for experiments at the HRS

The vast majority experiments that will be performed with the HRS will be with rare-isotope beams that are far from stability and beam intensities will typically be (much) less than  $10^6$ . The most demanding experiments with the highest scientific impact will be with beams of rare isotopes furthest from the valley of stability. For the majority of these experiments, the achievable luminosity is most important. The experimental luminosity is a product of three basic parameters: 1) the intensity of the rare-isotope beam produced in the ARIS Fragment Separator; 2) the transmission efficiency of rare-isotope beams from the fragment separator to the target station of the HRS; and 3) the thickness of the reaction target placed at the target station of the Spectrometer Section. These parameters and the specifications they impose on the HTBL are briefly discussed in the following subsections, followed by additional scientific specifications for the HTBL, which are related to the beam transport modes and beam diagnostics, tracking and other devices.



#### 4.3.2.1 The intensity of the rare isotope beam produced in the ARIS Fragment Separator

Figure 4-23 presents an overview of the estimated magnetic rigidities for which the rare-isotope beam production rate is maximized at the exit of the ARIS Fragment Separator for FRIB at 200 MeV/u. Except for the most proton-rich isotopes, the optimal rigidity exceeds 4 Tm and ranges up to 8 Tm for light, very neutron-rich isotopes. However, the magnetic spectrometers presently available at NSCL, the S800 spectrograph and the Sweeper magnet, as well as the beam lines leading to these devices are limited to a rigidity of about 4 Tm, resulting in significantly reduced rare-isotope beam intensities for FRIB. This limitation will prevent substantial segments of the science outlined in Section 4.2 from being accomplished. Therefore, it is important that the HTBL can transmit high-rigidity beams to the reaction target and that the Spectrometer Section can analyze the products produced from reactions with such beams.

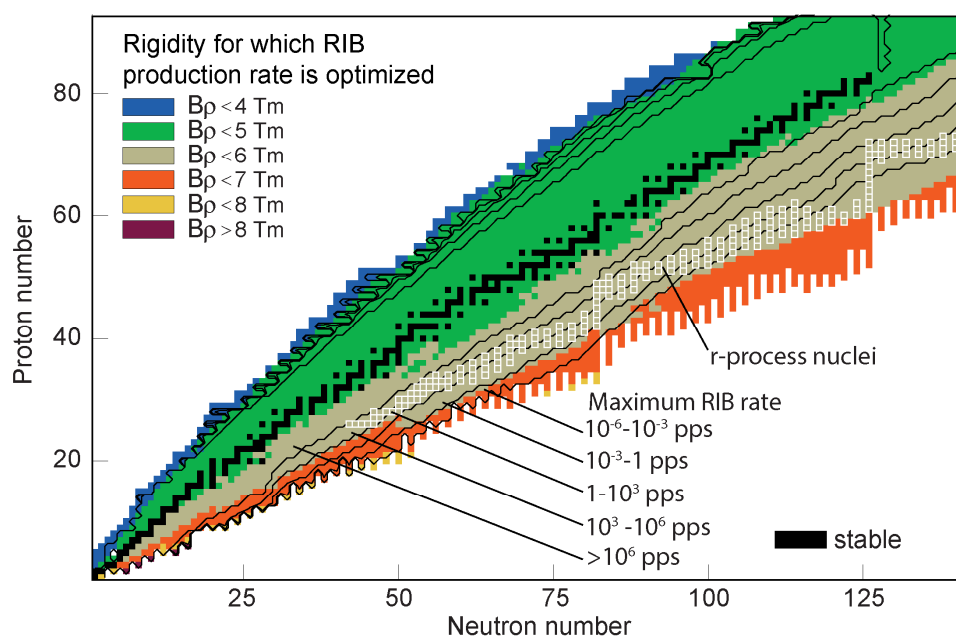


Figure 4-23 Magnetic rigidities for which the rare-isotope production rate across the chart of nuclei is optimized<sup>2</sup> for FRIB at 200 MeV/u (for FRIB at 400 MeV/u, see Section 4.3.2.6). This varies across the nuclear chart with the highest rigidities needed for the most neutron-rich species.

#### 4.3.2.2 The transmission efficiency of the beam line.

The beam line used to transport the rare-isotope beams from the ARIS Fragment Separator to the reaction target should accommodate the emittance and rigidity of these beams. Their emittance will exceed what can be accommodated in the beam lines to existing spectrometers at NSCL.

<sup>2</sup> From FRIB Estimated Rates Version 1.08 <https://groups.nsl.msu.edu/frib/rates/fribrates.html>

Therefore, the beam line to the target station of the HRS must be optimized to minimize transmission losses to less than 5% for the rare-isotope beams delivered by the ARIS Fragment Separator in achromatic beam-transport mode. Consequently, a significant gain in luminosity can be achieved with the HRS in comparison to experiments with the existing S800 Spectrograph and Sweeper Magnet. To perform these optimizations, six representative rare isotope beams which are important for the scientific program as discussed in Section 4.2, were selected for which full end-to-end simulations (from the production target in the fragment separator to the target station of the HRS) were performed, as detailed in Section 5.4. These beams are listed in Table 4-5. These six beams are representative of the envisioned program and are distributed across the chart of isotopes. Therefore, they provide a good sample to ensure that the specification for the transmission efficiency is met. Five of these beams are on the neutron-rich side of the chart of isotopes, where the required rigidities to optimize the beam intensity are highest, and one is on the proton-rich side of the chart of isotopes. The table lists the rigidity of each beams before the wedge (which serves as the upper limit of the rigidity for which each beam can be produced) and after the wedge, which for each case was selected to optimize the purity of the rare isotope beams. The latter values were used in the end-to-end simulations.

*Table 4-5 Overview of six representative rare-isotope beams that were used to optimize the transmission efficiency of the beam line from the ARIS Fragment Separator to the Targets Station of the HRS. Transmission studies were performed in end-to-end Monte-Carlo simulations (from the production target at the ARIS Fragment Separator to the Target Station of the Spectrometer Section), including the placement of a wedge to optimize the purity of the beams.*

Transmission of Representative RIBs	Production Mechanism	Rigidity at maximum RIB intensity (Tm)	Rigidity after wedge (Tm)
<sup>40</sup> Mg	fragmentation	7.25	6.68
<sup>60</sup> Ca	fragmentation	6.43	5.94
<sup>84</sup> Ni	in-flight fission	6.16	5.80
<sup>100</sup> Sn	fragmentation	4.15	3.73
<sup>140</sup> Sn	fragmentation	5.44	4.88
<sup>204</sup> Pt	fragmentation	5.05	3.98





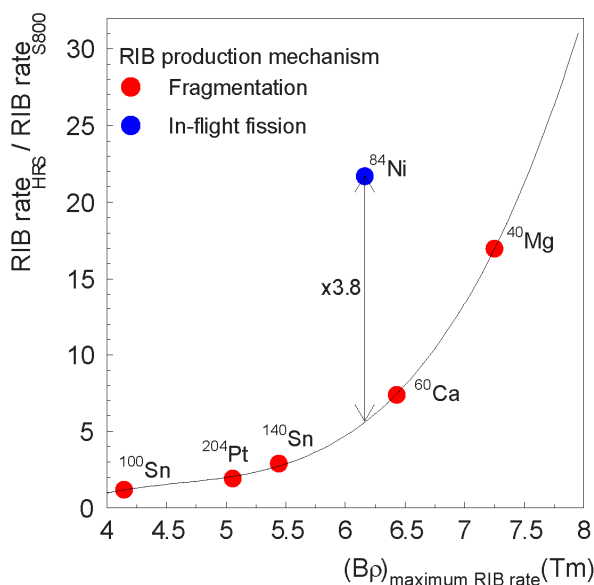


Figure 4-24 Gain in rare-isotope beam rate in the HRS compared to performing experiments with the existing S800 Spectrograph. These gains are estimated in end-to-end Monte-Carlo simulations as detailed in Section 5.4. The solid line indicates the trend of the gain in rate as a function of magnetic rigidity for rare isotopes produced by in-beam fragmentation. For rare isotopes produced via in-flight fission (here exemplified by  $^{84}\text{Ni}$ ) the gain is much higher than indicated by this trend line, due to the severe limitations imposed by the transmission to the S800 compared to the HRS.

The rare-isotope beam intensity at the target station of the HRS for each of these beams was compared with the beam intensity that can be achieved by using the S800 spectrograph instead of the HRS, taking into account the rigidity limitation of 4 Tm for the latter and transporting the beams through the existing beam line to the S800 spectrograph. The results of that study are shown in Figure 4-24, where the ratio of the rare-isotope beam rate for HRS and the S800 Spectrograph are plotted as a function of the rigidity for which the rare-isotope beam rate is optimized. For isotopes produced by in-flight fragmentation, the gain factor increases to about 17 for the case of  $^{40}\text{Mg}$ . The case of  $^{84}\text{Ni}$  doesn't follow the smooth trend line established for the other cases because it is produced by in-flight fission rather than fragmentations. Since isotopes produced by in-flight fission have very large beam emittance associated with the fission cone, the development of an optimized beam line is especially important for achieving a high transmission to the experimental station.

#### 4.3.2.3 Charge-state production

The production of charge states when rare-isotope beams interact with tracking detectors, targets, and other materials that are placed in the path of the beam are an important consideration for the design of experiments with the HRS. An optimized beam line allows tracking detectors to be inserted for the purpose of measuring event-by-event the momentum and time-of-flight of isotopes in the beam. These event-by-event measurements allow individual beam ions to be identified. Although tracking detectors are thin and the energy losses are relatively small, a significant complication arises from the production of different charge states of a single isotope upon passage through these detectors, which results in a loss of beam intensity and contamination of the secondary beams. A similar issue occurs at the target of the experimental station. The production



of multiple charge states increases significantly for high- $Z$  beams and at lower beam energies. To study such effects, calculations were performed with the code GLOBAL [SCH98], which is integrated in LISE++ [TAR16]. GLOBAL was developed for beam energies in the range of 80 to 1000 MeV/u. The production of charge-states for the following scenarios was considered:

- Equilibrium charge-state production (e.g. through thick reaction targets).  ${}^9\text{Be}$  was chosen as a typical target material.
- Charge-state production through a 130- $\mu\text{m}$  thick plastic scintillator, which is a typical thickness for a beam-line timing detector.
- Charge-state production through a set of PPAC tracking detectors systems. These PPACs, which have an effective thickness of about 1.8 mg/cm<sup>2</sup> are discussed in more detail in section 7.3.1.2.
- Charge-state production for the case in which the beam line has no tracking detectors or other materials, except for the rest gas present at the required vacuum levels ( $10^{-5}$  Torr)

Except for case 3, for which only the nucleus  ${}^{204}\text{Pt}$  was studied, calculations were performed for initial beams of  ${}^{60}\text{Ca}$  ( $Z=20$ ),  ${}^{140}\text{Sn}$  ( $Z=50$ ), and  ${}^{204}\text{Pt}$  ( $Z=78$ ,  $Z-Q=2$ ) for magnetic rigidities ranging from 4 Tm to 8 Tm. These beams are representative for the scientific program with the HRS and span a wide  $Z$  range. The results are shown in Figure 4-25. The left column shows the results for charge-state production in  ${}^9\text{Be}$  at equilibrium thickness, which ranges from  $\sim 20$  mg/cm<sup>2</sup> for  ${}^{60}\text{Ca}$  at 4 Tm to  $\sim 420$  mg/cm<sup>2</sup> for  ${}^{204}\text{Pt}$  at 8 Tm. Clearly, for  $Z=20$  ( ${}^{60}\text{Ca}$ ), charge-state production is very small. For  $Z=50$  ( ${}^{140}\text{Sn}$ ), an increase in beam energy results in an increase in  $Z-Q=0$  charge-state production, and a higher rigidity is clearly advantageous. For  $Z=78$ , with  $Z-Q=2$  ( ${}^{204}\text{Pt}^{76+}$ ), the situation is more complex: at lower rigidities, the production of the  $Z-Q=2$  charge state is dominant, but at higher rigidities, the production of the  $Z-Q=1$  charge state is strongest. For experiments with high- $Z$  beam, experiments must be carefully designed to strike an optimal balance between charge-state production, target thickness, and other considerations that affect the choice of beam energy.

For beams passing through materials that are thinner than the equilibrium thickness (scintillator and PPACs) for which the results are shown in the middle and right columns of Figure 4-25, the results for  $Z=20$  and  $Z=50$  are comparable to the results for passing through  ${}^9\text{Be}$  at equilibrium thickness, although the gain made in predominantly populating the  $Z-Q=0$  charge state for  $Z=50$  is significantly stronger with increasing beam rigidity. For  $Z=78$ , the production of the  $Z-Q=2$  charge state is rather independent of the rigidity, but doesn't exceed 60% after passing through the PPACs. Consequently, the use of timing and tracking detectors in the beam transport must be carefully considered in the planning of experiments as well.

Finally, the charge-state production in the rest gas of the beam line vacuum was evaluated. It was found that, even for the highest  $Z$ , the production of charge states different from that of the initial



rare-isotope beam is less than 0.1% at a pressure of  $10^{-5}$  Torr, when considering the whole distance from the beginning of the HTBL to the final focal plane of the HRS. This is much smaller than the charge-state production in tracking detectors and targets.

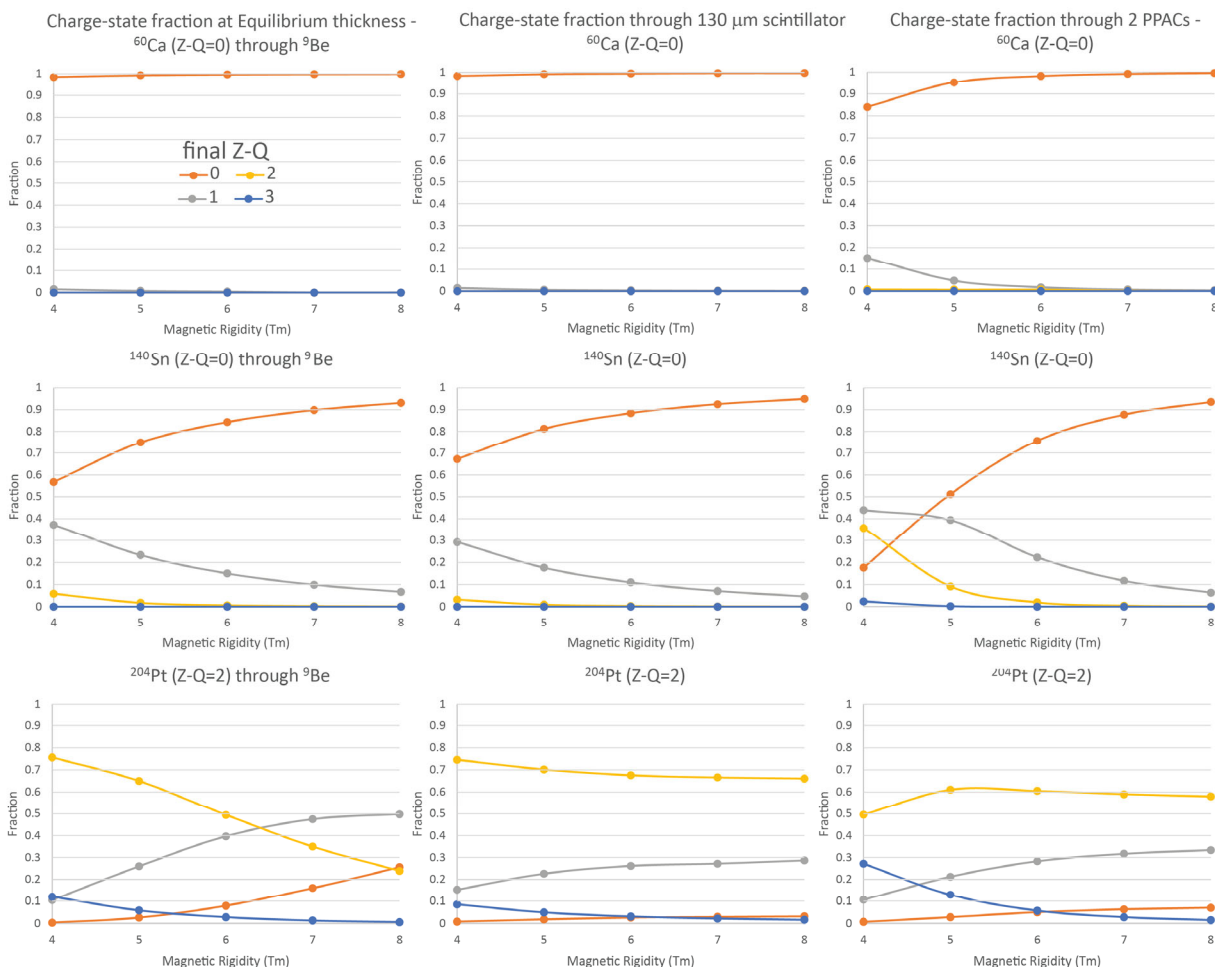


Figure 4-25 Charge-state distributions after  $^{60}\text{Ca}$  (top row),  $^{140}\text{Sn}$  (middle row), and  $^{204}\text{Pt}$  (bottom row) beams pass through a  $^9\text{Be}$  target at equilibrium thickness (left column), a 130- $\mu\text{m}$  thick plastic scintillator (middle column), and a set of tracking PPACs (right column). Orange, grey, yellow, and blue lines refer to final charge states of  $Z-Q=0, 1, 2,$  and  $3,$  respectively.

#### 4.3.2.4 The thickness of the reaction target at the spectrometer.

By performing experiments at higher beam energies, the luminosity can be increased significantly due to the fact that thicker reaction targets can be used. The impact of this effect is exemplified in Figure 4-26(a) for the case of in-beam  $\gamma$ -ray spectroscopy after proton knockout from  $^{61}\text{Sc}$  in a  $^9\text{Be}$



target. To achieve a Doppler-reconstructed  $\gamma$ -ray energy resolution of 2%, the change in rigidity due to the loss in velocity [ $\Delta(v/c)$ ] in the target must be limited to 5%. At a rigidity of 4 Tm, a target thickness of less than 175 mg/cm<sup>2</sup> would be required. At a rigidity of 5.95 Tm, at which the production rate of <sup>61</sup>Sc is maximized, a target thickness of less than 700 mg/cm<sup>2</sup> would be required. From this consideration, an increase by a factor of 4 in luminosity is achieved by operating at the higher rigidity and allowing for a thicker target. Figure 4-26(b) shows the gain factor in luminosity of performing experiments at the HRS with a maximum rigidity of 8 Tm compared to performing experiments at the S800 spectrograph with a maximum rigidity of 4 Tm, as a function of proton number  $Z$  and the magnetic rigidity of the HRS

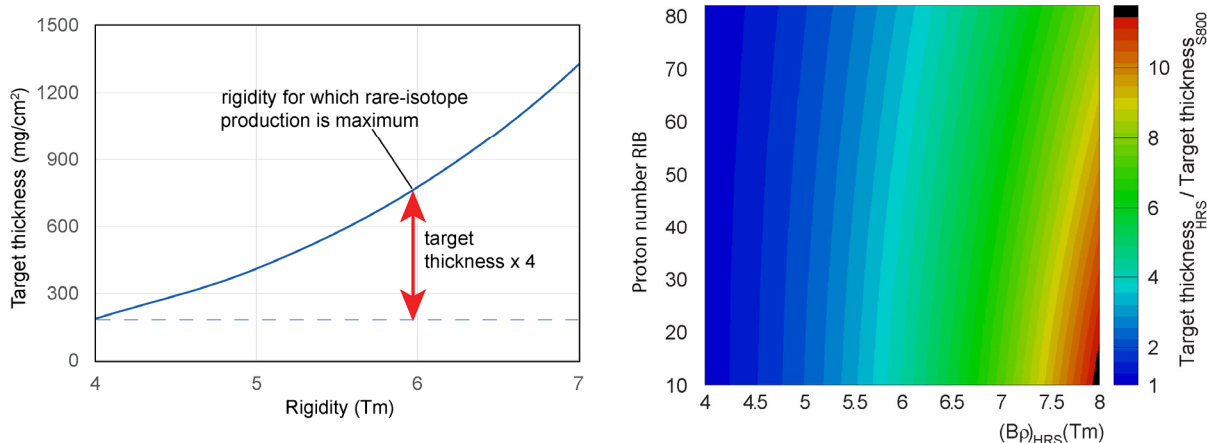


Figure 4-26 (a) Illustration of the luminosity gain that can be achieved by performing experiments at rigidities for which the rare-isotope production rate is maximum. In the case of proton knockout from <sup>61</sup>Sc, populating <sup>60</sup>Ca, a 4 times thicker target can be used assuming that the change in velocity in the target does not exceed 5% in order to maintain a Doppler-reconstructed  $\gamma$ -ray energy resolution of better than 2%. (b) Luminosity gain factor due to the use of thicker reaction targets achieved by performing experiments up to 8 Tm by using the HRS compared to performing at 4 Tm by using the S800 magnetic spectrograph, as a function of proton number of the rare-isotope beam (y-axis) and rigidity used in the HRS (x-axis).

#### 4.3.2.5 Overall luminosity gains with the HRS

The luminosity for experiments is a combination of the rare-isotope beam production rate, the transmission efficiency, and the target thickness that can be utilized in the experiments, with the exception of ToF- $B\rho$  measurement for which the target thickness does not contribute. Based on the combined production and transmission efficiency studies of Sections 4.3.2.1 and 4.3.2.2, and the gains achieved by using thicker targets discussed in Section 4.3.2.4, the total luminosity gain by using the HRS compared to using the existing S800 Spectrograph was calculated with:



$$\text{luminosity gain} = \frac{\text{RIB Rate at HRS Reaction Target}}{\text{RIB rate at S800 Reaction Target}} \times \frac{\text{HRS Reaction Target Thickness}}{\text{S800 Reaction Target Thickness}}$$

The results for the six representative beams of Table 4-5 are shown in Table 4-6. The gains are small for proton-rich  $^{100}\text{Sn}$  for which the rigidity at which the production rate is optimized is close to 4 Tm, but become very high for very neutron-rich rare-isotope beams that require the high magnetic rigidity of the HRS. The gain factor for the most rigid representative beam ( $^{40}\text{Mg}$ ) exceeds 100. Based on the systematics established in the previous section, the luminosity gains were estimated for all isotopes across the chart of nuclei, as shown in Figure 4-27.

Table 4-6 Luminosity gains for experiments at the HRS compared to performing experiments at the existing S800 Spectrometer for the six representative rare-isotope beams of Table 4-5.

Representative RIB	Rigidity (Tm) after FRIB separator for maximum RIB rate	(RIB Rate at HRS reaction target)/ (RIB Rate at S800 reaction target)	(HRS reaction target thickness)/ (S800 reaction target thickness)	Luminosity gain = product of ratios
$^{40}\text{Mg}$	6.68	17	6	102
$^{60}\text{Ca}$	5.94	7.4	3.2	24
$^{84}\text{Ni}$	5.80	22	3.6	79
$^{100}\text{Sn}$	3.73	1.2	1	1.2
$^{140}\text{Sn}$	4.88	2.9	1.9	5.5
$^{204}\text{Pt}$	3.98	1.9	1	1.9

For over 90% of the neutron-rich rare isotopes, gain factors in luminosity of 2 to 100 are achieved. For the most asymmetric neutron-rich isotopes, such as  $^{40}\text{Mg}$ , luminosity gains of more than a factor of 50 can be achieved. For neutron-rich isotopes up to  $N=50$  that are produced with rates of 0.001-1 pps, luminosity gain factors exceed a factor of 20. For heavier neutron-rich isotopes, gain factors of 2-10 are achieved. For nearly all nuclei in the path of the  $r$ -process, the gain factors lie between 5 and 20. The average luminosity gain factor for neutron-rich isotopes is about 10. On the proton-rich side of the chart of the nuclides, gain factors of up to 2 are achieved, with an average of 1.5.

For ToF- $B\rho$  experiments, in which case no gain in luminosity is achieved by using a thick reaction target, the gain is solely due to the increased rare-isotope beam rate by being able to run at high rigidities, as listed in the 3<sup>rd</sup> column of Table 4-6. Gains range from ~2-20 for neutron-rich isotopes, including those in the path of the  $r$  process.



Finally, we note that for each experiment, the rigidity and target thickness will have to be optimized as part of the proposal and experiment preparation process. There are other factors that play a role in determining the optimal choices and the results presented here are to illustrate the impact that the increase rigidity capability has on the science program. For individual experiment, further optimization could lead to additional increases in luminosity, or for gains in luminosity to be somewhat lower than presented in this section.

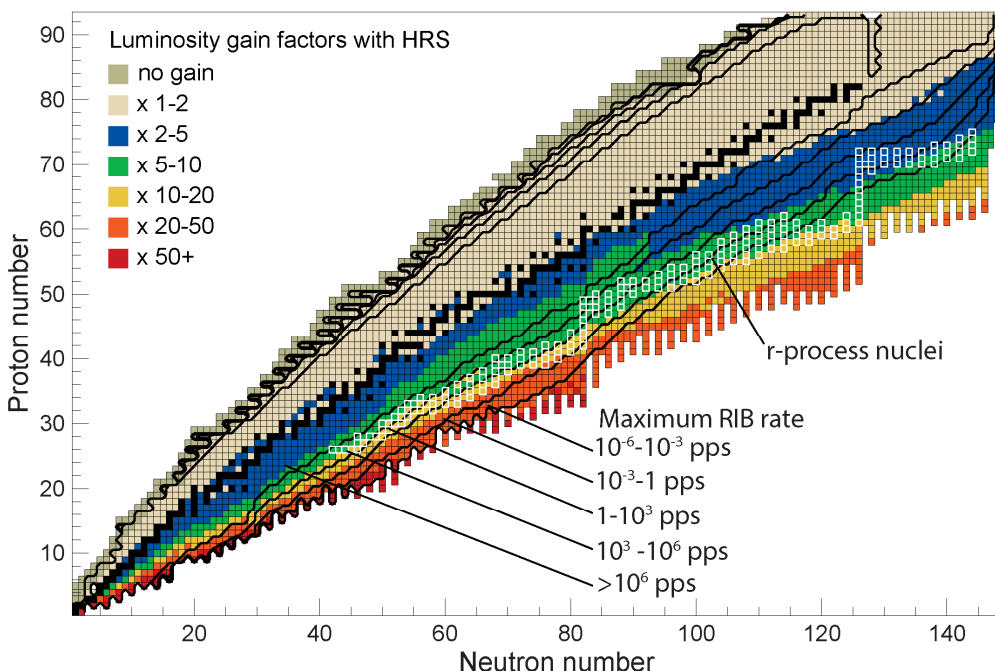


Figure 4-27 Estimated luminosity gain factors that can be achieved by using the HRS compared to using the existing S800 Spectrometer across the chart of nuclei. The rare-isotope production rates are indicated by solid lines and the nuclei shown with white boundaries correspond to the path of the astrophysical *r* process.

#### 4.3.2.6 Additional luminosity gains with the HRS after an upgrade of FRIB to 400 MeV/u

The optimum magnetic rigidities shown in Figure 4-23 are for the present (200 MeV/u) capabilities of FRIB. As discussed below, a magnetic rigidity of 8 Tm is appropriate even with upgraded FRIB (400 MeV/u) energy.

An energy upgrade of the FRIB accelerator is envisioned in the future, which would increase the optimum rigidity for the production of RIBs as well. Therefore, even though the specification for achieving a rigidity of 8 Tm in the HTBL and the Spectrometer Section of the HRS is only necessary for relatively light neutron-rich isotopes, a much larger region of nuclei will benefit from the 8-Tm rigidity capability once an upgrade from 200 MeV/u to 400 MeV/u for FRIB has been



completed. The estimated gains in beam intensity delivered to the HRS target station in light of a possible 400-MeV/ $u$  energy upgrade of FRIB are shown in Figure 4-28, assuming that the HTBL and Spectrometer Section of the HRS can bend rare isotopes that have rigidities of up to 8 Tm. Strong gains (more than a factor of 4) are predicted across a very large fraction of the chart of nuclides. Elements produced by in-flight fission ( $20 < Z < 40$  and  $40 < N < 80$ ) benefit strongly (up to a factor of 15) as the fission-cone becomes more forward peaked.

In addition to the gains in beam intensity, the luminosity for experiments at the HRS when FRIB is upgraded to 400 MeV/ $u$  increases further due to the fact that even thicker reaction targets can be used at the target station FS0. For the most neutron-rich nuclei the additional gain in luminosity due the ability to use thicker reaction targets, is on average a factor of 3, based on a similar analysis as the ones discussed in Section 4.3.2.4.

In Figure 4-29, the magnetic rigidities for which the production of rare-isotope beams is optimized are plotted across the chart of nuclei. Because of the higher beam energies, it becomes highly advantageous to use thick production targets because multi-step reactions can strongly increase the yield for the most exotic systems. As a consequence, the optimum magnetic rigidities are lower than what might have been expected on the basis of extrapolations from the calculations at 200 MeV/ $u$ , where targets of sufficient thickness to optimize the contribution from multistep production mechanisms are for most cases not feasible. In addition, due to the strong contribution from multi-step processes to the production of rare isotopes, the yield as a function of target thickness (and magnetic rigidity) for FRIB at 400 MeV/ $u$  changes much more slowly compared to the production rate for FRIB at 200 MeV/ $u$ . Consequently, except for a region of light neutron-rich isotopes below  $Z=25$  and around  $Z=45$ , magnetic rigidities of 8 Tm are sufficient to achieve the optimum production rates of rare isotopes. For the lighter neutron-rich isotopes, relatively high production rates are already achieved at FRIB 200 MeV/ $u$  and the gains at 400 MeV/ $u$  are minor. For the neutron-rich systems around  $Z=45$ , the gain in production rate when operating at optimal rigidity ( $\sim 8.5$ -9 Tm) is small compared to operating at 8 Tm (less than a factor of 2). It is concluded that a magnetic rigidity of 8 Tm is sufficient to achieve the optimum production rate for the vast majority of rare isotopes produced at FRIB at 400 MeV/ $u$ , and that the gains by achieving an even higher rigidity are small.





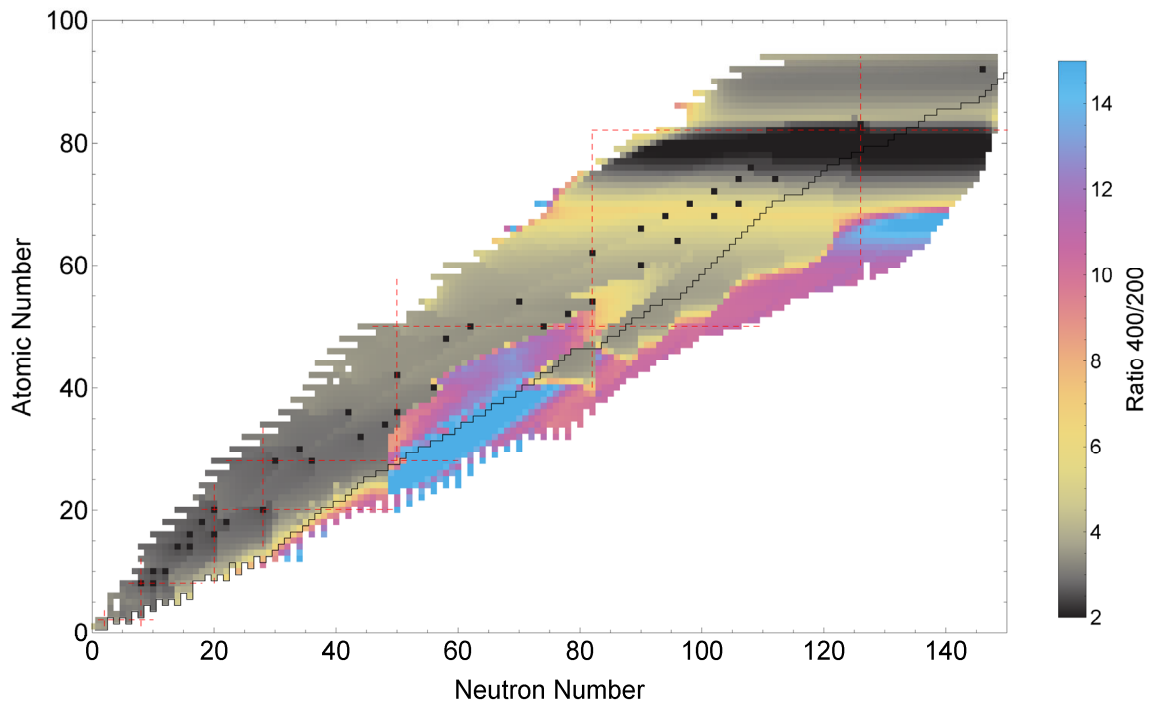


Figure 4-28 Ratio of RIB yields for FRIB with 200 MeV/u capability and 400 MeV/u capability after an energy upgrade. The gain in beam intensity is a factor of 5-10 for the most neutron-rich isotopes, assuming that beams with a rigidity of up to 8-Tm can be transmitted to the target station of the HRS. The black squares designate primary beams used.

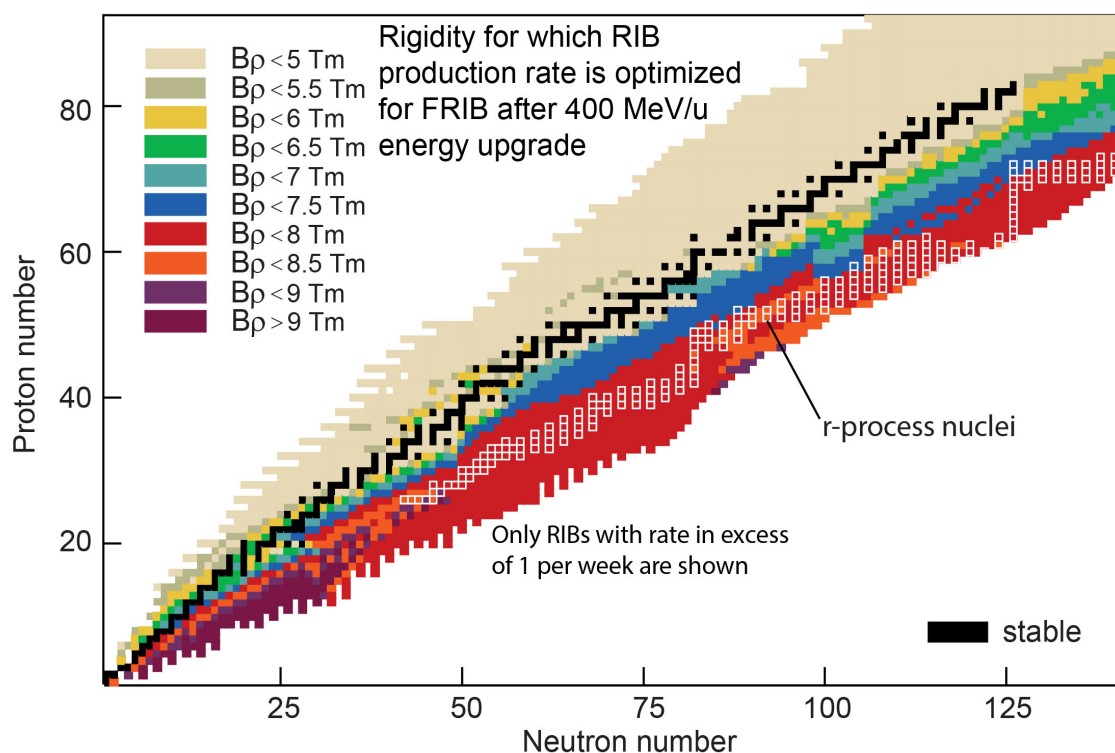


Figure 4-29 Estimated rigidities for which the production rates of rare isotope beams is optimized after a 400 MeV/u energy upgrade of FRIB.

#### 4.3.2.7 Additional specifications for the beam transport from the ARIS Fragment Separator to the target station of the HRS.

In addition to the specifications on the transmission of the rare-isotope beams, there are additional scientific specifications for the beam transport from the ARIS Fragment Separator [ARI13] to the target station at the entrance of the Spectrometer Section. These pertain to the different beam transport modes that the HTBL must accommodate (see Section 4.3.2.7.1), as well as the need to insert beam-diagnostic and tracking-detector stations in the beam line (Section 4.3.2.7.2), an RF fragment separator for beam purification of proton-rich rare-isotope beams (Section 4.3.2.7.3), and the length of the HTBL for the purpose of TOF- $B\rho$  mass measurements (Section 4.3.2.7.4).

##### 4.3.2.7.1 Beam transport modes

The HTBL must be able to be operated in an achromatic mode, as well as in a dispersion-matched mode. The choice of which beam transport to use depends on the type and scientific goals of the experiment and both beam-transport modes have been used in the operation of the S800



Spectrograph at NSCL, as well as other spectrometers operated at other (rare-isotope beam) facilities.

In the achromatic beam-transport mode, for which the beam is doubly focused ( $x$  and  $y$ ) and doubly achromatic (lateral and angular) at the reaction target, the transmission of rare-isotope beams to the reaction target is optimized. In this mode, the momentum spread of the beam particles in contributes to the momentum spread of ejectiles from the reaction target, as shown in Figure 4-30(a). Therefore, the momentum resolution in the focal plane is limited by the momentum spread of the beam. In addition, beam particles that do not react in the target produce a wide image in a focal plane of the spectrometer as they are laterally dispersed and cannot be easily blocked. To improve the momentum and angular resolutions in the achromatic beam transport mode, it is necessary to measure the momentum and angle of individual beam particles with tracking detectors in the beam lines, so that they can be corrected for on an event-by-event basis. However, such event-by-event tracking imposes restrictions on the beam intensity and induces the production of charge-states.

In experiments at the HRS in which the momentum resolution must be better than the momentum spread of the beam particles without employing event-by-event tracking, or in which the unreacted beam particles must be focused in a focal plane such that they can be blocked prior to entering the detector systems, the dispersion matching technique must be applied, as shown in Figure 4-30(b). In this beam-transport mode, the beam is dispersed on the target such that it matches the dispersion matching condition, i.e. the dispersion of the beam line is the same as that of the reverse spectrometer. In addition to lateral dispersion matching, angular dispersion matching is also applied to cancel the angular spread of the beam particles associated with their differences in momenta. The disadvantage of the dispersion-matched beam transport is that the momenta of the beam particles must be restricted in order to not create too large of a beam spot on the target.



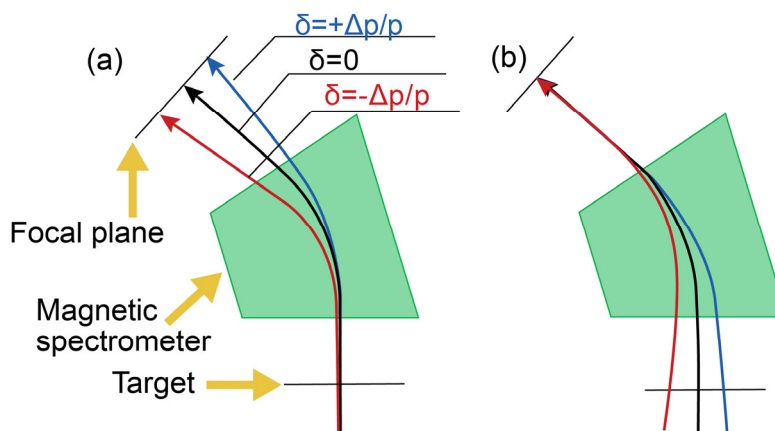


Figure 4-30 Illustration of different beam transport modes: (a) achromatic beam transport, in which the momentum spread ( $\pm\Delta p/p$ ) in the beam contributes to the size of the image in the focal plane of the spectrometer; (b) lateral and angular dispersion-matched beam transport, in which the dispersion on target is additionally correlated with the angles of the incoming particles, such that the angular spreads of the beam particles associated with their differences in momenta are cancelled out in the spectrometer. The rays indicate particles with different momenta. Figure is adapted from [FUJ02].

#### 4.3.2.7.2 Beam tracking and diagnostics specifications

Secondary rare-isotope beams produced by in-flight projectile fragmentation have relatively large beam emittances and are often a mixture of several isotopes. The presence of cocktails of isotopes in the beam is advantageous for efficiently measuring reactions on more than one rare isotope simultaneously, as long as reactions involving different components in the cocktail beam can be identified by using detector in the beam line. Therefore, depending on the specific experiment performed at the HRS, a variety of diagnostics and tracking detectors are required, for which appropriate space must be made available in the HTBL. For beam tuning purposes, viewers are necessary to quickly inspect the beam spots at various locations along the beam line. Timing detectors are needed to perform event-by-event beam particle identification and are also necessary to determine beam intensities. Tracking detectors are required for measuring the momenta and angles of beam particles in the achromatic beam transport mode. The momentum resolving power for the incoming beam must be compatible with that specified for the experimental programs in Table 4-4 ( $R_p > 1500$ ). For the determination of the angle at the reaction target in front of the Spectrometer Section of the incoming beam particles a resolution of 5 mrad must be achieved. This is particularly important for experiments where stringent angular cuts are necessary (e.g. for heavy-ion Coulomb excitation) or where the accurate knowledge of the reaction angle is critical for reducing the uncertainties in the kinematical reconstruction (e.g. in invariant-mass spectroscopy). These detector systems must have appropriately sized sensitive areas to diagnose the full emittances of the rare-isotope beams based on the ion-optical properties of the HTBL discussed in Section 5, achieve the position (better than 1 mm), timing (better than 150 ps for most

experiments, and better than 30 ps for the ToF- $B\rho$  measurements) for analyzing the properties of the beam, and be able to operate at high rates (a few hundred kHz for tracking detectors and at least 1 MHz for timing detectors) to perform event-by-event tracking when necessary for the experiments.

#### 4.3.2.7.3 Accommodation of a RF Fragment Separator for the purification of proton-rich rare-isotope beams.

The HTBL must provide a slot of sufficient length for the future insertion of an RF fragment separator (RFFS), although the RFFS is not part of the scope of the HRS project. An RFFS can be very useful for improving the purity of very proton-rich beams, for which less proton-rich contaminants can otherwise attain levels that hinder the experiment or render it unfeasible. As an example, for measurements with doubly magic  $^{100}\text{Sn}$  (see Section 4.2.3.1), the availability of an RFFS will be extremely beneficial.

At beam energies available at FRIB, momentum distributions of fragments produced via projectile fragmentation exhibit exponential-like tails on the low momentum side. Since proton-rich isotopes are found at lower magnetic rigidities than their more stable counterparts, low momentum tails of more abundant contaminants will overlap the region of interest for the desired nucleus, leading to significant levels of unwanted fragments. In the case of  $^{100}\text{Sn}$ , the purity of the beam is estimated at about  $1.2 \times 10^{-5}$ . With a production rate of about 8  $^{100}\text{Sn}$  isotopes per second, about  $7 \times 10^5$  contaminant isotopes would be in the beam, making it very difficult to track and isolate the events of interest.

The RFFS uses the time microstructure of the beams accelerated by the FRIB accelerator (with an RF frequency of 80.5 MHz) to deflect particles according to their time-of-flight, in effect producing a phase filtering [BAZ09]. The deflected, unwanted contaminants are then blocked by slits placed downstream of the RFFS. Based on simulations in LISE<sup>++</sup> [BAZ02,TAR08,TAR16] (see also Figure 4-32), a deflection angle of  $\pm 8.5$  mrad is required to efficiently improve the purity of a  $^{100}\text{Sn}$  beam by a factor of  $\sim 300$  (from a fraction of  $^{100}\text{Sn}$  in the beam of  $1.2 \times 10^{-5}$  to  $4 \times 10^{-3}$ ), assuming a realistic beam spot image size of 5 mm (FWHM). At this improved level of purity, only 2000 contaminant isotopes per second are in the beam, making it feasible to track and identify events associated with  $^{100}\text{Sn}$  particles. To obtain this level of purification, operation at 20.125 MHz is required as at higher RF frequencies, the RF bunches overlap, as shown in Figure 4-32. To operate at 20.125 MHz, it is required that the FRIB accelerator delivers the beams at a frequency of 20.125 MHz, which can be achieved by using a beam chopper.

Besides the RFFS itself, a station for diagnosing the filtering is required, which can coincide with diagnostics and tracking detectors needed for general beam diagnostics and tracking as discussed in Section 4.3.2.7.2. To perform particle identification of the components in the beam after the



RFFS, which is necessary for diagnosing the operation of the RFFS, detectors to measure energy loss are additionally required for particle identification.

A conceptual design of an RFFS that would provide the necessary level of contaminant reduction was developed by the FRIB Accelerator Physics Department to estimate the space specifications in the HTBL from the ARIS Fragment Separator to the Spectrometer Section. This conceptual design, shown in Figure 4-31, is based on a Double Quarter-Wave Resonator (QWR) cavity [BLA85] and has a large gap of 18 cm between the 1.86-m long electrodes, which is necessary to transmit large emittance rare-isotope beams [KUT20]. It operates at 20.125 MHz and has a gradient of 20.2 kV/cm to achieve the angular deflection of  $\pm 8.6$  mrad. The total length of this RFFS is 2.2 m long and has a height of 3.72 m. Additional magnetic steering magnets placed immediately prior and after the RFFS are required to keep the particles of interest along the central beam axis for further transmission along the beam line.

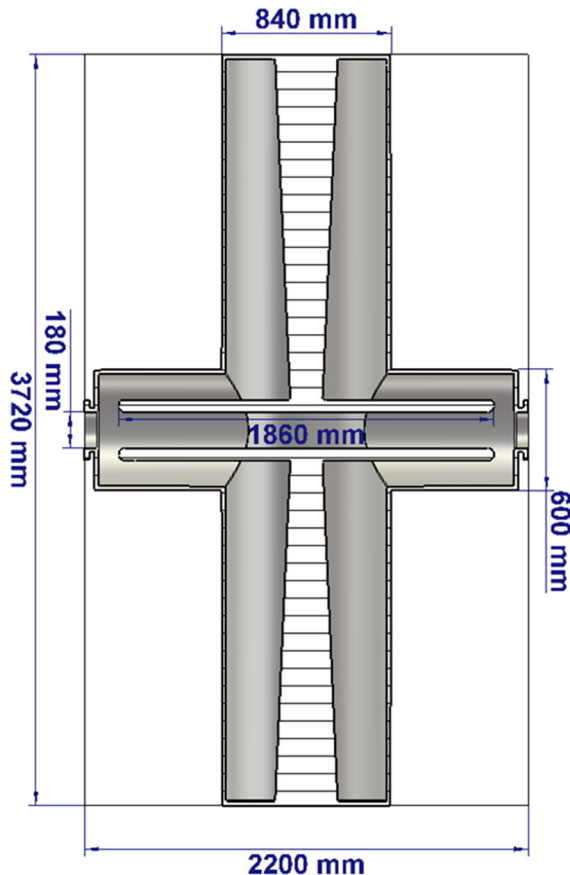


Figure 4-31 Conceptual design of a Double Quarter-Wave Resonator (QWR) cavity that serves as an RF Fragments Separator for the HRS. It operates at 20.125 MHz and provides an angular deflection of  $\pm 8.6$  mrad to achieve a contaminant suppression of a factor of about 300 for the case of  $^{100}\text{Sn}$ . The dimensions in the figure are in mm



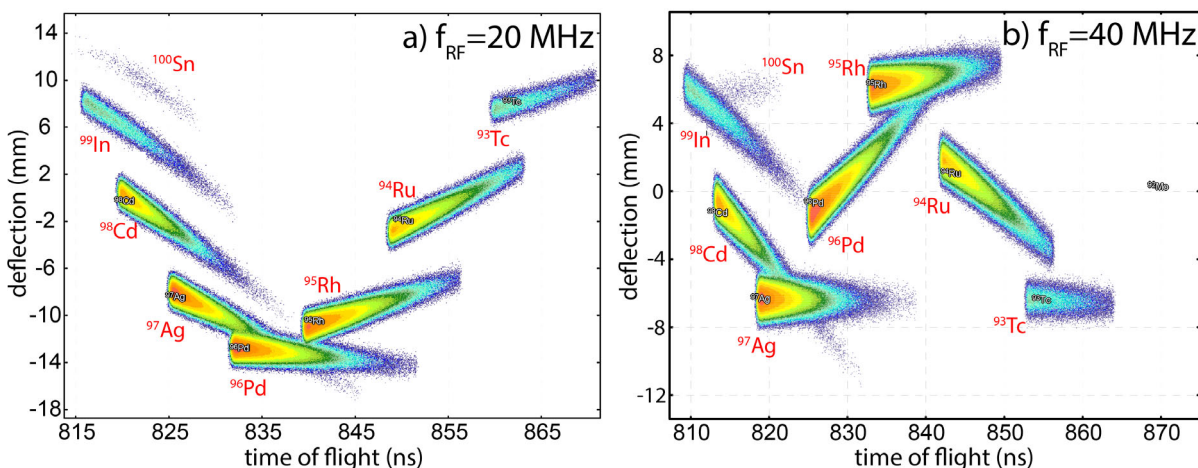


Figure 4-32 LISE<sup>++</sup> Simulation of the operation of an RFFS placed in the HTBL for the purification of a <sup>100</sup>Sn beam. In a) the operation at a frequency of 20.125 MHz is simulated. With a cut on the deflection position (y-axis) by using slit, it is possible to reduce the contamination from particle other than <sup>100</sup>Sn particles by a large fraction. At a frequency of 40.25 MHz, shown in panel b), the RF bunches overlap and the ability to purify the <sup>100</sup>Sn beam by using slits is strongly reduced compared to operation at 20.125 MHz.

#### 4.3.2.7.4 Constraints on the length of the HTBL for the purpose of ToF- $B\rho$ mass measurements.

The HTBL plays a special role in ToF- $B\rho$  mass measurements (see Section 4.2.2.1). Besides the delivery of the beams to the Spectrometer Section in dispersion-matched beam-optics mode, the HTBL contributes majorly to the flight-path length from the start (in the Reconfigured A1900 of the ARIS Fragment Separator) to the end (in the final focal plane of the Spectrometer Section) of the ToF measurement. With a position resolution for the tracking detectors of 0.3 mm (FWHM), and a ToF resolution of 30 ps, the total flight-path length has to exceed 90 m to achieve a mass resolving power of 10000. For the position measurements and the ToF measurements, dedicated detectors can be used, as relatively small areas need to be covered in the direction transverse to the beam line. These dedicated detectors are outside of the scope of the HRS.

#### 4.3.2.8 Summary of the Specifications for the High Transmission Beam Line

In Table 4-7 the main specifications for the HTBL discussed in in this section are summarized. These include the specifications for the optimized transmission of rare-isotopes beams, the magnetic rigidity, beam-transport modes, the length of the beam line, and the ability to perform tracking and diagnosis of beam particles and to insert an RF fragment separator in the future.

*Table 4-7 Scientific Specifications for the Beam Transport through the High Transmission Beam Line to the Spectrometer Section of the HRS.*

Specification for	Specification
Maximum rigidity	8 Tm
Minimum beam transport efficiency	95% in achromatic beam transport mode
Available beam transport modes	Achromatic and dispersion-matched modes that deliver beams to the Spectrometer Section with properties appropriate for achieving the scientific program of the HRS
Minimum time-of-flight path length for ToF-Bp mass measurements	90 m when combined with the ARIS Reconfigured A1900 and the Spectrometer Section of the HRS
Beam tracking capabilities	Ability to determine the momentum (with a resolving power of at least 1500) and angle (with a resolution of better than 5 mrad) at the Spectrometer Section reaction target by using tracking stations in the HTBL
Rare isotope separation	Ability to insert a Radio-Frequency Fragment Separator with a length of 2.2 m as well as associated steering magnets



## 4.4 References

- [ABB17] B. P. Abbott et al. (LIGO Scientific Collaboration and Virgo Collaboration), *Phys. Rev. Lett.* 119, 161101 (2017).
- [ABR12] S. Abrahamyan et al., *Phys. Rev. Lett.* 108, 112502 (2012)
- [ADR05] P. Adrich et al., *Phys. Rev. Lett.* 95, 132501 (2005)
- [AFA13] A. V. Afanasjev, S. E. Agbemava, D. Ray, P. Ring, *Phys. Lett. B* 726, 680 (2013).
- [ALA96] N. Alamanos and P. Chomaz-Roussel, *Ann. Phys. Fr.* 21, 601 (1996)
- [ALK97] G. D. Alkhozov et al., *Phys. Rev. Lett.* 78, 2313 (1997)
- [AMO06] K. Amos et al., *Phys. Rev. Lett.* 96, 032503 (2006).
- [AND10] A. Andreyev et al., *Phys. Rev. Lett.* 105, 252502 (2010)
- [ARI99] A. Arima, *Nucl. Phys. A* 646, 260 (1999).
- [AYY17] Y. Ayyad et al., *Nucl. Instr. And Meth*, in *Phys. Res. A* 880, 166 (2017)
- [AST17] A. Arcones et al., *Prog. Part. Nucl. Phys.* 94, 1, (2017)
- [BAU05] T. Baumann et al., *Nucl. Instr. and Meth.* A543, 517 (2005)
- [BAU12] T. Baumann, A. Spyrou and M. Thoennessen, *Rep. Prog. Phys.* 75, 036301 (2012)
- [BAZ02] D. Bazin et al., *Nucl. Instrum. Meth. Phys. Res. A* 482, 307 (2002)
- [BAZ03] D. Bazin et al., *Nucl. Instrum. Meth. Phys. Res. B* 204, 629 (2003)
- [BAZ09] D. Bazin et al., *Nucl. Instrum. Meth. Phys. Res. A* 606, 314 (2009)
- [BAZ09] D. Bazin et al., *Phys. Rev. Lett.* 102, 232501 (2009)
- [BEN07] M.A. Bentley and S.M. Lenzi, *Prog. in Particle and Nucl. Phys.* 59, 497 (2007)
- [BER83] A.M. Bernstein et al., *Comments Nucl. Part. Phys.* 11, 203 (1983)
- [BER88] Carlos A. Bertulani and Gerhard Baur, *Phys. Rep.* 163, 299 (1988)
- [BET79] H. A. Bethe et al., *Nucl. Phys. A* 324, 487 (1979)
- [BLA85] E. W. Blackmore et al., *Nucl. Instr. And Meth*, in *Phys. Res. A* 234, 235 (1985)
- [BLA92] B. Blank et al., *Z. Phys. A* 343, 375 (1992)
- [BLA07] B. Blank and M. Borge, *Prog. Part. Nucl. Phys.* 60(2) 403 (2007)
- [BRA00] F. Brachwitz et al., *Astrophys. J.* 536, 934 (2000)
- [BRO88] B. A. Brown and B. H. Wildenthal, *Annu. Rev. Nucl. Part. Sci.*, 38, 29 (1988)
- [BRO00] B.A. Brown, *Phys. Rev. Lett.* 85, 5296 (2000)
- [BRO13] B.A. Brown, *Phys. Rev. Lett.* 111, 232502 (2013)
- [BRO20] K. Brown, Technical Note on the insertion of a TPC in the HRS DS1 magnet.
- [CAA13] M. Caamano et al, *Phys. Rev. C* 88, 024605 (2013)
- [CLA03] B.C. Clark, L.J. Kerr and S. Hama, *Phys. Rev. C* 67, 054605 (2003)
- [COL14] G. Colò, U. Garg, and H. Sagawa, *Eur. Phys. J A* 50, 26 (2014)
- [COU15] A. J. Couture, LANL report LA-UR-15-28115 (2015)
- [DAN02] P. Danielewicz, R. Lacey, W.G. Lynch, *Science* 298, 1592 (2002)
- [DAN03] P. Danielewicz, *Nucl. Phys. A* 727, 233 (2003)
- [DAN17] Paweł Danielewicz, Pardeep Singh, Jenny Lee, *Nucl. Phys. A* 958, 147 (2017)



- [DOB07] J. Dobaczewski et al., *Prog. In Part. and Nucl. Phys.* 59, 432 (2007)
- [ERI73] M. Ericson and A. Figureau and C. Thévenet, *Phys. Lett. B* 45, 19 (1973).
- [ERL12] J. Erler et al., *Nature* 486, 509 (2012) and references therein.
- [ERL12a] J. Erler et al, *Phys. Rev. C* 85, 025802 (2012)
- [EST11] A.Estrade et al., *Phys. Rev. Lett.* 107, 172503 (2011)
- [EST14] A. Estrade et al., *Phys. Rev. Lett.* 113, 132501 (2014)
- [FAM06] M.A. Famiano et al., *Phys. Rev. Lett.* 97, 052701 (2006)
- [FAL16] P. Fallon, A. Gade, and IY Lee, *Annu. Rev. of Nucl. and Part. Sci.* 66, 321 (2016)
- [FEY58] R. P. Feynman and M. Gell-Mann, *Phys. Rev.* 109, 139 (1958)
- [FLA12] F. Flavigny et al., *Phys. Rev. Lett.* 108, 252501 (2012)
- [FOR13] C Forssén et al., *Phys. Scr. T152*, 014022 (2013).
- [FRA05] S. Fracasso and G. Colò, *Phys. Rev. C* 72, 064310 (2005)
- [FRA85] M.A. Franey and W.G. Love, *Phys. Rev. C* 31, 488 (1985)
- [FUJ02] H. Fujita et al., *Nucl. Instrum. Meth. Phys. Res. A* 484, 17 (2002)
- [GAA81] C. Gaarde et al., *Nucl. Phys. A369*, 258 (1981)
- [GAA85] C. Gaarde, *Proc. Niels Bohr Centennial Conference on Nuclear Structure, Copenhagen*, 449c (1985)
- [GAD05] A. Gade et al., *Phys. Rev. C* 71, 051301(R) (2005)
- [GAD08a] A. Gade and T. Glasmacher, *Prog. in Part. and Nucl. Phys.* 60, 161 (2008)
- [GAD08b] A. Gade et al., *Phys. Rev. C* 77, 044306 (2008)
- [GAD14] A. Gade et al., *Phys. Rev. Lett.* 112, 112503 (2014)
- [GAD15] A. Gade, *Eur. Phys. J. A* 51, 118 (2015)
- [GAD16] A. Gade and S. N. Liddick, *J. Phys. G: Nucl. Part. Phys.* 43, 024001 (2016)
- [GAN12] S. Gandolfi, J. Carlson, S. Reddy, *Phys. Rev. C* 85,032801(R) (2012)
- [GLA98] T. Glasmacher, *Annu. Rev. Nucl. Part. Sci.* 48, 1 (1998)
- [GOR13] S. Goriely et al, *Phys. Rev. Lett.* 111, 242502 (2013)
- [GOR15] S. Goriely et al., *Mon. Not. R. Astron. Soc.* 452, 3894 (2015)
- [GRE17] GRETA Conceptual Design Report (2017)
- [GUP06] Sanjib Gupta et al., *Astrophys. J.* 662, 1188 (2006)
- [HAG12] G. Hagen et al., *Phys. Rev. Lett.* 109, 032502 (2012)
- [HAG16] G. Hagen, G. R. Jansen, T. Papenbrock, *Phys. Rev. Lett.* 117, 172501 (2016)
- [HAM14] Ikuko Hamamoto and Hiroyuki Sagawa, *Phys. Rev. C* 90, 031302(R) (2014).
- [HAN03] P.G. Hansen, J.A. Tostevin, *Annu. Rev. Nucl. Part. Sci.* 53, 221 (2003)
- [HAR01] M.N. Harakeh and A. van der Woude, *Giant Resonances, Fundamental High-Frequency Modes of Nuclear Excitations, Oxford Studies in Nuclear Physics* 24, Clarendon Press, Oxford, 2001
- [HAR14] J.C.Hardy and I.S.Towner, *Phys. Rev. C* 91, 025501 (2015)
- [HAU13] M. Hausmann, *Nucl. Instrum. Meth. in Phys. Res. B*, 317, 349 (2013)
- [HEB10] K. Hebel, A. Schwenk, *Phys. Rev. C* 82, 014314 (2010)



- [HER14] H. Hergert et al., Phys. Rev. C 90, 041302(R) (2014)
- [HEG01] A. Heger, S.E. Woosley, G. Martinez-Pinedo, K. Langanke, Ap. J. 560, 307 (2001)
- [HEY11] Kris Heyde and John L. Wood, Rev. Mod. Phys. 83, 1467 (2011)
- [HIX03] W.R. Hix et al., Phys. Rev. Lett. 91, 201102 (2003)
- [HOL12] J. D. Holt et al., J. Phys. G: Nucl. Part. Phys. 39, 085111 (2012)
- [HOL14] J. D. Holt et al., arXiv.1405.7602 (2014)
- [HOR14] C.J. Horowitz et al., J. Phys. G 41, 093001 (2014)
- [HRS14] HRS Working group, A high Rigidity Spectrometer for FRIB (2014)
- [HUC85] A. Huck et al., Phys. Rev. C 31, 2226 (1985)
- [HYU80] H. Hyuga and A. Arima and K. Shimizu, Nucl. Phys. A 336, 363 (1980)
- [IWA99] K. Iwamoto et al., Astrophys. J. Suppl. 125, 439 (1999)
- [IWA16] H. Iwasaki et al., Nucl. Instrum. Method. in Phys. Res. A 806, 123 (2016)
- [JAN07] H.-T. Janka et al., Phys. Rep. 442, 38 (2007)
- [JAN13] M. Jandel, et al., Los Alamos Report LA-UR-12-24975, 2013
- [JHA16] G. Jhang et al., Journal of Korean Physics Society, 69, 144 (2016)
- [JIA07] Wei-Zhou Jiang, Bao-An Li, and Lie-Wen Chen, Phys. Rev. C 76, 044604 (2007)
- [KAS17] D. Kasen et al., Nature 551, 80 (2017)
- [KAR02] S. Karataglidis et al., Phys. Rev. C 65, 044306 (2002)
- [KHA11] E. Khan, N. Paar, D. Vretenar, Phys. Rev. C 84, 051301(R) (2011)
- [KHA13] E. Khan et al., Phys. Rev. C 87, 064311 (2013)
- [KOB12] N. Kobayashi et al., Phys. Rec. C. 86, 054604 (2012)
- [KOH13] Z. Kohley et al., Phys. Rev. Lett. 110, 152501 (2013)
- [KOU05] H. Koura, T. Tachibana, M. Uno, and M. Yamada, Prog. Theor. Phys., vol. 113, 305 (2005)
- [KOR12] O. Korobkin et al., Mon. Not. R. Astron. Soc. 426, 1940 (2012)
- [KOS20] E. Koshchiy et al., Nucl. Instrum. Meth. Phys. Res. A 957, 163398 (2020)
- [KRA99] A. Krasznahorkay et al., Phys. Rev. Lett. 82, 3216 (1999)
- [KRE95] G. Krein et al., Phys. Rev. C 51, 2646 (1995)
- [KUT20] S. V. Kutsaev et al., EPJ Techn. Instrum. 7, 4 (2020).
- [LAN03] K. Langanke, G. Martinez-Pinedo, Rev. Mod. Phys. 75, 819 (2003)
- [LAT01] J. M. Lattimer, M. Prakash, ApJ, 550, 426 (2001)
- [LAT04] J.M. Lattimer, M. Prakash, Science 304, 536 (2004)
- [LAT13] J. M. Lattimer and Y. Lim, ApJ 771, 51 (2013)
- [LAT16] J. M. Lattimer and M. Prakash, Phys. Rep. 621, 127 (2016)
- [LEN10] S. M. Lenzi, F. Nowacki, A. Poves, and K. Sieja, Phys. Rev. C 82, 054301 (2010)
- [LI02] B. A. Li, Nucl. Phys. A 708, 365 (2002)
- [LI05] B.A. Li, L.W. Chen, Phys. Rev. C 72, 064611 (2005)
- [LI05b] B.A. Li, G.C. Yong, W. Zuo, Phys. Rev. C 71, 014608 (2005)
- [LI07] T. Li et al., Phys. Rev. Lett. 99, 162503 (2007)





- [Li08] Bao-An Li et al., *Phys. Rep.* 464, 113 (2008)
- [Li93] G. Q. Li and R. Machleidt, *Phys. Rev. C* 48, 1702 (1993)
- [Li94] G. Q. Li and R. Machleidt, *Phys. Rev. C* 49, 566 (1994)
- [LIP18] S. I. Lipschutz, Ph.D. Thesis, Michigan State University (2018); S. I. Lipschutz et al., submitted for publication
- [LOC14] Bui Minh Loc, Dao T. Khoa, and R. G. T. Zegers, *Phys. Rev. C* 89, 024317 (2014)
- [LOC17] Bui Minh Loc, Naftali Auerbach, and Dao T. Khoa, *Phys. Rev. C* 96, 014311 (2017)
- [LOV81] W. G. Love and M. A. Franey, *Phys. Rev. C* 24, 1073 (1981)
- [LOV20] A. Lovell, private communication
- [LRP07] The Frontiers of Nuclear Science, A Long Range Plan, Nuclear Science Advisory Committee (2007)
- [LRP15] Reaching For the Horizon, The 2015 Long Range Plan for Nuclear Science, The Nuclear Science Advisory Committee (2015)
- [MAH14] M.H. Mahzoon et al., *Phys. Rev. Lett.* 112, 162503 (2014)
- [MAM13] J. Mammei et al. (CREX Collaboration), Proposal to Jefferson Lab PAC 40, CREX: Parity-violating measurement of the weak charge distribution of Ca to 0.02 fm accuracy (unpublished)
- [MEI11] K. Meierbachtol et al., *Nucl. Instrum. Method. in Phys. Res. A* 652, 668 (2011)
- [MEH12] R. Meharchand et al., *Phys. Rev. Lett.* 108, 122501 (2012)
- [MEI13] Z. Meisel and S. George, *IJMS* 349, 145 (2013)
- [MEI15] Z. Meisel et al., *Phys. Rev. Lett.* 114, 022501 (2015)
- [MIL16a] S. A. Milne, M. A. Bentley et al., *Phys. Rev. Lett.* 117, 082502 (2016)
- [MIL16b] S. A. Milne, M. A. Bentley et al., *Phys. Rev. C* 93, 024318 (2016)
- [MOE95] P. Moeller, J.R. Nix, and W.J. Swiatecki, *At. Data Nucl. Data Tables* 59, 185 (1995)
- [MON08] C. Monrozeau et al., *Phys. Rev. Lett.* 100, 042501 (2008)
- [MRI09] MRI-Consortium: Development of a Neutron Detector Array by Undergraduate Research Students for Studies of Exotic Nuclei, NSF grants 0922335, 0922409, 0922446, 0922462, 0922473, 0922537, 0922559, 0922622, and 0922794
- [MUE11] J.M. Mueller et al., *Phys. Rev. C* 83, 064605 (2011)
- [MUM16] M.R. Mumpower et al., *Prog. Part. Nucl. Phys.* 86, 86 (2016)
- [Nav16] P. Navrátil, S. Quaglioni, G. Hupin, C. Romero-Redondo and A. Calci, *Phys. Scr.* 91, 053002 (2016).
- [NAZ14] W. Nazarewicz, P.-G. Reinhard, W. Satuła, and D. Vretenar, *Eur. Phys. J. A* 50, 20 (2014).
- [NDB14] Neutrinoless Double Beta Decay Report, NSAC, (2014).
- [NOJ14] S. Noji et al., *Phys. Rev. Lett.* 112, 252501 (2014)
- [NOJ15] S. Noji et al., *Phys. Rev. C* 92, 024312 (2015)
- [NOJ18] S. Noji et al., *Phys. Rev. Lett.* 120, 172501 (2018)





- [NOW16] F. Nowacki, A. Poves, E. Caurier, and B. Bounthong, *Phys. Rev. Lett.* 117, 272501 (2016)
- [NRC07] Scientific Opportunities with a Rare-Isotope Facility in the United States, National Research Council; Division on Engineering and Physical Sciences; Board on Physics and Astronomy; Rare-Isotope Science Assessment Committee (2007)
- [NRC13] National Research Council. *Nuclear Physics: Exploring the Heart of Matter*. Washington, DC: The National Academies Press, 2013
- [OBS13] A. Obserstedt, et al., *Phys. Rev. C* 87, 051602(R) (2013)
- [OST92] F. Osterfeld, *Rev. Mod. Phys.* 64, 491 (1992)
- [OTS16] H. Otsu et al., *Nucl. Instrum. Meth. in Phys. Res. B* 376, 175 (2016)
- [PAA07] N. Paar, D. Vretenar, E. Khan, and G. Colò, *Rep. Prog. Phys.* 70, 691 (2007).
- [PAI07] S. Pain et al., *Nucl. Instr. And Meth, in Phys. Res. B* 261, 1122 (2007)
- [PAN05] I. V. Panov et al, *Nucl. Phys. A* 747, 633 (2005)
- [PAS11] K. Paschke, K. Kumar R. Michaels, P.A.Souder, G.M. Urciuoli et al., JLAB Exp E12-11-101, PREX-II: PRECISION PARITY-VIOLATING MEASUREMENT OF THE NEUTRON SKIN OF LEAD
- [PAT12] D. Patel et al., *Phys. Lett. B* 758, (2012)
- [PER12] G. Perdikakis et al., *Nucl. Instr. And Meth, in Phys. Res. A* 686, 117 (2012)
- [PET16] W. A. Peters, *Nucl. Instr. And Meth, in Phys. Res. A* 836, 122 (2016)
- [PEL13] E. Pellereau et al, *EPJ Web of Conf.* 62, 06005 (2013)
- [RAD18] D. Radice et al., *Ap. J. Lett.* 852, 1 (2018)
- [RIB07] Report to NSAC of the Rare-Isotope Beam Task Force
- [RIC17] S. Richers et al., *Phys. Rev. D* 95, 063019 (2017)
- [ROG11] A.M. Rogers et al., *Phys. Rev. Lett.* 106, 252503 (2011)
- [RUS11] P. Russotto et al., *Phys. Lett. B* 697, 471 (2011)
- [SAG07] H. Sagawa et al., *Phys. Rev. C* 76, 024301 (2007)
- [SAM06] F. Sammarruca and P. Krastev, *Phys. Rev. C* 73, 014001 (2006)
- [SAS11] M. Sasano et al., *Phys. Rev. Lett.* 107, 202501 (2011)
- [SAS12] M. Sasano et al., *Phys. Rev. C* 86, 034324 (2012)
- [SAS21] M. Sasano, private communication
- [SAV13] D. Savran, T. Aumann, and A. Zilges, *Prog. Part. Nucl. Phys.* 70, 210 (2013)
- [SCH98] C. Scheidenberger, Th. Stöhlker, W.E. Meyerhof, H. Geissel. P.H. Mokler, B. Blank, *Nucl. Instr. Meth. Phys. Res. B* 142, 441 (1998).
- [SCH01] K.-H. Schmidt, *Nucl. Phys. A* 693, 169 (2001)
- [SCH02] H. Schatz et al, *Astrophys. Jour.* 579, 626 (2002)
- [SCH13] H. Schatz et al., *Nature (London)* 505, 62 (2013)
- [SCO17] M. Scott et al., *Phys. Rev. Lett.* 118 172501 (2012)
- [SEG01] W. F. Mueller et al., *Nucl. Instr. and Meth. A* 466, 492 (2001)
- [SMI18] K. Smith et al., *Nucl. Instr. And Meth, in Phys. Res. B* 414, 190 (2018)



- [SPY12] A. Spyrou et al., *Phys. Rev. Lett.* 108, 102501 (2012)
- [STE05] A.W. Steiner, M. Prakash, J.M. Lattimer, P.J. Ellis, *Phys. Rep.* 411, 325 (2005)
- [STE13] D. Steppenbeck et al., *Nature* 502, 207 (2013)
- [STE13a] I. Stetcu, et al., *Phys. Rev. C* 88 (2013) 044603
- [SUL16] C. Sullivan et al., *Ap. J.* 816, 44 (2016)
- [SUH17] J. T. Suhonen, *Front. Phys.* 5, 55 (2017) and references therein.
- [SUZ90] Yasuyuki Suzuki, Kiyomi Ikeda and Hiroshi Sato, *Prog. Theor. Phys.* 83, 180 (1990).
- [TAL12] P. Talou, et al., *Proceedings of the 5th International Conference on Fission, Sanibel Island, Nov. 2012* (pp. 581-588)
- [TAL13] P. Talou et al., *Physics Procedia* 47, 39 (2013)
- [TAR16] O. B. Tarasov and D. Bazin, *Nucl. Instr. And Meth, in Phys. Res. B* 376, 185 (2016)
- [TAR08] O. B. Tarasov and D. Bazin, *Nucl. Instr. And Meth, in Phys. Res. B* 266, 4657 (2008)
- [TER14] S. Terashima et al., *Prog. Theor. Exp. Phys.* 101D02,(2014)
- [TIT19] R. Titus et al, *Phys. Rev. C* 100 045805 (2019)
- [THI83] F.-K. Thieleman et al, *Z. Phys. A* 309, 301 (1983)
- [TOS01] J.A. Tostevin, *Nuclear Phys. A* 682, 320c (2001)
- [TOS99] J.A. Tostevin, *J. Phys. G* 25, 735 (1999)
- [TSA12] M.B. Tsang et al., *Phys. Rev. C* 86, 015803 (2012)
- [ULL14] J. L. Ullmann, et al., *Phys. Rev. C* 89, 034603 (2014)
- [VAN14] M. Vandebrouck et al., *PRL* 113, 032504 (2014)
- [VIL04] A.R. Villarreal, T.E. Strohmayer, *ApJ*, 614, L121 (2004)
- [VRE03] D. Vretenar, N. Paar, T. Niksic, P. Ring, *Phys. Rev. Lett.* 91, 262502 (2003)
- [WAK97] T. Wakasa et al., *Phys. Rev. C* 55, 2909 (1997)
- [WAL07] M.S. Wallace et al., *Nucl. Instr. And Meth, in Phys. Res. A* 583, 302 (2007)
- [WAR06] D.D. Warner, M.A. Bentley, and P. Van Isacker, *Nature Physics* 2, 311 (2006)
- [WEI10] D. Weisshaar et al., *Nucl. Instr. And Meth, in Phys. Res. A* 624, 615 (2010)
- [WIM14] K. Wimmer et al., *Nucl. Instr. And Meth, in Phys. Res. A* 769, 65 (2014)
- [XIA08] Zhigang Xiao et al., *Phys. Rev. Lett.* 102, 062502 (2009)
- [YAK05] K. Yako et al., *Phys. Lett. B* 615, 193 (2005).
- [YAK06] K. Yako, H. Sagawa, and H. Sakai, *Phys. Rev. C* 74, 051303(R) (2006)
- [YAM11] T. Yamaguchi et al., *Phys. Rev. Lett.* 107, 032502 (2011)
- [ZAM19] J. C. Zamora et al., *Phys. Rev. C* 100, 032801(R) (2019)
- [ZEG08] R.G.T. Zegers et al., *Phys. Rev. C* 77, 024307 (2008)
- [ZEG10] R.G.T. Zegers et al., *Phys. Rev. Lett.* 104, 212504 (2010)
- [ZEG20] R.G.T. Zegers, *Technical Note: Detection of fission products in the HRS based on the LANL theoretical fission distributions* (2020).
- [ZEL06] Vladimir Zelevinsky and Alexander Volya, *AIP Conf. Proc.* 819, 493 (2006)

## 5 High Transmission Beam Line (HTBL) of the HRS

This section describes the beam physics of the High Transmission Beam Line (HTBL) of the HRS, which has been designed based on the functional requirements stipulated in Section 4.3.2. The Work Breakdown Structure (WBS) for this section is given in Table 5-1. After a brief overview of the HTBL in Section 5.1, the functional requirements are revisited and reproduced in Section 5.2, and the design approach and the preferred alternative are presented in Section 5.3. In Section 5.4, the performance of the HTBL is demonstrated by end-to-end simulations, and the angular and momentum resolutions and acceptances are given in Sections 5.5 and 5.6, respectively. The capabilities afforded by the preferred alternative of the HTBL are summarized in Section 5.7. The functional specifications of the magnetic elements, the diagnostics and detectors, and the vacuum components are given in Section 5.8, which serve as functional requirements for the corresponding systems. Commissioning plans for the HTBL are given in Section 8.

Table 5-1 WBS for the HTBL beam physics.

<b>Experimental Systems - High Rigidity Spectrometer</b>	<b>HRS.3</b>
<b>High Transmission Beamline (HTBL)</b>	<b>HRS.3.01</b>
<b>High Transmission Beamline Beam Physics</b>	<b>HRS.3.01.01</b>

The ion-optical calculations for the HTBL (and the Spectrometer Section described in Section 6) were performed with the transfer-matrix-type ion-optics code COSY Infinity (simply referred to as COSY hereafter) [COS11], which, by utilizing differential-algebraic techniques, is capable of computing Taylor maps for complicated fields (including fringe fields) to arbitrary order. COSY performs all its calculations in the following coordinate system: the positions in the horizontal dispersive ( $x$ ) and vertical non-dispersive planes ( $y$ ), the normalized momenta  $a = p_x/p_0$  and  $b = p_y/p_0$ , which are the ratios of the dispersive ( $p_x$ ) and non-dispersive ( $p_y$ ) momenta to the total central momentum ( $p_0$ ), and the energy deviation  $\delta_K = \delta K/K_0$ , with  $\delta K$  being the deviation from the central kinetic energy  $K_0$ . It is noted that  $x$ - $a$  and  $y$ - $b$  are canonically conjugate to each other, and  $a$  and  $b$  are approximately equal to the dispersive and non-dispersive geometrical angles ( $x'$  and  $y'$ ), respectively, when they are small. For simplicity,  $\delta_K$  will be converted to the normal momentum deviation  $\delta_p = \delta p/p_0$  in this document.

For the calculations presented here, COSY Infinity version 9.1 was used, with some extensions implemented as described in Ref. [POR16]. This is the same code system as that used for ion-optical calculations for the FRIB ARIS Fragment Separator. Tools have been developed to export the transfer matrices to other beam simulation codes such as LISE<sup>++</sup>[BAZ02,TAR08,TAR16]. The field profiles of the magnetic elements are reproduced using COSY's standard element types. The excitation dependence of the shapes of the fringe fields and that of the effective field lengths have been incorporated in the calculations. The parameters that describe the field profiles were obtained



from analyses of field-map data or magnetostatic calculations: The quadrupole magnets will be of the same design as the existing quadrupoles in the A1900 Fragment Separator as described in Section 9.4.1, the parameters were obtained from the actual field-map data. As for the dipole magnets, field profiles obtained in magnetostatic analysis in ANSYS Maxwell [ANS19] based on its preliminary design were used.

## 5.1 Introduction and overview

The layout of the HTBL is shown in Figure 5-1. The naming convention of the components is described in Figure 5-2. The HTBL starts at the final focal plane of the Fragment Separator (FB0) and ends at the location of the reaction target of the Spectrometer Section (FS0). The HTBL has eight quadrupole triplets (TB1 through TB8), four dipole magnets (DB1 through DB4), and two vertical steering magnets (SB1 and SB2). The intermediate foci FB1 and FB3 will be equipped with beam diagnostics equipment and detectors for the tracking of positions and angles of the beam on an event-by-event basis and for particle identification. Though not part of the HRS project, space has been provided for a Radio-Frequency Fragment Separator (RFFS) at FB2 that may be installed in the future to perform rare-isotope-beam separation for proton-rich species.

The initial section of the HTBL, namely the TB1 triplet and the DB1 dipole, is also used to deliver beams to the beam-stopping areas and to the other fast-beam areas as shown in Figure 5-1. The beam-stopping areas provide thermalized beams to the experimental areas focused on in-beam laser-spectroscopy, high-precision mass spectroscopy and other high-precision studies, and decay spectroscopy with thermalized beams. The beam-stopping areas also provide thermalized beams to the Reaccelerator (ReA), which provides beams with an energy of several MeVs to additional experimental areas at FRIB. Fast beams in S2 are used for a variety of experiments and, prior to the completion of the HRS, neutron invariant-mass experiments with the existing sweeper magnet and the MoNA-LISA neutron array will be carried out in this vault. The S3 vault houses the S800 spectrometer. The Sweeper magnet and S800 spectrometers have maximum magnetic rigidities of 4 Tm. The FRIB Decay Station consists of a versatile setup for the detection of photons, charged particles, and neutrons emitted from rare isotopes that are stopped in the center of the station. In addition, the TB2 triplet and the DB2 dipole will be delivering beams to a future experimental area.





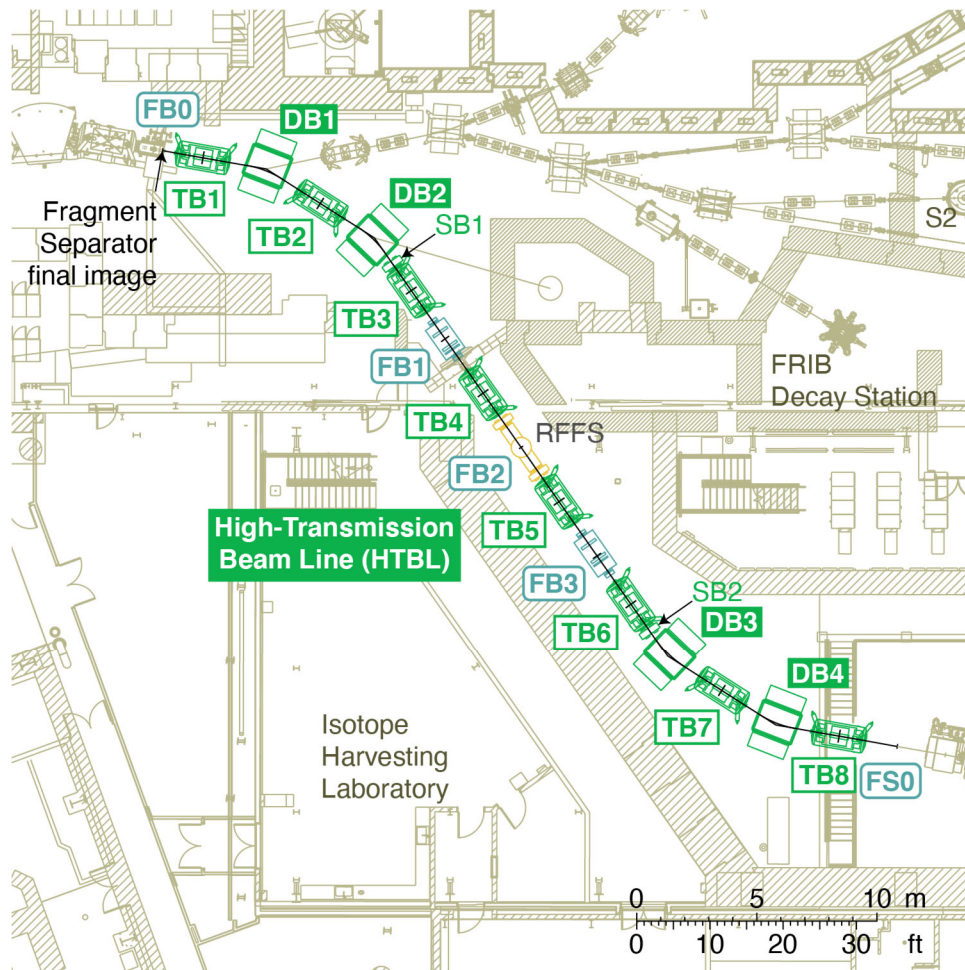


Figure 5-1 Layout of the High-Transmission Beam Line (HTBL).

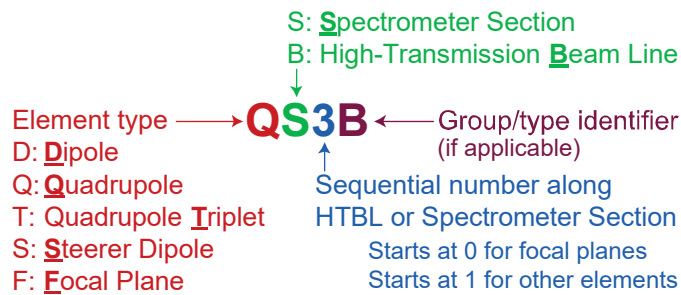


Figure 5-2 Naming convention of the components of the HTBL and Spectrometer Section of the HRS.



## 5.2 Functional Requirements for the HTBL

Section 4.3.2 detailed the functional specifications for the HTBL, which were summarized in Section 4.3.2.8. In it, given in Table 4-7 were a total of six functional requirements for the HTBL, which are reproduced here as Table 5-2 for convenience.

The functional requirements for the HTBL are as follows: (1) To optimize the luminosity for experiments at the HRS, the HTBL must be able to transport beams with a magnetic rigidity of up to 8 Tm as discussed in Section 4.3.2.1. (2) The HTBL must optimize the transmission of rare-isotope beams from the Fragment Separator at the magnetic rigidities at which the production rates of those beams are maximized. (3) The rare-isotope-beam transport efficiency must exceed 95%. (4) The HTBL must also be able to dispersion-match the Spectrometer Section by creating the matching resolving power of that of the Spectrometer Section as described in Section 4.3.2.7.1. (5) For ToF- $B\rho$  mass measurements, the flight-path length must be larger than 90 meters, when the HTBL is combined with the Fragment Separator and the Spectrometer Section, as described in Section 4.3.2.7.4. The HTBL must accommodate beam tracking and diagnostic stations, as described in Sections 4.3.2.7.2 and 4.3.2.7.3. (6) Finally, the HTBL must be able to accommodate rare-isotope-beam separation for proton-rich species with an RFFS, as described in Section 4.3.2.7.3, for which the HTBL must provide 2.2 meters of space for inserting an RFFS as well as associated steering magnets in the future.

Table 5-2 Requirements for the design of the HTBL. This table reproduces the specifications of Table 4-7.

Requirement	Description
Maximum rigidity	8 Tm
Minimum beam transport efficiency	95% in achromatic beam transport mode
Available beam transport modes	Achromatic and dispersion-matched modes that deliver beams to the Spectrometer Section with properties appropriate for achieving the scientific program of the HRS
Minimum time-of-flight path length for ToF- $B\rho$ mass measurements	90 m when combined with the ARIS Fragment Separator and the Spectrometer Section of the HRS
Beam tracking capabilities	Ability to determine the momentum (with a resolving power of at least 1500) and angle (with a resolution of better than 5 mrad) at the Spectrometer Section reaction target by using tracking stations in the HTBL
Rare isotope separation	Ability to insert a Radio-Frequency Fragment Separator with a length of 2.2 m as well as associated steering magnets





### 5.3 Design approach and preferred alternative for the HTBL

To connect the Fragment Separator and the Spectrometer Section, the HTBL must transport the beam over a significant distance (~40 m) while providing the ion-optical properties suited for the scattering of the beam particles at the reaction target placed at the entrance of the Spectrometer Section.

A combination of bending (dipole) and focusing (quadrupole, sextupole, and octupole) magnets is required to achieve such a transport. In addition, the layout must enable the beam delivery to the other experimental areas of FRIB. As described in Section 4.3.2.7.1, to be able to operate in dispersion-matched beam transport mode, sufficient resolving power must be created in the HTBL to meet the dispersion-matching conditions. The resolving power can only be created by the dipole field and hence the total bending angle in the HTBL must be sufficiently large. Finally, the symmetry of the layout of the entire beam line is beneficial for reducing the higher-order aberrations.

Based on these considerations, the HTBL has been designed as follows: The HTBL has four dipole magnets, the first (DB1) and second (DB2) of which bend the beam to the right, and the third (DB3) and fourth (DB4) dipoles to the left towards the Spectrometer Section. Each of the four dipoles bend the beam by 22.5 degrees, and the entrance and exit sections of the HTBL are parallel to each other, *i.e.*, it has no net bending angle. These dipoles will be required to bend beams with rigidities of up to 8 Tm. The HTBL has quadrupole magnets to shape the beam to achieve good transmission efficiency and necessary ion-optical properties.

These dipoles and the quadrupoles are placed so that the section from FB0 to FB1 is symmetric with respect to TB2. The section from FB1 to FB3 is symmetric with respect to FB2. The section from FB3 to FS0 is symmetric with respect to TB7. The entire HTBL is symmetric with respect to FB2, with the exception of minor modifications due to the placement of the DB1 and DB2 dipoles for the optimal beam delivery to all the beamlines, and due to the space constraints around FB0 and FS0. At FB0 the space is constrained by the Fragment Separator and the other beamlines, while at FS0, a large space is required for the installation of large auxiliary detector systems such as GRETA. Achieving complete symmetry was attempted in the early stage of the HTBL design. However, the symmetry was broken because it was not possible to gain additional space at FB0 or to reduce space at FS0 and still meet the science requirements. Nonetheless, the HTBL design provides excellent performance meeting the science requirements.

#### 5.3.1 Realization of achromatic and dispersive transport modes

Figure 5-3 schematically illustrates how the HTBL realizes both achromatic and dispersive transport modes.



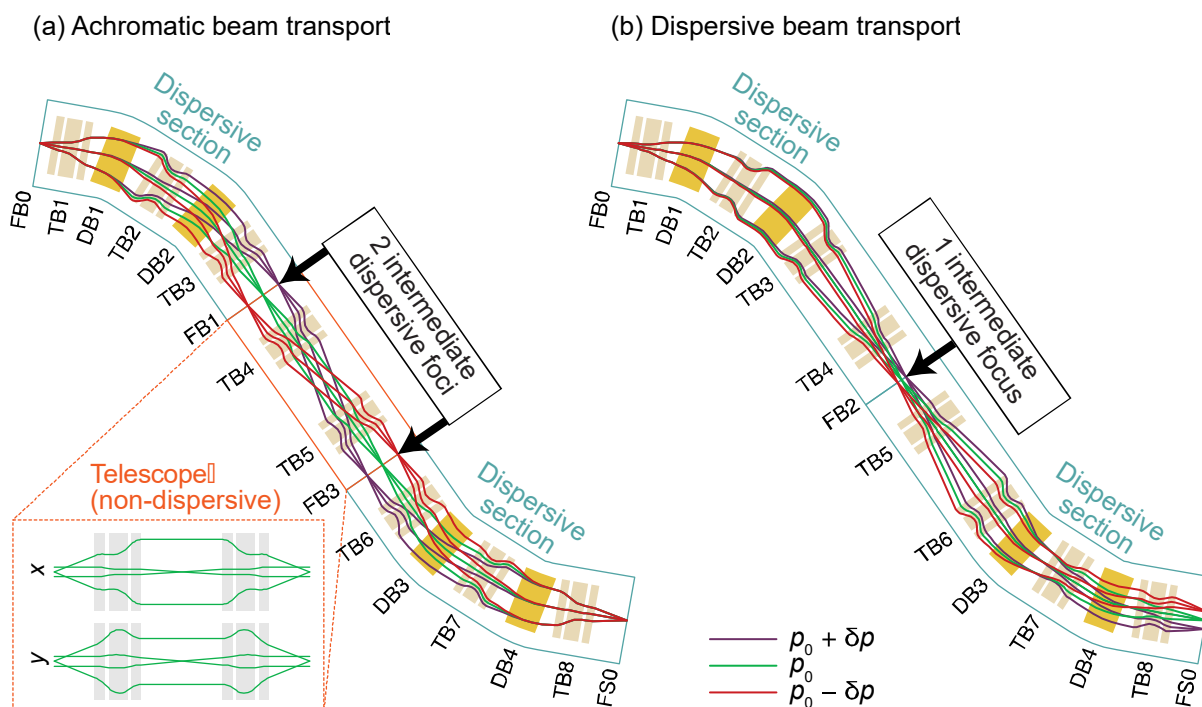


Figure 5-3 This figure schematically illustrates how the HTBL realizes both (a) achromatic and (b) dispersive beam-transport modes. See text for details.

To make the HTBL achromatic, the dispersion created by the first two dipoles (DB1 and DB2) and by the last two dipoles (DB3 and DB4) must cancel each other. This is done by implementing an even number of intermediate foci between dipoles DB2 and DB3. Since it is not feasible to transport the beam without any focus between DB2 and DB3, two foci were created as shown in Figure 5-3(a). Two dispersive sections (TB1 through TB3 and TB6 through TB8) are connected by a non-dispersive telescope consisting of TB4 and TB5. The first dispersive section makes a dispersive focus at FB1, while the telescope makes the next dispersive focus at FB3, at which the sign of the dispersion is reversed. The momentum tracking can be performed at FB1 and FB3. The dispersion accumulated up to this point is cancelled in the second dispersive section, and the target location FS0 becomes achromatic  $[(x|\delta) = (x'|\delta) = 0]$ . At FS0, in addition to point-to-point focusing  $[(x|x') = (y|y') = 0]$ , parallel-to-parallel imaging  $[(x'|x) = (y'|y) = 0]$  is achieved. A parallel beam in the non-dispersive direction at FB2 is achieved, as needed for operating the RFFS.

To make the HTBL dispersive, it is tuned such that the dispersion created by the four dipole magnets accumulates. This is accomplished by providing an odd number of foci between the right-bending DB2 and the left-bending DB3 dipole magnets. The simplest solution has only one focus in the middle of the HTBL, at which the upstream dispersive section (TB1 through TB4) and the downstream dispersive section (TB5 through TB8) are directly connected to each other.

### 5.3.2 Achromatic beam-transport mode

Figure 5-4 shows first-order beam transport in the achromatic mode, and Table 5-3 lists the first-order transfer matrix elements at the focal planes FB1, FB3, and FS0. Since the space around FS0 is stretched compared to that around FB0, the position magnifications from FB0 to FS0 in the dispersive and non-dispersive planes are larger than unity, which in turn makes the angular magnifications smaller than unity.

At the location of the dispersive foci FB1 and FB3, it is possible to track the momenta of beam particles by measuring the position deviation with position-sensitive tracking detectors. Such momentum tracking is necessary to achieve a better momentum resolution in the reaction analysis in the Spectrometer Section than the momentum spread of the beam. The momentum resolving power is about 1/1700 with realistic beam properties of beams delivered by the ARIS Fragment Separator (see Table 5-4). Likewise, measuring angles at FB1 and FB3 using a pair of tracking detectors will allow for inferring the beam angle incoming at FS0. Such angle tracking is necessary to achieve a better angular resolution in the reaction analysis in the Spectrometer Section than the angular spread of the beam at FS0.

As described in Section 6.3.1.6, when the Spectrometer Section is operated in the neutron invariant-mass mode, the reaction target is installed at FS0' between its QS2B and DS1 magnets. This means that the Spectrometer Section's two first quadrupoles, QS1A and QS2B, will be combined with the HTBL to transport the beam to FS0' with the proper beam conditions. In this beam transport, FS0 will no longer be a focus in both dispersive and non-dispersive planes, because the focusing powers of the two quadrupoles are not strong enough to achieve a point-to-point focus from FS0 to FS0', rendering it impossible to achieve the required magnetic rigidity of 8 Tm. Therefore, the combined beamline will be tuned such that the point-to-point focus is achieved from FB3 to FS0'. One caveat is that, due to the long drift around FS0, secured for the GRETA installation, the position magnifications in both planes will be as large as ~5, negatively impacting the resolution that can be achieved by the spectrometer. Tracking detectors can be used to track the position and angle of the incoming beam on the target in cases where that is beneficial for the experiment.



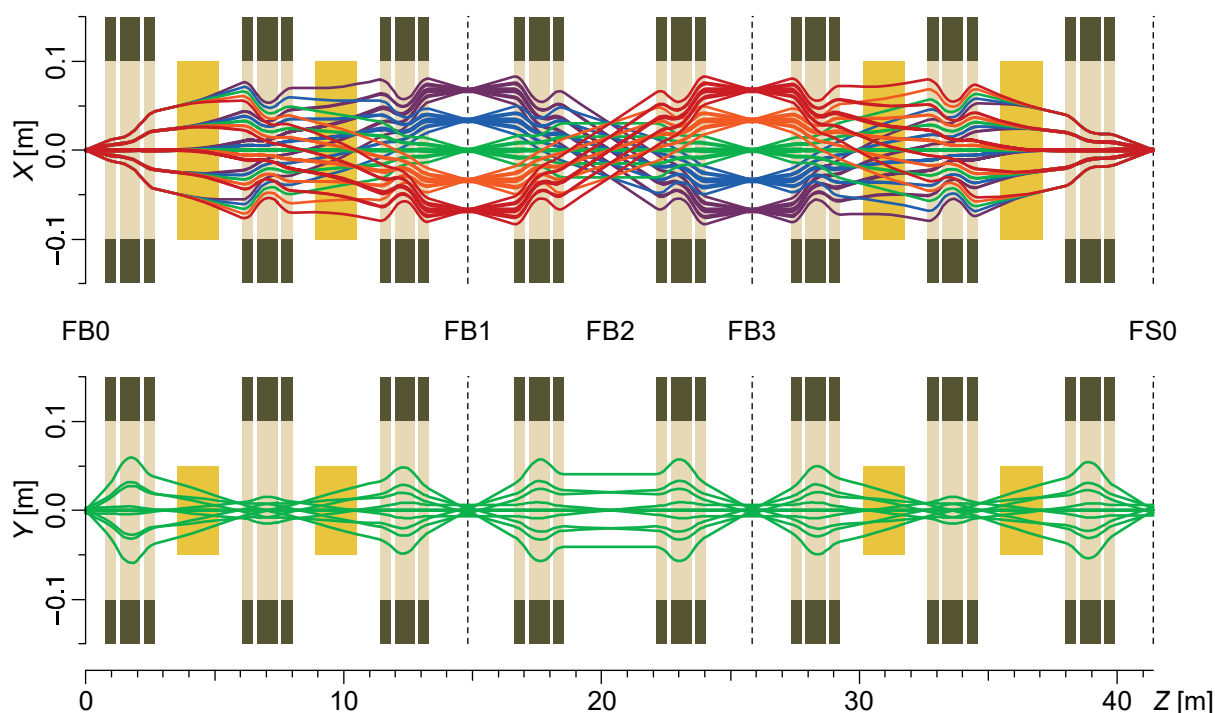


Figure 5-4 Trajectory plots for the achromatic beam transport through the HTBL in the dispersive (top) and the non-dispersive (bottom) planes in first order. The dipole magnets are shown as orange boxes, with their heights representing the good-field regions ( $\pm 10$  cm) and vertical gaps ( $\pm 5$  cm). The quadrupoles are shown as light-brown boxes, with their heights representing the warm-bore aperture sizes. The dark boxes on both ends extending to the pole-tip radii (15 cm), denote the cryostat vessels in which the sextupole and octupole coils are housed. The ensemble of rays correspond to the  $2\sigma$  values of the phase space of  $^{40}\text{Mg}$  coming out from the ARIS Fragment Separator with its optimal settings:  $\delta x_{\text{max}} = 1.2$  mm,  $\delta x'_{\text{max}} = 12.5$  mrad,  $\delta y_{\text{max}} = 3.4$  mm,  $\delta y'_{\text{max}} = 31.2$  mrad, and  $\delta p_{\text{max}}/p = 1.54\%$ . The different colors for the dispersive-plane trajectories correspond to the different momenta, which all coincide in the non-dispersive plane in this first-order plot.

### 5.3.3 Dispersion-matching beam transport mode

Figure 5-5 shows the first-order beam transport in dispersion-matching mode, where the lateral and angle dispersions are matched to those of the full Spectrometer Section. Table 5-3 lists the first-order matrix elements at the focal planes FB2 and FS0. To achieve dispersion matching between the HTBL and the Spectrometer Section, the position and angular dispersions need to meet the conditions set by the ion-optical properties of the Spectrometer Section. The condition for the lateral dispersion is  $(x|\delta)_B = -(x|\delta)_S / (x|x)_S$  and that for the angular dispersion is  $(x'|\delta)_B = (x'|x)_S (x|\delta)_S - (x|x)_S (x'|\delta)_S$ , where the subscripts B and S denote the beamline (HTBL) and the spectrometer (Spectrometer Section), respectively. Note that the angular dispersion  $(x'|\delta)_B$  of the

HTBL will be zero when dispersion-matched in the current design of the Spectrometer Section since both  $(x'|x)_s$  and  $(x'|\delta)_s$  are zero as presented in the next section.

Because of the large  $(x|\delta)_B$  value, the beam spot size in the dispersive plane at FS0 becomes large: For example, for a momentum spread  $\delta p/p$  of  $\pm 0.5\%$  a beam spot size is as large as about  $\pm 4$  cm. It is understood that the transmission efficiency of this mode will have to be compromised due to this expanded beam envelope. The transmission efficiency depends on the emittance of the rare-isotope beam, and thus they need to be evaluated on a case-by-case basis. Also note that the large beam-spot size at FS0 may affect the placement and use of ancillary detectors.

In this mode, high momentum resolution can be achieved without momentum tracking of the beam. Therefore, the use of tracking detectors at the dispersive foci FB2 and FS0 is, in general, not foreseen during these experiments. However, for specific applications where it is required to precisely determine the scattering angle at the target, it will be necessary to do so by both measuring the incoming angle at FS0 and reconstructing the outgoing angle from the positions and angles at the focal plane. Here, owing to the zero angular dispersion at FS0 as mentioned above, the incoming angle of the beam does not depend on the momentum, which obviates momentum corrections.

The dispersion-matched beam transport of the HTBL is also used for ToF- $B\rho$  mass measurements (see Section 4.3.1.5). The entire HRS becomes achromatic, and the magnetic rigidity ( $B\rho$ ) is determined by measuring the position at FS0. By combining the Fragment Separator (40.14 m), the HTBL (41.40 m), and the Spectrometer Section (31.72 m), a total flight-path length of 113 m is created, which meets the requirement that the flight-path length be greater than 90 m.

The use of dispersion-matched beam transport is useful for unreacted-beam rejection because the beam will be well localized at the final achromatic focus. When the full Spectrometer Section is dispersion-matched, the unreacted beam comes into a sharp focus at FS2, where the beam can be blocked with variable slits. It is also possible to do the partial dispersion-matching to the first half of the Spectrometer Section only, from FS0 to FS1. In this case the matching conditions are different from those for the full dispersion-matching case, and accordingly the beam transport is different from what is shown in Figure 5-5. Depending on the difference between the rigidity of the reaction product of interest and that of the beam, the partial dispersion matching may be beneficial, because by blocking the beam at FS1, one can keep the intense beam from reaching to the final focus without having to intercept the desired reaction products and prevent possible background counts on the focal-plane detectors by stopping the beam far upstream. The present layout of the HRS allows for the flexibility to choose the best point to intercept the beam depending on the specific experimental conditions.





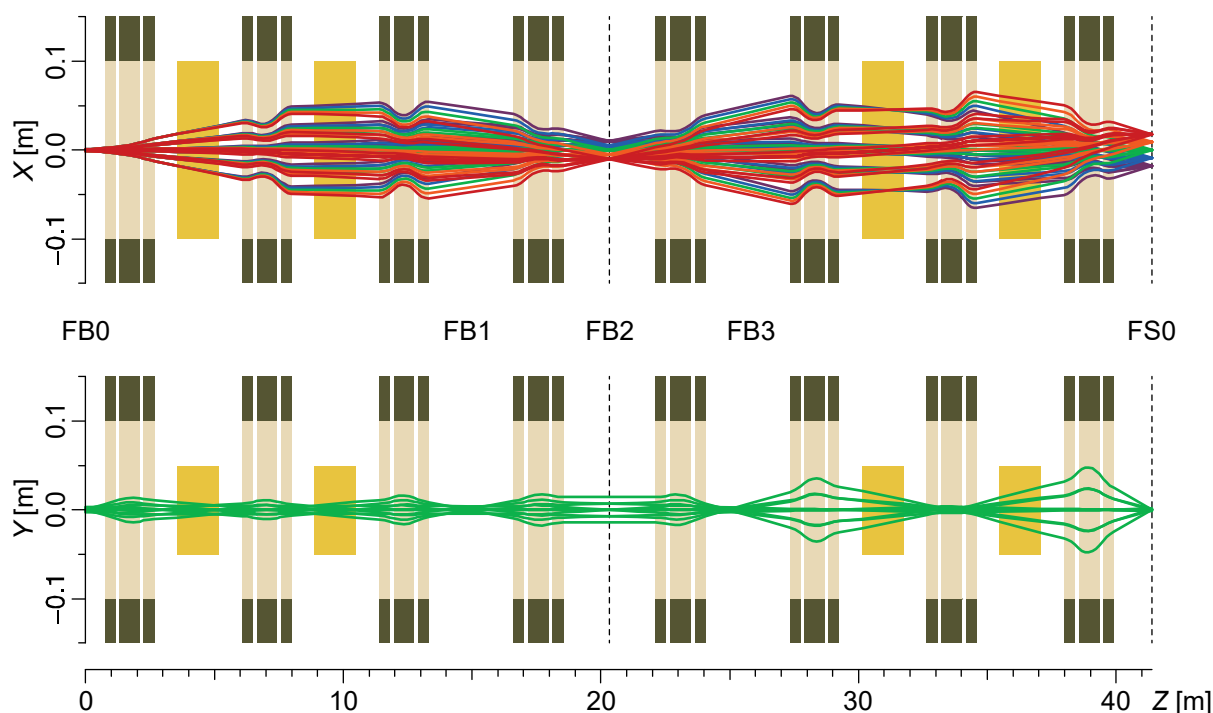


Figure 5-5 Same as Figure 5-4, but for the dispersion-matched beam transport. The ensemble of rays correspond to the  $2\sigma$  values of the phase space of  $^{204}\text{Pt}$ :  $\delta x_{\text{max}} = 1.0 \text{ mm}$ ,  $\delta x'_{\text{max}} = 3.2 \text{ mrad}$ ,  $\delta y_{\text{max}} = 2.9 \text{ mm}$ ,  $\delta y'_{\text{max}} = 8.0 \text{ mrad}$ , and  $\delta p_{\text{max}}/p = 0.25\%$ .

Table 5-3 First-order matrix elements of the HTBL in the achromatic beam-transport mode and in the dispersion-matched beam-transport mode. Only the ten non-trivial matrix elements are listed

	Achromatic			Dispersion-matched	
	FB1	FB3	FS0	FB2	FS0
$(x x) = R_{11}$	-1.57	1.75	-0.96	-0.48	0.36
$(x x') [\text{m/rad}] = R_{12}$	0.05	0.00	0.00	0.00	0.00
$(x' x) [\text{rad/m}] = R_{21}$	-0.03	0.04	0.04	-0.60	0.82
$(x' x') = R_{22}$	-0.64	0.57	-1.04	-2.07	2.76
$(x \delta) [\text{m}] = R_{16}$	4.53	-5.03	0.00	4.06	-7.13
$(x' \delta) [\text{rad}] = R_{26}$	0.00	0.04	0.00	-0.26	0.00
$(y y) = R_{33}$	2.06	-2.07	-1.65	0.00	-0.48
$(y y') [\text{m/rad}] = R_{34}$	-0.06	0.01	0.00	1.78	0.00
$(y' y) [\text{rad/m}] = R_{43}$	0.00	0.04	-0.01	-0.56	-0.25
$(y' y') = R_{44}$	0.49	-0.48	-0.61	0.00	-2.10



### 5.3.4 Higher-order ion optics

It is important for the HTBL to minimize higher-order aberrations by using sextupole and octupole correctors. As opposed to the spectrometer proper downstream of the reaction target where higher-order corrections can also be done by software (as are done for the S800 Spectrograph), the efficacy of software corrections before the reaction target is limited. In Figure 5-6, COSY calculations up to 5<sup>th</sup> order with and without the hardware correctors are compared.

Here, the field profiles from quadrupole triplet field measurements were used. Even without the hardware correctors [Figure 5-6(a)], the higher-order aberrations are not large, due to the symmetric design of the HTBL, and do not cause significant transmission losses. However, they cause inclinations of the dispersive foci at FB1 and FB3 and an increased beam spot size at FS0, which would result in deteriorated resolutions in momentum tracking of the beam or in reaction analysis in the Spectrometer Section. These aberrations can almost completely and sufficiently be corrected by the corrector coils, as shown in Figure 5-6(b). The effects above the 6<sup>th</sup> order are insignificant, and those for the dispersion-matched mode are not large and can be corrected in the same way.



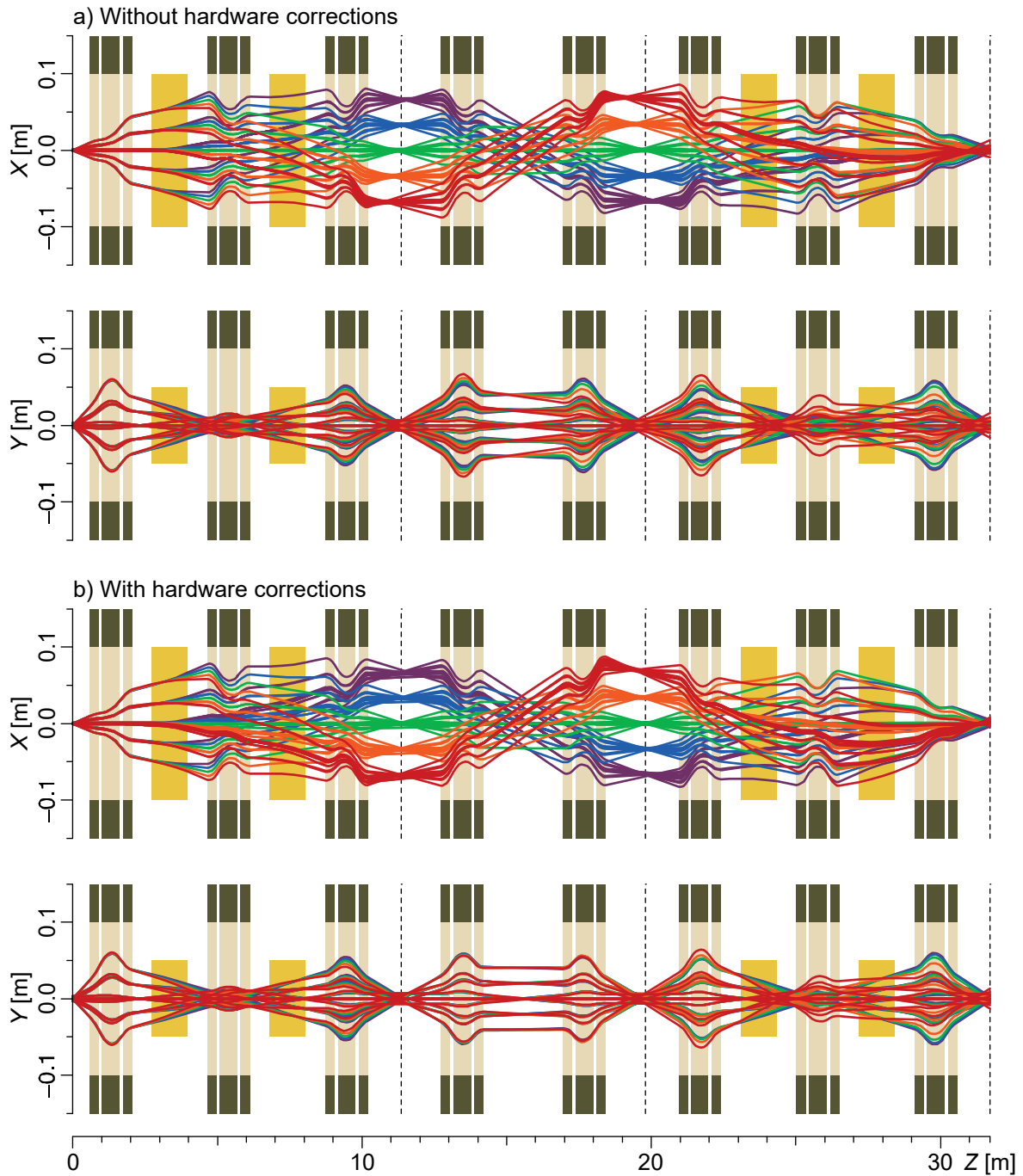


Figure 5-6 Same as in Figure 5-4 but in 5<sup>th</sup> order, a) with and b) without higher-order correctors.

## 5.4 End-to-end simulations

To understand the detailed properties of the HTBL and to realistically estimate the transmission of the rare-isotope beams through the HTBL, end-to-end simulations were performed including the transfer matrices of all the ion-optical elements of the HTBL as well as their aperture sizes.

Here, RIB-specific output of the ARIS Fragment Separator at FB0 was used as input to the HTBL and the beam was transported through to the Spectrometer Section target at FS0. The beams used for these studies were chosen based on the scientific program of the HRS as discussed in Section 4.3.2.2 and listed in Table 4-5. These beams are reproduced in Table 5-4 for convenience. Of the beams produced by in-beam fragmentation ( $^{40}\text{Mg}$ ,  $^{60}\text{Ca}$ ,  $^{100}\text{Sn}$ ,  $^{140}\text{Sn}$ , and  $^{204}\text{Pt}$ ),  $^{40}\text{Mg}$  has the largest phase space. However, its phase space is still significantly smaller than that of  $^{84}\text{Ni}$ , which is produced by in-flight fission. For the present studies, third-order transport matrices calculated in COSY were loaded into LISE<sup>++</sup> [BAZ02,TAR08,TAR16]. The physical aperture sizes of the beam lines, magnet bores and dipole gaps were used in estimating the transmission efficiencies.

For each beam, elements of and transport through the ARIS Preseparator and Fragment Separator were optimized to achieve the highest production rate with a reasonable purity in a similar fashion as is in preparation of a real experiment, resulting in the phase spaces provided in Table 5-4. The results for the case of  $^{40}\text{Mg}$  and  $^{84}\text{Ni}$  beams are shown in Figure 5-7. Although not shown in these figures, these simulations included the transport to the Preseparator and Fragment Separator, so that the details of the transport through these stages are included in the transmission through the HTBL, rather than parametrizing the phase space at the entrance of the HTBL. Simulated beam envelopes in the HTBL in the dispersive ( $x$ ) and non-dispersive ( $y$ ) planes are shown. Also shown are samples of  $x$ - $y$  images and their projections onto both axes with the aperture sizes.

Table 5-4 Rare-isotope beam phase spaces at the end of the ARIS Fragment Separator (FB0) obtained from Monte-Carlo Simulations in LISE<sup>++</sup>. The dimensions shown in the table are  $\pm 2\sigma$  values.

RIB (production mechanism)	$x$ [mm]	$x'$ [mrad]	$y$ [mm]	$y'$ [mrad]	$\delta p/p$ [%]
$^{40}\text{Mg}$ (fragmentation)	$\pm 1.2$	$\pm 12.5$	$\pm 3.4$	$\pm 31.2$	$\pm 1.54$
$^{60}\text{Ca}$ (fragmentation)	$\pm 1.0$	$\pm 12.8$	$\pm 1.7$	$\pm 32.6$	$\pm 1.44$
$^{84}\text{Ni}$ (in-flight fission)	$\pm 1.0$	$\pm 20.5$	$\pm 1.7$	$\pm 63.3$	$\pm 1.6$
$^{100}\text{Sn}$ (fragmentation)	$\pm 0.7$	$\pm 9.5$	$\pm 3.4$	$\pm 10.3$	$\pm 0.6$
$^{140}\text{Sn}$ (fragmentation)	$\pm 1.0$	$\pm 6.8$	$\pm 2.0$	$\pm 16.9$	$\pm 1.0$
$^{204}\text{Pt}$ (fragmentation)	$\pm 1.0$	$\pm 3.2$	$\pm 2.9$	$\pm 8.0$	$\pm 0.25$



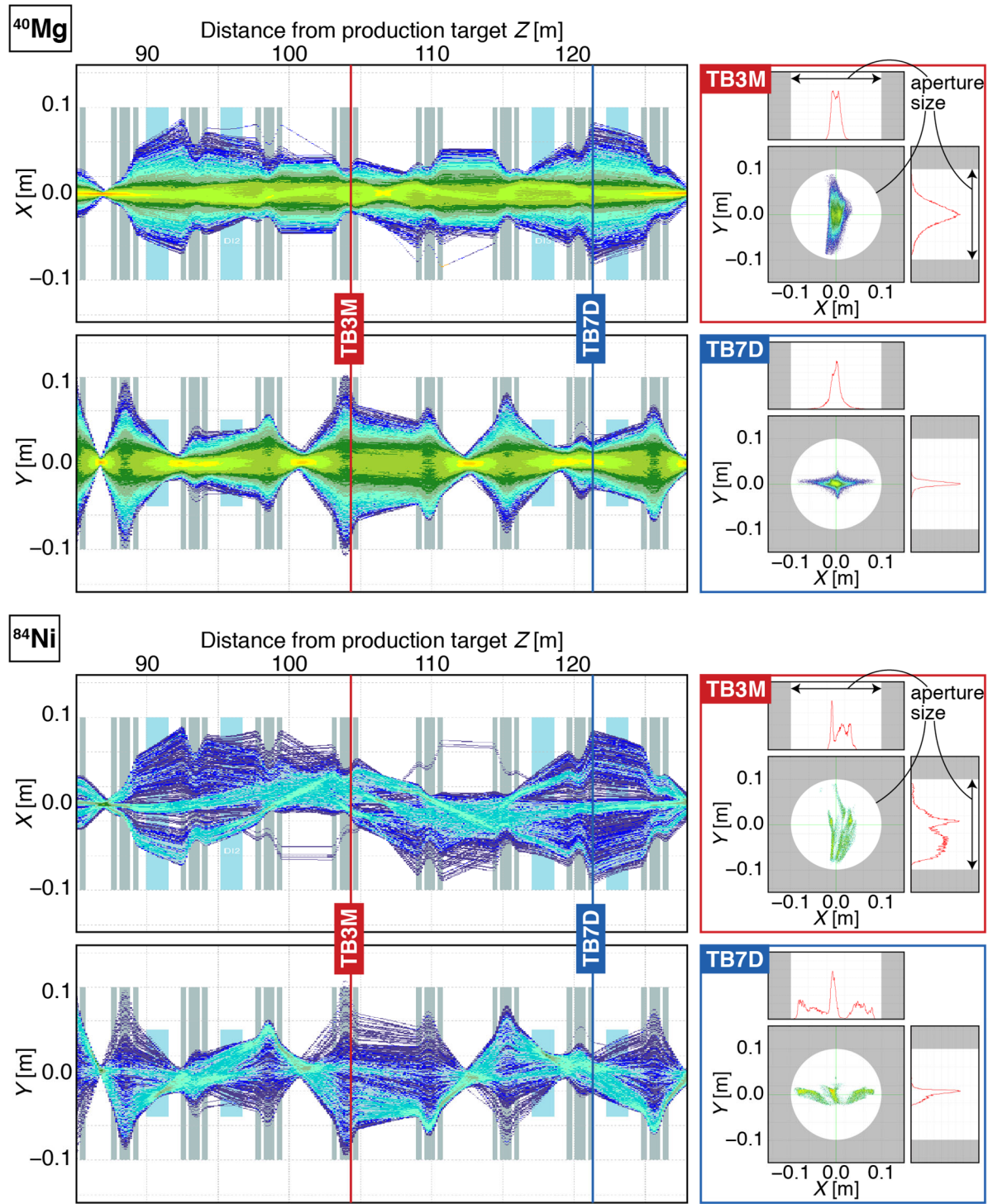


Figure 5-7 Results of end-to-end simulations for  $^{40}\text{Mg}$  and  $^{84}\text{Ni}$  in LISE<sup>++</sup> in 3<sup>rd</sup> order. See text for details.



The main results of the simulations for each of the representative beams are provided in Table 5-5. Besides the transmission (in the final two columns), this table also provides the basic parameters for the production of each of the rare-isotope beams. The transmission is from the end of the ARIS fragment separator (FB0) until the end of the HTBL (FS0). For all the six representative beams, the transmission efficiencies through the HTBL are 100% for the achromatic transport mode.

In a simulation performed using the dispersion-matched transport with  $^{204}\text{Pt}$ , a 100% transmission to FS0 was achieved, albeit for a limited momentum acceptance of  $\pm 0.5\%$  corresponding to a beam-spot size of target of about  $\pm 5$  cm. For the lighter beams, the transmission in the dispersion-matched transport is lower, owing to the larger beam emittances. The transmission in dispersion-matched transport mode for the case of  $^{84}\text{Ni}$ , produced by fission, will require further study and optimization and, therefore, listed as “To be determined”.

*Table 5-5 Overview of the results from the end-to-end simulations performed in LISE<sup>++</sup>. The primary beam, production target, momentum acceptance in the Preseparator (prior to momentum compression), degrader, and rigidity used in the simulations are listed with the transmission efficiencies in the achromatic and dispersion-matched modes.*

RIB	Primary beam	Target thickness (Carbon)	Momentum acceptance achromatic/dispersion matched	Al degrader thickness	Magnetic rigidity of HTBL	Transmission achromatic transport	Transmission dispersion-matched transport
$^{40}\text{Mg}$	$^{48}\text{Ca}$ , 239.5 MeV/u	11 mm	$\pm 5\%/\pm 0.5\%$	4.1 mm	6.68 Tm	100%	82%
$^{60}\text{Ca}$	$^{82}\text{Se}$ , 236.6 MeV/u	5.87 mm	$\pm 5\%/\pm 0.5\%$	2.5 mm	5.94 Tm	100%	81%
$^{84}\text{Ni}$ (fission)	$^{238}\text{U}$ , 202 MeV/u	1.35 mm	$\pm 5\%/\pm 0.5\%$	2 mm	5.80 Tm	100%	TBD
$^{100}\text{Sn}$	$^{112}\text{Sn}$ , 242.4 MeV/u	3.6 mm	$\pm 3.3\%/\pm 0.5\%$	1 mm	3.72 Tm	100%	96%
$^{140}\text{Sn}$	$^{160}\text{Gd}$ , 218.5 MeV/u	2.9 mm	$\pm 5\%/\pm 0.5\%$	1.5 mm	4.89 Tm	100%	98%
$^{204}\text{Pt}$	$^{208}\text{Pb}$ , 209.9 MeV/u	1.8 mm	$\pm 1.55\%/\pm 0.5\%$	2 mm	3.98 Tm	100%	100%



## 5.5 Angular and momentum resolutions

The angular and momentum resolutions were evaluated by means of Monte-Carlo simulations. The beam particles were transported using transfer maps calculated up to 5<sup>th</sup>-order in COSY, where trajectory reconstruction was done using inverse maps that were also calculated up to 5<sup>th</sup>-order in COSY. At the locations of the tracking detectors, some disturbance was added to emulate the finite detector resolutions and the effect of straggling in the detector materials. The resolutions evaluated this way provide the closest correspondence to the needs of the science program.

For the achromatic mode, the <sup>40</sup>Mg beam was used because it has the largest phase space at FB0. Figure 5-8 shows the angular and momentum resolutions, calculated as the difference between the reconstructed and initial angle/momentum. The angular and momentum resolutions have FWHM of 3.2 mrad and 1/1670, meeting the requirements of 5 mrad and 1/1500, respectively.

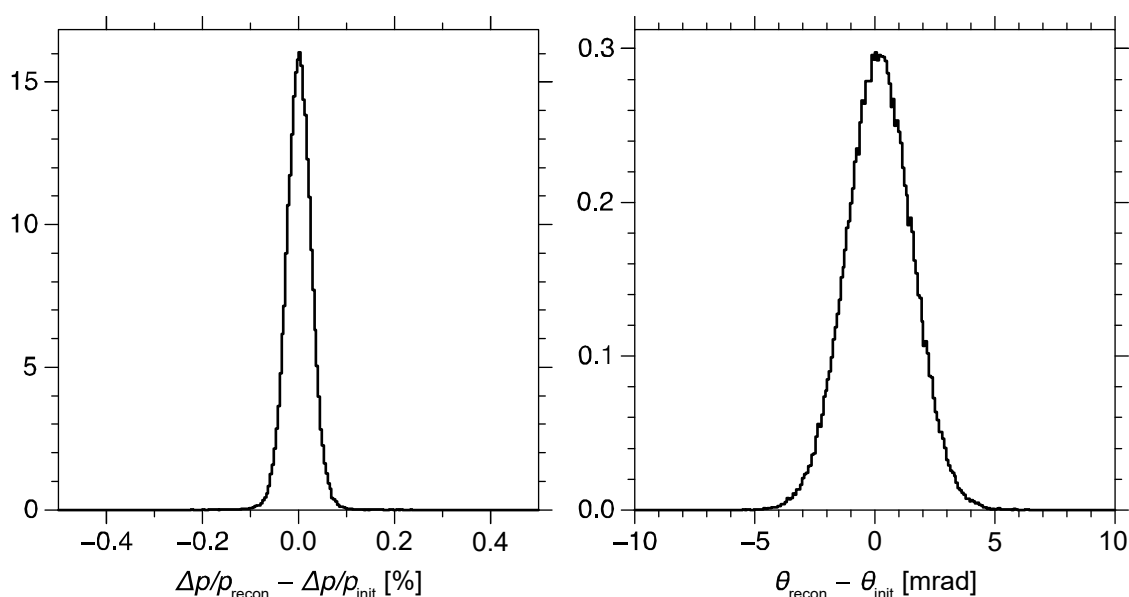


Figure 5-8 Angular and momentum resolutions in the achromatic mode calculated as the difference between the reconstructed and initial angle/momentum in trajectory-reconstruction simulations using COSY-calculated maps including up to 5<sup>th</sup> order.

Measurements at FB1 and FB3 may be combined to achieve an even more precise determination of the momentum and angle. In Figure 5-9 the momentum and angular resolutions achieved by a measurement at FB1 or FB3 alone are compared to the combination of the two. When they are combined, a momentum resolution of 1/1870 (FWHM) and an angular resolution of 2.3 mrad (FWHM) can be achieved—improvements by 10% and 40%, respectively.

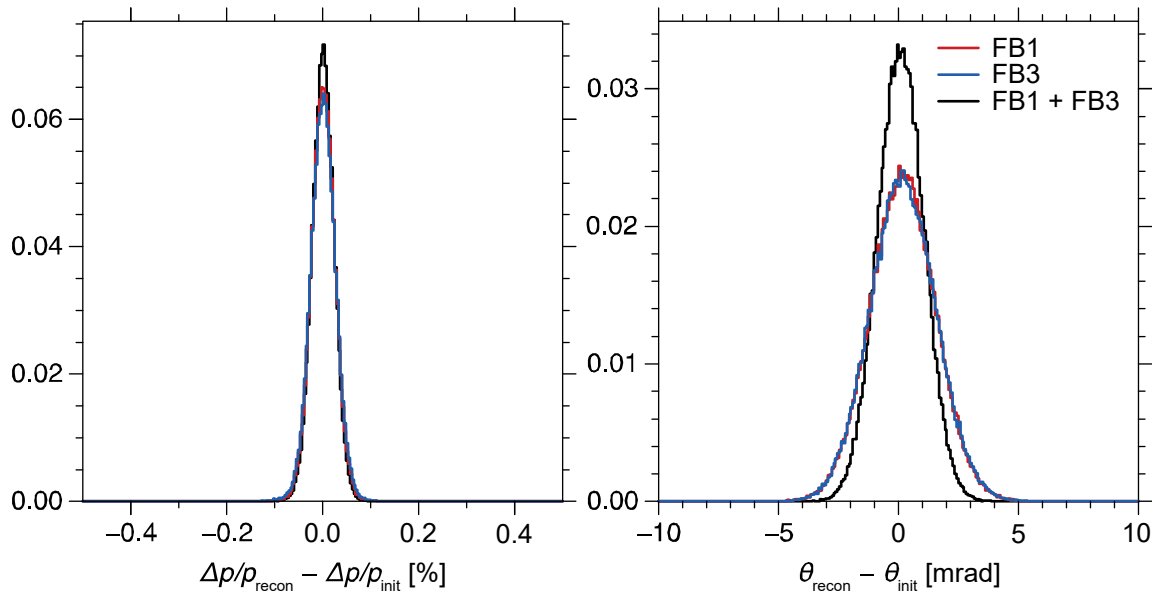


Figure 5-9 Momentum and angular resolutions in the achromatic mode. Those achieved by a measurement at FB1 or FB3 alone are compared to the combination of those at FB1 and FB3.

The momentum resolution in the dispersion-matched mode was evaluated in the same way. Figure 5-10 shows the difference between the reconstructed and initial momentum, having an FWHM of 1/12000, meeting the requirement of 1/10000.

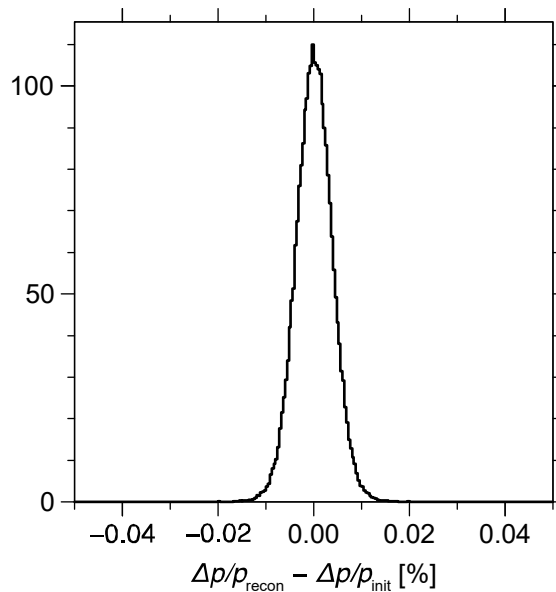


Figure 5-10 Momentum resolution in the dispersion-matched mode.

## 5.6 Angular and momentum acceptances

The angular and momentum acceptances were also evaluated by means of Monte-Carlo simulations. In these simulations, just as for the end-to-end simulations presented in Section 5.4, fifth-order transfer matrices calculated in COSY were loaded in LISE<sup>++</sup>, with the warm-bore aperture sizes for the quadrupoles, the good-field regions in the dispersive plane, and the vertical gap sizes in the non-dispersive plane for the dipoles all being considered. Transmitted from a point source at FB0, beam particles having a sufficiently large uniform phase-space (momentum and angles) distribution were transported through the HTBL.

In Figure 5-11, the initial phase space variables for the particles that were achromatically transported and eventually reached FS0 are plotted as three 2D histograms; For a specific beam, for a set of the phase-space variables ( $x'$ ,  $y'$ ,  $\delta p/p$ ), a particle is either accepted or rejected. The acceptance can be depicted as a volume in a 3D space. The 2D correlations  $x'$ - $y'$ ,  $x'$ - $\delta p/p$ , and  $y'$ - $\delta p/p$  are projections of this 3D volume onto the 2D planes and represent the acceptances of the HTBL. The angular acceptances for the achromatic mode thus evaluated are  $\Delta x' = \pm 20$  mrad and  $\Delta y' = \pm 50$  mrad, and the momentum acceptance is  $\Delta p/p = \pm 2\%$ .

Figure 5-12 shows the momentum and angular acceptances of the HTBL in the dispersion matched mode. The angular acceptances are  $\Delta x' = \pm 9$  mrad and  $\Delta y' = \pm 24$  mrad, and the momentum acceptance is  $\Delta p/p = \pm 0.7\%$ .



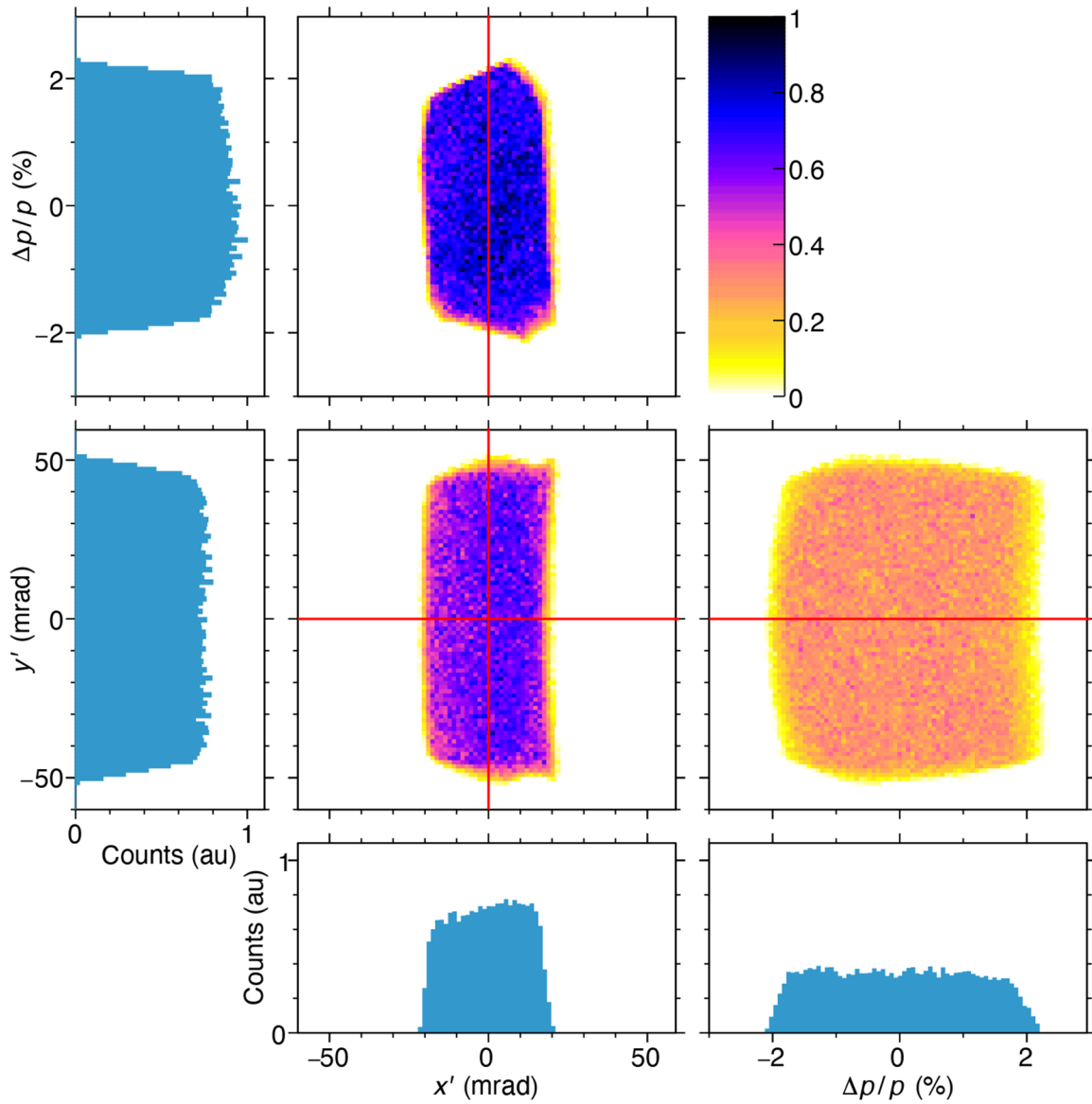


Figure 5-11 Angular and momentum acceptances for the achromatic beam-transport modes of the HTBL as simulated in LISE<sup>++</sup> loaded with fifth-order transfer matrices obtained in COSY. The three 2D histograms show the angle-angle or angle-momentum correlations. The four 1D histograms are their slices around  $x' = 0$  mrad or  $\Delta p/p = 0\%$  as indicated by the red lines.



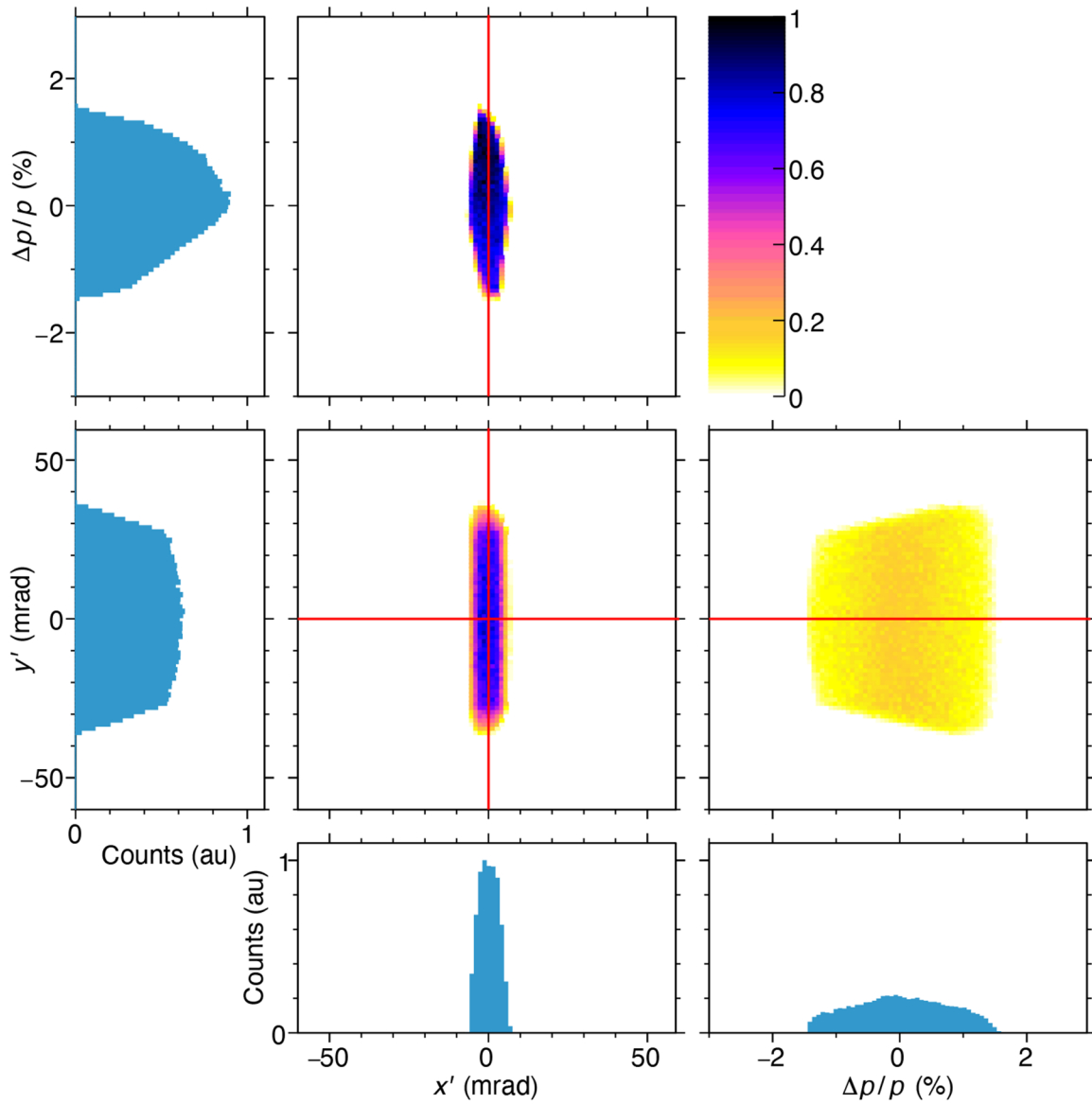


Figure 5-12 Same as Figure 5-11, but for the dispersion-matched mode.

## 5.7 Preferred HTBL alternative meets requirements

The capabilities of the HTBL afforded by the preferred ion-optical alternative regarding the functional requirements are summarized as follows.

- The ion optics of the preferred alternative is feasible at the required maximum magnetic rigidity of 8 Tm.
- As demonstrated by the end-to-end simulations, the transmission efficiencies through the HTBL exceed 95% for all the representative rare-isotope beams.
- Both achromatic and dispersive beam-transport modes are available, and the latter realizes the dispersion matching to the Spectrometer Section.
- The flight-path length of the HTBL is 41.40 m, and when combined with the ARIS Fragment Separator (40.14 m) and the Spectrometer Section (31.72 m), it provides a 113-m long flight path for ToF- $B\rho$  mass measurements, meeting the 90-m requirement.
- The momentum resolving power of 1700 (FWHM) is achieved, which exceeds the required momentum resolving power of 1500. Also, the angular resolution of 3 mrad (FWHM) is achieved, which exceeds the required 5 mrad (FWHM).
- The HTBL can accommodate an RFFS with a length of 2.2 m as well as associated steering magnets at FB2. The beam is parallel in the non-dispersive plane at FB2 both in achromatic and dispersive beam-transport mode, which is suited for the operation of an RFFS.

## 5.8 Functional specifications for the HTBL

This section stipulates the functional specifications for the HTBL to realize its functional requirements. The specifications of the magnetic elements are given in Section 5.8.1, those of the diagnostics and detectors are given in Section 5.8.2, and those of the vacuum systems are given in Section 5.8.3.

### 5.8.1 Magnetic elements

As shown in Figure 5-1, the HTBL contains 24 quadrupole magnets (in 8 triplets), four main dipole magnets, and two steering dipole magnets. The functional specifications of these magnets as used in the ion-optical simulations of the preferred layout are presented in this section. Preliminary designs of the magnetic elements that meet these functional specifications will be presented in Section 9.



### 5.8.1.1 Quadrupole triplets

All the eight quadrupole triplets are of the same design. The triplet used in the HTBL consists of three quadrupoles that have short (upstream), long (middle), and short (downstream) field lengths, where the up- and downstream quadrupoles are identical. All the three quadrupoles must have embedded sextupole and octupole coils to correct for higher-order aberrations as discussed in Section 5.3.4. Detailed specifications are summarized in Table 5-6.

One of the three types of the quadrupole triplets that are presently used in the NSCL A1900 Fragment Separator and will be used in the ARIS Fragment Separator satisfies the specifications given in Table 5-6. Therefore, these quadrupole triplets will be based on the design of the A1900 triplet, as described in Section 9.4.1. This triplet type is referred to as the “T2” type, consisting of the short FSQB and long FSQC quadrupoles, as indicated in Table 5-6. It is regarded as a natural choice because it matches the phase space of rare-isotope beams delivered by the ARIS Fragment Separator in which the same magnet design is used. The measured field data of these triplets were included in detailed ion-optical models, the calculations presented in Sections 5.3 and 5.4 utilized them to emulate all effects, such as the dependence of the effective length on the field gradient magnitude.

The measured field data of these triplets at various excitation were available. To assess the effects of the field quality on the ion optics, the field-map data were parametrized and included in detailed ion-optical models. They were used in the calculations presented in Sections 5.3 and 5.4 to emulate all effects, such as the variation of the effective length or the field shapes as a function of the field strength. It was verified by these calculations that the designed ion-optical properties could be realized by employing the existing triplet design.

Also note that Table 5-6 includes the base magnetic field requirements as determined from ion-optical calculations needed to achieve the design beam transport in both operations modes at the maximum magnetic rigidities of 8 Tm, as well as the magnetic field requirements with tuning margin to ensure project specifications are met. The magnet designs are based on the magnetic field requirements with tuning margin, and therefore the power supply voltage and currents include tuning margin.



Table 5-6 Functional specifications of the quadrupole magnets for the HTBL. Each quadrupole has superimposed sextupole and octupole corrector coils. These quadrupoles are packaged in triplets (FSQB-FSQC-FSQB; FSQB repeats), which are labeled as TB1 through TB8 in Figure 5-1.

Label	FSQB	FSQC
Quantity (in 8 quadrupole triplets)	16	8
Effective field length (nominal) (m)	0.40	0.79
Pole-tip radius (m)	0.15	0.15
Warm-bore radius (m)	0.10	0.10
Quadrupole maximum field strength (T@poletip, base requirement)†	2.34	2.48
Quadrupole maximum field strength (T@poletip, with 10% tuning margin)†	2.57	2.73
Quadrupole field integral (T, base requirement)†	6.24	13.06
Quadrupole field integral (T, with 10% tuning margin)†	6.86	14.37
Quadrupole good-field region radius (m)	0.10	0.10
Sextupole maximum field strength (T/m <sup>2</sup> , base requirement)	10	10
Sextupole maximum field strength (T/m <sup>2</sup> , with 10% tuning margin)†	11	11
Octupole maximum field strength (T/m <sup>3</sup> , base requirement)	50	50
Octupole maximum field strength (T/m <sup>3</sup> , with 10% tuning margin)†	55	55

†: This table includes the base magnetic field requirements as determined from ion-optical calculations, needed to achieve the design beam transport in both operations modes at the maximum magnetic rigidities of 8 Tm. Additionally this table includes magnetic field requirements with tuning margin to ensure project specifications are met. The magnet designs are based on the magnetic field requirements with tuning margin, and therefore the power supply voltage and currents include tuning margin.

### 5.8.1.2 Dipole magnets

All the four dipole magnets are of the same design. They are rectangular magnets whose entrance and exit pole faces are rotated by half the bending angles. The use of rectangular magnets optimizes the beam delivery to the other experimental areas of FRIB and does not negatively impact the beam transport in the HTBL. The specifications are listed in Table 5-7. As will be described in Section 9.4.2, the actual implementation of these dipoles is based on an existing Transfer-Hall dipole but scaled to a higher rigidity.

The magnetic field profiles at various excitations from ANSYS Maxwell analyses of the dipole magnet designs (See Section 9) have been included in ion-optical simulations using 5<sup>th</sup>-order transfer maps calculated in COSY. It has been concluded that the science requirements can be met by the magnet designs in their present form.



Table 5-7 Functional specifications of the dipole magnets for the HTBL. These dipoles are labeled as DB1 through DB4 in Figure 5-1.

Label	DBx (x = 1, 2, 3, 4)
Quantity	4
Bending radius (m)	4.10
Maximum rigidity (Tm)	8.0
Maximum field (T, base requirement)†	1.95
Maximum field (T, with 5% tuning margin)†	2.05
Bending angle (deg)	22.5
Arc length for central ray (m)	1.61
Field integral (Tm, base requirement)†	3.15
Field integral (Tm, with 5% tuning margin)†	3.30
Vertical gap size (m)	±0.05
Good field region (m)	±0.10
Pole-face rotation entrance (deg)	11.25
Pole-face rotation exit (deg)	11.25

†: This table includes the base magnetic field requirements as determined from ion-optical calculations, needed to achieve the design beam transport at the maximum magnetic rigidities of 8 Tm. Additionally this table includes magnetic field requirements with tuning margin to ensure project specifications are met. The magnet designs are based on the magnetic field requirements with tuning margin, and therefore the power supply voltage and currents include tuning margin.

### 5.8.1.3 Steerer dipole magnets

The design of the HTBL includes two vertically steering dipole magnets, SB1 and SB2, as indicated in Figure 5-1. The upstream steerer (SB1) adjusts the beam centroid at the middle of the HTBL (FB2), and the downstream steerer (SB2) adjusts the trajectory to the reaction target location (FS1). The magnitude of the first-order matrix element ( $y|y'$ ) is about 1 for both from SB1 to FB2 and from SB2 to FS0. To be able to adjust the beam centroid by 10 mm at FB2 and FS0, a 10-mrad vertical angle deflection at the steerer location is required. The current design of these steerers has a length of 40 cm, which corresponds to a bending radius of 40 m. For a rigidity of 8 Tm, the required field strength is 0.2 Tesla. The specifications for the steerer magnets are listed in Table 5-8.



Table 5-8 Functional specifications of the steerer dipole magnets for the HTBL. These steerer dipoles are labeled as SB1 and SB2 in Figure 5-1.

Label	SBx (x = 1, 2)
Quantity	2
Length (m)	0.40
Gap size (m)	±0.10
Maximum Rigidity (Tm)	8
Maximum deflection angle (mrad)	10
Maximum field (T, base requirement)†	0.20
Maximum field (T, with 10% margin)	0.22

†: These tables include the base magnetic field requirements as determined from ion-optical calculations, needed to achieve the design beam transport in both operations modes at the maximum magnetic rigidities of 8 Tm. Additionally, this table includes magnetic field requirements with tuning margin to ensure project specifications are met. The magnet designs are based on the magnetic field requirements with tuning margin, and therefore the power supply voltage and currents include tuning margin.

## 5.8.2 Diagnostics and detectors

The goals of HTBL diagnostics and detector system are defined as follows:

- To facilitate initial commissioning of the HRS,
- To facilitate tuning prior and during experiments by enabling characterization of beam properties and transmission efficiency,
- To provide event-by-event tracking and timing information for physics analysis, and
- To enable long-term stable operation and provide appropriate machine protection.

To achieve these goals, the specifications for the diagnostics and detectors have been formulated.

As shown in Figure 5-1, the preferred alternative of the HTBL contains two primary diagnostic stations, located at FB1 and FB3. These stations contain a variety of systems to diagnose the properties of the rare-isotope beam and to provide event-by-event tracking capability for the experimental program. The following provides a summary of the required diagnostics systems for the HTBL. These systems are selected based on nearly two decades of experience with tuning beam of rare isotopes from the A1900 Fragment Separator to the existing spectrometers at NSCL and are further detailed in Section 7.

- FB1, FB2, and FB3 must contain simple beam viewer systems with corresponding cameras that provide immediate visual feedback for beam tuning
- FB1 and FB3 must contain a set of fast position detectors that provide event-by-event position and angle information





- FB1 and FB3 must contain plastic scintillator timing detectors that provide event-by-event timing measurement for beam-particle identification
- In addition, FB3 must be equipped with an energy loss detector appropriate for beam-particle identification. This is not only useful for regular beam-tuning purposes, but also crucial for tuning and diagnosing the operation the RFFS (see Section 4.3.2.7.3).

It should be noted that, depending on the requirements for a particular experiment, timing, position, and angular tracking might be required just prior to the reaction target at FS0. Therefore, a beam viewer, tracking detectors and a fast-timing detector should be available for FS0 as well. These tracking detectors can also be used for beam tracking at FS0'.

Figure 5-13(a) and (b) show schematic layouts of the detector configuration of the diagnostic systems used at FB1/FS0 and FB3, respectively.

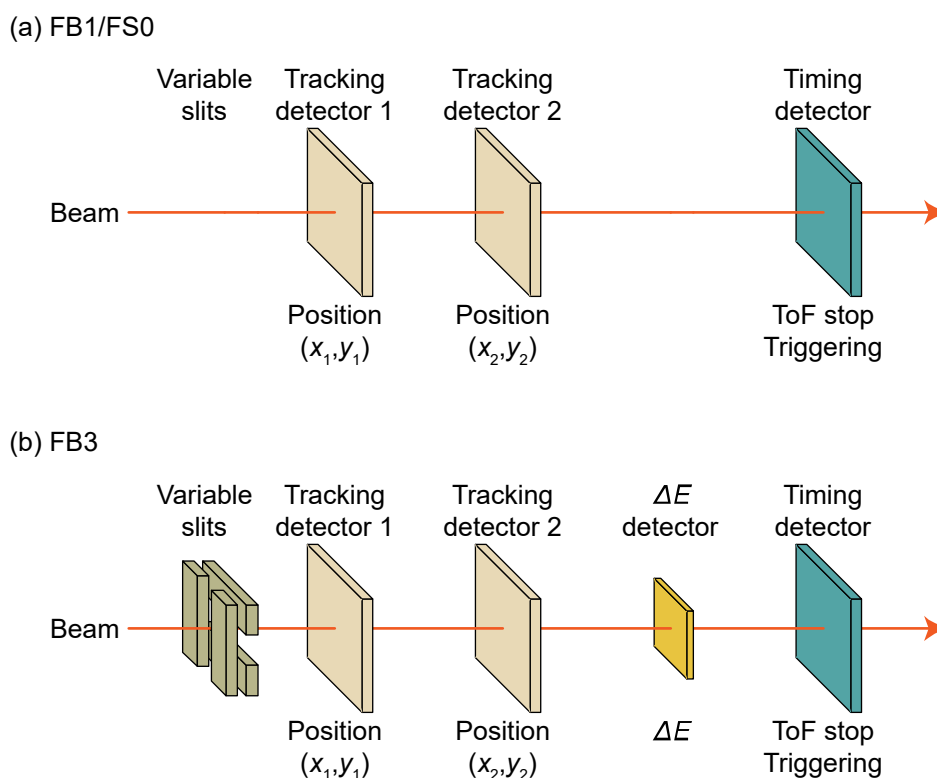


Figure 5-13 Schematic layout of the detector configuration of the diagnostic systems used at (a) FB1/FS0 and (b) FB3.

The properties of the position tracking detectors are determined by the need to achieve a sufficiently accurate determination of the momentum and angle of the incoming rare-isotope beam.

The main requirement is a momentum resolving power of 1500 (See Table 4-4). This means that in achromatic beam-transport mode, the momentum of the incoming beam must be determined with a significantly better resolution so as not to limit the resolving power of the measurements in the Spectrometer Section. Based on the ion-optical properties of the HTBL shown in Table 5-3, and realistic beam dimensions (see Table 5-4) at the entrance of the HTBL, a momentum resolving power of  $\sim 1/1700$  can be achieved with a position resolution of 1 mm (FWHM) in a tracking detector placed at FB1 or FB3. This is sufficient not to limit the momentum resolution of the measurement in the Spectrometer Section. Momentum tracking in both the FB1 and FB3 boxes can be combined to further improve the resolving power of the beam-momentum tracking as shown in Figure 5-9. In addition, position and angle tracking detectors, as well as a timing detector, can be installed just prior to the reaction target at FS0, depending on the needs of a particular experiment. Momentum tracking in both the FB1 and FB3 chambers is also important during the tuning of the beam transport, especially since correlations between the beam properties at each location can be studied.

When event-by-event tracking needs to be performed, the maximum intensity of the rare-isotope beams is limited by the rate capabilities of the tracking detectors. Therefore, fast tracking detectors must be employed that can operate at rates of at least several hundred kHz. Timing measurements should be performed at rates that exceed 1 MHz with a resolution of better than 150 ps.

Based on extensive experience with energy-loss detectors for particle identification, the energy loss detector in FB3 should achieve an energy resolution of better than 3% for  $\alpha$  particles of 5.5 MeV. It has been shown that this allows for the charge separation of up to  $Z \sim 92$  using small stacks of such silicon PIN detectors [KWA18,TAR20]. Note that these energy-loss detectors are only used during beam characterization and not during regular data taking for experiments. Therefore, they do not need to be operated at high beam rates.

All detectors used in the HTBL should be sufficiently large to cover the transverse beam profiles at their locations. Although the beam envelopes at FB1 and FB3 are relatively small in the vertical direction, the tracking detectors should accommodate larger envelopes that might be encountered in the beam tuning. Therefore, the dimensions in the horizontal and vertical directions of the tracking detectors are chosen to be  $20 \times 20 \text{ cm}^2$ . The energy-loss detector in FB3 must cover an area of  $20 \times 5 \text{ cm}^2$ .

The diagnostics and detector systems installed in FB1 and FB3 must be retractable. All detectors will be read out through data acquisition systems that run Laboratory-supported data-acquisition software. For personnel protection purposes, near the location of FB1 a beam blocker and a wall-plug must be installed, which are similar to such devices used at NSCL, to safely intercept the rare-isotope beams prior to entering the HRS experimental areas.



The functional specifications for the diagnostics and detector systems of the HTBL are summarized in Table 5-9, Table 5-10, Table 5-11, and Table 5-12.

Table 5-9 General functional specifications for the diagnostics and detector systems for the HTBL.

Parameter	Specification
Remotely retractable	Yes
Positioning accuracy	≤ 0.5 mm (transverse to the beam) ≤ 1 mm (along the beam axis)
Accessibility	Replacement possible within < 4 hours
Vacuum requirement	10 <sup>-5</sup> Torr vacuum compatible

Table 5-10 Functional specifications for the viewer systems for the HTBL.

Parameter	Specification
Single particle detection	No
Transmission	No
Coating	Thin luminescent layer: emits light when exposed to heavy ion beam
Effective area	20 × 20 cm <sup>2</sup> (with fiducials for calibration)

Table 5-11 Functional specifications for the tracking and timing detectors for the HTBL.

Parameter	Specification	
Transmission	100%	
Single particle detection	Yes	
Thickness	Tracking	≤ 10 mg/cm <sup>2</sup>
	Timing	≤ 100 mg/cm <sup>2</sup>
Effective area	Tracking	20 × 20 cm <sup>2</sup>
	Timing	20 × 20 cm <sup>2</sup>
Resolution (FWHM)	Position	≤ 1 mm
	Timing	≤ 150 ps
Rate capability	Tracking	a few hundred kHz
	Timing	≥ 1 MHz



Table 5-12 Functional specifications for the energy-loss detectors for the HTBL.

Parameter	Specification
Transmission	100%
Effective area	5 × 5 cm <sup>2</sup> each (with fiducials for calibration) 4 aligned detector for 20 × 5 cm <sup>2</sup> coverage
Thickness	≤ 500 μm
Energy resolution	≤ 3% (@ 5.5 MeV α-particles)
Rate capability	≥ 1000 Hz

### 5.8.3 Vacuum systems

With the lattice design of the HTBL established, the locations of the magnet are fixed on the floor layout. With the preliminary designs of the magnets, the dimensions of the vacuum chambers (beam pipes) have been identified. Also, with the standard sets of diagnostic instruments defined, the dimensions of the diagnostic chambers have been identified.

The general specification for the vacuum systems for the HTBL is that the systems be able to evacuate to the pressure of  $10^{-5}$  Torr (see also Section 6.5.3). At this level, the lateral, angular, and energy spreads due to interactions with residual gas in the beam line do not contribute significantly to the uncertainties in the tracking of the particles. The production of charge states other than that of the rare-isotope beam in the rest gas at this pressure level is negligible (<0.1%), especially when compared to charge-state production in beam line tracking detectors and the reaction target, as discussed in Section 4.3.2.3. Hence, it does not pose an additional constraint on the vacuum level that must be achieved.

Turbo-molecular pumping (TMP) systems are sensitive to the presence of magnetic fields and cannot operate in fields in excess of 50 Gauss. For some of the magnets with significant stray fields, such as DS1 (see Figure 6.12), this requires that these pumps are placed at appropriate distances from such magnets. The exact location of each TMP will be confirmed by performing a detailed magnetic field analysis around each large magnet in the HRS. Similar consideration will also be given to vacuum gauging, some of which has maximum magnetic field limits specified by the supplier.

Finally, the locations of necessary bellows to accommodate alignment have been identified.

## 5.9 References

[ANS19] ANSYS Electromagnetics Suite, Release 2019 R3.7 (2019).

[BAZ02] D. Bazin et al., Nucl. Instrum. Methods Phys. Res., Sect. A 482, 307 (2002).



- [BAZ03] D. Bazin et al., Nucl. Instrum. Methods Phys. Res., Sect. B 204, 629 (2003).
- [COS11] M. Berz and K. Makino, COSY Infinity 9.1, “Programmer’s Manual” MSU Report MSUHEP 101214 (2011); “Beam Physics Manual” 060804-rev (2013).
- [POR16] M. Portillo, M. Hausmann, and S. Chouhan, Nucl. Instrum. Methods Phys. Res., Sect. B 376, 150 (2016).
- [TAR08] O. B. Tarasov and D. Bazin, Nucl. Instrum. Methods Phys. Res., Sect. B 266, 4657 (2008).
- [TAR16] O. B. Tarasov and D. Bazin, Nucl. Instrum. Methods Phys. Res., Sect. B 376, 185 (2016).



## 6 Spectrometer Section of the HRS

This section describes the beam physics of the Spectrometer Section of the HRS, designed based on the functional requirements stipulated in Section 4.3. The Work Breakdown Structure (WBS) is given in Table 6-1. After a brief overview of the Spectrometer Section is given in Section 6.1, the functional requirements are revisited and reproduced in Section 6.2, and the design approach and the preferred alternative are presented in Section 6.3. The capabilities afforded by the preferred alternative are summarized in Section 6.4. The functional specifications of the magnetic elements, the diagnostics and detectors, and the vacuum components are given in Section 6.5, which serve as the functional requirements for the corresponding subsystems. Commissioning plans for the Spectrometer Section are given in Section 8.

As in the case of the HTBL in Section 5, the ion-optical calculation for the Spectrometer Section were performed with COSY Infinity [COS11]. The magnetic field profiles extracted from the magnetostatic models in ANSYS Maxwell [ANS19] based on the preliminary designs of the magnets, as described in Section 9.2.2, have been incorporated in the COSY calculations.

Table 6-1 WBS for the Spectrometer beam physics.

<b>Experimental Systems - High Rigidity Spectrometer</b>	<b>HRS.3</b>
<b>Spectrometer Section</b>	<b>HRS.3.02</b>
<b>Spectrometer Section Beam Physics</b>	<b>HRS.3.02.01</b>

### 6.1 Introduction and overview

The layout of the Spectrometer Section is shown in Figure 6-1. The Spectrometer Section starts at FS0, the location of the reaction target. A variety of ancillary devices can be placed around the reaction target (see Figure 4-17). In Figure 6-1, GRETA is shown at FS0, being the largest of these ancillary devices which are now foreseen to be used at the HRS. FS0 is followed by two quadrupole magnets (QS1A and QS2B), which guide the trajectories of the desired reaction fragments into the rest of the Spectrometer Section. QS2B is followed by the large-gap sweeper dipole magnet DS1, which bends the charged fragments to the left by 35°. DS1 is followed by two quadrupoles, QS3B and QS4B, which guide the particles to the first focal plane FS1. FS1 is followed by two additional large-bore quadrupoles, QS5A and QS6A, which guide the particles into the spectrometer dipole DS2. DS2 bends the particles to the right by 60° into the final focal plane FS2.

Most experiments envisioned with the HRS must use the full Spectrometer Section to achieve the scientific goals. However, for invariant-mass spectroscopy experiments that involve fast neutron detection with the MoNA-LISA neutron-detector array installed at forward angles, the reaction target is placed just in front of DS1 (denoted FS0') so that neutrons can be detected with optimal





acceptance through the gap of DS1, not limited by the apertures of the quadrupoles QS1A and QS2B, as shown in Figure 6-1. In that case, the measurement with ancillary detectors requires that they are placed just prior to DS1 as well, as indicated by the placement GRETA at FS0' in the figure. The intermediate focus FS1 serves as the final focus, and the downstream magnets (QS5A, QS6A, and DS2) are not used.

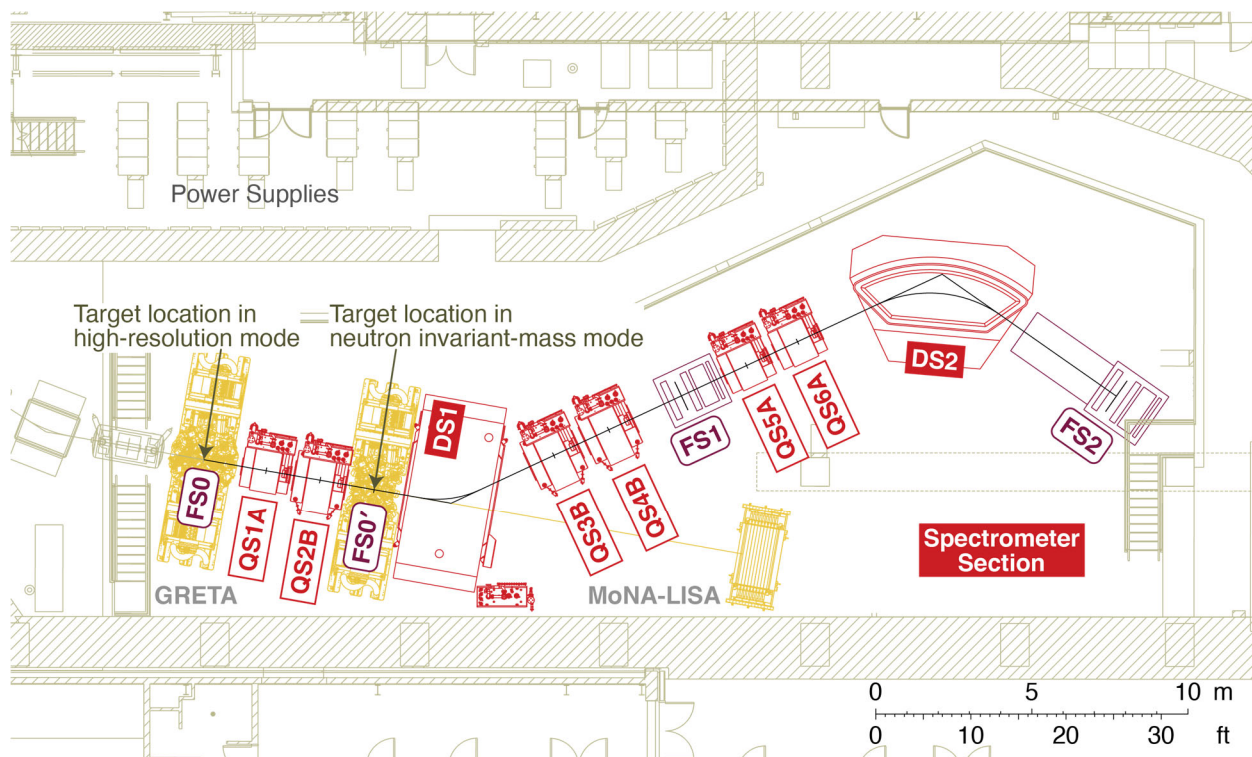


Figure 6-1 Layout of the Spectrometer Section of the HRS starting at FS0, showing dipoles DS1 and DS2, quadrupoles QS1A, QS2B, QS3B, QS4B, QS5A, and QS6A, focal planes FS1 and FS2, and possible locations for GRETA and MoNA-LISA.

## 6.2 Functional Requirements for the Spectrometer Section

The Spectrometer Section must enable the diverse scientific program described in Section 4.2 with requirements for a wide range of experiment types described in Table 4-4. Based on the functional requirements for the Spectrometer Section discussed in Section 4.3, three operational modes were identified in Section 4.3.1.6, with the functional requirements for each detailed in Table 4-1. For convenience, Table 4-1 is reproduced as Table 6-2. The three operational modes are (1) the high-resolution mode, which is used for a large fraction of the experiment types, (2) the neutron invariant-mass mode, which is only used for invariant-mass spectroscopy in which the MoNA-

LISA neutron detector array is employed, and (3) the ToF- $B\rho$  mass-measurement mode, which is only utilized for mass-measurement experiments.

While the ion-optical layout of the high-resolution mode is the same as that of the ToF- $B\rho$  mass-measurement mode, the neutron invariant-mass mode has a distinct layout, but with the same hardware configuration as the other two modes. The maximum magnetic rigidity for each of these modes is 8 Tm, but the requirements are mostly different otherwise

Table 6-2 Functional requirement for the three operational modes of the Spectrometer Section of the HRS (see also Table 4-4).

Requirements	High-resolution	Neutron invariant-mass	ToF- $B\rho$ mass-measurement
Maximum mass number	238	132	238
Mass resolving power (FWHM)	400	220	10000
Charge resolving power (FWHM)	156	85	156
Time-of-flight resolution (FWHM) (ps)	150	150	30
Flight path for charged particles (m)	25	11	90
Momentum resolving power (FWHM)	1500	290	>10000
Spectrometer solid angle (msr)	15	10	3
Angular resolution (mrad)	5	5	5
Space around target (cm)	123	90	-
Momentum acceptance ( $\delta p/p$ in %)	$\pm 2.5$	$\pm 5$	$\pm 0.5$
Neutron solid angle (msr)	-	32	-
Gap for Time Projection Chamber	-	60	-
Neutron flight-path length (m)	-	15	-
Unreacted beam rejection	yes	yes	-
Maximum magnetic rigidity (Tm)	8	8	7

### 6.3 Design approach and preferred alternative for the Spectrometer Section

In the following, the design approach for each of the three operational modes is described within the framework of the preferred layout of the Spectrometer Section.

#### 6.3.1 High-resolution mode

The high-resolution mode is required for a large fraction of the experiment types. Since experiments performed in this mode will involve rare isotopes across the chart of nuclei, including very heavy isotopes, this mode must achieve good mass resolving power *via* a time-of-flight measurement, requiring a flight path of at least 25 m. This is achieved by utilizing the full



Spectrometer Section as shown in Figure 6-2. The reaction target is located at FS0, around which large space is reserved for ancillary detectors, represented by GRETA, the largest of the ancillary detector systems foreseen to be installed at the HRS.

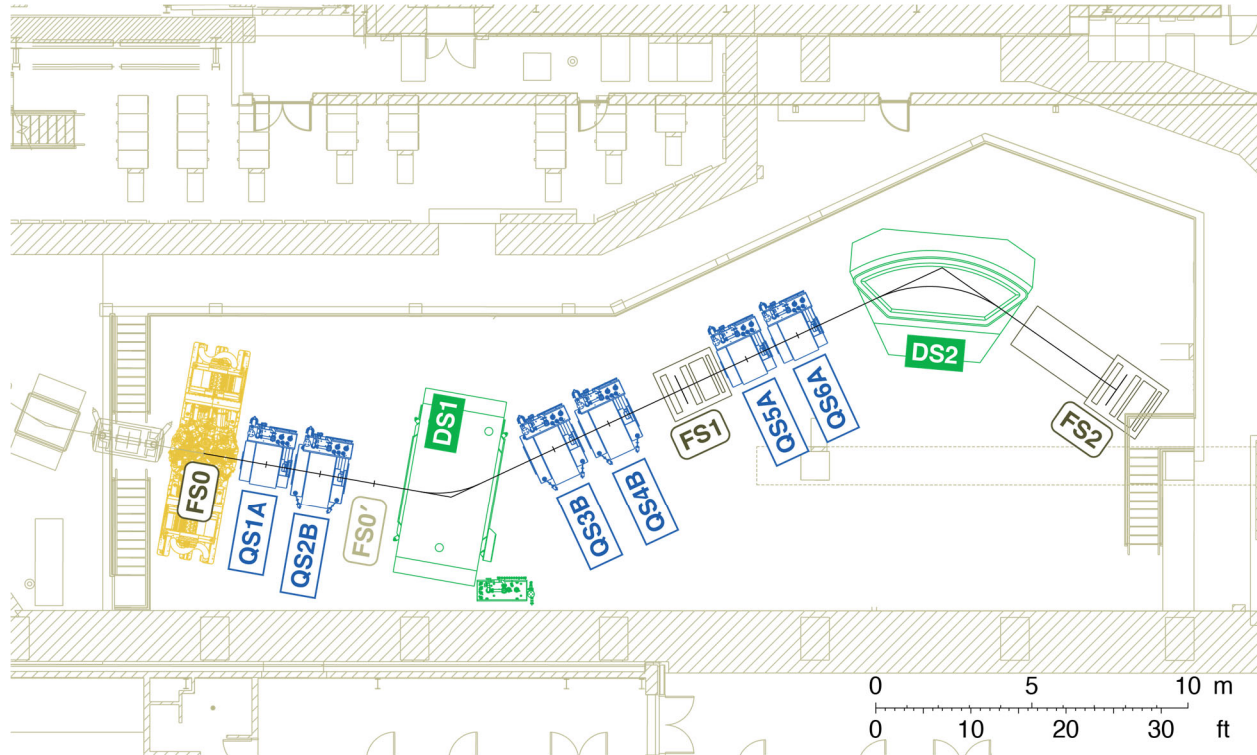


Figure 6-2 The layout for the high-resolution mode of the Spectrometer Section.

### 6.3.1.1 First-order ion optics

The first-order ion-optical description is the most important for understanding the concept and main performance parameters of the ion-optical layout of the high-resolution mode. Figure 6-3 shows the first-order ion-optical plot of the Spectrometer Section in the high-resolution mode. The upper panel shows the beam transport in the dispersive ( $x$ ) plane and the lower panel shows that in the non-dispersive ( $y$ ) plane. The first-order transfer-matrix elements of the high-resolution mode are listed Table 6-3.

In this first-order ion-optical design, the following has been considered:

- Quadrupole QS1A expands the beam in the dispersive direction to increase the magnetic flux enclosed by the rays passing through DS1 to achieve the required resolving power,

while it focuses the beam in the non-dispersive direction. QS2B, with a large bore size, having the opposite polarity to QS1A, optimize the transmission through the dipole DS1.

- DS1 is rectangular in shape and is installed so that particles enter DS1 perpendicular to its pole face, which facilitates the implementation of ancillary detectors. The exit pole face makes an angle of  $35^\circ$  with the central trajectory, which causes the defocusing (focusing) effect in the dispersive (non-dispersive) direction. This obviates an additional quadrupole magnet.
- Quadrupoles QS3B and QS4B must capture the particles exiting from DS1 and direct them through the rest of the Spectrometer Section. These quadrupoles must be placed sufficiently far downstream of DS1 to ensure they do not interfere with the path of neutrons for the neutron invariant-mass mode.
- Since the two dipole magnets bend the beam in the opposite directions, an intermediate focus at FS1 is needed to accumulate dispersions.
- At the intermediate focus FS1, after a flight path of 16.1 m from the FS0, point-to-point focusing  $[(x|x')=0]$  is achieved in the dispersive plane. The ion optics is tuned to optimize the transmission: the angular dispersion vanishes  $[(x'\delta) = 0]$  in the dispersive plane, and parallel-to-point  $[(y|y) = 0]$  and point-to-parallel  $[(y'|y') = 0]$  imaging conditions are achieved in the non-dispersive plane. The point-to-point focus in the dispersive plane allows for efficient beam rejection at this location.
- Quadrupoles QS5A and QS6A transport the beam particles to DS2. These have smaller bore sizes than QS3B and QS4B, sufficient to achieve the required momentum acceptance of  $\pm 2.5\%$ . In the horizontal plane, the beam is expanded in DS2 to gain resolving power, while in the vertical direction a focus is created inside of DS2 to optimize the transmission.
- DS2 is a sector magnet with pole-face rotations of  $20^\circ$  at the entrance and the exit (symmetric with respect to the center). The pole-face rotations are such that they provide horizontal focusing and vertical defocusing, shaping the beam envelope toward the final focus FS2.
- At FS2, after a flight path of 31.7 m from FS0, point-to-point focusing  $[(x|x')=0]$  is achieved in the dispersive plane. In the non-dispersive plane, parallel-to-point  $[(y|y)=0]$  imaging is achieved to provide the highest accuracy in the reconstruction of the vertical component of the scattering angle after the target.
- The intermediate focus FS1 can be utilized to intercept the unreacted beam and prevent it from entering the final focus FS2. It can also provide additional beam tracking.
- The quadrupole field strengths at warm bore will not exceed 2.5 Tesla at the maximum magnetic rigidity of 8 Tm.





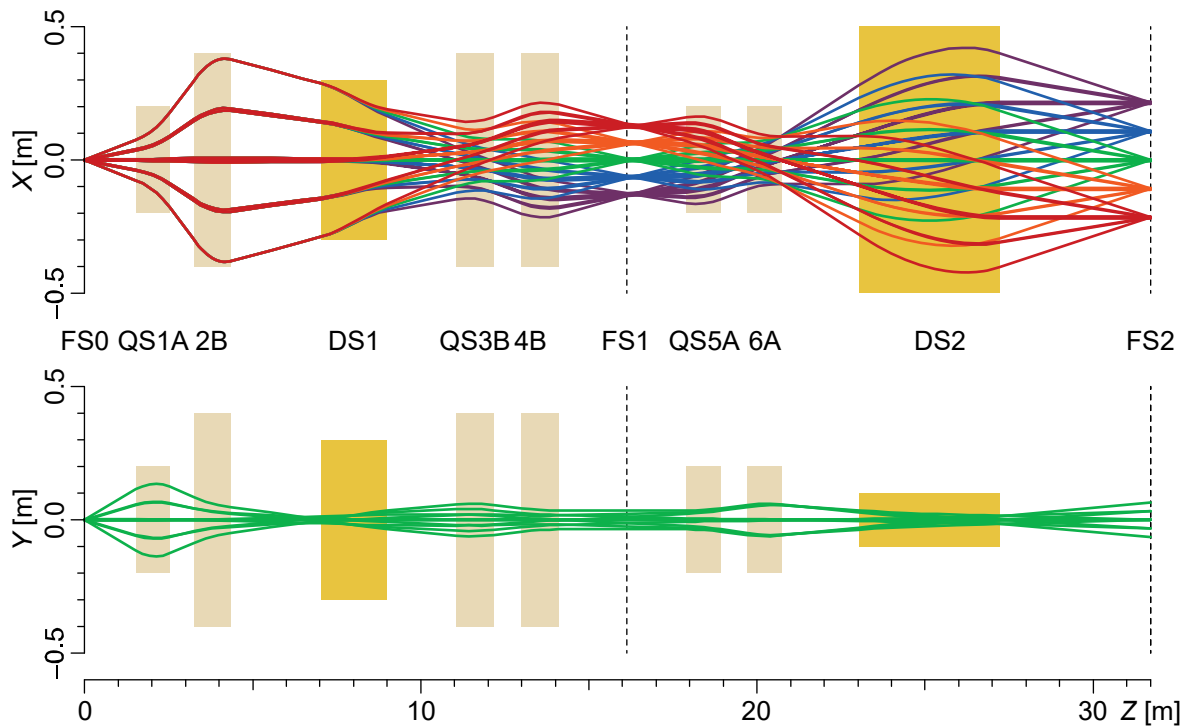


Figure 6-3 Trajectory plots for the high-resolution mode of the Spectrometer Section in the dispersive (top) and the non-dispersive (bottom) planes in first order. The ensemble of trajectories correspond to those within the acceptance limits defined by the scientific requirements, i.e.,  $\delta x'_{max} = 50$  mrad,  $\delta y'_{max} = 75$  mrad, and  $\delta p_{max}/p = 2.5\%$ . Position divergences at FS0 of  $\delta x_{max} = \delta y_{max} = 3$  mm are used for visualization purposes. As in the previous figures, the heights of the orange and light-brown boxes represent aperture sizes of the dipole and quadrupole magnets, respectively.

Table 6-3 First-order transfer-matrix elements for the high-resolution mode.

		FS1	FS2
$(x x)$	$= R_{11}$	-1.75	1.21
$(x x')$ [m/rad]	$= R_{12}$	0.11	0.00
$(x' x)$ [rad/m]	$= R_{21}$	-0.05	0.00
$(x' x')$	$= R_{22}$	-0.57	0.83
$(x \delta)$ [m]	$= R_{16}$	-5.18	8.61
$(x' \delta)$ [rad]	$= R_{26}$	0.31	0.00
$(y y)$	$= R_{33}$	3.84	0.00
$(y y')$ [m/rad]	$= R_{34}$	-0.47	0.87
$(y' y)$ [rad/m]	$= R_{43}$	2.12	-1.15
$(y' y')$	$= R_{44}$	0.00	0.15

### 6.3.1.2 Higher-order ion optics

Modeling and understanding the contributions from the higher-order aberrations is particularly important for the Spectrometer Section because of the large solid-angle and momentum acceptances.

Ion-optical calculations were performed up to 5<sup>th</sup> order and effects of higher-order aberrations were investigated, as well as the ability to correct for aberrations by hardware using sextupole and octupole coils. In COSY calculations, the magnetic field profiles from magnetostatic analyses in Maxwell were used (the calculated field profiles will be replaced by those from actual field mapping, as has been done for the HTBL quadrupoles, when the magnets are built). The magnetostatic analyses were performed so that the excitations of the magnets would cover the entire operation range of the HRS, namely from 4 to 8 Tm. The features such as the field shape variation (field length and fringe fields) as a function of excitation have been parametrized and included in the ion-optical calculations. The results are shown in Figure 6-4. The higher-order aberrations cause the trajectories to become distorted [see Figure 6-4(a)], although the acceptance losses are relatively small. These losses can be prevented by using the nested sextupole and octupole coils [Figure 6-4(b)].





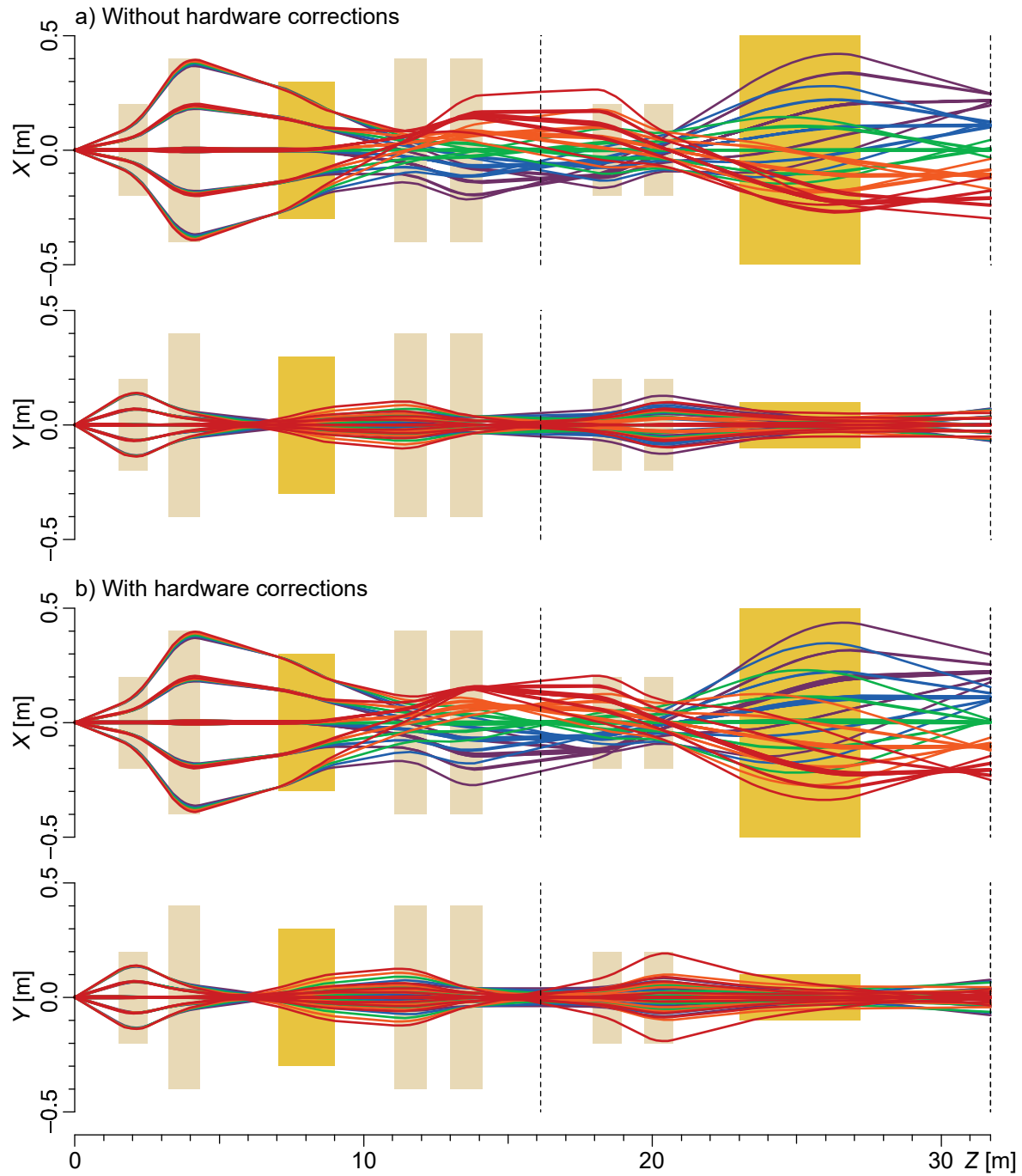


Figure 6-4 Same as Figure 6-3 but in 5<sup>th</sup> order. Those with and without higher-order corrections are compared.



### 6.3.1.3 *Use of hardware and software corrections for higher-order aberrations*

The hardware corrections provided by the sextupole and octupole coils by themselves are not intended to correct for all the higher-order aberrations for the Spectrometer Section. For example, the focal planes at FS1 and FS2 are tilted due to the large second-order matrix elements ( $x|x'\delta$ ), even after the hardware corrections are applied. Methods aimed at reducing the ( $x|x'\delta$ ) term had detrimental effects on other terms and hence not pursued. Therefore, in the analysis of data taken with the HRS, software corrections based on the inverse raytrace matrix will be employed. Such a technique has been successfully used for the S800 Spectrometer [BAZ03,BER93] at NSCL. This is also true for the neutron invariant-mass mode described in Section 6.3.1.6.

### 6.3.1.4 *Angular and momentum resolutions*

The angular and momentum resolutions were evaluated by means of Monte-Carlo simulations, in a similar way to what was done for the HTBL. Beam particles emitted from FS0 were transported through FS2 via the 5<sup>th</sup>-order transfer maps calculated in COSY, using the magnetic field profiles from ANSYS Maxwell analyses. At the locations of the tracking detectors, some disturbance was added to emulate the finite detector resolutions and the effect of straggling in the detector materials. Subsequently, the particles were traced backward to FS0 via the 5<sup>th</sup>-order inverse maps to deduce the scattering angle and the momentum, which were then compared with the original angle and the momentum.

Figure 6-5 shows the angular and momentum resolutions, calculated as the difference between the reconstructed and initial angle/momentum. For the initial beam-spot size at FS0, which was estimated for the <sup>40</sup>Mg beam, 3.0 mm ( $x$ )  $\times$  8.2 mm ( $y$ ) in FWHM, was used. The angular resolution has an FWHM of 2.5 mrad and the momentum resolution has an FWHM of 1/2350, meeting the requirements of 5 mrad and 1/1500, respectively.



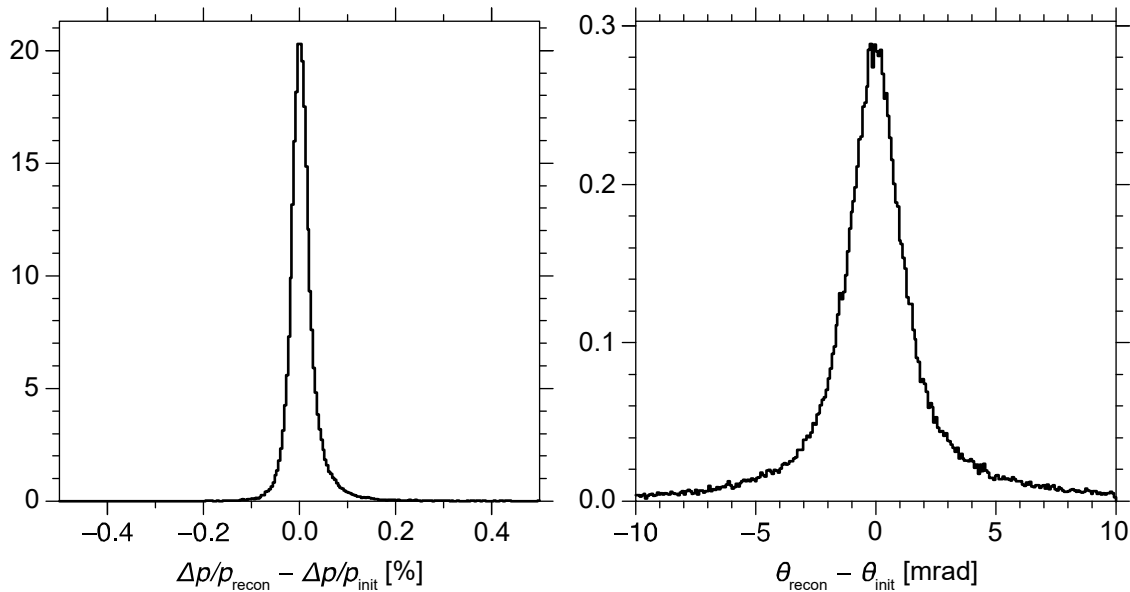


Figure 6-5 Angular and momentum resolutions in the high-resolution mode calculated as the difference between the reconstructed and initial angle/momentum in trajectory-reconstruction simulations using COSY-calculated maps including up to 5<sup>th</sup> order.

### 6.3.1.5 Angular and momentum acceptances

The angular and momentum acceptances were evaluated by means of Monte-Carlo simulations in LISE<sup>++</sup> [BAZ02,TAR08,TAR16] with COSY-calculated fifth-order transfer matrices loaded, in the same way as described in Section 5.6.

The results are shown in Figure 6-6. Note that the dimensions of the detectors allow for the detection of particles outside the required momentum range of  $\pm 2.5\%$ . However, the magnet apertures are primarily constrained by the need to meet the angular acceptance requirements. Consequently, by using focal plane detectors that cover the apertures in the system, a larger momentum acceptance can be achieved (albeit with a dependence on angle). In other words, the detectors do not restrict the momentum acceptance afforded by the magnets, and their large apertures are fully utilized.

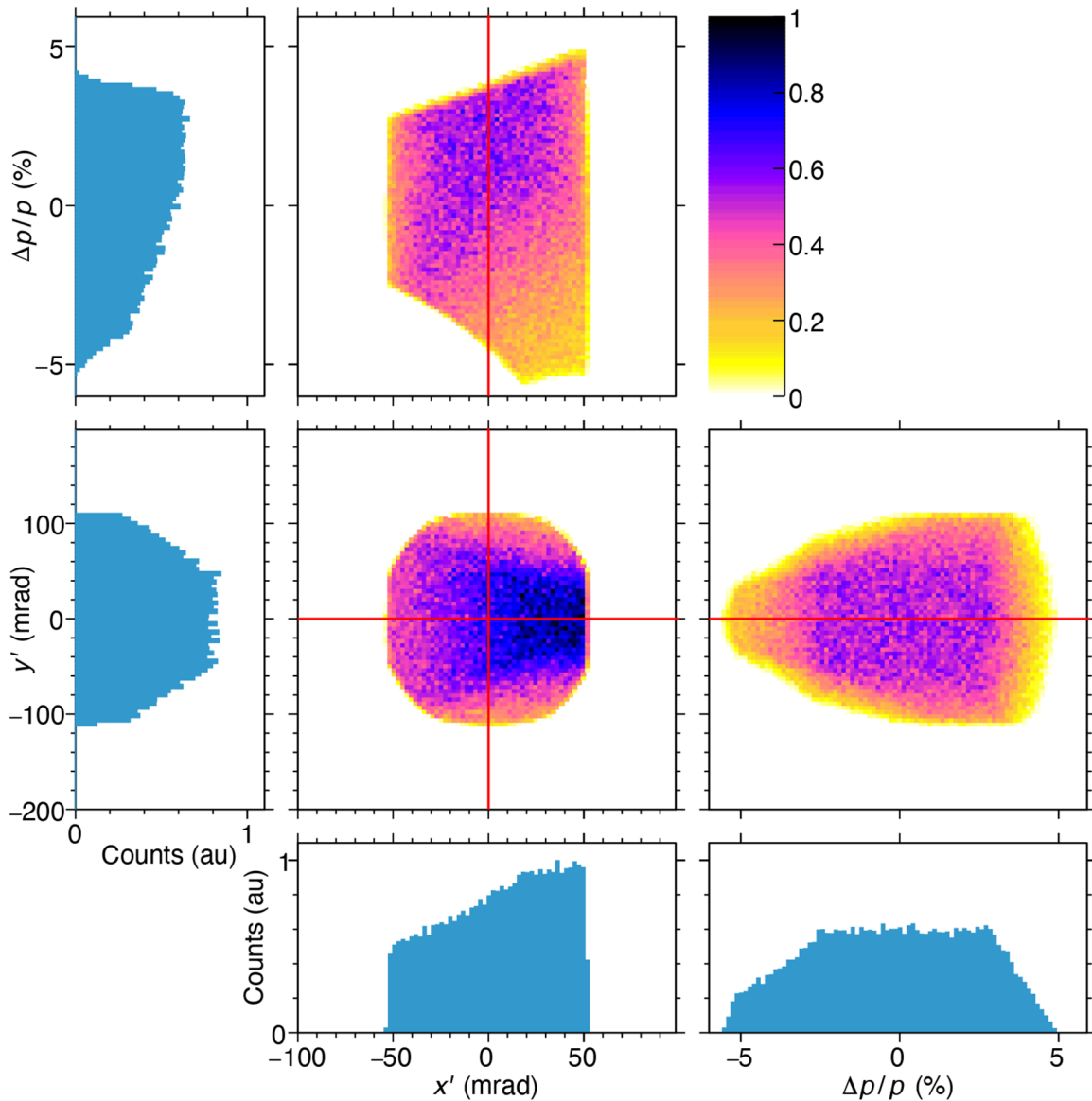


Figure 6-6 Angular and momentum acceptances for the high-resolution mode represented in the same way as in Figure 5-11.

### 6.3.1.6 Ion-optical solutions at various magnetic rigidities

Ion-optical calculations at different magnetic rigidities were also performed. The variation in magnetic field profiles as a function of excitation has been characterized in Maxwell with analysis at various excitations covering the entire dynamic range of operation, namely from 4 to 8 Tm. Figure 6-7 shows the quadrupole components of the magnetic field distributions  $b_{20}(z)$  of QSA and QSB of the Spectrometer Section for various excitations. Similar analyses have been done for the

dipoles DS1 and DS2. The effective field length and the Enge-function coefficients are extracted for each profile. In the fitting procedure, the field length is interpolated, while the nearest neighbors are used for the Enge-function coefficients to model the field profiles of these magnets at the magnetic rigidity of interest.

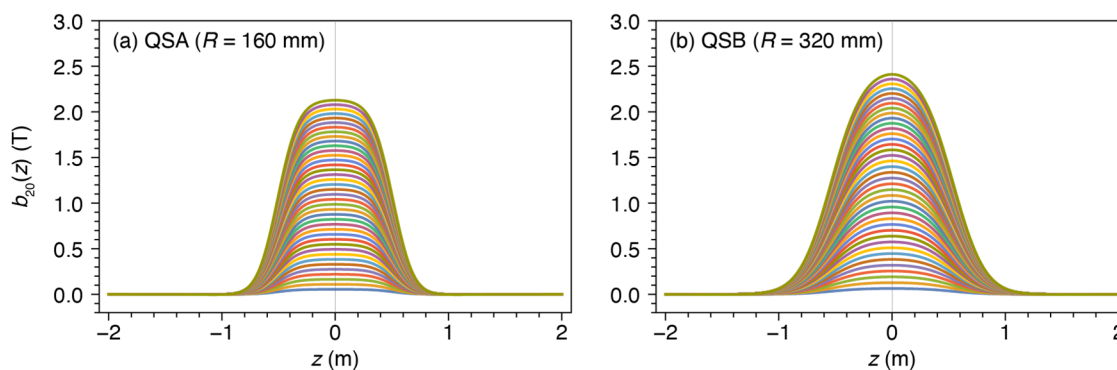


Figure 6-7 Quadrupole components of the magnetic fields of the quadrupole magnets of the Spectrometer Section, (a) QSA and (b) QSB, calculated in Maxwell at the radii 160 mm and 320 mm, respectively (80% of the warm-bore radii). Different curves (40 each) correspond to different excitations covering the entire dynamic ranges of operation

Fifth-order ion-optical calculation results with aberration corrections using sextupoles and octupoles at different magnetic rigidities, 4 Tm, 6 Tm, and 8 Tm are shown as trajectory plots in Figure 6-8. Table 6-4 lists key first-order transfer-matrix elements. Although the values of the key matrix element do change slightly as a function of rigidity, as indicated by the maximum deviation  $\Delta_{max}$  (%) in Table 6-4, all the features of the ion-optical design, such as the magnifications and the dispersion, are achieved.

Table 6-4 Key first-order transfer-matrix elements at the final focus (FS2) of the Spectrometer Section for different magnetic rigidities. The last row shows the ratio of the dispersion to the magnification, the measure of the resolving power of the spectrometer.  $\Delta_{max}$  indicates the maximum deviation (in %) between the matrix elements for different rigidities.

Matrix elements	4 Tm	6 Tm	8 Tm	$\Delta_{max}$ (%)
$\langle x x \rangle$	1.22	1.21	1.21	0.8%
$\langle x \delta \rangle$	8.70	8.63	8.61	1.0%
$\langle x \delta \rangle / \langle x x \rangle$	7.10	7.12	7.13	0.4%

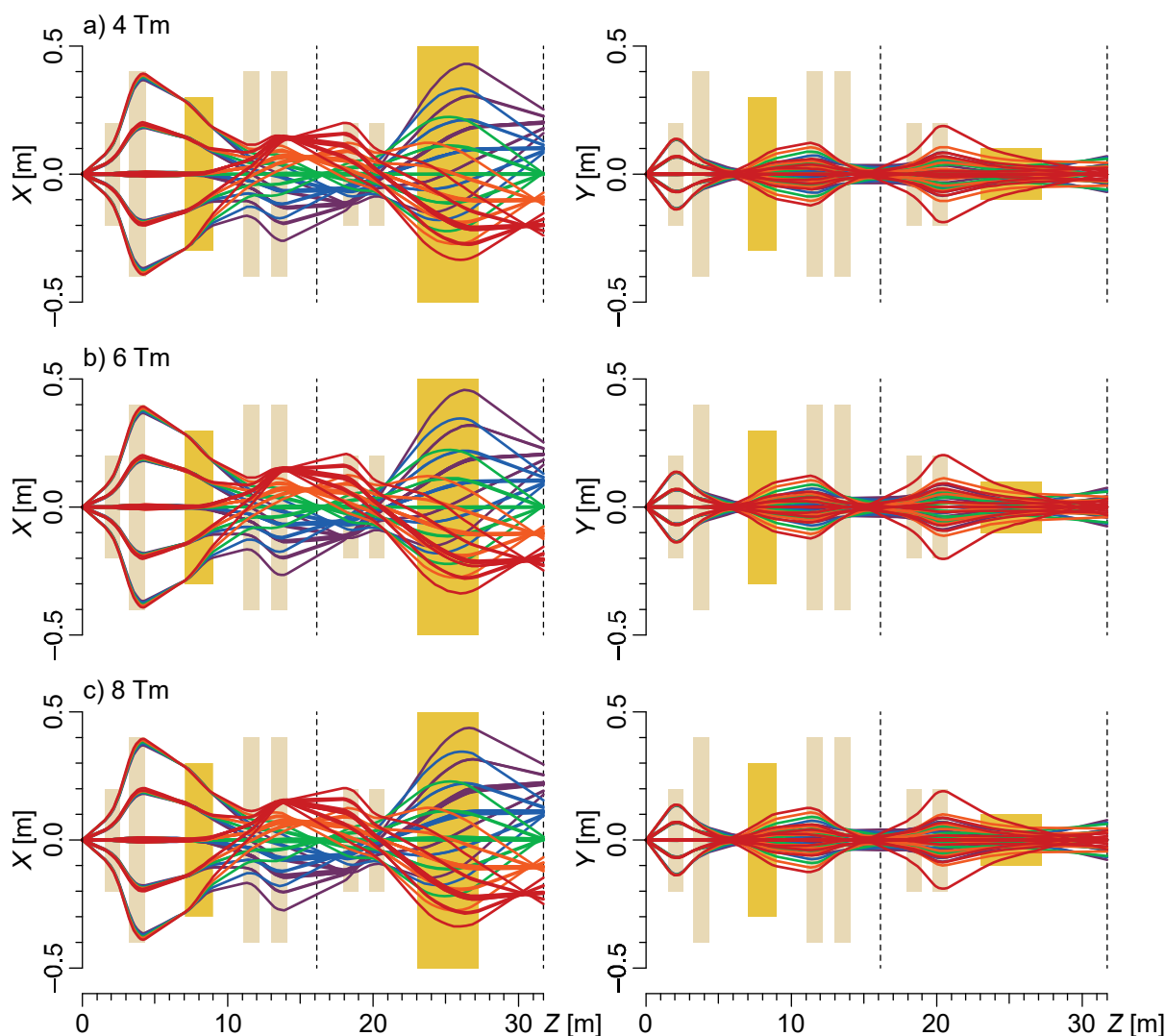


Figure 6-8 Fifth-order ion-optical plots for the high-resolution mode of the Spectrometer Section at different magnetic rigidities, (a) 4 Tm, (b) 6 Tm, and (c) 8 Tm with corrections with sextupoles and octupoles. Trajectories are shown for  $\delta x = \pm 3.0$  mm,  $\delta x' = \pm 50$  mrad,  $\delta y = \pm 3.0$  mm,  $\delta y' = \pm 75$  mrad, and  $\delta p/p = -2.5, -1.25, 0, 1.25, 2.5\%$  denoted by different colors. The projections onto the dispersive (x) and non-dispersive (y) planes are shown in left and right columns, respectively. The yellow boxes denote the dipole magnets (DS1 and DS2), and the light-brown boxes the quadrupole magnets.



### 6.3.1.7 Blocking of unreacted beams

As discussed in Section 5.3.3, the use of dispersion-matched beam transport is useful for unreacted-beam rejection because the beam will be well localized at the final achromatic focus.

Figure 6-9 shows a comparison of the beam images at the final focus (FS2) between the dispersion-matched and achromatic beam transport for the one-neutron-knockout reaction from a  $^{204}\text{Pt}$  beam as an example. It is seen that the unreacted beam is narrower when dispersion-matched, intruding less into the region of the focal plane where the reaction products of interest,  $^{203}\text{Pt}$ , are located, compared to when the beam is delivered in the achromatic mode.

The blocking of the beam has to be optimized on an experiment-by-experiment basis, but generally, the dispersion matching enables a more efficient blocking of the beam, without having to obstruct the detection of the desired reaction products.

### 6.3.1.8 Establishing ion optics

The aberrations in the ion-optics will lead to a rather complex trajectory reconstruction, complicated further by possible dependence of the ion-optics on the  $B\rho$  setting. The scope of the HRS includes tracking detectors at FS0, which will provide event-by-event tracking information. Such information will be used to verify the ion optics.

It is noted that at other magnetic spectrometers, such as the Grand Raiden spectrometer at RCNP, Osaka, sieve slits (collimators) are used at the location immediately downstream of the reaction target to define well-known scattering angles. A similar technique is also used at J-Lab. This provides known fiducial rays across the acceptance, propagating to the tracking detectors further downstream. This provides the similar information as tracking detectors at the target.



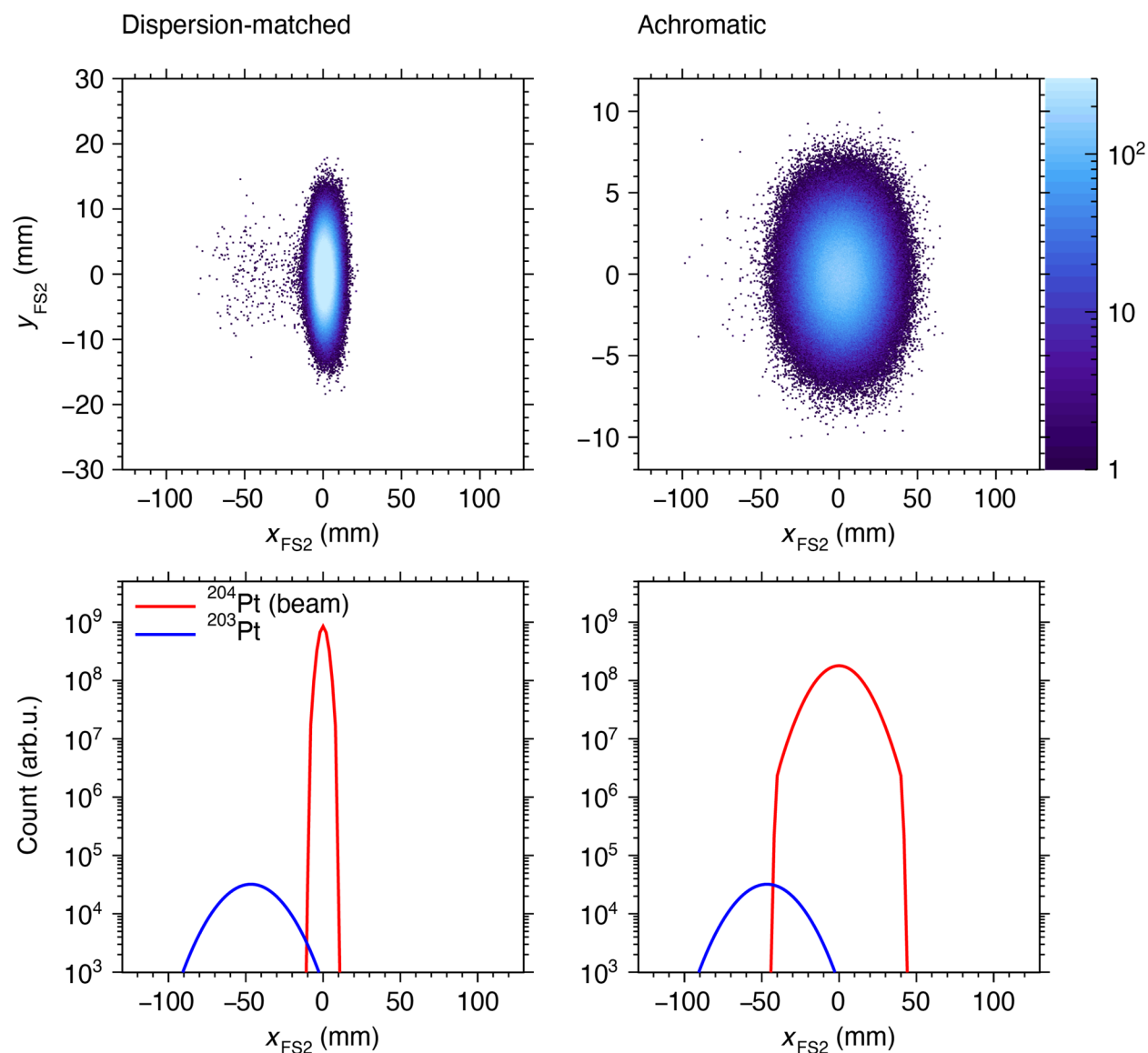


Figure 6-9 Example of the images at FS2 of the unreacted beam and the reaction product for the one-neutron-knockout reaction from  $^{204}\text{Pt}$  at 100 MeV/u with a 100-mg/cm<sup>2</sup>-thick Be target. The top panels show the xy images (in 5<sup>th</sup> order) and the bottom panels show their x projections (in 1<sup>st</sup> order). The left panels are those with the HTBL in the dispersion-matched beam-transport mode, and the right panels are for the achromatic mode. The simulations were done in LISE<sup>++</sup> with the transfer matrices calculated in COSY included.

### 6.3.2 Neutron invariant-mass mode

The neutron invariant-mass mode is optimized to operate in combination with the MoNA-LISA neutron-detector array, which is placed at forward scattering angles. Because the neutrons emitted in a cone around zero degrees must be able to reach MoNA-LISA, it is required that the sweeper dipole magnet DS1 have a large vertical gap (In addition, the insertion of a TPC in DS1 for certain experimental also necessitates a large gap.) The optimal use of this large gap size can be made by placing the reaction target as close as possible to DS1. Therefore, rather than at FS0, it is highly preferable to place the target in between QS2B and DS1, denoted FS0' in Figure 6-10. As mentioned in Section 5.3.2, QS1A and QS2B then serve as extensions of the HTBL and provide the proper beam conditions at FS0'.

In this mode, the final focal plane will be placed at FS1 without using QS5A, QS6A, and DS2. In such a configuration the functional requirements for the momentum resolving power and maximum mass of the particles to be analyzed can be met. The quadrupoles QS3B and QS4B are used to optimize the transport after DS1 at the focal plane FS1. As mentioned in Section 6.3.1, the location of QS3B and the bend angle provided by DS1 are critical parameters, as it is important to ensure that QS3B does not interfere with the path of the neutrons. Since the ion optics enabling large solid-angle and momentum acceptances is designed for the target position immediately in front of DS1, solutions all the way to FS2 come with much reduced acceptances and with compromised ion-optical properties. However, as noted above, the functional requirements for the momentum resolving power and the flight-path length are nonetheless already satisfied by the ion-optical solution up to FS1. Neutron invariant-mass spectroscopy experiments at the HRS require a neutron flight path up to 15 m from the reaction target to MoNA-LISA detector array. This can be accommodated as shown in the layout in Figure 6-10.

The exact location of the reaction target is in principle flexible and can be adjusted depending on the needs of each experiment. In the ion-optical calculations shown here, we assumed that the target is placed at the center of GRETA installed between QS2B and DS1. It should be noted that, when GRETA is installed at this location, 10 of its 30 Quad detector modules on the forward and aft rings will be unmounted (See Section 4.3.1.3). The distance between the flanges of QS2B and DS1 is 184 cm, which is necessary to provide for the 180 cm width of GRETA and an additional 4 cm to provide clearance for installing and removing GRETA. A technically risky and costly approach of having QS1A and QS2B movable on a rail was evaluated, but several low cost, low risk modifications not involving the movable quadrupoles were implemented so that the functional requirements are met.





Figure 6-10 Layout of the neutron invariant-mass mode of the Spectrometer Section. The target station FS0' is located between QS2B and DS1.

### 6.3.2.1 First-order ion optics

The first-order ion-optical plots are shown in Figure 6-11. The downstream edge of DS1 has a defocusing effect on the rays in the dispersive plane, while the same edge provides a focusing effect in the non-dispersive plane, which helps to reduce the magnitude of the vertical envelope after the dipole. To sustain a dispersive-angular acceptance of  $\pm 70$  mrad over the required momentum acceptance, a large-aperture quadrupole QS3B is necessary. Since this QS3B expands the vertical envelope, another large-aperture quadrupole QS4B is necessary to maintain a sizable non-dispersive-angular acceptance of  $\pm 36$  mrad. Note that the aperture sizes of these quadrupoles are only needed for this mode to afford the required solid-angle acceptance, but they are not fully utilized in the high-resolution mode. These quadrupoles extend the flight path of charged particles, enabling a high mass resolving power without the need of a very large focal-plane detector system.

Table 6-5 lists the first-order transfer-matrix elements. A point-to-point imaging in the dispersive plane  $[(x|x') = 0]$ , in combination with a parallel-to-point imaging in the non-dispersive plane  $[(y|y') = 0]$  with a large value for  $(y|y') = 2.54$  is advantageous for achieving high accuracy in the reconstruction of the vertical component of the scattering angle.

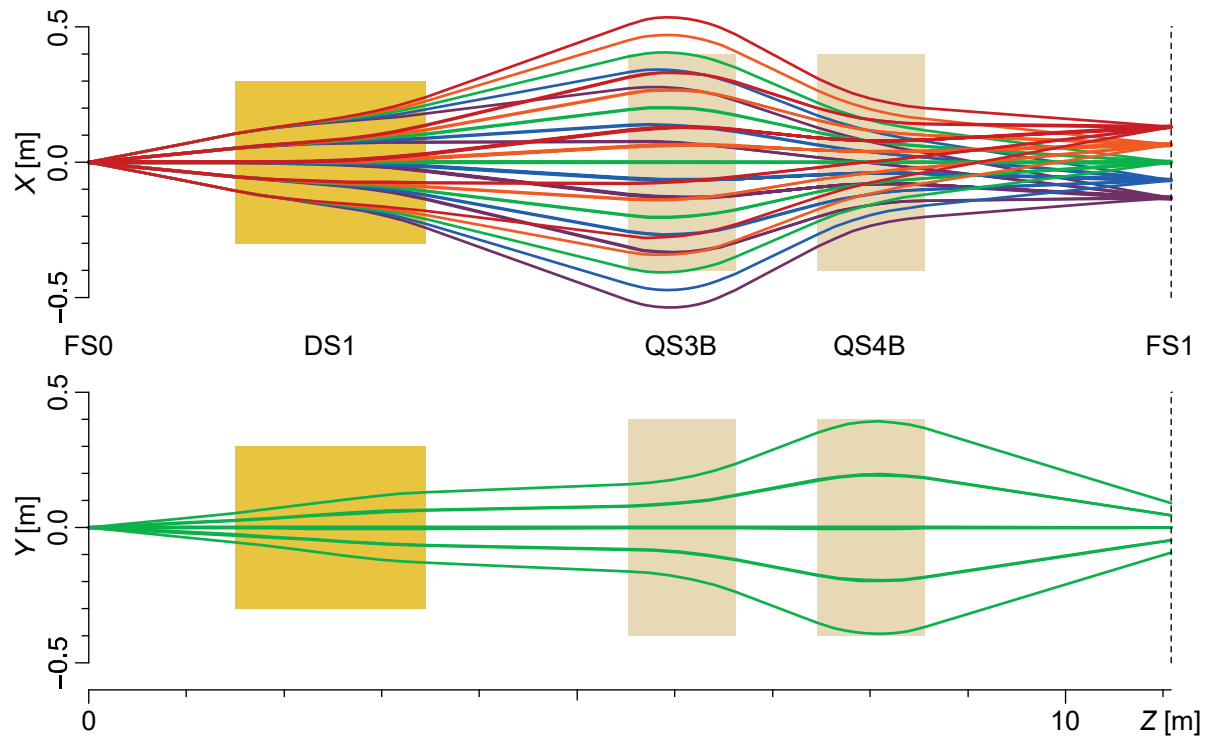


Figure 6-11 Same as Figure 6-3, but for the neutron invariant-mass mode. The ensemble of trajectories correspond to those within the acceptance limits defined by the scientific requirements, i.e.,  $\delta x'_{max} = 70$  mrad,  $\delta y'_{max} = 36$  mrad, and  $\delta p_{max}/p = 5\%$ . Position divergences at FS0' of  $\delta x_{max} = \delta y_{max} = 3$  mm are used to depict the trajectories.

Table 6-5 First-order transfer-matrix elements for the neutron invariant-mass mode.

		FS1
$(x x)$	$= R_{11}$	-1.49
$(x x')$ [m/rad]	$= R_{12}$	0.00
$(x' x)$ [rad/m]	$= R_{21}$	-0.48
$(x' x')$	$= R_{22}$	-0.67
$(x \delta)$ [m]	$= R_{16}$	-2.19
$(x' \delta)$ [rad]	$= R_{26}$	-0.32
$(y y)$	$= R_{33}$	0.00
$(y y')$ [m/rad]	$= R_{34}$	2.54
$(y' y)$ [rad/m]	$= R_{43}$	-0.39
$(y' y')$	$= R_{44}$	-3.04

### 6.3.2.2 Higher-order ion optics

Higher-order ion-optical simulations were also performed for the neutron invariant-mass mode. Figure 6-15 shows the results of these simulations. Panel a) shows the angular and momentum acceptances without the use of sextupole and octupole coils in the QS3B and QS4B magnets. Since the first magnetic element is a dipole in this mode, the momentum acceptance strongly depends on the angle in the dispersive plane, although the acceptance requirements are met even without the use of the higher-order multipole magnets. In panel b) the sextupole and octupole strengths in QS3B and QS4B are optimized and the acceptances are improved and less distorted. Similar to the high-resolution mode, the hardware corrections provided by the sextupole and octupole coils by themselves are not intended to correct for the higher-order aberrations in the focal plane FS1. Therefore, in the analysis of data taken in this mode, software corrections based on the inverse raytrace matrix will be also employed.





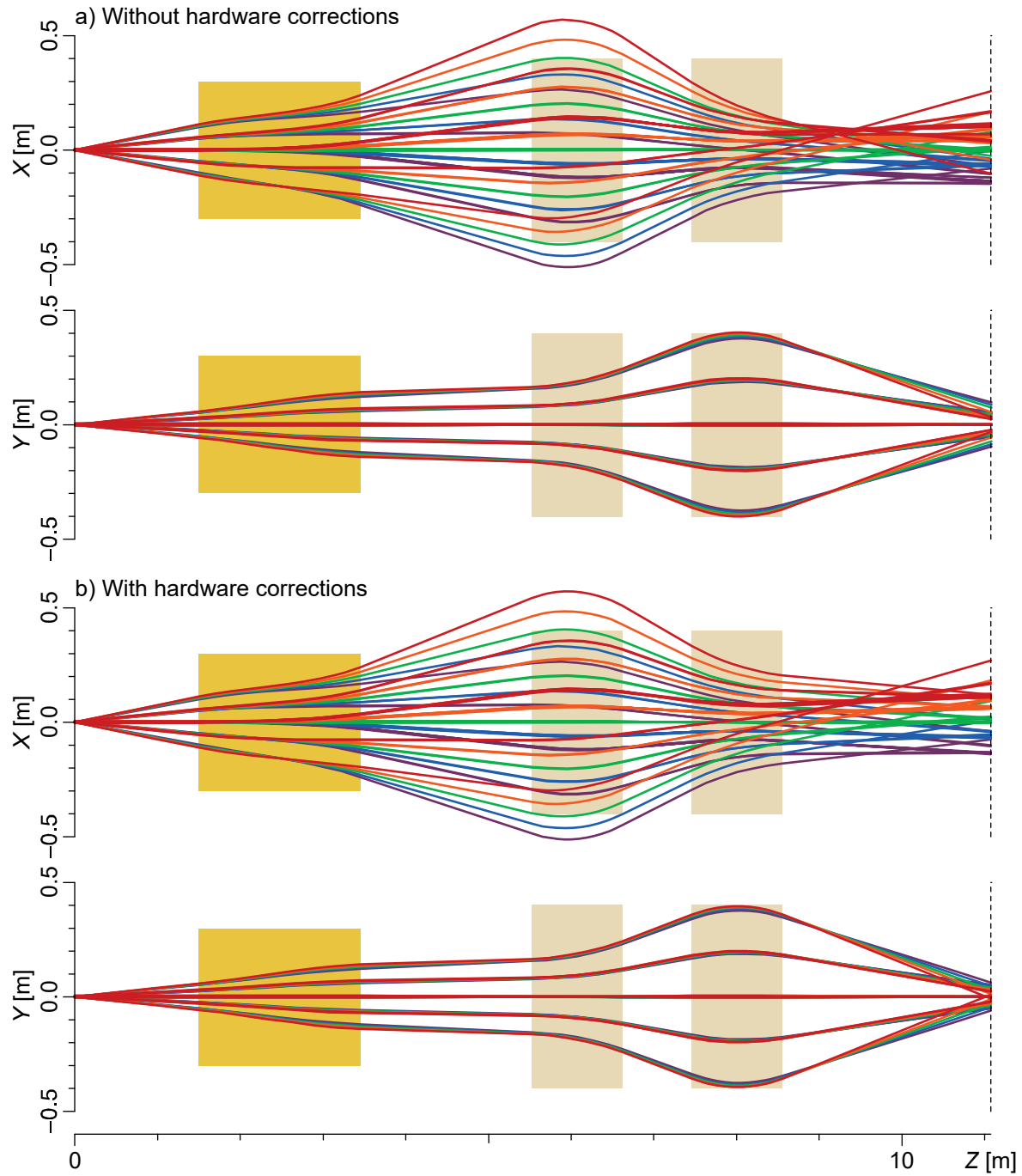


Figure 6-12. Same as Figure 6-11 but in 5<sup>th</sup> order. Those with and without higher-order corrections are compared.

### 6.3.2.3 Angular and momentum resolutions

Higher-order ion-optical simulations were also performed for the neutron invariant-mass mode. The angular and momentum resolutions were evaluated by means of Monte-Carlo simulations. For the initial beam-spot size at FS0', estimated for the  $^{40}\text{Mg}$  beam, dimensions of 7.8 mm ( $x$ )  $\times$  25.4 mm ( $y$ ) in FWHM were used. Figure 6-13 shows the angular and momentum resolutions, calculated as the difference between the reconstructed and initial angle/momentum. The angular resolution is 3.3 mrad (FWHM), which meets the requirement of 5 mrad. On the other hand, without tracking of the incoming beam particles, the relative momentum resolution has an FWHM of 1/226, which is less than the required 1/290. This means that without beam tracking, the mass separation between neighboring isotopes is better than 4 standard deviations up to mass number 113, rather than 132. The main reason for this is the large beam spot at FS0', especially in the dispersive plane ( $x$ ). Note that for the inverse mapping, it is assumed that the particle is emitted at the object plane at  $x = 0$ . To meet the requirement of the momentum resolving power, it is necessary to perform tracking of the beam particles in the object plane. In Figure 6-13, the momentum resolving power that is achievable with beam tracking is also shown, and it is 1/778, which significantly exceeds the requirement. The angular resolution is also improved, 2.7 mrad (FWHM) as opposed to 3.3 mrad (FWHM).

Neutron invariant-mass spectroscopy experiments at the HRS can be performed with and without tracking detectors at FS0' and that decision must be made on the basis of a number of factors for each experiment. In Figure 6-14, the impact of using tracking detectors at FS0' are presented, based on Monte-Carlo simulation of an unbound nucleus with  $A=40$ . In the simulations, the properties of the MONA-LISA neutron detector array that impact the resolution of the invariant-mass reconstruction were kept fixed. Simulations were performed for two distances between the location of the target (FS0') and the MoNA-LISA detector array: 8 m and 15 m. Simulations were performed for a perfect spectrometer, the HRS with the use of tracking detectors at FS0', and the HRS without the use of tracking at FS0'. Although the properties of the MONA-LISA detectors system and the distance between FS0' and MONA-LISA are the dominant factors in determining the resolution that can be achieved, it is clear that with tracking detectors at FS0' a significant improvement of the invariant-mass resolution can be achieved, close to the resolutions that would be achieved with a perfect spectrometer. The simulations were also carried out for an  $A=132$  unbound system and the results were nearly identical.



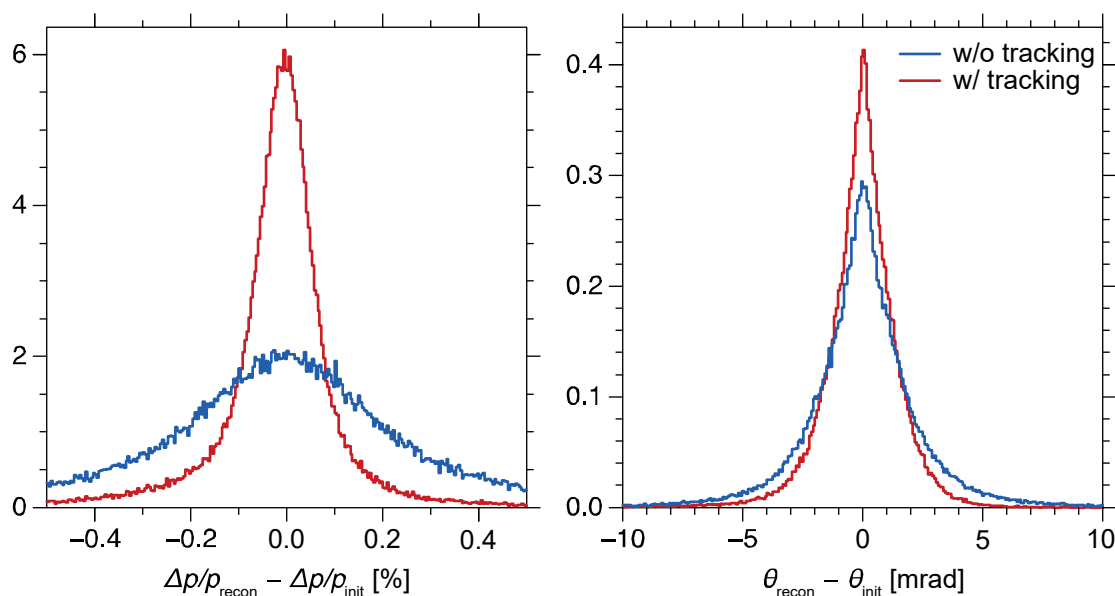


Figure 6-13 Angular and momentum resolutions in the neutron invariant-mass mode. Those without (blue) and with (red) beam tracking are compared.

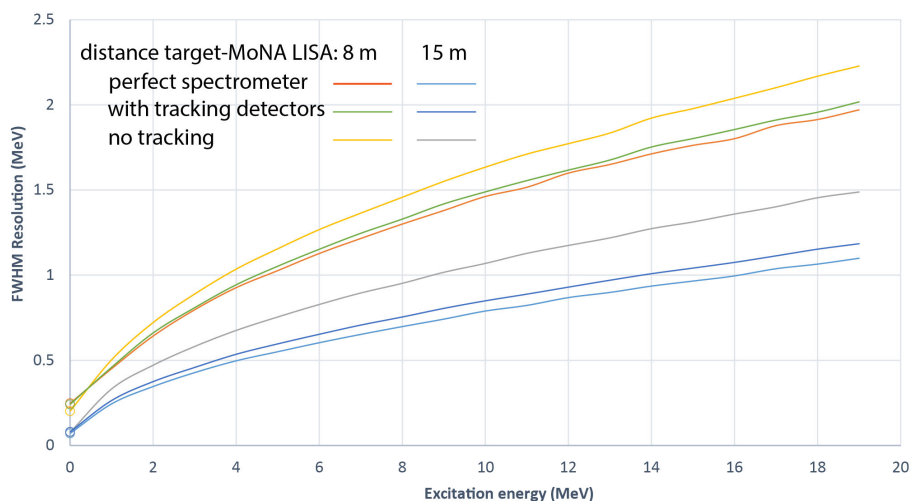


Figure 6-14 Resolution (FWHM) that can be achieved in neutron invariant-mass spectroscopy as a function of excitation energy in the neutron-unbound system based on Monte-Carlo simulations. For two distances between the location of the target and the MoNA-LISA detector array (8 m and 15 m), resolutions are plotted for a perfect spectrometer, operation of the HRS with tracking detectors at FS0', and operation of the HRS with tracking detectors. The properties of the MONA-LISA array were kept fixed and a unbound system with  $A=40$  was used. The results for an  $A=132$  are very similar.

### 6.3.2.4 Angular and momentum acceptances

Figure 6-15 shows the angular and momentum acceptances. Since the first magnetic element is a dipole in this mode, the momentum acceptance strongly depends on the angle in the dispersive plane, although the acceptance requirements are met even without the use of the higher-order multipole magnets.

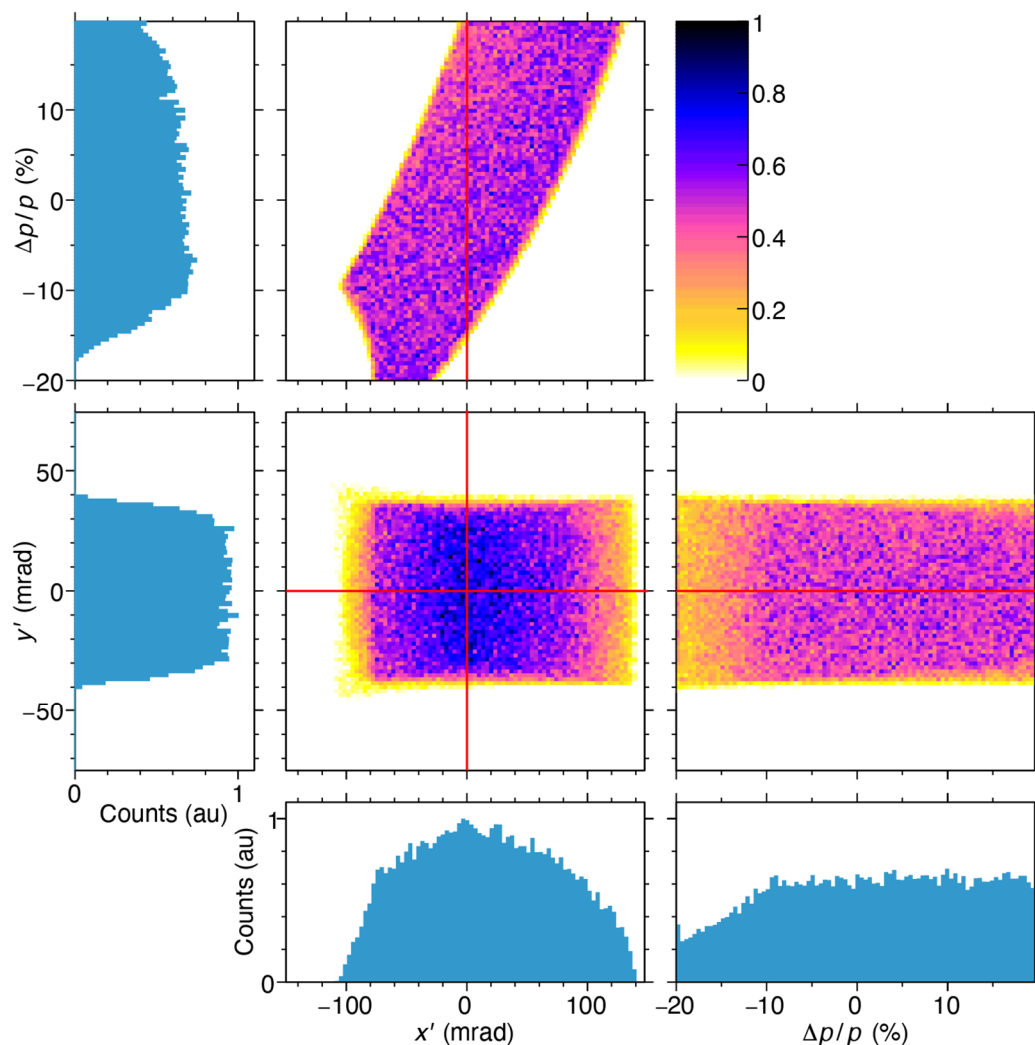


Figure 6-15 Angular and momentum acceptances for the neutron invariant-mass mode.

### 6.3.3 ToF- $B\rho$ mass-measurement mode

The ToF- $B\rho$  mass-measurement mode serves only that particular type of experiment (see Section 4.3.1.5). A very long flight path (113 m) is created by combining the ARIS Fragment Separator

(40.14 m), the HTBL (41.40 m), and the Spectrometer Section (31.72 m) of the HRS, as shown in Figure 6-16.

The Spectrometer Section is operated in the same manner as for the high-resolution mode described in Section 6.3.1 and the HTBL is operated in dispersion-matched beam-transport mode described in Section 5.3.3. No target is placed at FS0. The long flight path is important for reducing the relative uncertainty of the ToF measurement. Because of the use of the dispersion-matched beam-transport mode in the HTBL, the lateral and angular dispersions are matched to those of the Spectrometer Section, and the full beam transport to FS2 is point-to-point in the dispersive direction [ $(x|x') = 0$ ] and achromatic [ $(x|\delta) = (x'|\delta) = 0$ ]. This ion-optical beam transport is shown in first order in Figure 6-17. Only the transport through the Spectrometer Section is shown, since the transport through the HTBL is identical to that of Figure 5-5, and only the transport in the dispersive plane is shown, since the transport in the non-dispersive plane is identical to that of Figure 6-3. Due to these ion-optical properties, the position and angle at FS2 are independent of the momentum of the particles and the spectrometer's highest resolution can be obtained. The position at FS0 is measured with high precision (0.3 mm FWHM) by using a dedicated tracking detector to determine the rigidity of the isotopes on an event-by-event basis. Timing measurements with small, dedicated timing detectors are performed to determine the ToF from the beginning of the ARIS Fragment Separator to FS2 with very high precision (30 ps).



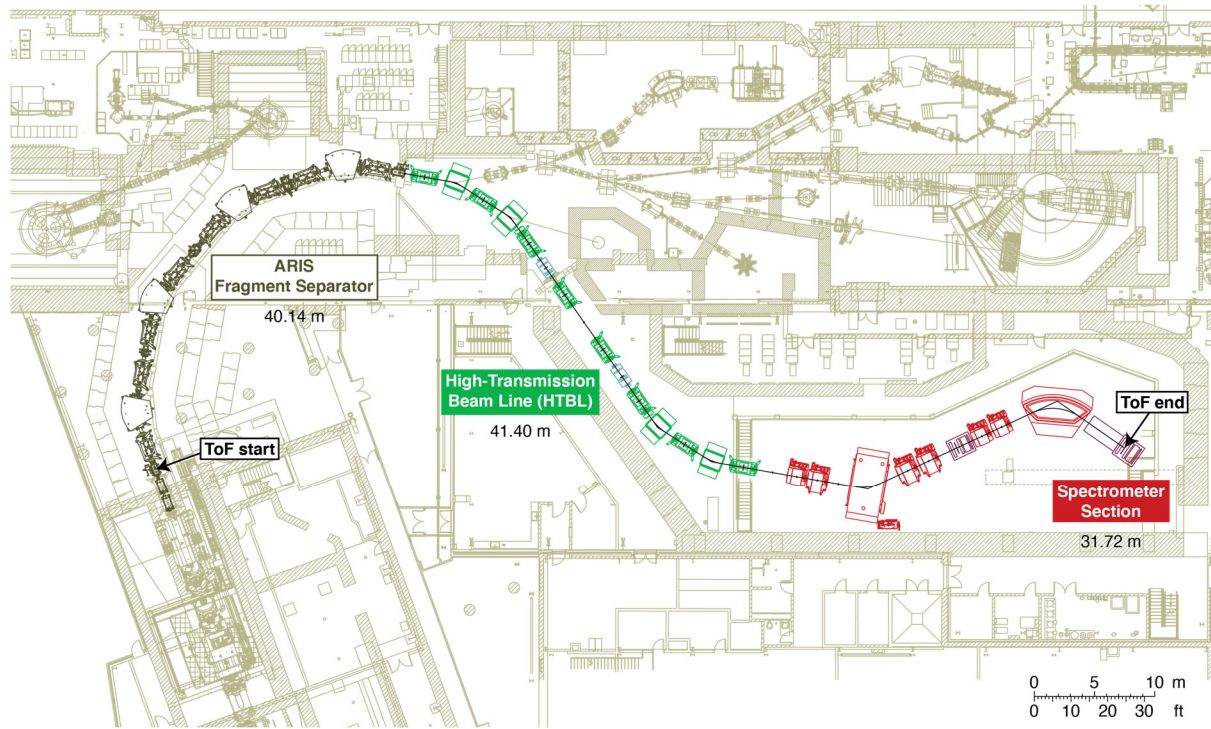


Figure 6-16 Layout of the HTBL and the Spectrometer Section of the HRS, together with the ARIS Fragment Separator for the ToF- $B\rho$  mass-measurement mode utilizing a 113-meter-long flight path.



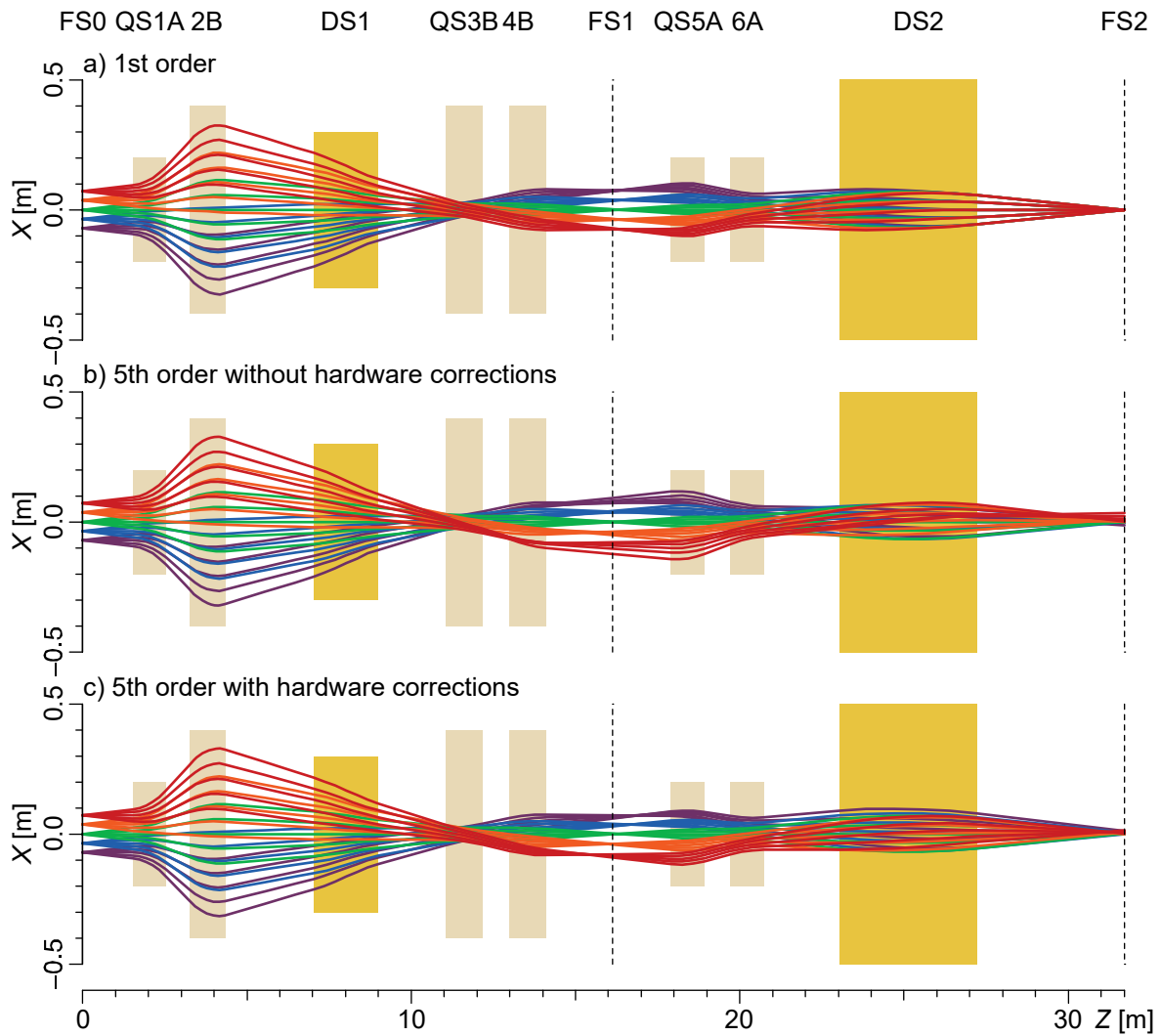


Figure 6-17 a) Trajectory plot for the high-resolution mode in the dispersive plane in first order. The spectrometer settings are the same as those in Figure 6-3, but the beam is momentum-dispersed at the entrance by the HTBL in the dispersion-matched mode. The trajectories in different colors correspond different momentum components. Only the transport in the dispersive plane is shown, since the transport in the non-dispersive plane is identical to that of Figure 6.3. b) Same as a) but in fifth order without hardware corrections. c) Same as b) but with hardware corrections.

## 6.4 Preferred Spectrometer Section alternative meets requirements

The capabilities of the Spectrometer Section afforded by the preferred ion-optical alternative with regard to the scientific requirements described in Section 6.2 are summarized as follows.

### 6.4.1 High-resolution mode

The functional requirements for the high-resolution mode and the capabilities afforded by the preferred ion-optical design are compared as follows and summarized in Table 6-6.

- As shown above, the preferred ion-optical alternative is feasible at the maximum magnetic rigidity of 8 Tm.
- The flight-path length is 31.72 m from the reaction target at FS0 to the final focus at FS2.
- The distance of 123 cm from the target position to the flange of QS1A is available for the placement of auxiliary detectors.
- As shown in Figure 6-3, Figure 6-4, and Figure 6-6 the angular acceptance in the dispersive (non-dispersive) plane is  $\pm 50$  (75) mrad, corresponding to a solid angle of 15 msr.
- The momentum acceptance of  $\pm 2.5\%$  is achieved at all angles, and it is larger at some angles (see Figure 6-6).
- The unreacted beam will be localized in the dispersive plane at the intermediate focus FS1 or at the final focus FS2, which facilitates its rejection at these locations.
- The angular resolution has an FWHM of 2.5 mrad and the momentum resolving power has an FWHM of 1/2350, meeting the requirements of 5 mrad and 1/1500, respectively.
- The mass resolving power for  $E = 160$  MeV/ $u$  is 800 for a ToF resolution of 150 ps.
- The charge resolving power is 156 for a resolution in energy loss of 1.3%.

The preferred alternative meets the requirements for the high-resolution mode.



Table 6-6 Comparison between the functional requirements for high-resolution mode and the capabilities achieved by the preferred alternative.

High-resolution mode	Requirements	Preferred alternative
Maximum mass	238	238
Mass resolving power	400	910
Charge resolving power	156	>156
Time-of-flight resolution (ps)	150	150
Flight path for charged particles (m)	25	31.7
Momentum resolving power	1500	2350
Spectrometer solid angle (msr)	15	15
Angular resolution (mrad)	5	3
Space around target (cm)	123	123
Momentum acceptance ( $\delta p/p$ in %)	$\pm 2.5$	$\pm 2.5$
Unreacted beam rejection	yes	yes
Maximum Rigidity (Tm)	8	8

#### 6.4.2 Neutron invariant-mass mode

The requirements for the neutron invariant-mass mode and the capabilities afforded by the preferred ion-optical alternative are compared as follows and summarized in Table 6-8.

- As shown in Section 6.3.1.6, the preferred ion-optical alternative is feasible at the maximum magnetic rigidity of 8 Tm.
- The flight-path length is 11.1 m from the reaction target at FS0' to the final focus at FS1.
- The distance of 90 cm from the target position to the entrance flange of DS1 is available for the placement of auxiliary detectors.
- As shown in Figure 6-15, the angular acceptance in the dispersive (non-dispersive) plane is  $\pm 70$  (36) mrad, corresponding to a solid angle of 10 msr.
- A momentum acceptance of  $\pm 5\%$  is achieved at all angles (see Figure 6-15).
- The neutron solid angle is 32 msr, which effectively constrains the vertical angular acceptance for neutrons to  $\pm 90$  mrad for a distance between the target and the neutron-detector array is 8 m.
- The maximum neutron flight-path length is 15 m.
- The S $\pi$ RIT TPC can be inserted in DS1 if DS1 has a vertical gap size of  $\pm 30$  cm or larger.
- The unreacted beam will be localized in the dispersive direction at the focus FS1, which facilitates its rejection at this location.



- The angular resolution has an FWHM of 3.3 mrad and the momentum resolution has an FWHM of 1/226 without beam tracking. With beam tracking at FS0', an angular resolution of 2.7 mrad and a momentum resolving power of 1/778 can be achieved.
- At  $E = 160 \text{ MeV}/u$ , the mass resolving power is 193 for a ToF resolution of 150 ps without tracking. With tracking at FS0', the mass resolving power is 335.
- The charge resolving power is 156 for a resolution in energy loss of 1.3%.

The preferred alternative meets the functional requirements for the neutron invariant-mass mode.

Table 6-7 Comparison between the functional requirements for neutron invariant-mass mode and the capabilities achieved by the preferred alternative.

Neutron Invariant-Mass Mode	Requirements	Preferred Alternative
Maximum Mass	132	132
Mass Resolving Power	220	193/335*
Charge Resolving Power	85	156
Time of Flight Resolution (ps)	150	150
Flightpath charged particles (m)	11	11
Momentum Resolving power	290	226/778*
Spectrometer solid angle (msr)	10	10
Angular resolution (mrad)	5	3
Space around target (cm)	90	90
Momentum acceptance ( $\delta p/p$ in %)	$\pm 5$	$\pm 5$
Neutron Solid Angle (msr)	32	32
Neutron flight-path length (m)	15	15
Gap for Time Projection Chamber (cm)	60	60
Unreacted beam rejection	yes	yes
Maximum Rigidity (Tm)	8	8

\* Values without/with beam tracking at FS0'.

### 6.4.3 ToF- $B\rho$ mass-measurement mode

The requirements for the neutron invariant-mass mode and the capabilities afforded by the preferred ion-optical alternative are compared as follows and summarized in Table 6-8.

- As shown in Section 6.3.1.6, the preferred ion-optical alternative is feasible at the maximum magnetic rigidity of 8 Tm, exceeding the required 7 Tm.
- The flight-path length of 113 m is achieved by combining the ARIS Fragment Separator (40.14 m), the HTBL (41.40 m), and the Spectrometer Section (31.72 m) of the HRS.



- The angular acceptance is the same as that of the high-resolution mode,  $\pm 50$  (75) mrad in the dispersive (non-dispersive) plane, corresponding to a solid angle of 15 msr. This is much larger than the 3 msr required for this mode. It is understood that the actual angular acceptance is dependent on the  $x$  position at FS0, due to the momentum-dispersed beam spot at this location, which does not negatively impact the ToF- $B\rho$  mass-measurement experiment.
- The momentum acceptance is  $\pm 0.5\%$ , which corresponds to a beam-spot size of  $\pm 4$  cm at FS0.
- The momentum resolving power has an FWHM of 1/12000 as described in Section 5.5 and shown in Figure 5-10, meeting the requirement of 1/1500, respectively.
- At  $E = 160$  MeV/ $u$ , the mass resolving power is 10000 (FWHM) for the resolution of the ToF determination of 30 ps (FWHM).

The preferred alternative meets the requirements for the ToF- $B\rho$  mass-measurement mode.

Table 6-8 Comparison between the functional requirements for ToF- $B\rho$  mass-measurement mode and the capabilities achieved by the preferred alternative. For the calculations,  $^{60}\text{Ca}$  at 6.43 Tm was assumed.

ToF- $B\rho$ mass measurement mode	Requirements	Preferred alternative
Maximum Mass	238	238
Mass Resolving Power	10000	10000
Time of Flight Resolution (ps)	30	30
Flightpath charged particles (m)	90	113
Momentum Resolving power	>10000	11000
Spectrometer solid angle (msr)	3	>3
Momentum acceptance ( $\delta p/p$ in %)	$\pm 0.5$	$\pm 0.5^*$
Maximum Rigidity (Tm)	7	8

\* This corresponds to a beam-spot size of  $\pm 4$  cm.

#### 6.4.4 Switching between different Spectrometer Section Modes

A relatively large fraction of experiments at FRIB will use the HRS, which means that experiments that run in different modes can run consecutively. It is straightforward to switch between operational modes of the HRS in terms of the field settings, but a significant amount of set-up and take-down time is associated with the placement of large ancillary experimental systems, such as GRETA, or the switch-over between using focal plane FS1 (in the neutron invariant-mass mode) and FS2 (in the high-resolution or ToF- $B\rho$  mass measurement mode). Therefore, it will be advantageous to run several experiments with the same ancillary device or the same Spectrometer Section mode one after another in campaigns. Such campaigns are already used for experiments at the S800 Spectrometer, combined with, for example, GRETINA.



## 6.5 Functional specifications for the Spectrometer Section

This section stipulates the functional specifications for the Spectrometer Section to realize its functional requirements. The specifications of the magnetic elements are given in Section 6.5.1, those of the diagnostics and detectors are given in Section 6.5.2, and those of the vacuum systems are given in Section 6.5.3.

### 6.5.1 Magnetic elements

As shown in Figure 6-1, the Spectrometer Section contains six quadrupole (singlet) magnets and two dipole magnets. The functional specifications of these magnets as used in the ion-optical simulations of the preferred layout are presented in this section. Preliminary designs of the magnetic elements that meet these functional specifications will be presented in Section 9.

#### 6.5.1.1 Quadrupole magnets

The quadrupole magnets in the Spectrometer Section have large bore diameters to accommodate the large envelopes of the particles emerging from the reaction target at FS0 in the high-resolution mode or at FS0' in the neutron invariant-mass mode. Moreover, each quadrupole has sextupole and octupole coils superimposed to be able to control and correct for higher-order aberrations. There are two different types (denoted A and B) of quadrupole magnets, which primarily differ in their bore diameters. The functional specifications for each magnet type as used in the ion-optical simulations of the preferred alternative are provided in Table 6-9.

The primary constraint for the quadrupole magnets with superconducting coils was to make them relatively short to optimize the transmission through the Spectrometer Section, while keeping the field strength at warm bore below a sustainable 2.5 T. This maximum field strength of 2.5 T and larger bore diameter render the field gradients relatively small, and hence the Lorentz forces on the coils manageable.

The ion-optical calculations and the magnetostatic design of the quadrupole magnets have progressed interactively: To assess the effects of the field quality on the ion optics, 3D field maps were extracted from the ANSYS Maxwell models (see Section 9), analyzed in a similar manner as discussed in Ref. [TAK13], and included in the calculations in COSY up to 5<sup>th</sup> order. It was verified by these calculations that the desired ion-optical properties are realized by the quadrupole-magnet designs as presented in Section 9.

The quadrupole magnets employed in the HRS have large aperture-to-length ratios, and their field profiles are dominated by the fringe fields, having virtually no flat region. It is noteworthy that, as pointed out in Ref. [BAA12], this feature is not necessarily detrimental to the ion optics in regard





to the higher-order aberrations: fifth and higher order aberrations diverge at the hard-edge limit. For the current design of the quadrupoles, the strength functions are already smooth, having no flat region, and the higher-order aberrations are under control. The “American-football”-shaped quadrupoles presented in Ref. [BAA12] had been considered in the early design phase, but in the end, we opted for a more traditional quadrupole configuration as described in Section 9.

### 6.5.1.2 Dipole magnets

The Spectrometer Section of the HRS contains two large dipoles, the Sweeper Dipole (DS1) and the Spectrometer Dipole (DS2). A variety of considerations were made in deciding the designs of the dipole magnets in the preferred layout. The functional specifications for both dipole magnets as used in the ion-optical simulation of the preferred layout are shown in Table 6-10.

DS1 has simple rectangular-shaped poles. The bend angle is  $35^\circ$ , and the entrance pole face is perpendicular to the beam axis. The maximum field strength is less than 2.5 T. This high field helps the length of the magnet relatively short, which enhances the acceptance for neutrons at forward scattering angles in neutron invariant-mass spectroscopy experiments with the MoNA-LISA neutron detector array. Compared to what was described in the Conceptual Design Report, the vertical gap size has been increased from  $\pm 24$  cm  $\pm 30$  cm. This change enables installation of the S $\pi$ RIT TPC in the beam chamber of the magnet. Also the magnetostatic design has been optimized, which has resulted in a large decrease of mass of iron, as described in Section 9.4.5.

DS2 is a  $60^\circ$ -bend, symmetric sector dipole with the maximum field of 2 T. The entrance and exit pole faces are rotated by  $20^\circ$  such that they have a horizontal focusing effect, obviating additional focusing magnets. Due to the vertical defocusing effect, the trajectories in the non-dispersive plane have a point-to-point image in the middle of the magnet gap. This helps improve the transmission through the magnet in the non-dispersive plane with a relatively small gap size of  $\pm 10$  cm.



Table 6-9 Quadrupole magnet specifications for the Spectrometer Section.

Label	A	B
Quantity	3	3
Location	QS1,5,6	QS2, 3, 4
Effective field length (m)	1.00	1.00
Warm-bore (WB) radius (m)	0.20	0.40
Quadrupole maximum field strength (T@WB, base requirement)†	1.46	2.03
Quadrupole maximum field strength (T@WB, with 10% tuning margin)†	1.61	2.23
Quadrupole field integral (T, base requirement)†	7.30	5.08
Quadrupole field integral (T, with 10% tuning margin)†	8.03	5.59
Quadrupole good-field region radius (m)	0.16	0.32
Sextupole maximum field gradient (T/m <sup>2</sup> , base requirement)†	4.5	2.4
Sextupole maximum field gradient (T/m <sup>2</sup> , with 10% tuning margin)†	5.0	2.6
Octupole maximum field gradient (T/m <sup>3</sup> , base requirement)†	8.2	2.5
Octupole maximum field gradient (T/m <sup>3</sup> , with 10% tuning margin)†	9.0	2.8

†: This tables include the base magnetic field requirements as determined from ion-optical calculations, needed to achieve the design beam transport at the maximum magnetic rigidities of 8 Tm. Additionally, this table includes magnetic field requirements with tuning margin to ensure project specifications are met. The magnet designs are based on the magnetic field requirements with tuning margin, and therefore the power supply voltage and currents include tuning margin.

Table 6-10 Dipole magnet specifications for the Spectrometer Section.

Label	DS1	DS2
Quantity	1	1
Bending radius (m)	3.2	4.0
Maximum rigidity (Tm)	8.0	8.0
Bending angle (deg)	-35	60
Arc length for central ray (m)	1.95	4.19
Field integral (Tm, base requirement)†	4.89	8.38
Field integral (Tm, with 5% tuning margin)†	5.13	8.80
Vertical gap size (m)	±0.30	±0.10
Good field region width (m)	±0.30	±0.50
Pole-face rotation entrance (deg)	0	-20
Pole-face rotation exit (deg)	35	-20

†: This tables include the base magnetic field requirements as determined from ion-optical calculations, needed to achieve the design beam transport at the maximum magnetic rigidities of 8 Tm. Additionally, this table includes magnetic field requirements with tuning margin to ensure project specifications are met. The magnet designs are based on the magnetic field requirements with tuning margin, and therefore the power supply voltage and currents include tuning margin.



### 6.5.1.3 Stray fields around the target stations

Stray fields for the magnets around the targets have been investigated for the purpose of assessing the field strengths at the locations at which auxiliary detector systems are installed. For this purpose, the latest designs of the magnets, as presented in Section 9 were used.

As discussed in Section 4.3.1.6 the operation of GRETA requires fields generally below 600 G, although locally levels of 700-900 Gauss can be tolerated locally [ROD21]. Figure 6-18 shows the stray field of DS1 at its maximum excitation corresponding to the maximum magnetic rigidity of 8 Tm. The excitation current (magnetomotive force) is 710 kA (Ampère-turn), yielding the field strength of  $\sim 2.2$  Tesla at its center. In the figure, the box ( $\pm 3.5$  m  $\times$  1.5 m  $\times$   $\pm 0.9$  m) at the origin representing the region which GRETA occupies, with the negative  $y$  cut out due to the symmetry of the model space (*i.e.*, the flux is normal to the  $z$ - $x$  plane). The field strengths exceed 600 Gauss in a few regions, especially in the vicinity of the coil. These regions have been investigated by the GRETA project team and it was concluded the operational integrity of GRETA would not be affected [ROD21].

The top panel of Figure 6-19 shows the magnetic field due to DS1 along the beam axis, where the fields are maximum. At FS0' fields exceed the limit for detector systems that utilize PMTs, so alternatives have to be used as discussed in Section 4.3.1. Although it might be possible to reduce the fields further, by using field clamps or other shielding techniques, they are not compatible with the placement of GRETA at FS0', so they will have to be removable. This will be further investigated in the detailed design stage. The bottom panel of Figure 6-19 shows the fields of quadrupole magnet QS1B. Its stray field near FS0' is much smaller of that of DS1.

From the same figure, it is observed that the maximum magnetic field at FS0 due to DS1 is about 18 G in the area where detector systems might be placed. This is close to the limit of what PMTs with magnetic shields can handle. The stray fields of QS1A add to the field experienced by detectors in this area as shown in middle panel of Figure 6-19. In this figure the quadrupole fields at the radial distance of 20 cm from the beam axis are plotted. The combination of these fields require that additional shielding is placed to achieve stray fields below 25 G. This can be accomplished by placing a shielding plate just upstream of QS1A, similar to what is presently done for the S800 Spectrograph. The design of the shield used at the S800 is shown in Figure 6-20. Usage of this plate is optional.

The MoNA-LISA detectors will be placed as close as 8 m downstream of FS0' for neutron invariant-mass experiments. From the top panel of Figure 6-19, it can also be deduced that stray fields from the DS1 magnet have dropped to about 15 G at this distance and the shielding that the MoNA-LISA PMTs already use will be sufficient to handle this field. At a distance of 15 m



downstream of FS0' (maximum distance to MoNA-LISA), the magnetic stray field due to DS1 is only 1.7 G.

For completeness, the stray fields of QS1A and QS2B are shown in Figure 6-21 (upstream of QS1A) and Figure 6-22 (downstream of QS1B). Figure 6-23 (DS1), Figure 6-24 (QS1A and QS1B in the high-resolution mode), and Figure 6-25 (QS1A and QS1B in the invariant mass mode) provide 2D overviews of the magnetic fields in the median plane.

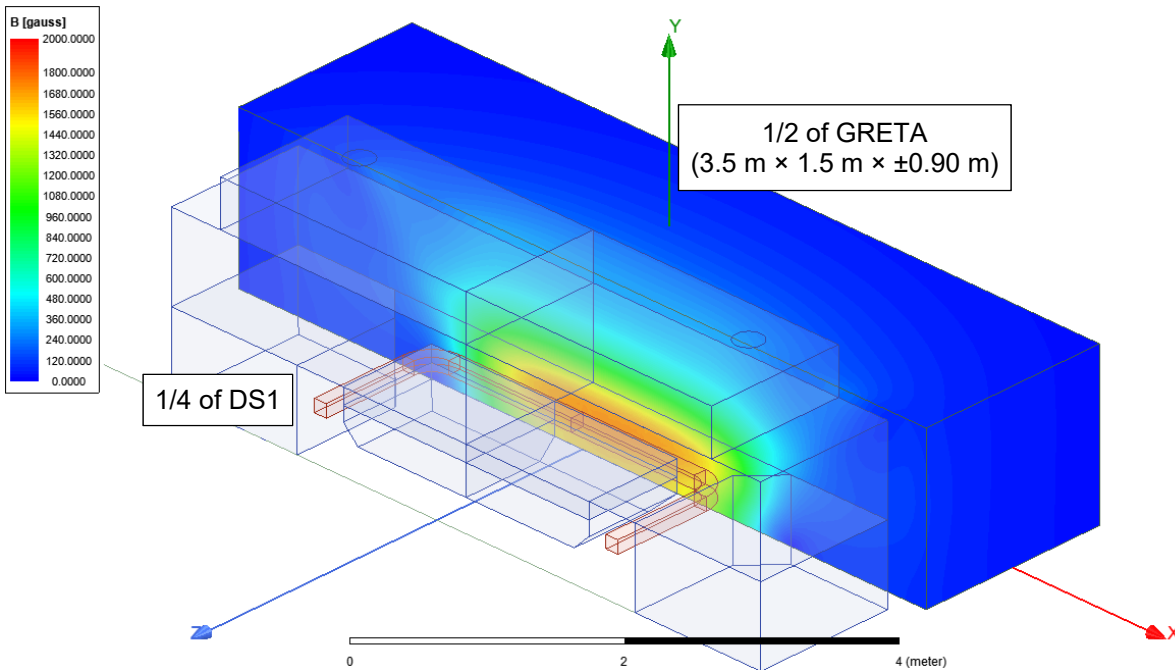


Figure 6-18 Stray field of DS1 at the maximum excitation. The box ( $\pm 3.5\text{ m} \times 1.5\text{ m} \times \pm 0.9\text{ m}$ ) representing the footprint of GRETA placed at FS0' in the neutron invariant-mass mode. Only a quarter of DS1 is shown, where the other quarters were cut out of the model due to the symmetry. The stray fields in very close proximity of the coils are approximately 1800 Gauss, and at the locations of some of the digitizers they exceed the 600-Gauss limit set by GRETA.

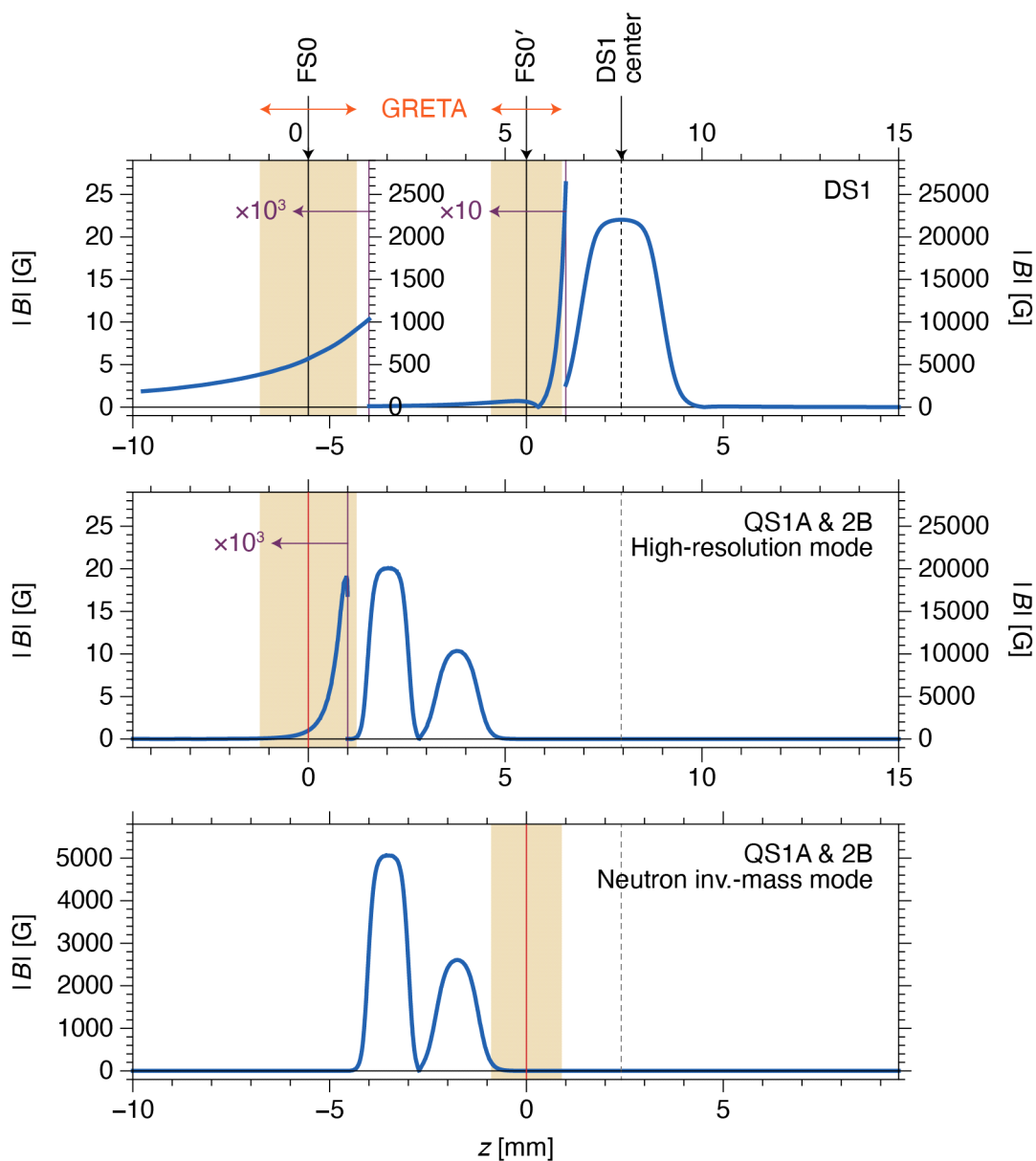
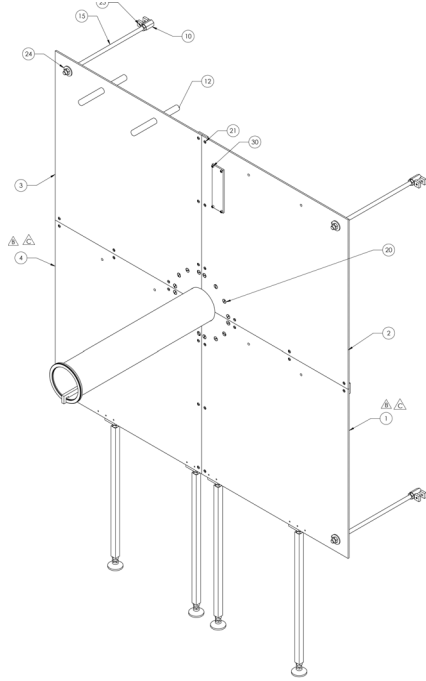


Figure 6-19 Field distributions of DS1, QS1A, and QS2B at the maximum excitation along the beam direction. For the quadrupole fields (middle and bottom), the field strengths at a distance of 20 cm from the beam axis are shown. FS0, FS0', and the center of DS1 are denoted. The footprint of GRETA is shown by the light-brown boxes. The graphs are magnified as indicated for clarity.



*Figure 6-20 Magnetic shielding plate as used downstream of the target location at the S800. A similar shielding plate will be adopted for FS0. Usage of the plate is optional.*



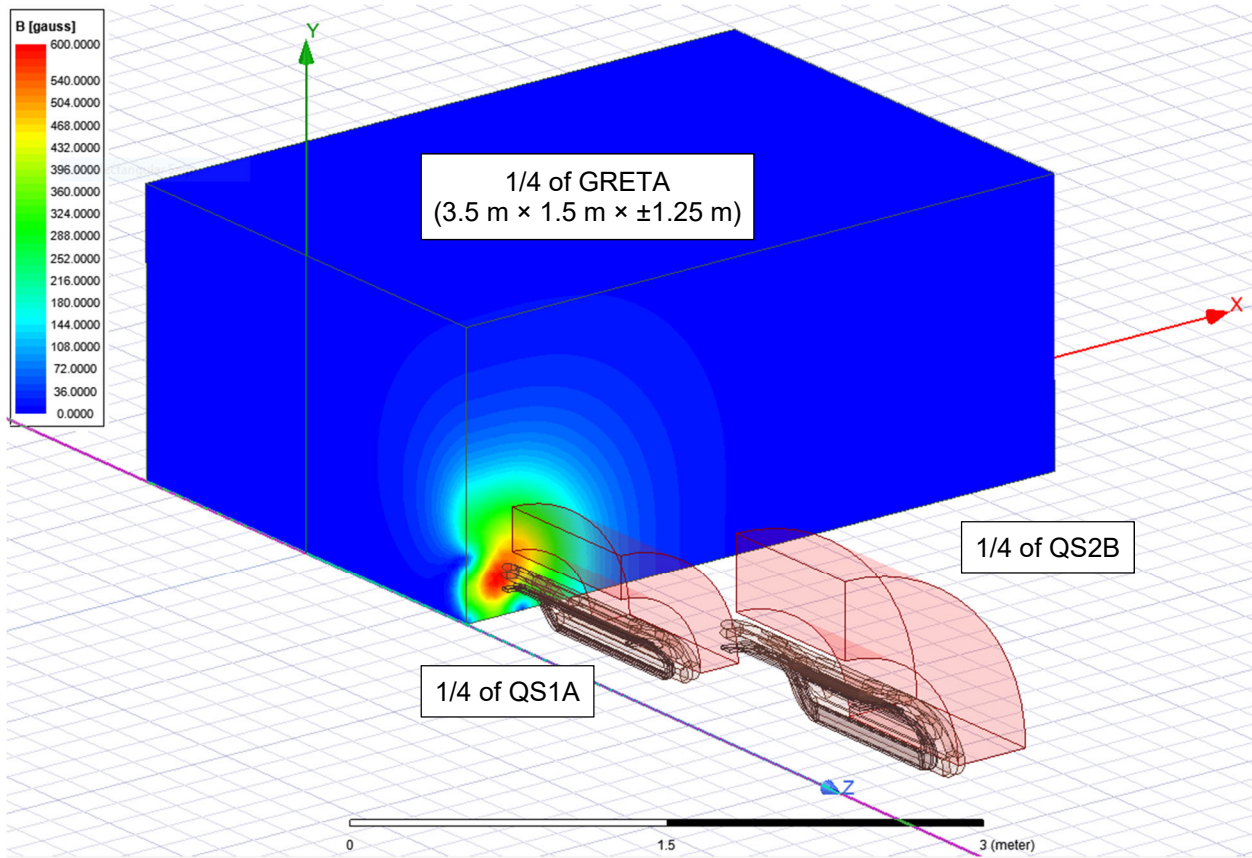


Figure 6-21 Stray field of QS1A and QS2B at the maximum excitation in the high-resolution mode. The box at the origin ( $3.5\text{ m} \times 1.5\text{ m} \times \pm 1.25\text{ m}$ ) represents the GRETA footprint. Only quarters of QS1A and QS2B are shown, where the other three quarters were cut out of the model due to the symmetry. The flux is normal to the yz and zx planes.

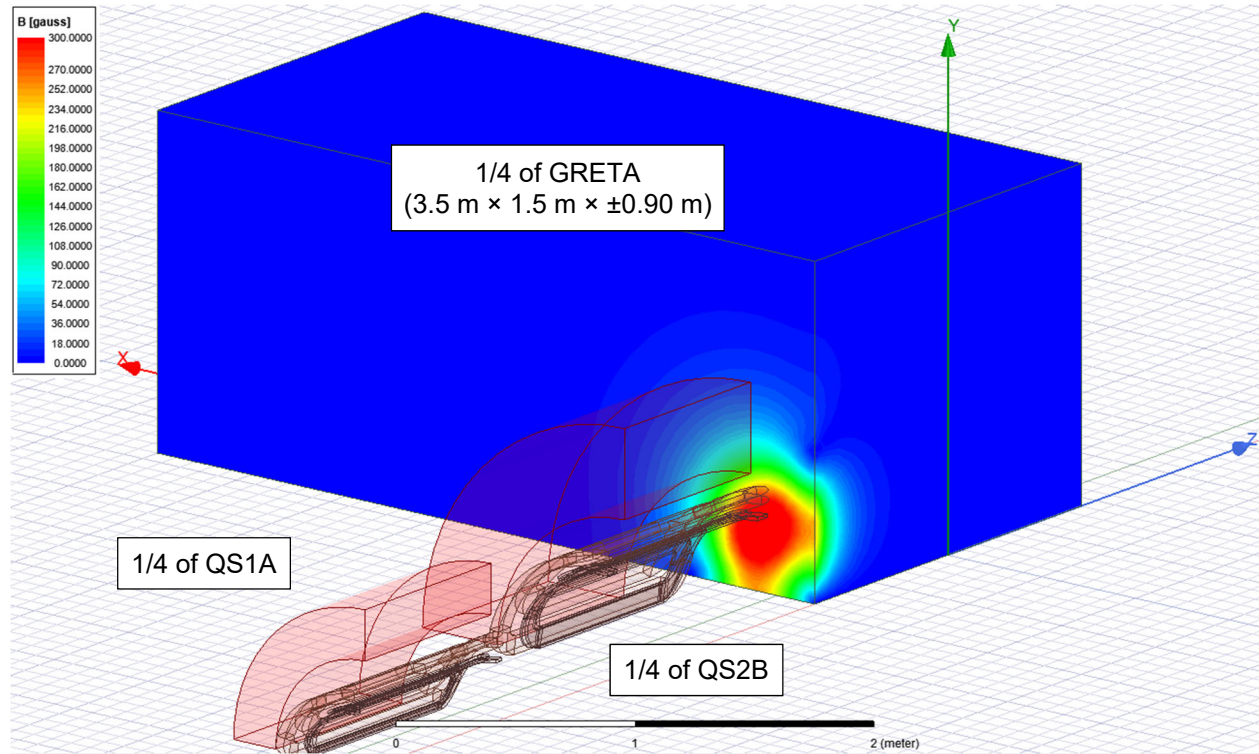


Figure 6-22 Stray field of QS1A and QS2B at the maximum excitation in the neutron invariant-mass mode. The box at the origin ( $3.5\text{ m} \times 1.5\text{ m} \times \pm 0.90\text{ m}$ ) represents the GRETA footprint. Only quarters of QS1A and QS2B are shown, where the other three quarters were cut out of the model due to the symmetry. The flux is normal to the yz and zx planes.

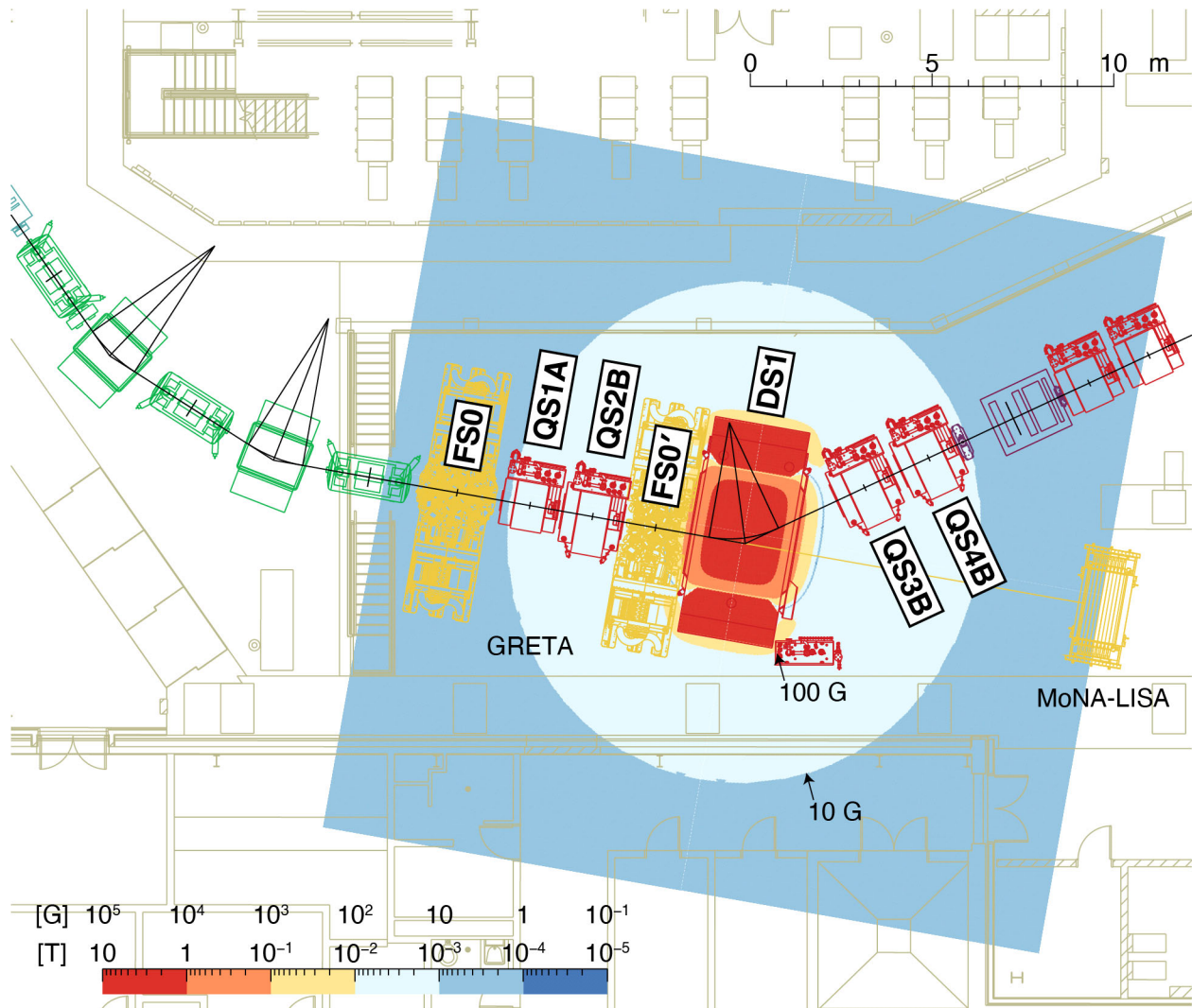


Figure 6-23 Stray field of DS1 at the maximum excitation on the median plane plotted on top of the layout graphics. The 100-G and 10-G boundaries are denoted. GRETA are shown at FS0 (for the high-resolution mode) and at FS0' (for the neutron invariant-mass mode), and MoNA-LISA is shown at 12 meters from FS0'.



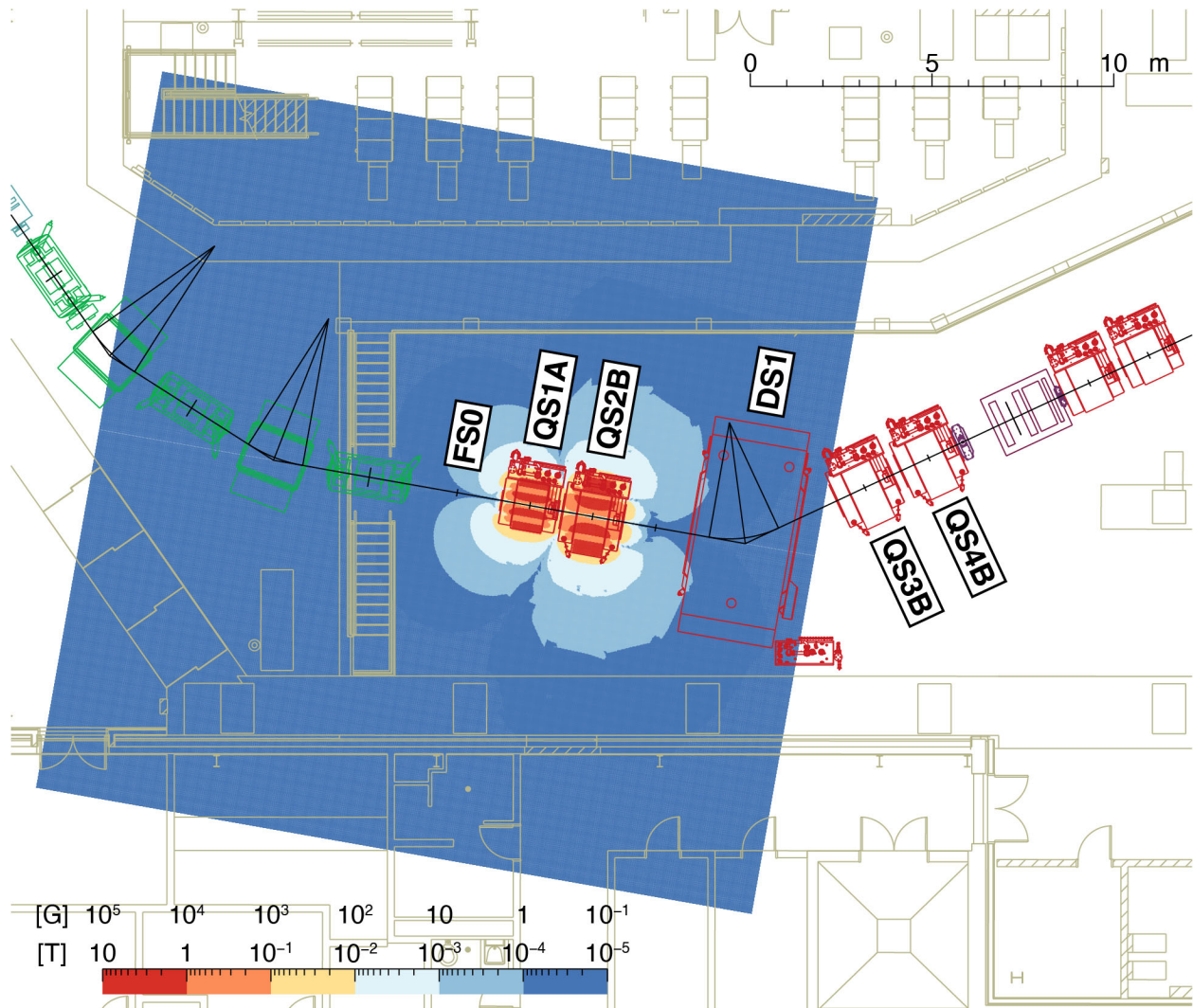


Figure 6-24 Stray field of QS1A and QS2B at the maximum excitation in the high-resolution mode on the median plane plotted on top of the layout graphics. GRETA is not shown in the interest of showing the field map.

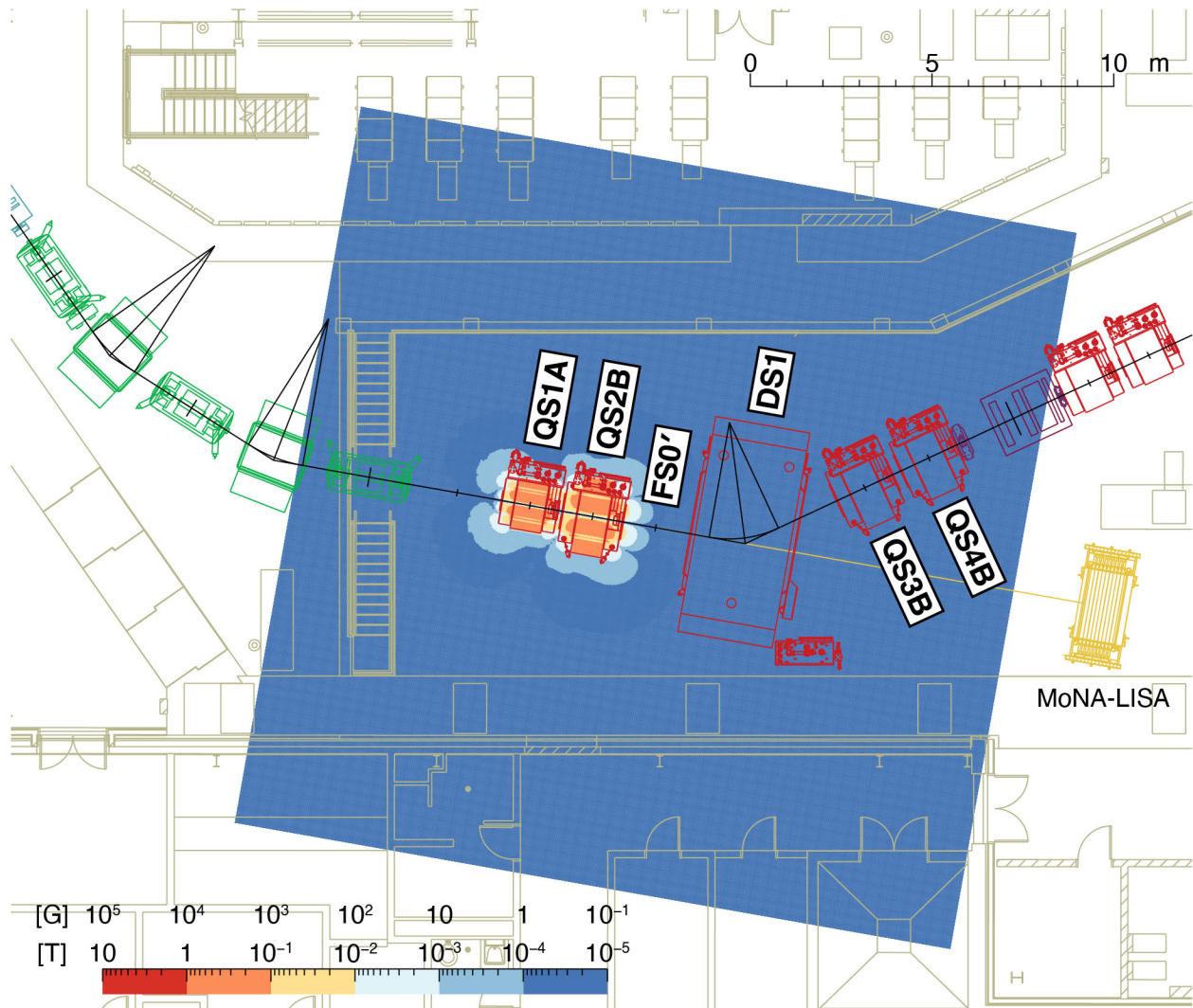


Figure 6-25 Stray field of *QS1A* and *QS2B* at the maximum excitation in the neutron invariant-mass mode on the median plane plotted on top of the layout graphics. *GRETA* is not shown in the interest of showing the field map. *MoNA-LISA* is shown at a distance of 12 meters from *FS0'*.

## 6.5.2 Diagnostics and detectors

Similar to the HTBL, the goals of the Spectrometer-Section diagnostics and detector system are defined as follows:

- To facilitate initial commissioning of the HRS
- To facilitate beam tuning and reaction-product identification and characterization
- To provide event-by-event tracking information (momentum, position, angle) and particle identification (energy-loss and total-kinetic-energy measurements) for physics analysis
- To enable long-term stable operation and provide appropriate machine protection

To achieve these goals, the specifications for the diagnostics and detectors have been formulated as described in this section.

As shown in Figure 6-1, the Spectrometer Section has two focal planes, FS1 and FS2. FS1 is primarily used for experiments in the neutron invariant-mass mode (See Section 6.3.1.6), although tracking detectors at this location can also be used in combination with detectors installed at FS2 to gain additional accuracy for tracking through the full Spectrometer Section to FS2. The trajectory information obtained at FS1 and FS2 is used to reconstruct the trajectories at the FS0 through an event-by-event inverse raytracing procedure. The energy-loss and total-kinetic-energy information is used to identify the isotope species by their mass and atomic numbers on an event-by-event basis. Based on the ion-optical properties of the Spectrometer Section and ample experience with running fast beam experiments with the S800 Spectrograph and Sweeper magnet at NSCL, the suite of detectors installed for neutron invariant-mass mode experiments at FS1 and for high-resolution mode experiments at FS2 must include the following:

- Tracking detectors that provide accurate and high-resolution position [1 mm (FWHM)] and angle information [2 mrad (FWHM)] to determine the trajectories of particles transported through the Spectrometer Section of the HRS on an event-by-event basis. They must be highly efficient (close to 100%), while being thin (less than 6 mg/cm<sup>2</sup>) to reduce multiple scattering effects. The horizontal and vertical dimensions of the tracking detectors must be 100 × 60 cm<sup>2</sup> at FS1 and FS2 to cover the envelope of the beam trajectories. These detectors also need be able to operate at a rate of at least 10 kHz.
- An energy loss ( $\Delta E$ ) detector with an effective area and rate capability matching the values of the tracking detectors. The  $\Delta E$  detector must achieve a resolution of  $\sigma_{\Delta E}/\Delta E$  of 1.3% (2.3%) (FWHM) to achieve 4 $\sigma$  separation between isotopes that differ in charge number by one for  $Z = 92$  ( $Z = 50$ ).





- A timing scintillator with an area matching that of the tracking detectors providing a timing resolution of better than 150 ps. Two thicknesses must be available ( $100 \text{ mg/cm}^2$  and  $300 \text{ mg/cm}^2$ ). The rate capability of the scintillator must be 1 MHz.
- A total kinetic energy (TKE) detector (hodoscope). It should have a surface and rate capability matching that of the tracking detectors and be sensitive to charged particles (TKE measurement) and  $\gamma$  rays (for isomer tagging and particle identification purposes). The resolution of the hodoscope should be better than 7% for 662 keV  $\gamma$ -rays, which corresponds to a light output resolution for the stopping of heavy ions of 0.8% (FWHM) [ME111].

A schematic layout of the detector configuration at FS1 and FS2 is shown in Figure 6-26.

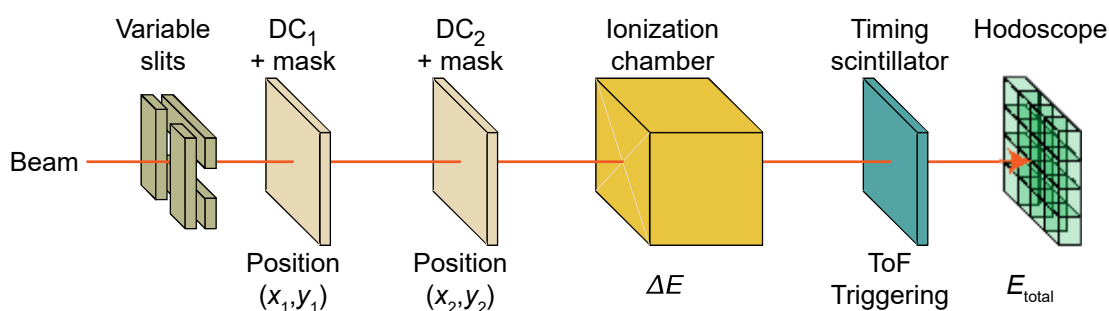


Figure 6-26 Schematic layout of the detector configuration of the diagnostic systems used at FS1 and FS2.

The detector suites are installed in vacuum chambers that are equipped with drives to insert masks in front of the tracking detectors. These masks are inserted for the purposes of the position calibration of the tracking detectors and removed during regular data taking. In addition, the chambers are equipped with beam blockers/slits that can be inserted and positioned to intercept unreacted beam particles.

All detectors will be read out through data acquisition systems that run Laboratory supported data-acquisition software. The data acquisition system and software must facilitate efficient and high-performance integration with the data acquisition systems of ancillary detector systems.

The detector suite in FS1 must be easily retractable and insertable to accommodate efficient switches between the neutron invariant-mass and high-resolution modes. The tracking detectors at FS1 must be insertable remotely so that they can be activated and used in combination with the detector suite at FS2.

The functional specifications for the diagnostics and tracking detectors for the Spectrometer Section are summarized in Table 6-11, Table 6-12, and Table 6-13.

Table 6-11 General functional specifications for the diagnostics and detector systems of the Spectrometer Section.

Parameter	Specification	
Remote retractability	FS1	Yes
	FS2	No
Position alignment accuracy	≤ 0.5 mm transverse to the beam axis	
	≤ 1 mm along the beam axis	
Accessibility	Replacement possible within < 6 hours	
Vacuum requirement	10 <sup>-5</sup> Torr vacuum compatible	

Table 6-12 Functional specifications for the tracking and timing detectors for the Spectrometer Section.

Parameter	Specification	
Transmission	100%	
Single particle detection	Yes	
Thickness	Tracking	≤ 6 mg/cm <sup>2</sup>
	Timing	100–300 mg/cm <sup>2</sup>
Sensitive area	FS1	100 × 60 cm <sup>2</sup>
	FS2	100 × 60 cm <sup>2</sup>
Resolution (FWHM)	Position	≤ 1 mm
	Timing	≤ 150 ps
Rate capability	Tracking	≥ 10,000 Hz
	Timing	≥ 1 MHz

Table 6-13 Functional specifications for the energy-loss detectors for the Spectrometer Section.

Parameter	Specification	
Transmission	Ion Chamber	100%
	Hodoscope	No
Sensitive area	FS1	100 × 60 cm <sup>2</sup>
	FS2	100 × 60 cm <sup>2</sup>
Energy resolution	Ion Chamber	1.3%
	Hodoscope	≤ 7% (662 keV γ-rays)
Rate capability	≥ 10,000 Hz	



### 6.5.3 Vacuum systems

With the lattice design of the Spectrometer Section established, the locations of the magnet are fixed on the floor layout with the preliminary designs of the magnets complete, the dimensions of the vacuum chambers (beam pipes) have been identified. Also, with the standard sets of diagnostic instruments defined, the dimensions of the diagnostic chambers have been identified. These are being refined in final design.

The general specification for the vacuum systems for the Spectrometer Section is that the systems be able to evacuate to the pressure of  $10^{-5}$  Torr. At this level, the lateral, angular, and energy spreads due to interactions with residual gas in the beam line do not contribute significantly to the uncertainties in the tracking of the particles. At  $10^{-5}$  Torr, the lateral spread can become  $\sim 150$   $\mu\text{m}$  (FWHM) over the full length of the HTBL and Spectrometer Section, which is still much smaller than the position resolutions of the focal plane tracking detectors. At  $10^{-4}$  Torr, the lateral spread increases to  $\sim 500$   $\mu\text{m}$  (FWHM), which is comparable to the position resolutions of the detector systems. In addition, a pressure of  $10^{-5}$  is required for the operation of cryogenic targets (*e.g.* a Liquid Hydrogen Target) at FS0. At higher pressures, the residual gas that freezes on the surfaces of the cryogenic systems reduces the ability to reflect heat and the target becomes less stable.

The operation of the Spectrometer Section requires gate valves to isolate diagnostic equipment in beam chambers needed during maintenance. Gate valves separate each section with dedicated pumping station with vacuum gauging. Finally, the locations of bellows necessary to accommodate alignment have been identified.

Turbo-molecular pumping (TMP) systems are sensitive to the presence of magnetic fields and cannot operate in fields in excess of 50 Gauss. For some of the magnets with significant stray fields, such as DS1 (see Figure 6-18), this requires that these pumps are placed at appropriate distances from such magnets. The exact location of each TMP will be confirmed by performing a detailed magnetic field analysis around each large magnet in the HRS to include all the dipoles and the QSA and QSB magnets. Similar consideration will also be given to vacuum gauging, some of which has maximum magnetic field limits specified by the supplier.



## 6.6 References

- [ANS19] ANSYS Electromagnetics Suite, Release 2019 R3.7 (2019).
- [BAA12] R. Baartman, Phys. Rev. ST Accel. Beams 15, 074002 (2012).
- [BAZ02] D. Bazin et al., Nucl. Instrum. Methods Phys. Res., Sect. A 482, 307 (2002).
- [BAZ03] D. Bazin et al., Nucl. Instrum. Methods Phys. Res., Sect. B 204, 629 (2003).
- [BER93] M. Berz et al., Phys. Rev. C 47, 537 (1993).
- [COS11] M. Berz and K. Makino, COSY Infinity 9.1, “Programmer’s Manual” MSU Report MSUHEP 101214 (2011); “Beam Physics Manual” 060804-rev (2013).
- [ROD21] GRETA Support Structure Materials – Records of Decision, May 7, 2021.
- [TAK13] H. Takeda et al., Nucl. Instrum. Methods Phys. Res., Sect. B 317, 798 (2013).
- [TAR08] O. B. Tarasov and D. Bazin, Nucl. Instrum. Methods Phys. Res., Sect. B 266, 4657 (2008).
- [TAR16] O. B. Tarasov and D. Bazin, Nucl. Instrum. Methods Phys. Res., Sect. B 376, 185 (2016).



## 7 Diagnostics and Detectors

### 7.1 Introduction and overview

The Diagnostics and Detectors scope includes the materials and manpower needed to acquire, bench test, install, test in situ, and perform the final integrated testing without beam. The scope is visualized in Figure 7-1 and the associated WBS elements are shown in Table 7-1.

Table 7-1. Diagnostics and Detectors WBS.

<b>Experimental Systems - High Rigidity Spectrometer</b>	<b>HRS.3</b>
<b>High Transmission Beamline (HTBL)</b>	<b>HRS.3.01</b>
<b>High Transmission Beamline Diagnostics and Tracking</b>	<b>HRS.3.01.02</b>
<i>HTBL Diagnostic Devices</i>	<i>HRS.3.01.02.01</i>
<i>HTBL Tracking Detectors</i>	<i>HRS.3.01.02.02</i>
<b>Spectrometer Section</b>	<b>HRS.3.02</b>
<b>Spectrometer Section Structural Support and Access to Detector Systems</b>	<b>HRS.3.02.04</b>
<i>Spectrometer Section Detector Support and Access at Reaction Target</i>	<i>HRS.3.02.04.01</i>
<i>Spectrometer Section Detector Support for MoNA-LISA Detector System</i>	<i>HRS.3.02.04.02</i>
<i>Spectrometer Section Detector Access Platforms</i>	<i>HRS.3.02.04.03</i>
<b>Spectrometer Section Focal Plane Detector Systems</b>	<b>HRS.3.02.05</b>
<i>Spectrometer Section High Resolution Mode Focal Plane Detector Systems</i>	<i>HRS.3.02.05.01</i>
<i>Spectrometer Section Invariant Mass Mode Focal Plane Detector Systems</i>	<i>HRS.3.02.05.02</i>

To support the diverse scientific program of the HRS described in Section 4, it is important that the HTBL and the Spectrometer Section of the HRS are provided with the necessary diagnostics and detectors for tuning and tracking the rare isotopes. Based on the requirements summarized in Section 5.8.2 for the HTBL and in Section 6.5.2 for the Spectrometer Section, appropriate diagnostics and detector systems were selected as presented in this Section. Figure 7-1 outlines the schematic layout of the detector technologies that meets the scientific requirements of the HRS; the basic concepts, operational conditions and performance optimization of the planned detector technologies are based on the solid experience matured in running with similar detector systems at the NSCL facility over several decades, including the A1900 Fragment Separator [MOR03], the S800 Spectrograph [YUR99], and the Sweeper Magnet [BIR05] system.

It is important to realize that, although in Section 4, the envisioned scientific program is used to determine the overall requirements for the diagnostics systems of the HRS, in practice, the setups for different experiment are optimized on a case-by-case basis. The usage of specific detectors and diagnostics tools depends on many factors and can be quite different even when the reaction types



studied are quite similar, for example because different user supplied detectors are employed or beam intensities and/or event rates vary significantly.

### 7.1.1 The HTBL diagnostics and tracking systems

The HTBL has four diagnostics boxes, as shown in Figure 7-1. The first (FB1) and third (FB3) box provide detailed beam diagnostics tracking stations. The second station (FB2) only serves to visually inspect the beam at that location. The fourth diagnostic station is at the end of the HTBL and beginning of the spectrometer section, near FS0. Note that the choice of what diagnostic tools to use at FB1, FB2, FB3, and FS0 will depend on the particular experiment and must be decided on a case-by-case basis. For example, some experiments will require event-by-event beam tracking in the HTBL, whereas for other experiments it is better to avoid doing so, for example to reduce charge-state production (see Section 4.3.2.3).

The main goals of the HTBL diagnostics and detector systems are to:

- Facilitate initial commissioning of the HRS;
- Facilitate tuning prior and during experiments run with the HRS by providing the necessary characterization of the beam properties. This includes measurements of 2D beam profiles, trajectory angles, and transmission through the HTBL;
- Provide event-by-event tracking information (momentum, position, angle) for the physics analysis of events recorded in the HRS;
- Provide long-term stable beams operations by monitoring service for beam transport and machine protection (see also Section 7.3.5)

As described in Section 5.3, the HTBL accommodates two ion-optical beam-transport modes: the achromatic and dispersion-matched modes. The relationships of these modes to the tracking detector stations in the HTBL are shown in Figure 7-2.

In the achromatic beam-transport mode, the event-by-event measurements of the momentum and angle of the beam particles are required if the momentum and angular resolution of particles detected in the focal plane of the HRS must be better than the momentum and angular spreads in the beam prior to the reaction target at FS0. This can be accomplished by using tracking detectors located at FB1 and/or FB3 (See Section 5.3.2).





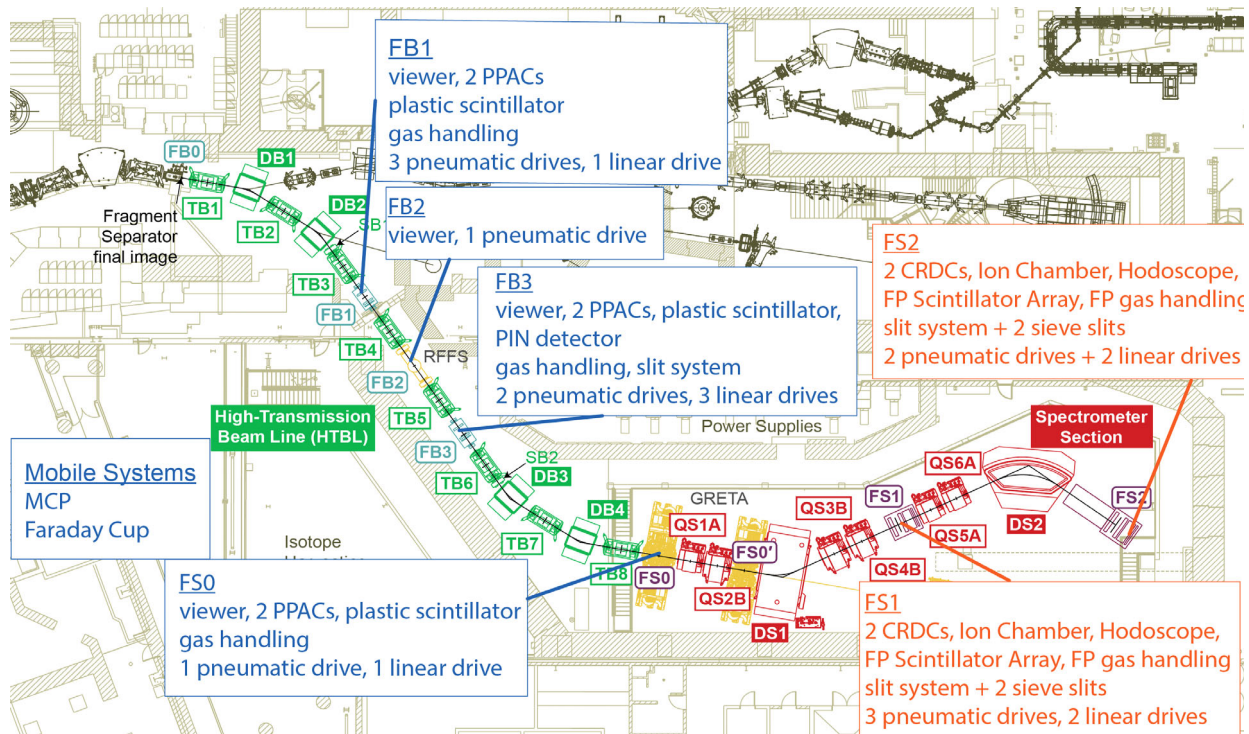


Figure 7-1. Schematic layout of the diagnostics/detector systems for the HRS. Systems at FB1, FB2, FB3, FS0, and mobile systems (blue border) are part of WBS element TPC.T.3.01. Systems at FS1 and FS2 are part of WBS element TPC.T.3.02.

Table 7-2 Overview of the detectors systems of the HRS, by location and purpose.

HTBL		
Location	Detector	Purpose
FB1	Viewer	Visual inspection of beam spot during tuning
	PPACs (2)	Position and angle tracking for diagnostic purposes or event-by-event tracking
	Plastic Scintillator	Beam rate and time-of-flight measurements
FB2	Viewer	Visual inspection of beam spot during tuning
FB3	Viewer	Visual inspection of beam spot during tuning
	PPACs (2)	Position and angle tracking for diagnostic purposes or event-by-event tracking
	Plastic Scintillator	Beam rate and time-of-flight measurements
	PIN Detector	Energy-loss measurement
Spectrometer Section		
Location	Detector	Purpose
FS0, FS0'	Viewer	Visual inspection of beam spot during tuning
	PPACs (2)	Position and angle tracking for diagnostic purposes or event-by-event tracking
	Plastic Scintillator	Beam rate and time-of-flight measurements
FS1	Drift chambers (2)	Position and angle tracking for diagnostic purposes or event-by-event tracking
	Ion Chamber	Energy-loss measurement
	Hodoscope	Total kinetic energy measurements
	Scintillator	trigger and timing detectors, rate determination, energy-loss measurement
FS2	Drift chambers (2)	Position and angle tracking for diagnostic purposes or event-by-event tracking
	Ion Chamber	Energy-loss measurement
	Hodoscope	Total kinetic energy measurements
	Scintillator	trigger and timing detector, rate determination, energy-loss measurement
Other		
Location	Detector	Purpose
Various	Multi-Channel Plate	Position determination
Various	Faraday Cup	Unreacted beam interception

The dispersion-matched mode allows for the measurement of tracks in the Spectrometer Section with momentum resolutions better than the momentum spreads in the beam without the need for event-by-event tracking in the HTBL, as described in Section 5.3.3. However, for ToF- $B\rho$  mass measurements, the momentum of the particles is determined by measuring the position of the beam



particles at FS0 (See Section 6.3.3). In addition, for some experiments it might be important to know the hit-position and/or angle at an event-by-event basis at the target location FS0 in order to optimize the operation of ancillary detectors. For example, the Doppler reconstruction for in-beam  $\gamma$ -ray spectroscopy with GRETA can benefit from the accurate determination of the hit location on the target, in particular when the dispersion-matched beam optics is employed and the beam spot on the reaction target (FS0) is large.

In both beam transport modes, viewers that can be monitored by camera are very beneficial for beam tuning purposes. Hence, the HTBL must accommodate such viewers at FB1, FB2, FB3, and FS0.

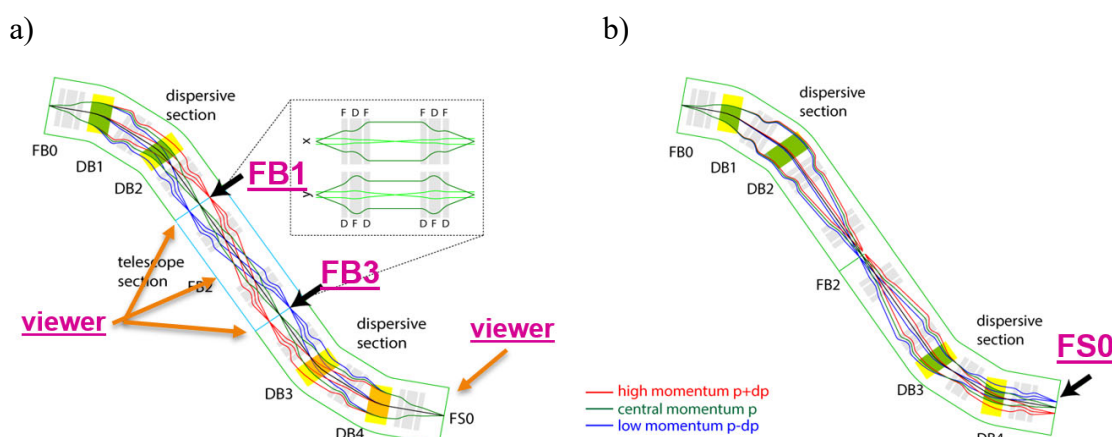


Figure 7-2. Schematic of the basic diagnostic systems configurations along the HTBL, used for the achromatic mode of operation (a) and for the dispersion-matched mode (b).

### 7.1.2 The Spectrometer Section diagnostics and detectors systems

The main goals of the diagnostics and detector systems of the Spectrometer Section are to:

- Facilitate initial commissioning of the HRS;
- Facilitate beam tuning and reaction-product identification and characterization
- Provide event-by-event tracking information (momentum, position, angle) and identification (energy loss and total energy measurements) for the physics analysis of events recorded in the HRS;
- Provide long-term stable beams operations by monitoring service for beam transport and machine protection.

The preliminary designs of the detector systems for the Spectrometer Section of the HRS are based on existing systems used at NSCL for the S800 spectrograph [YUR99] and Sweeper magnet system [BIR05]. Their use is supported by decades of experience in developing, maintaining and

operating these devices [GAD16]. High-resolution identification of reaction products generated in the heavy-ion reactions exploits the dispersion of magnetic spectrometers in conjunction with sophisticated particle detectors. The ion-optical calculations of Section 6.3 imply the need of covering a large surface at the focal planes. From this point of view, gaseous detectors are a convenient solution for providing good tracking capability for event-by-event momentum vector determination. They also deliver good resolution for charge ( $q$ ) measurements and for energy ( $E$ )/energy-loss ( $\Delta E$ ) spectroscopy, which is crucial for an efficient particle identification. As discussed in Section 6, particle trajectories are reconstructed by software using the momentum vectors measured in the focal plane of the Spectrometer Section (either at FS1 or FS2). The timing and energy-loss measurements provide the information to perform particle identification. Furthermore, measurement of the total kinetic energy allows one also to disentangle the ambiguities in the charge distributions of the reaction products generated in the target for each energy, mass and nuclear charge.

As discussed in Section 6, the Spectrometer Section was designed to operate in three basic modes, each of them with specific demands in term of focal-plane detector performance - the relationships of these modes to the tracking detector stations in the HTBL are shown in Figure 7-3:

- The high-resolution mode of operation, discussed in Section 6.3.1, provides the full spectroscopy capability of the HRS. To achieve the highest mass and momentum resolving powers for heavy rare isotopes, a long flight path is required (in excess of 25 m; the preferred layout achieves 33.6 m) and the focal plane at FS2 is used. The space around the FS0 reaction target station provides the opportunity to install ancillary detectors, including additional tracking detectors
- In the neutron invariant-mass mode, discussed in Section 6.3.1.6, the momentum vectors of the all reaction products, including the neutrons, need to be measured. The reaction target is placed immediately in front of the sweeper magnet, while the focal plane detector system is placed at the focal plane FS1. In this configuration, only part of the spectrometer is engaged as the transmission through the full Spectrometer Section is compromised by placing the reaction target right in front of the DS1 Sweeper dipole magnet. The fast neutrons emitted within a cone in the forward direction are detected by the MoNA-LISA array [BAU05,MRI09] and their momenta are assessed through a time-of-flight measurement. The required accuracy for the reconstruction of the momentum vector of the charged particles is lower compared to the experiments performed in the high resolution mode.
- For ToF- $B\rho$  mass measurements, discussed in Section 6.4.3, the HTBL is operated in dispersed-matched configuration, with no reaction target at FS0. Instead, the position at FS0 is measured with a dedicated high-resolution tracking detector to determine the rigidity of the beam particles on an event-by-event basis. The time-of-flight of the particles is



measured with dedicated high-precision timing detectors between the ARIS Fragment Separator and the FS2 focal plane in order to create a very long flight path (of 115 m in the preferred layout).

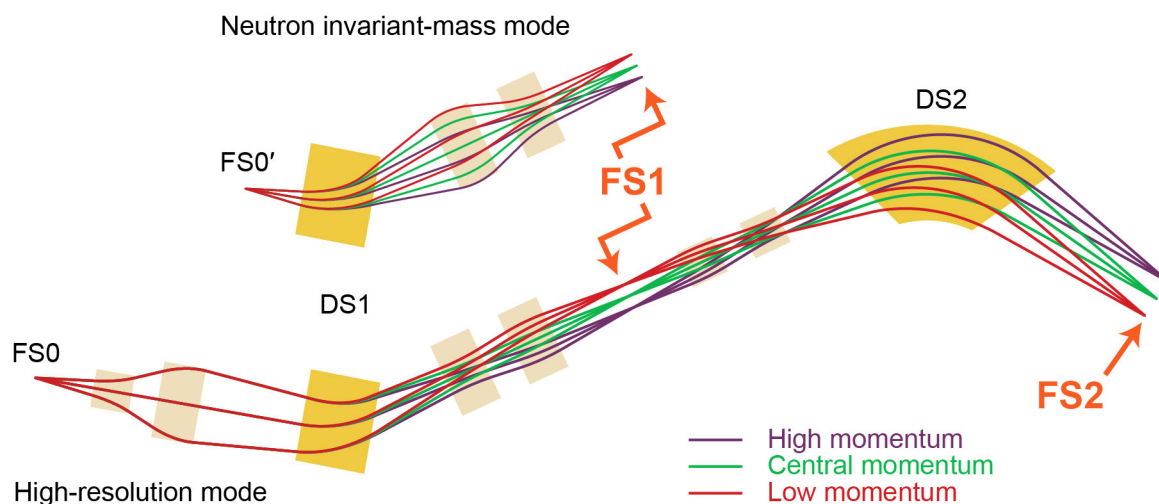


Figure 7-3 Schematic of the location of the diagnostic systems along the HRS, used for the neutron invariant-mass mode (top) and for the high-resolution mode (bottom).

## 7.2 Requirements and performance

To meet the scientific specifications discussed in Section 4, the diagnostic systems and tracking detectors for the HRS must satisfy technical requirements discussed in Section 5.8.2 for the HTBL and in Section 6.5.2 for the Spectrometer Section. These are reiterated here, in relation to specific detector technologies that will be employed and discussed in more detail in Section 7.3.

### 7.2.1 Requirements for the HTBL diagnostics and detector systems

General requirements for the HTBL diagnostic systems are summarized in Table 7-3. All the devices installed in the chambers along the HTBL must be retractable using remotely-controlled linear or pneumatic drives. Typical positioning accuracies of 0.5 mm, in the direction transverse to the beam, and 1 mm, along of the beam axis, are achieved by precise mechanical alignment of the drives. All the instrumentation installed in the HTBL image boxes are accessible through dedicated access ports and flanges, providing the capability for the repair or replacement of



damaged devices within 4 hours. For delicate gas-filled detectors that are equipped with thin vacuum windows, spares must be available. In addition, all the devices mounted inside the chambers are required to be vacuum compatible at a level of  $10^{-5}$  Torr to ensure negligible interference with the operation of all systems and the transport of heavy-ion beams.

Table 7-3 General functional requirements for the diagnostics and detector systems for the HTBL.

Parameter	Requirement
Remotely retractable	Yes
Positioning accuracy	$\leq 0.5$ mm (transverse to the beam) $\leq 1$ mm (along the beam axis)
Accessibility	Replacement possible within < 4 hours
Vacuum requirement	$10^{-5}$ Torr vacuum compatible

As discussed in Section 7.3, the primary type of particle-tracking detector for the HTBL is the Delay-line Parallel-Plate Avalanche Counter (D-PPAC) [KUM01,KUM13], and the requirements for these detectors are provided in Table 7-4. The tracking detectors provide event-by-event particle detection at FB1, FB3 and FS0, with 100% transmission and a spatial resolution of better than 1 mm (FWHM). Minimum energy loss and low angular straggling require low material budgets: the D-PPACs have thicknesses below  $10$  mg/cm<sup>2</sup>. For applications in which the thickness of the tracking medium must be minimized, the use of position-sensitive micro-channel plate (MCP) detectors [MON05] is an alternative, for example for tracking near the reaction target at FS0 (see Section 7.3.1.5) when reducing of materials placed just prior to the reaction target is critical or for reducing charge-state production in the HTBL. MCPs also find use as tracking devices in ToF-B $\rho$  mass measurements. The rate capabilities of the tracking detectors achieve a few hundred kHz for both D-PPACs and MCPs.

Table 7-4 Functional requirements for the tracking and timing detectors for the HTBL, satisfied by D-PPAC and plastic scintillators, respectively.

Parameter	Requirement	
Transmission	100%	
Single particle detection	Yes	
Thickness	Tracking	$\leq 10$ mg/cm <sup>2</sup>
	Timing	$\leq 100$ mg/cm <sup>2</sup>
Effective area	Tracking	$20 \times 20$ cm <sup>2</sup>
	Timing	$20 \times 20$ cm <sup>2</sup>
Resolution (FWHM)	Position	$\leq 1$ mm
	Timing	$\leq 150$ ps
Rate capability	Tracking	a few hundred kHz
	Timing	$\geq 1$ MHz





The principal timing detectors (at FB1, FB3, and FS0) will be plastic scintillators coupled to vacuum photo-multiplier tubes (PMTs) [HOI11], for which the requirements are also listed in Table 7-4. The plastic scintillators for timing measurements can be operated above 1 MHz and have thicknesses below 100 mg/cm<sup>2</sup>. Timing resolutions of better than 150 ps should be obtained.

Energy loss measurement for particle identification (PID) at FB3 is achieved using thin ( $\leq 500$  micron) silicon PIN diode [GRO75], for which the requirements are listed in Table 7-5. Commercially available silicon PIN detectors have a maximum area of 5x5 cm<sup>2</sup>, which ensures optimum performance in terms of resolution and rate. In order to cover the full dispersive coordinate for the energy-loss measurement at the FB3 chamber, an array of 4 PIN elements of 5x5 cm<sup>2</sup> will be carefully assembled to minimize dead areas in between the elements. To achieve charge separation up to high Z ( $\sim 92$ ), small stacks of such PIN detectors can be used [KWA18,TAR20]. Note that energy-loss measurements with this system are only meant for diagnostics purposes and not for event-by-event tracking.

In Table 7-6, the requirements for the viewer systems are provided. These relatively simple systems provide visual feedback for beam-tuning purposes.

*Table 7-5 Functional requirements for the energy-loss detectors for the HTBL, satisfied by the usage of silicon PIN diode detectors.*

Parameter	Requirement
Transmission	100%
Effective area	5 × 5 cm <sup>2</sup> each (with fiducials for calibration) 4 aligned detector for 20 × 5 cm <sup>2</sup> coverage
Thickness	$\leq 500 \mu\text{m}$
Energy resolution	$\leq 3\%$ (@ 5.5 MeV $\alpha$ -particles)
Rate capability	$\geq 1000 \text{ Hz}$

*Table 7-6 Functional requirements for the viewer systems for the HTBL.*

Parameter	Requirement
Single particle detection	No
Transmission	No
Coating	Thin luminescent layer: emits light when exposed to heavy ion beam
Effective area	20 × 20 cm <sup>2</sup> (with fiducials for calibration)



## 7.2.2 Requirements for the Spectrometer Section diagnostics and detector systems

General requirements for the tracking detectors in the Spectrometer Section are provided in Table 7-7. Typical positioning accuracies of 0.5 mm in the direction transverse to the beam, and 1 mm, in the direction along the beam axis are achieved through precise mechanical alignment. All the instrumentation installed in the focal-plane vacuum chambers are accessible through dedicated access ports and flanges. Expedient replacement of damaged devices must be achieved within 6 hours and for the relatively delicate gas-filled tracking detector systems with thin exit and entrance foils, spares must be available. All the devices mounted inside the chambers are required to be vacuum compatible at a level of  $10^{-5}$  Torr to ensure negligible interference with the operation of all subsystems and the transport of heavy-ion beams. The tracking detectors at FS1 are primarily used for invariant-mass spectroscopy experiments, but can also serve as additional tracking for experiments in which the full Spectrometer Section up to FS2 is utilized. Hence, these tracking detectors should be retractable. The ionization chamber and hodoscope at FS1 must be easily removable so as not to obstruct particles that are to be transported to FS2. The detector systems mounted at FS2 do not need to be retractable.

*Table 7-7 General functional requirements for the diagnostics and detector systems of the Spectrometer Section.*

Parameter	Requirement	
Remote retractability	FS1	Yes
	FS2	No
Position alignment accuracy	$\leq 0.5$ mm transverse to the beam axis	
	$\leq 1$ mm along the beam axis	
Accessibility	Replacement possible within < 6 hours	
Vacuum requirement	$10^{-5}$ Torr vacuum compatible	

The requirements for the tracking detectors used in the Spectrometer Section of the HRS are provided in Table 7-8. The tracking detectors at the focal planes provide event-by-event particle detection, with 100% transmission. To avoid significant multiple scattering and to minimize energy losses, the thicknesses of the tracking detectors are kept small. The detector systems in the focal planes of the Spectrometer Section (FS1 and FS2) must cover large areas. Therefore, for the transverse position and angle tracking, a set of gas-filled Drift Chambers (DCs), located about 1 m apart, are used. They must provide the position with a spatial resolution of 1 mm (FWHM) and be able to handle rates in excess of 10 kHz. A thick plastic scintillator must provide the timing signal and cover the same area as the tracking detectors. The timing resolution should be better than 150 ps. The rate capability of the scintillator should exceed 1 MHz.



Table 7-8 Functional requirements for the tracking and timing detectors for the Spectrometer Section.

Parameter	Requirement	
Transmission	100%	
Single particle detection	Yes	
Thickness	Tracking	$\leq 6 \text{ mg/cm}^2$
	Timing	100–300 $\text{mg/cm}^2$
Sensitive area	FS1	$100 \times 60 \text{ cm}^2$
	FS2	$100 \times 60 \text{ cm}^2$
Resolution (FWHM)	Position	$\leq 1 \text{ mm}$
	Timing	$\leq 150 \text{ ps}$
Rate capability	Tracking	$\geq 10,000 \text{ Hz}$
	Timing	$\geq 1 \text{ MHz}$

The energy-loss and total kinetic energy of the particles that enter the focal planes at FS1 and FS2 must be determined with good precision. The requirements are provided in Table 7-9. An ion-chamber is needed for an accurate energy-loss measurement with a resolution in energy loss of 1.3% (FWHM) to achieve  $4\sigma$  separation between isotopes with neighboring charge number up to  $Z=92$ . For the total kinetic energy measurement, which is important for separating charge-states that enter the focal planes, the particles are stopped in a hodoscope that must have a resolution of better than 7% for 662-keV  $\gamma$  rays. Such crystals achieve a light output resolution of 0.8% for the total kinetic energy measurement of heavy ions [MEI11]. The sensitivity to  $\gamma$ -rays is helpful for experiments in which isomers are produced that emit photons after being stopped in the focal plane. In this manner events in which isomers are created can be identified. Both the energy-loss and total kinetic-energy measurements should be performed at rates in excess of 10 kHz. It is noted that the plastic scintillator used for timing purposes also provides an energy-loss signal, but with relatively poor resolutions compared to an ion chamber. The combination of the timing, energy-loss, and total kinetic-energy signals provides the particle identification capability of the Spectrometer Section of the HRS.



Table 7-9 Functional requirements for the energy-loss detectors for the Spectrometer Section.

Parameter	Requirement	
Transmission	Ion Chamber	100%
	Hodoscope	No
Sensitive area	FS1	100 × 60 cm <sup>2</sup>
	FS2	100 × 60 cm <sup>2</sup>
Energy resolution	Ion Chamber	1.3%
	Hodoscope	≤ 7% (662 keV $\gamma$ -rays)
Rate capability	≥ 10,000 Hz	

### 7.3 The detector systems of the HRS

The necessary specifications can be met by utilizing designs in use at NSCL that have long-term proven performance and benefit from continuous development and optimization. Therefore, the preferred alternatives of the detector systems of the HRS are based on these existing technologies, which have been vetted against alternative technologies through years of performing experiments with fast beams at NSCL. Therefore, no special development program is required and the systems selected carry low risk with known performance and cost. For some detector systems, upgrades of technologies used at NSCL are ongoing and the preferred alternative benefits from these upgrades, which will be tested with rare-isotope beam prior to the implementation of the HRS. In the following, each of the detector and diagnostics systems are briefly discussed.

#### 7.3.1 The focal planes of the HTBL

As outlined in figure 7-1, the diagnostics system includes several diagnostics stations deployed along the HTBL. The first chamber (FB1) is positioned after the first bending dipole of the ARIS Fragment Separator in the HTBL and is equipped with two delay-line parallel-avalanche counters (D-PPACs) that serve to determine the beam-particle position and angle, and a plastic scintillator for providing a local timing signal. The schematic layout is provided in figure 7-4. This information is recorded on an event-by-event basis so that it can be correlated with measurements in other detector systems.



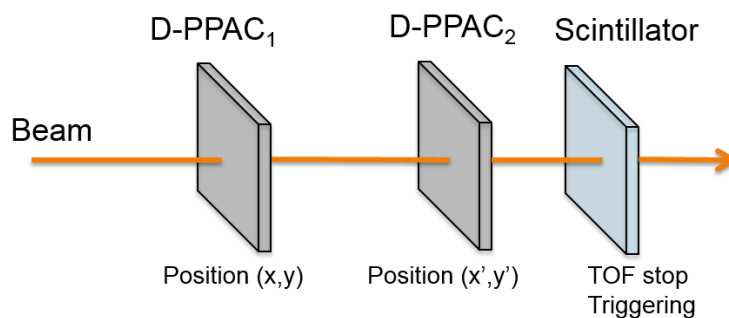


Figure 7-4. Schematic layout of the detector configuration of the diagnostic systems used at FB1 and FS0.

The third diagnostics chamber (FB3) is placed before the bend to the target station (FS0). It has a similar detector layout as the FB1 station, with the addition of a silicon PIN diode for the measurement of energy-loss, as schematically depicted in figure 7-5. The diagnostic chamber at FB3 also includes a variable slit system, which allows for beam shaping and background rejection. In addition, the slit system is necessary for a future insertion of a RF Fragment Separator at FB2, as discussed in Section 4.3.2.7.3.

FB2 is located in between the FB1 and FB3 and will only be equipped with a beam viewer for visual tuning of the beam through the HTBL. FB2 is otherwise reserved as the future location of a RF Fragment Separator.

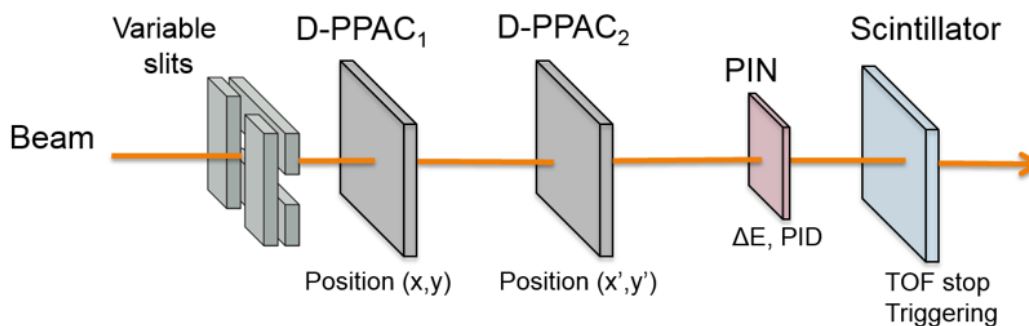


Figure 7-5. Schematic layout of the detector configuration of the third diagnostics station (FB3), which include a tracking system (two D-PPACs), a PIN diode for energy-loss measurement for PID, a plastic scintillator, as well as a system of variable slits for beam tuning and other diagnostic purposes.

The HTBL ends at the reaction target station (FS0), which can, if desirable for the experiment, be equipped with a set of D-PPACs for tracking and a thin plastics scintillator for timing, just like FB1. The detailed configuration of the setup around FS0 will vary from one experiment to another. Often, no tracking or timing detectors will be placed at FS0, but for a subset of experiments, high

precision tracking or timing is required at the target. An MCP detection system for accurate position determinations at high rates can also be placed at FS0.

All the diagnostics boxes along the HTBL are equipped with a scintillating viewer plate (red CRT phosphor –  $Y_2O_2S:Eu$ ) monitored by a ultra-low light bullet-type camera.

Most of the detector systems utilized at stations FB1, FB2, FB3, and FS0 can be inserted with pneumatic drives that move the detectors in or out of the path of the beam. Plastic scintillators are operated with linear drives, as the detectors should be moved by small amounts from time-to-time to prevent excessive localized radiation damage that deteriorates the signal quality. The slit system at FB3 is operated with linear drives as well.

All diagnostics chambers that have PPACs have dedicated gas handling systems. All chambers provide access to the front-end electronics, HV power supplies, and other signal and control system via flanges equipped with appropriate feedthroughs.

#### 7.3.1.1 HTBL diagnostics chamber

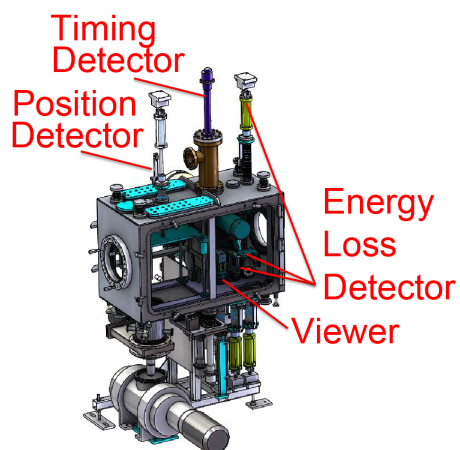
The preliminary designs of the chambers FB1, FB3, and FS0 for the HTBL are based on the chamber used at the NSCL A1900 fragment separator focal plane, which is shown in figure 7-6a. The vacuum chamber is a large-volume box of stainless steel, a side of which (perpendicular to the beam trajectory) can be fully opened for easy access to its contents. The top and bottom plates have several ports for mounting the device drives and pumping equipment. The compact, but versatile design of this diagnostic chamber makes it suitable for use in the HTBL. The boxes will be dielectrically decoupled from the beam line.

At FB2, a relatively simple system is required for inserting a viewer and a standard cross chamber (figure 7-6b) presently used at various locations in NSCL for similar purposes serves as the concept for use at the HRS. For all the diagnostic chambers, dedicated flanges are used to mount the drives that move devices into the beam path and to provide electrical/signal feedthroughs or vacuum gauges.





a)



b)

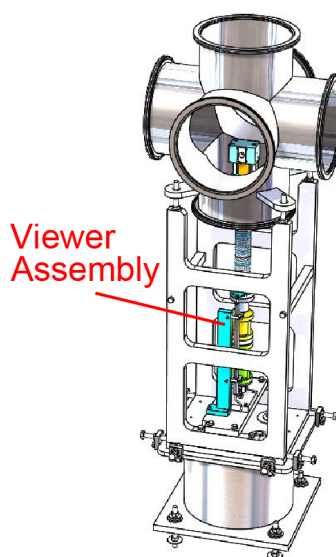


Figure 7-6. a) Design of the Image box of the A1900 Fragment Separator, which serves as the model for the design of the HTBL diagnostics boxes FB1 and FB3. B) Design of a standard cross chamber used to insert viewers and other simple diagnostics and detector system, which serves as model for the box at FB2.

### 7.3.1.2 The delay-line parallel-plate avalanche counters (D-PPACs)

The positions of the ions transported along the HTBL are measured at stations FB1, FB3, and FS0 by pairs of two-dimensional delay-line parallel plate avalanche counters (D-PPACs) [SWA74,HEM75,PUL02,CAR13,KUM13]. From these position measurements, the trajectory angle can also be determined. In the achromatic beam-transport mode, the momentum of the beam particles can also be determined (see Section 5.3.2). Each D-PPAC has an active area of 20 cm by 20 cm and is filled with isobutane at a typical pressure of 5-6 Torr by using a gas handling system. The detector consists of a cathode foil with a series of aluminum strips oriented in the non-dispersive direction, followed by an anode plate and a second cathode foil with the strips oriented in the dispersive direction. The strips are coupled to a discrete LC delay-line circuit and the position of the impinging particle is derived from the time difference between induced signals propagating along the delay-line circuit. Because the drift direction of the electrons is parallel to the beam direction, the drift-times are short, and the D-PPACs can operate at high rates without pile-up effects.

The tracking system based on D-PPACs provides:

- A position resolution of about 1 mm (FWHM) over the entire active area (20×20 cm<sup>2</sup>)

- A high counting-rate capability of a few hundred kHz
- Energy-losses that are low and independent of hit position for the particles passing through the detector
- Good signal-to-noise ratio for heavy-ions
- Cost-effective production in combination with a relative ease of maintaining and repairing the detectors

### 7.3.1.3 The plastic scintillator

In order to determine the Time-Of-Flight for the particle identification and to provide trigger signals for other tracking detectors, the HTBL includes plastic scintillators at chambers FB1, FB3, FS0. The detectors (ELJEN plastic scintillator type EJ-230 with a light output of 64% anthracene and a rise time of 0.5 ns [ELJ18]) have an active area that matches that of the tracking detectors (20×20 cm<sup>2</sup>). Thinner scintillator detectors are used for heavier ion species. The scintillation light emitted by the scintillator is read out by vacuum photomultipliers (HAMAMATSU type R4998, with TTS 0.16 ns; QE 22 %, assembly H6533).

For high-precision timing measurements, required for ToF- $B\rho$  mass-measurements, specialized systems will be adopted, which are outside of the scope of the HRS, such as small plastic scintillators fitted with two or more photomultipliers (see e.g. [MAT12]). These detectors are relatively inexpensive, but benefit from continuous development specific for particular experiments.

### 7.3.1.4 The silicon PIN detector

The charge and mass identifications are based on the combined measurements of energy loss and time-of-flight of the beam particles transported along the HTBL. An accurate energy loss spectroscopy for the atomic-number identification is performed with a thin silicon PIN detector [HAR96,TIN08] mounted in chamber FB3. The ability to identify atomic numbers of fission fragments of known mass and velocity using the energy-loss method depends on the difference in mean energy loss of adjacent atomic numbers, the energy-loss straggling, and the precision of the energy-loss measurement. The limiting factor for atomic-number resolution of the beam particles using the energy-loss method is charge-transfer straggling and electronic energy straggling. Other contributions to the energy-loss width such as absorber path length difference must be kept to a minimum. The energy-loss measurement must be performed in extremely thin and uniform absorbers due to the large stopping powers of heavy-ions. Note that the insertion of PIN detectors at FB3 is only meant for diagnostic purposes – they will not be inserted during regular data runs.

A large assortment of silicon-based detector technologies for energy-loss measurement are commercially available. Typical energy resolution are within the range of a few percent at 5.5



MeV ( $\alpha$  particle), depending of the thickness of the detector effective area, which can be made as thin as 100 microns. Good resolution is achieved thanks to the excellent thickness uniformity across the detector area, made possible by current advanced silicon production technologies. This allows for the charge separation of up to  $Z \sim 92$  using small stacks of such silicon PIN detectors [KWA18,TAR20].

#### 7.3.1.5 The position-sensitive multi-channel plate (MCP)

Detectors for heavy-ions based on Micro-Channel Plates (MCP) have been widely used for many years in experimental set-ups for nuclear physics studies at low and intermediate energies [JAG02,ARN14,MEI15,ROG15,HON16]. These detectors can withstand incident-beam intensities of around 100 kHz at long exposure before degradation in resolution and they are characterized by an extremely low material budget ( $\sim 70 \mu\text{g}/\text{cm}^2$ ). Such features make MCPs desirable as tracking detectors for experiments requiring high intensity rare-isotope beams and/or when minimum energy loss is required. Accurate position sensitivity (below 1 mm) in one or two directions can be achieved by suitable read-out systems. Although less convenient to utilize and requiring more calibration and service than PPACs for tracking, for specific applications the use of an MCP is desirable. MCP detectors require a vacuum of  $10^{-6}$  Torr. Since this is a more stringent requirement than for the rest of the beam line, it can be addressed by adding local pumping capacity, as is presently done when MCPs are used in combination with the S800 Spectrograph at NSCL.

### 7.3.2 The focal planes of the Spectrometer Section

The focal planes of the Spectrometer Section are equipped with various detectors for trajectory reconstruction as well as particle identification (PID). The basic detector system configuration planned for the Spectrometer Section is based on the focal plane detector array of the NSCL S800 Spectrometer [YUR99,BAZ03], and was described in section 7.2.2. It consists of a series of two x/y drift chambers, an ionization chamber, a plastic scintillator for timing and a hodoscope, as schematically depicted in figure 7-7.



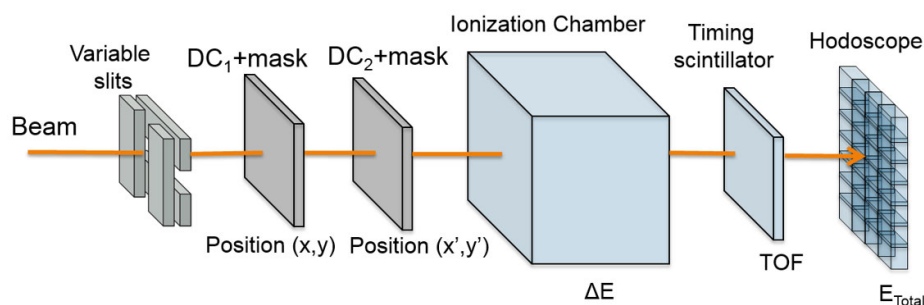


Figure 7-7. Schematic layout of the detector configuration of the focal planes of the Spectrometer Section.

### 7.3.2.1 Focal plane vacuum chamber

The vacuum chambers for the focal plane detector system of the Spectrometer Section are large and must maintain a vacuum of  $10^{-5}$  Torr. Therefore, they will be constructed from welded stainless-steel plates. The concept for these chambers is similar to the one used for the Sweeper Magnet system at NSCL. The main difference between the existing system (depicted in figure 7-8) and the system required for the HRS is the size of the chamber, as the focal-plane detectors are larger.

The focal plane vacuum chamber will be equipped with an internal rail system to support and accurately locate the detectors and adjust their positions along the beam axis. The chamber will have a suitable “cable race” at the bottom for the routing of the power cables, cooling, and gas lines needed to operate the detectors. Pneumatically driven rotary actuators are located outside the vacuum chamber for turning the drive shafts attached to the mask assemblies, which allow to raise and lower the DC masks for position calibration. These mask have small holes that, when impinged by beam, will leave a pattern in the drift chamber that can be used to calibrate the drift velocity and timing offset. The masks are not in place during regular data runs. In addition, a linear drive is used to control a blocker for intercepting unreacted beam particles in front of the tracking detectors in case the rigidity of the particles of interest are close to that of the unreacted beam during regular data taking. In addition, the chamber will have several access ports and flanges for the mechanical/turbo vacuum pumps, pressure transducers, the signals and HV bias feedthroughs, and cooling system for the detector front-end electronics; several access panels for installing and removing the instrumentation from the chamber.

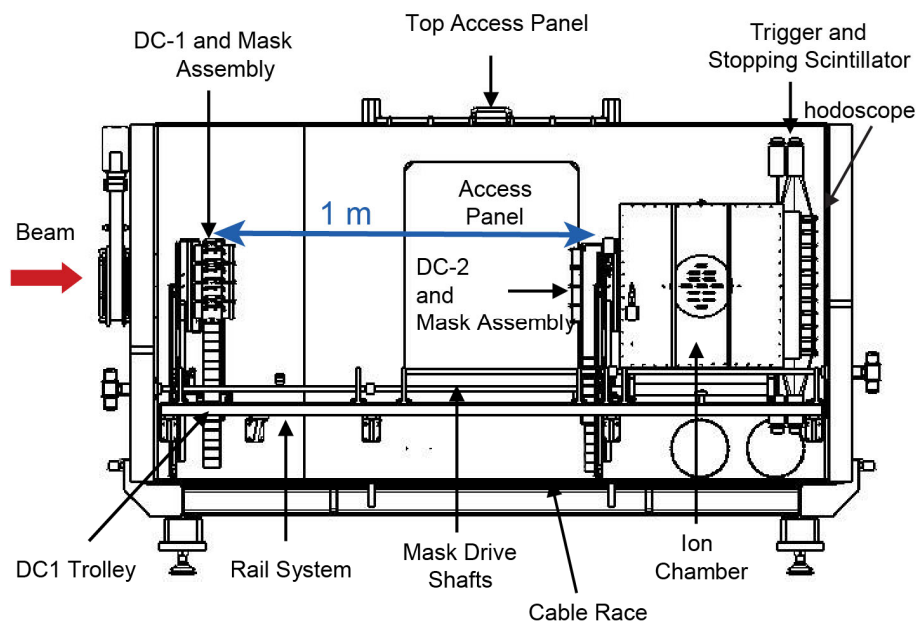


Figure 7-8. Layout of the existing charged-particle detector chamber as presently used for experiments with the Sweeper Magnet at NSCL. The focal-plane detector chambers for the HRS have comparable layout, but are larger in size to accommodate the larger detector systems.

### 7.3.2.2 The drift chamber (DC)

Two large-area Drift Chambers (DCs) that will be placed 1 meter apart are used to measure the positions and derive the angles in each of the focal planes at FS1 and FS2 of the Spectrometer Section. The required position resolution is 1 mm (FWHM), from which the angle of the trajectory can be determined with a resolution of better than 2 mrad, even if multiple scattering effects in the detector planes are considered [BAZ03,S800]. As the windows utilized are thin ( $\sim 0.1 \text{ mg/cm}^2$ ) polypropylene foils and operating pressures of the gas (80%  $\text{CF}_4$  and 20% of  $\text{iC}_4\text{H}_{10}$ ) is  $\sim 40$  Torr, multiple straggling of even the heaviest isotopes at the lower rigidities (4 Tm) is less than 0.25 mrad, hardly increasing the limit of 1.4 mrad that can be achieved with a position resolution of 1-mm in each detector plane. This is sufficient for performing an accurate reconstruction of the particle trajectory at the reaction target, as is presently also performed for experiments with the S800 Spectrograph at NSCL [BAZ03]. A schematic depiction of the DC layout is provided in Figure 7-9.

The dimension of the active area of the DCs is  $\pm 30$  cm in the non-dispersive direction and  $\pm 50$  cm in the dispersive direction for the FS1 and FS2 focal planes. The DC are filled with standard Ar-based mixtures (e.g. P10) at pressures in the range of 30-50 Torr. The maximum rate is approximately 20 kHz. Above this rate, efficiency losses due to space-charge effects are to be expected, in particular if the beam is concentrated on a small area of the detector. The use of D-

PPACs for the Spectrometer Section focal planes is not feasible, as the surface that needs to be covered is relatively large. It is not possible to make such large D-PPACs for which thin foils are used and the gap between the windows is consistent. In addition, when increasing the size of a D-PPAC, the delay lines become long and the signals deteriorate,

The DCs will be based on a design that is presently being constructed for use with the S800 Spectrometer. Instead of the present Cathode-Readout Drift Chamber used at the NSCL S800 spectrometer, the new DC designed for the HRS implements a more advanced hybrid micro-pattern gaseous detector readout; the latter comprises of a multi-layer Thick Gaseous Electron Multiplier (M-THGEM) [COR17] mounted on top of a position-sensitive Micromegas [GIO96] readout, as shown in Figure 7-10. This new position-sensitive hybrid readout configuration, originally developed and currently implemented as charge readout for the Active-Target Time Projection Chamber project [BAZ17], has the advantages of higher gas avalanche gain, excellent position resolution and better reduction of the ion-backflow, leading to overall improvement of the operational stability of the detector. Furthermore, in the conventional CRDC the typical drift times of the electrons to the anode wires are a few hundred ns to around 20  $\mu$ s, depending on the position of the track in the non-dispersive direction. The relatively long drift times limit the maximum rate that the detector can process properly to around 5-10 kHz. The new detector configuration offers the possibility to increase the field strength on the drift volume with a sizeable increase of the drift velocity of the electrons and thus a better rate capability. The signals from the micromegas readout pads (~2000 channels) are read out and processed by a GET electronics based DAQ system [POL12], characterized by low noise, high data transfer capabilities and multi-hit capability for an efficient digital rejection of pile-up events.

A prototype of the new drift chamber has been tested in the focal plane of the S800 Spectrograph [COR20] by using 150MeV/u  $^{78}\text{Kr}^{36+}$  beam as well as a heavy-ion fragmentation cocktail beam produced by this beam impinging on a thin beryllium target. In (a) the reconstructed pattern of a mask with holes and slits used for calibration of the drift chamber is shown. In (b), the image of one of the holes in the mask in the dispersive direction is shown. By taking into consideration the dimensions of the hole, a position resolution of 0.25 mm ( $\sigma$ ; 0.6 mm FWHM), was achieved, meeting the requirements for the HRS focal-plane tracking detectors.





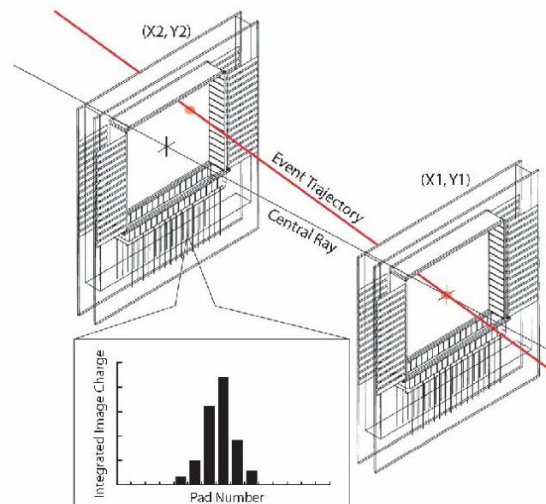


Figure 7-9. Schematic drawing of the tracking system of the spectrometer focal plane as it is presently used in the S800 Spectrograph at NSCL. The focal-plane tracking detectors of the HRS are upgraded versions of these detectors.

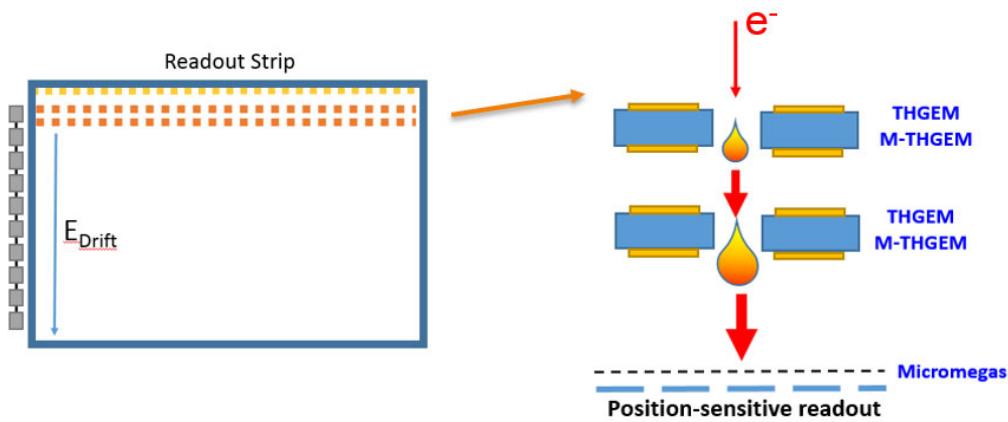


Figure 7-10. Position-sensitive readout of the DC to be implemented for tracking at the spectrometer focal plane.

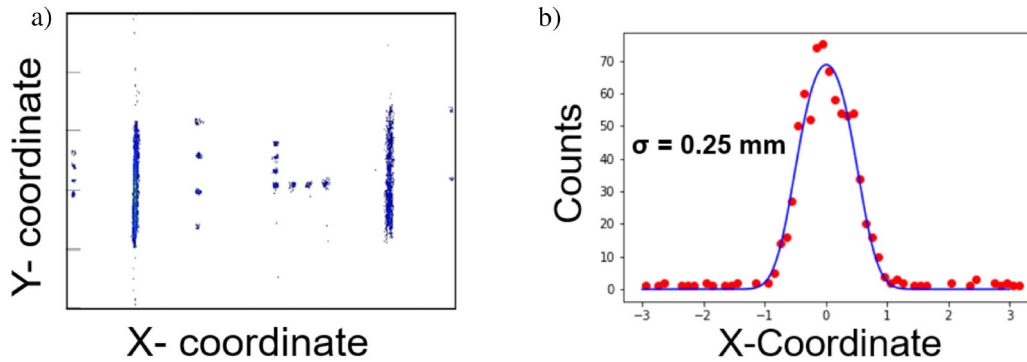
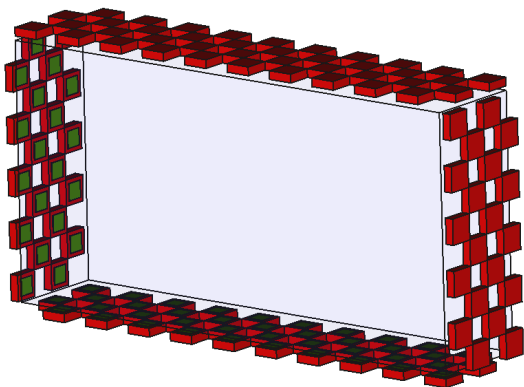


Figure 7-11(a) Reconstructed pattern of a mask with holes and slits placed in front of a prototype drift chamber for the S800 spectrograph [COR20] that operates in the same manner as the drift chambers of the Spectrometer Section focal planes. (b) Projection in the dispersive direction of the reconstructed pattern from one of the holes in the mask. A position resolution of 0.25 mm ( $\sigma$ ; 0.6 mm FWHM) is deduced.

### 7.3.2.3 The optical ionization chamber (OIC)

An Optical Ionization Chamber (OIC) installed downstream of the DCs is used to identify the atomic number of the transmitted nuclei from their energy loss. The OIC detectors have an active area that match the one of the DCs and a depth of about 150 mm. The OIC for the HRS is based on the OIC presently under construction for use in the S800 spectrograph focal-plane box, see figure 7-12. The OIC is filled with high-scintillation-yield gas, such as Xenon (Xe). The scintillation light emitted along the track of a beam particle that cross the OIC is intense (approximately 28 photons/keV, about 70% of that for NaI) and prompt (photons are emitted within a few nanoseconds - the decay time is 5 ns for the fast component and 30 ns for the slow component). The scintillation light is read out by an array of photodetectors that are placed around the detector volume.



*Figure 7-12. Schematic layout of the OIC presently under construction for the S800 Spectrograph at FRIB. The detector volume is filled with Xenon gas and surrounded by an array of photodetectors.*

The OIC has several advantages over traditional ion chambers that rely on the detection of electrons. The OIC is not limited by the long drift lengths for electrons in a traditional ion chamber and can provide a timing signal of good resolution ( $<50$  ps) and operate with higher beam intensities. The rate capability is expected to be at least 4 times higher than that of the traditional ion chamber ( $\sim 5$  kHz). The OIC has a very homogeneous medium and there is no risk of radiation damage. Unlike the traditional ion chamber, the OIC readout is decoupled from the sensitive medium, which is very beneficial for improving the signal-to-noise ratio. By using the signals from the photodetectors it is also possible to determine the hit position of the track with an expected precision of several millimeters, which could be beneficial for tracking purposes.

Simulations have been performed to estimate the improvement in energy-loss measurement resolution of the OIC compared to a traditional ion chamber. The OIC achieves a resolution of 1.2% ( $\sigma$ ). This makes the Z separation of even the heaviest elements possible, as shown in Figure 7-13. The design of the HRS OIC will be optimized based on the experiences with the S800 OIC.

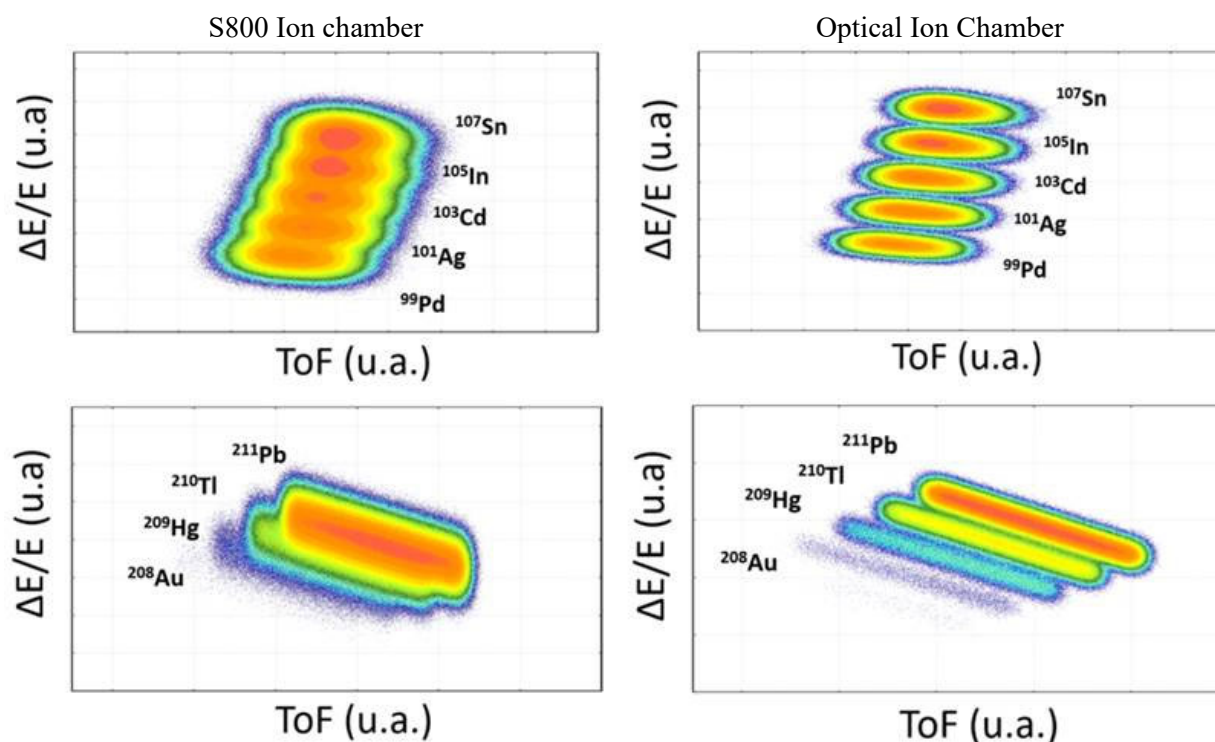


Figure 7-13 Illustration of the Improvement in particle identification ( $\Delta E$  vs. ToF in arb. units) through increased  $\Delta E$  resolution (sigma) through LISE++ simulations – Top: Sn, In, Cd and Ag for a traditional (S800) ion chamber (left) and optical ion chamber (right) resolution. Bottom: Pb, Tl, Hg, Au at current (left) and improved resolution (right). Simulations were performed for one reaction residue per relevant Z line to illustrate the  $\Delta E$  separation in the particle identification for example one-neutron knockout experiments from  $^{108}\text{Sn}$  and  $^{212}\text{Pb}$  projectiles to  $^{107}\text{Sn}$  and  $^{211}\text{Pb}$ .

#### 7.3.2.4 The plastic scintillator

The scintillation detectors are placed behind the Ionization Chamber and provide energy loss and timing information. The detector consists of a plastic scintillator sheet (~1-mm thick) that will match the areas of the other tracking detectors. The scintillator type is EJ-230 (Light output 64% Anthracene; Rise time 0.5 ns; attenuation length 120 cm), coupled to a series of H6533-assembled HAMAMATSU R4998 PMTs that surround the scintillator area. This configuration allows to reach an optimal photon-collection efficiency and an expected time resolution of the order of 150 ps (FWHM) or better. A similar design is presently being implemented for the S800 Spectrograph at NSCL, for which an illustration is provided in Figure 7-14. The scintillator for the focal-plane detector systems at FS1 and FS2 will have a similar layout but with dimensions (600 mm x 1000 mm) appropriate for the beam envelope at the HRS.

A prototype of a plastic scintillator based on the same principle, but smaller in size (300 mm x 150 mm) and only 6 PMTs was tested, in collaboration with researchers from Central Michigan University, by using a laser. This was done in part to prepare for the installing a detector with dimensions of 600 mm x 300 mm in the focal plane of the S800 Spectrograph. The timing resolution achieved with the prototype was 40 ps (FWHM). The larger size of the HRS focal plane requires that more PMTs must be used than for a smaller scintillator. Based on the measurements with the prototype, the response was modelled and the timing resolution achievable with larger-size scintillators was estimated. For the S800 spectrograph scintillator 12-14 PMTs are expected to be needed, and for the HRS scintillators, 26 PMTs are expected to be needed to achieve better than 150 ps across the detector plane, as shown in Figure 7-15.

The latter number will be finalized once the performance of the new S800 Spectrograph scintillator is known.

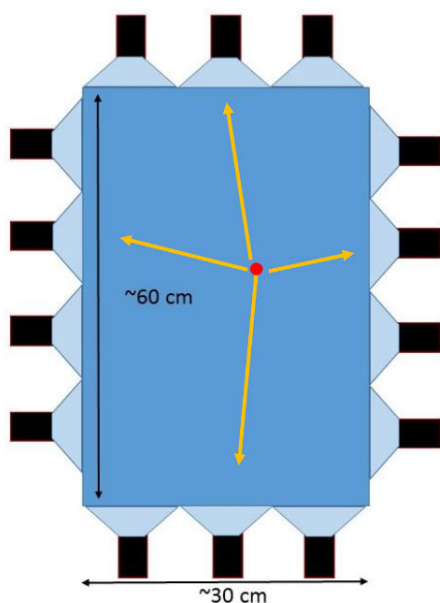


*Figure 7-14. Schematic drawing of the scintillator detector used for timing at the S800 spectrograph focal plane. A similar design will be used at focal planes FS1 and FS2 of the Spectrometer Section.*

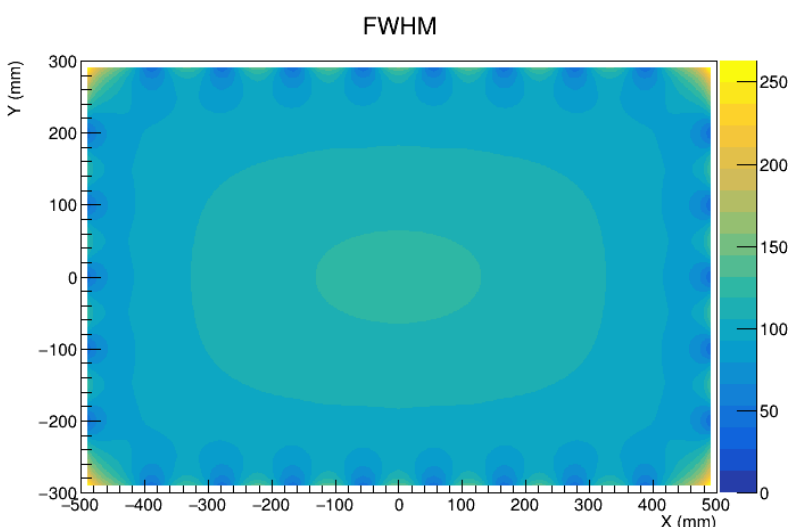


Figure 7-15 Estimated timing resolution of a plastic scintillator detectors for the Spectrometer Section focal planes. Light is detected through 26 PMTs attached to the sides of the scintillators. The estimates are based on the response measured with a smaller-sized prototype. A resolution of  $\sim 120$  ps or better is achieved in all areas where particles will be detected in the focal plane.

### 7.3.2.5 The hodoscope

A CsI(Na) hodoscope detector, located downstream of the plastic scintillator, is used to measure the total kinetic energy (TKE) of implanted nuclei, allowing for the identification of different atomic charge states. Additionally, the hodoscope can also be used to detect isomer gamma-rays emitted from the captured nuclei. This type of TKE detector has been successfully implemented at the S800 Spectrograph [MEI11] and is also used for isomer tagging [WIM14].

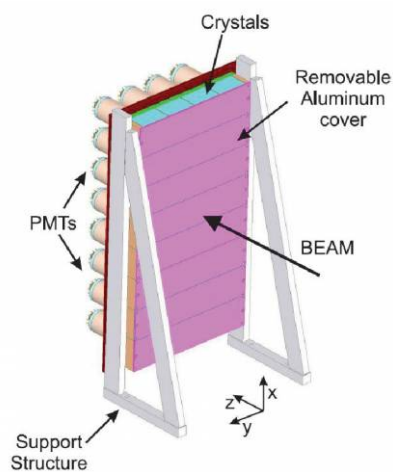


Figure 7-16. Schematic drawing of the hodoscope detector for TKE measurements as presently used in the S800 Spectrograph. The hodoscope that will be used in the focal planes of the Spectrometer Section of the HRS will be similar, but the area covered will be larger to account for the larger beam envelope.

The basic concept of the hodoscope includes a two-dimensional array of closely packed CsI(Na) scintillating crystals, attached to a vacuum photomultiplier (PMT). A good choice for the latter is the Hamamatsu R1307, for its photo-cathodes are made of a bi-alkali material with an responsivity



that perfectly matches the scintillation spectra of the CsI(Na) crystals. The crystals are arranged in a 2D array with a total effective area that allows to cover the full envelope of the particle tracks. The frontal and lateral sides of each crystal are covered with two 150- $\mu\text{m}$  thick layers of a reflective material (typically white Teflon) to provide light shielding between the crystals.

#### 7.3.2.6 The gas handling system

The spectrometer focal planes include three large-volume gaseous detectors, two drift chambers and one ionization chamber. Their gas handling systems (GHS) are designed to be a high purity gas delivery system to provide up to 50 sccm gas flow to the detectors. The systems are made up of four components: gas supply, the gas handling system control box, the detectors, and the roughing pumps. The GHS have two independent delivery systems for the two types of detectors in each focal plane chamber. One of the delivery systems is dedicated to the DCs and the other is dedicated to the Ion Chamber (IC).

#### 7.3.3 Data acquisition systems for the HRS

The detector systems for the HTBL and Spectrometer Section must be read out by appropriate data acquisition system and analyzed by efficient software. The existing NSCL Data acquisition system (NSCLDAQ) is a modular toolkit, for distributed data acquisition suitable for experimental nuclear physics. It is continuously improved and adapted for new hardware by FRIB Laboratory staff, in close coordination and collaboration with users of the facility. Present developments focus on high-rate data streaming and parallel processing capabilities. Such developments are very beneficial for experiment with the HRS. Therefore, the detector systems of the HRS will also employ this data acquisition framework.

NSCLDAQ features a generalized data flow architecture that supports delivery of data from an arbitrary set of sources to an arbitrary set of consumers on any other system reachable on the network. Consumers can, in turn, be sources for another stage of data flow. Simple proxy objects are used to perform traffic aggregation (data are only sent to a system with consumers once).

The system is open for expansion and is well documented [DAQ18]. Several frameworks have been provided to read out data from what have become standard data source types. These include frameworks for the VMUSB and CCUSB modules from Wiener/JTEC as well as a generic framework that is used both for legacy SBS/Bit3 PCI/VME bus bridges and to readout XIA Digital systems based on the PIXIE-16 module. The ability to acquire data from the Generalized Electronics for TPCs (GET) is implemented as well, which will, among others, be used to read out the DCs of the Spectrometer Section. Additional frameworks can relatively easily be included, so that FRIB is high adaptable to DAQ systems provided by the users that will operate in coincidence with the detectors of the HRS.



NSCLDAQ features a timestamped generic event builder. It can accept event fragments from segments of the dataflow system, order these data by timestamp and emit events that consist of fragments that are within a user specified coincidence window. These data are submitted back to the NSCLDAQ data flow system where they can be used in later stage event builders. This design allows for the combination of detectors with independent data acquisition systems without modification to each individual component: a procedure routinely done at NSCL and important for the HRS for reasons described above.

The openness of the data distribution system allows users to attach and operate any data analysis framework they choose, including the CERN ROOT system [ROOT97] for online analysis. NSCL provides a general histogramming framework called NSCLSpecTcl. NSCLSpecTcl can be used for online or offline analysis, and like NSCLDAQ, is supported by Laboratory staff. NSCL SpecTcl, is also well documented [SPEC18]. NSCL SpecTcl's model requires experimenters only to produce parameters of interest from incoming data. The user interface then supports dynamic creation of histograms and gates, and the application of gates to histograms. A rich set of histogram types and gate types allows for very generic analyses.

NSCLDAQ and NSCL SpecTcl are open source projects available for license by the MSU Board of Trustees under the GPLv2 license. SourceForge provides a public facing portal to download either of these systems [SFDAQ18, SFSPEC18].

The integration of multiple devices (both local and external) into the NSCLDAQ framework has been proven to be successful. A good example is the integration of the GREYTA and S800 Spectrograph DAQ systems [FOX18, REC13], which serves as a model for the integration of GREYTA and HRS DAQ systems in the future. Since then, the synchronization of data acquisition systems based on timestamping became the default requirement for many of the experimental campaigns. This technique has been developed and optimized for both VME, CAMAC, and DDAS electronics. Additional examples of those are the integration of the S800 Spectrograph DAQ systems with the LENDA neutron detector array [LIP18], CAESAR gamma-detector array [ELM17, LON18], and the ORRUBA charged-particle array [WAL19]. Integration of EPICS into event data streams has also been done, for example for mass measurement experiments [EST11, MAT12, MEI13, MEI15].

For the operation and commissioning of the HRS it is important that the information processed in the DAQ system is immediately processed and available for assessing the quality of the data taking and assessing of the beam transport functionality, including studies of the correlation between beam parameters at different focal planes and the ion-optical transfer matrix elements. Such analysis can conveniently be performed using the above-mentioned NSCLSpecTcl framework. This framework is presently used for the same purposes for the A1900 fragments separator and



the S800 spectrograph. Details of the S800 DAQ system can be found in reference [S800DAQ], including electronics diagrams. The HRS DAQ system will resemble this system.

### 7.3.4 Ancillary detector and support

The Spectrometer Section is equipped with a large, changeable multi-purpose station that precedes the target stations FS0 and FS0'. It can house various ancillary detectors (see Figure 4-17), including those that are large, such as GRETA. Therefore, the scope of the HRS includes platforms around the target stations to mount these detectors, based on existing designs for the placing of GRETINA in front of the S800 Spectrograph. As the Spectrometer Section is situated in a pit due to the large vertical sizes of the magnets, the platforms must be raised to the beam level. A 50-ton crane situated in the HRS high bay will be used to lift heavy items onto these platforms.

Similarly, the components of the MoNA-LISA detector array [BAU05, MRI09] must also be raised to beam height at their location behind the DS1 Sweeper magnet. For that purpose, additional platforms are included in the scope of the HRS. These platforms are simpler than the ones needed for the placement of GRETA, as their sole purpose is to place the MoNA-LISA detectors statically in the correct location, without the need for potentially complex adjustments during experiments. Hence, the main difference with existing detector stands used for the MoNA-LISA detectors is that they need to be raised sufficiently higher.

### 7.3.5 Alarms and interlocks for equipment protection

The HTBL diagnostics devices and the spectrometer focal plane detectors system will be protected from excessive beam rate by an automatic interlock system, blocking/dumping the beam whenever the pre-set count rate limit is exceeded. The measurement of the count rate will be performed with one of the HTBL PPACs or a dedicated plastic scintillator. The limit will be experiment specific since rate damage, especially in the tracking devices, has been observed to correlate with Z and intensity/area. The shutoff of the beam will be accompanied by a voice/visual alarm in the FRIB control room and in the user data station.

An alarm server will be used to monitor the gas handling system of the HTBL PPACs and of the focal-plane detectors (the drift chambers and the ionization chamber), and to monitor the HV power supply of the focal plane tracking systems, the ion chamber, and the tracking PPACs.

A “voice/visual” alarm in the user data station will be triggered whenever the pressure excursions in the gaseous detectors (PPACs, Drift Chamber and ion chamber) will be outside an acceptable range, signaling a failure of the gas handling system or a gas leakage along the beam line.



The high voltage of the above-mentioned detectors will be controlled by a dedicated application and an alarm is triggered when the read back value of the power supply does not match the set value: this will interlock the detector power supply and the event will be brought to the attention of the on-shift person immediately. The device or beam physicists provide instructions on the expected response to the possible alarms.

## 7.4 References

- [ARN14] C.W. Arnold et al., “Development of position-sensitive time-of-flight spectrometer for fission fragment research”, Nucl. Instr. and Meth. in Phys. Res. A, 764 (2014) 53-58
- [BAU05] T. Baumann et al., Nucl. Instr. and Meth. A543, 517 (2005)
- [BAZ03] D. Bazin et al., “The S800 spectrograph”, Nucl. Instrum. Methods Phys. Sect. B, 204 (2003), pp. 629–633.
- [BAZ17] D. Bazin et al., EPJ Web Conf. 163, 4 (2017).
- [BIR05] M. D. Bird et al., “System testing and installation of the NHMFL/NSCL sweeper magnet,” IEEE Trans. Appl. Supercond., vol. 15, no. 2, pp. 1252–1254, Jun. 2005.
- [BRA17] J. Bradt et al., “Commissioning of the Active-Target Time Projection Chamber,” Nucl. Instrum. Methods Phys. Res. Sect. Accel. Spectrometers Detect. Assoc. Equip., vol. 875, pp. 65–79, Dec. 2017.
- [CAR13] I.P. Carter et al., “An ion beam tracking system based on a parallel plate avalanche counter”. EPJ Web of Conferences, 63 (2013), p. 02022
- [COR17] M. Cortesi et al., “Multi-layer thick gas electron multiplier (M-THGEM): A new MPGD structure for high-gain operation at low-pressure,” Rev. Sci. Instrum., vol. 88, no. 1, p. 013303, Jan. 2017.
- [DAQ18]<http://docs.nsl.msui.edu/daq/newsite/nscldaq-11.2/index.html>;  
<http://docs.nsl.msui.edu/daq/>
- [ELJ18] <https://eljentechnology.com/products/plastic-scintillators/ej-228-ej-230>
- [ELM17] Elman B., “Quadrupole collectivity beyond N=50 in neutron-rich Se and Kr isotopes”, Phys. Rev. C 96, 044332 (2017).
- [EST14] A. Estrade et al., Phys. Rev. Lett. 113, 132501 (2014)
- [FOX12] Gretina User Documentation, Ron Fox, 2012
- [GAD16] A. Gade and B. M. Sherrill, “NSCL and FRIB at Michigan State University: Nuclear science at the limits of stability,” Phys. Scr., vol. 91, no. 5, p. 053003, 2016.
- [GIO96] Y. Giomataris, P. Rebourgeard, J. P. Robert, and G. Charpak, “MICROMEAS: a high-granularity position-sensitive gaseous detector for high particle-flux environments,” Nucl. Instrum. Methods Phys. Res. Sect. Accel. Spectrometers Detect. Assoc. Equip., vol. 376, no. 1, pp. 29–35, Jun. 1996.
- [GRO75] J. J. Grob, A. Grob, A. Pape, and P. Siffert, “Energy loss of heavy ions in nuclear collisions in silicon,” Phys. Rev. B, vol. 11, no. 9, p. 3273, 1975.



- [HAR96] R. Hartmann et al., “Low energy response of silicon pn-junction detector,” Nucl. Instrum. Methods Phys. Res. A, vol. A377, pp. 191–196, 1996.
- [HEM75] G. Hempel, F. Hopkins, and G. Schatz, “Development of parallel-plate avalanche counters for the detection of fission fragments,” Nucl. Instrum. Methods, 131 (1975), pp. 445–450.
- [HOI11] R. Hoischen et al., “Fast timing with plastic scintillators for in-beam heavy-ion spectroscopy,” Nucl. Instrum. Methods Phys. Res. Sect. Accel. Spectrometers Detect. Assoc. Equip., vol. 654, no. 1, pp. 354–360, Oct. 2011.
- [HON16] R. Hong et al., “High accuracy position response calibration method for a micro-channel plate ion detector” Nucl. Instr. and Meth. in Phys. Res. A, 835 (2016) 42-50
- [JAG02] O. Jagutzki, et al., “Position sensitive anodes for MCP read-out using induced charge measurement”, Nucl. Instrum. Methods Phys. Res. Sect. A: Accel. Spectrom. Detect. Assoc. Equip. 477 (1–3) (2002) 256–261
- [KUM01] H. Kumagai, A. Ozawa, N. Fukuda, K. Sümmerer, and I. Tanihata, “Delay-line PPAC for high-energy light ions,” Nucl. Instrum. Methods Phys. Res. Sect. Accel. Spectrometers Detect. Assoc. Equip., vol. 470, no. 3, pp. 562–570, 2001.
- [KUM03] H. Kumagai et al., “Development of Parallel Plate Avalanche Counter (PPAC) for BigRIPS fragment separator,” Nucl. Instrum. Methods Phys. Sect. B, 317 (2013), pp. 717–727.
- [KUM13] H. Kumagai et al., “Development of Parallel Plate Avalanche Counter (PPAC) for BigRIPS fragment separator,” Nucl. Instrum. Methods Phys. Res. Sect. B Beam Interact. Mater. At., vol. 317, pp. 717–727, 2013
- [KWA18] E. Kwan *et al.*, “Identification of Fission and Fragmentation Products from  $^{238}\text{U}$  at the NSCL”, 5<sup>th</sup> Joint Meeting of the APS Division of Nuclear Physics and the Physical Society of Japan, 63, 12, LB.00008 (2018); and to be published.
- [LIP18] S. I. Lipschutz, Ph.D. Thesis, Michigan State University (2018); S. I. Lipschutz et al., submitted for publication
- [LON18] Longfellow B., “Measurements of key resonances for the  $^{24}\text{Al}(p,g)^{25}\text{Si}$  reaction rate using in-beam gamma-ray spectroscopy”, Phys. Rev. C 97, 054307 (2018)
- [MAT12] M. Matoš et al., “Time-of-flight mass measurements of exotic nuclei,” Nucl. Instrum. Methods Phys. Res. Sect. Accel. Spectrometers Detect. Assoc. Equip., vol. 696, pp. 171–179, Dec. 2012.
- [MEI11] K. Meierbachtol et al., Nucl. Instrum. Method. in Phys. Res. A 652, 668 (2011)
- [MEI13] Z. Meisel and S. George, IJMS 349, 145 (2013)
- [MEI15] Z. Meisel et al., Phys. Rev. Lett. 114, 022501 (2015)
- [MOR03] D. J. Morrissey et al., “Commissioning the A1900 projectile fragment separator”, Nucl. Instrum. Methods Phys. Res. Sect. B Beam Interact. Mater. At., vol. 204, pp. 90–96, 2003.
- [MRI09] MRI-Consortium: Development of a Neutron Detector Array by Undergraduate Research Students for Studies of Exotic Nuclei, NSF grants 0922335, 0922409, 0922446, 0922462, 0922473, 0922537, 0922559, 0922622, and 0922794





- [POL12] E. Pollacco et al., “GET: A Generic Electronic System for TPCs for Nuclear Physics Experiments”, *Physics Procedia* 37, 1799 (2012)
- [PUL02] A. Pullia, W. F. J. Muller, C. Boiano, and R. Bassini, “Resistive or capacitive charge-division readout for position-sensitive detectors,” *IEEE Trans. Nucl. Sci.*, 49 (2002), pp. 3269–3277.
- [ROOT97] ROOT - An Object Oriented Data Analysis Framework, *Proceedings AIHENP'96 Workshop*, Lausanne, Sep. 1996, *Nucl. Inst. & Meth. Phys. Res. A* 389 (1997) 81-86. See also <http://root.cern.ch/>
- [REC13] Recchia F. et al., “Configuration mixing and relative transition rates between low-spin states in  $^{68}\text{Ni}$ ”, *Phys. Rev. C* 88, 041302(R) (2013)
- [ROG15] A.M. Rogers *et al.*, Tracking rare-isotope beams with microchannel plates, *Nucl. Inst. & Meth. Phys. Res. A* 795, 325 (2015)
- [S800] S800 Spectrograph Wiki page
- [S800DAQ] <https://wikihost.nsl.mscl.msu.edu/S800Doc/doku.php?id=electronics>
- [SPEC18] <http://docs.nsl.mscl.msu.edu/daq/>
- [SWA75] D. Swan, J. Yurkon, and D. J. Morrissey, “A simple two-dimensional PPAC,” *Nucl. Instrum. Methods Sect. A*, 348 (1974), pp. 314–317.
- [TAR20] O. Tarasov, Workshop on Techniques and Detectors for Heavy-ion Charge-State Identification in High-acceptance Spectrometers, 16-17 December, 2020.
- [TIN08] C.S. Tindall et al., “Silicon Detectors for Low Energy Particle Detection”, *IEEE trans. On Nuclear Science*, Vol. 55, No. 2, April 2008.
- [WAL19] D. Walter et al., to be published
- [WIM14] K. Wimmer et al., *Nucl. Instr. And Meth, in Phys. Res. A* 769, 65 (2014)
- [YUR99] J. Yurkon et al., “Focal plane detector for the S800 high-resolution spectrometer,” *Nucl. Instrum. Methods Phys. Res. Sect. Accel. Spectrometers Detect. Assoc. Equip.*, vol. 422, no. 1, pp. 291–295, Feb. 1999.





## 8 Commissioning Plan

The commissioning plan for the HRS assumes that magnets, diagnostics systems, and auxiliary systems have been installed and that those subsystems have been verified to operate within design specifications. While commissioning will allow to demonstrate the key performance parameters (KPPs; see Section 3.4), the commissioning scope extends beyond the bare demonstration of KPPs.

The initial beam properties for commissioning purposes will be characterized at the ARIS fragment separator focal plane diagnostic box. Tracking detectors and slit systems in the HTBL and the spectrometer section are calibrated with sources and masks before actual commissioning starts. The calibration of the drift-chamber tracking detectors in the Spectrometer Section can be verified with masks that can be inserted during beam operation.

With tracking detectors installed at each focal plane, the actual ion-optical transfer matrix elements by analyzing the correlation of variables at the initial and final focal plane will be measured. Commissioning will make use of the inverted response matrix method for the quadrupole elements in the beam line. An ion-optical calculation with COSY INFINITY based on the measured field maps will yield the matrix elements at the focal planes in the beam line and spectrometer. Using a linear approximation, the change of the ion optical matrix elements as a function of the deviation of quadrupole fields can be calculated as a response matrix. After measurement of the beam trajectories with tracking detectors, optimized values of the quadrupole fields can be calculated by inversion of the response matrix.

For the HTBL, commissioning will start with the achromatic beam transport mode. The two tracking detectors at FB1 will be used to measure horizontal and vertical positions and angles for different beam momenta. The inverted response matrix method [UES12] will be used to optimize the quadrupole elements to simultaneously satisfy the focus condition  $[(x|x') = (y|y') = 0]$ , as well as nominal position and angle dispersion  $[(x|\delta), (x'|\delta)]$  and position magnifications. Similar approaches will be subsequently applied to FB3 and FS0. The pair of tracking detectors will be used to evaluate focus condition and achromaticity  $[(x|\delta) = (x'|\delta) = 0]$  at FS0 while maintaining nominal magnifications. Symmetry considerations can be used in cases with more available tuning parameters than ion-optical boundary conditions. The tuning of higher-order magnetic elements (sextupole and octupole corrector coils) can be optimized by minimization of the inclination of the dispersive focal planes at FB1 and FB3 using the tracking detectors at those positions. The transmission efficiency will be evaluated by comparing beam rates at FB1, FB3, and FS0 as a function of beam emittance and momentum deviation, characterized at the ARIS focal plane. In addition, it will be confirmed that the requirements for the reconstruction of the momentum (momentum resolving power of 1500) and angle (resolution of 5 mrad) at FS0 from the position and angle measurements at FB1 and FB3 (see Section 5.5) are met.



The commissioning of the high-resolution mode of the spectrometer section will commence with the optimization of the first four quadrupole elements to satisfy position focus conditions and to achieve nominal position and angle dispersion by application of the inverted matrix method. Tracking detectors at FS1 will be used to correlate the beam property measurements. The last two quadrupole elements will be tuned to achieve focus condition at the FS2 tracking detectors. The higher-order ion-optical aberrations will tilt the focal planes at FS1 and FS2 even with the sextupole and octupole corrections applied and an iterative process will be used to optimize transmission rather than optimizing the position of the focal plane.

For the commissioning of the dispersion-matched beam transport mode through the HTBL a similar approach as for the achromatic beam transport mode will be chosen. Foci, dispersion, and magnification at FS0, as well as vertical foci at FB1 and FB3 will be optimized with the tracking detectors at FB1, FB3, and FS0. The correct dispersion at FB2 can be verified with the viewer plate. If found necessary, a pair of smaller NSCL-type PPAC detectors could be installed temporarily in the FB2 beam line cross to verify focus conditions as well. Dispersion-matching into the spectrometer section, using the high-resolution spectrometer mode, will be optimized by achieving position focus and achromaticity at FS2. Tracking detectors at FS0, FS1, and FS2 will be used for this part of commissioning. The acceptance of the spectrometer section for both beam transports mode will be characterized by measuring the beam transport of a high emittance beam with a variable momentum spread to FS1 and FS2. This also commissions the HRS for the ToF-B $\rho$  mass-measurement mode, which uses the HTBL in dispersion-matched mode together with a high-resolution spectrometer mode.

The neutron invariant-mass mode of the spectrometer section can be commissioned with the FS1 detector setup. Higher order correction elements will be tuned to optimize acceptance.

Event-by-event particle identification detector setups at FS1 and FS2 (ionization chamber, timing scintillator, hodoscope) will be commissioned during the commissioning of the spectrometer section. Initial standard modes for particle identification including momentum corrections will be developed with a reaction target at FS0. This will then allow to demonstrate the key performance parameters by measuring a neutron knockout reaction. Through the above measurements of the Spectrometer Section, it will be confirmed that the scientific requirements (See Section 6.2) are met.

## 8.1 References

[UES12] T. Uesaka, S. Shimoura, and H. Sakai (for the SHARAQ Collaboration), “The SHARAQ spectrometer”, *Prog. Theor. Exp. Phys.* 2012, 03C007 (2012).



## 9 Magnets

### 9.1 Introduction and overview

The Magnet scope includes the materials and manpower needed for acquiring, bench testing, installing, in-situ testing, and final integrated testing without beam of the magnetic elements of the Magnet system WBS (See Table 9-1). This includes the nuclear magnetic resonance (NMR) probes used to measure the magnetic fields in the dipole magnets.

Table 9-1. Magnet system WBS.

<b>Experimental Systems - High Rigidity Spectrometer</b>	<b>HRS.3</b>
<b>High Transmission Beamline (HTBL)</b>	<b>HRS.3.01</b>
<b>High Transmission Beamline Magnets</b>	<b>HRS.3.01.03</b>
<i>HTBL Dipole Magnets</i>	<i>HRS.3.01.03.01</i>
<i>HTBL Quadrupole &amp; Multipole Magnets</i>	<i>HRS.3.01.03.02</i>
<i>HTBL Installation, Testing, and Magnet Mapping</i>	<i>HRS.3.01.03.03</i>
<b>High Transmission Beamline Alignment</b>	<b>HRS.3.01.08</b>
<b>Spectrometer Section</b>	<b>HRS.3.02</b>
<b>Spectrometer Section Magnets</b>	<b>HRS.3.02.03</b>
<i>Spectrometer Section Dipole Magnets</i>	<i>HRS.3.02.03.01</i>
<i>Spectrometer Section Quadrupole &amp; Multipole Magnets</i>	<i>HRS.3.02.03.02</i>
<i>Spectrometer Section Installation, Testing and Magnet Mapping</i>	<i>HRS.3.02.03.03</i>
<b>Spectrometer Section Alignment</b>	<b>HRS.3.02.10</b>

### 9.2 Requirements

The magnetic-element layout is shown in Figure 9-1. The requirements of the magnetic elements originate from the lattice design meeting the physics requirements (See Section 4) for the HTBL (See Section 5) and for the Spectrometer section (See Section 6).

#### 9.2.1 High Transmission Beam Line (HTBL) magnets requirements

The HTBL consists of eight quadrupole triplets, four bending dipoles, and two steerer dipole magnets. The quadrupole triplet design is the same as the T2 triplet with a FSQB-FSQC-FSQB configuration (FSQB repeats) as presently used at NSCL in the A1900 Fragment Separator with each quadrupole having sextupole and octupole coils to correct for higher-order aberrations. The magnet specifications are provided in Table 9-2.



The four dipole (DB1-DB4) magnets are a larger version of an existing NSCL XPF 6 Tm dipole design to accommodate a rigidity of 8 Tm. The magnet specifications are provided in Table 9-3. The two steerer dipole magnets (SB1, SB2) requirements are given in Table 9-4.

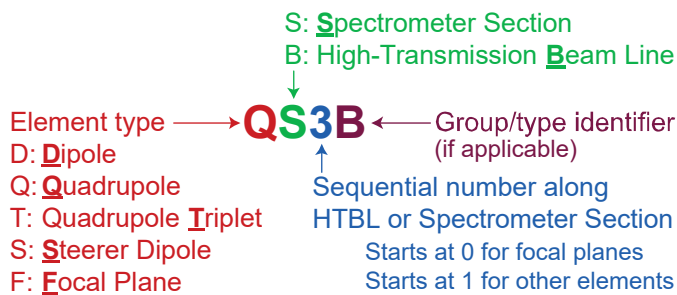
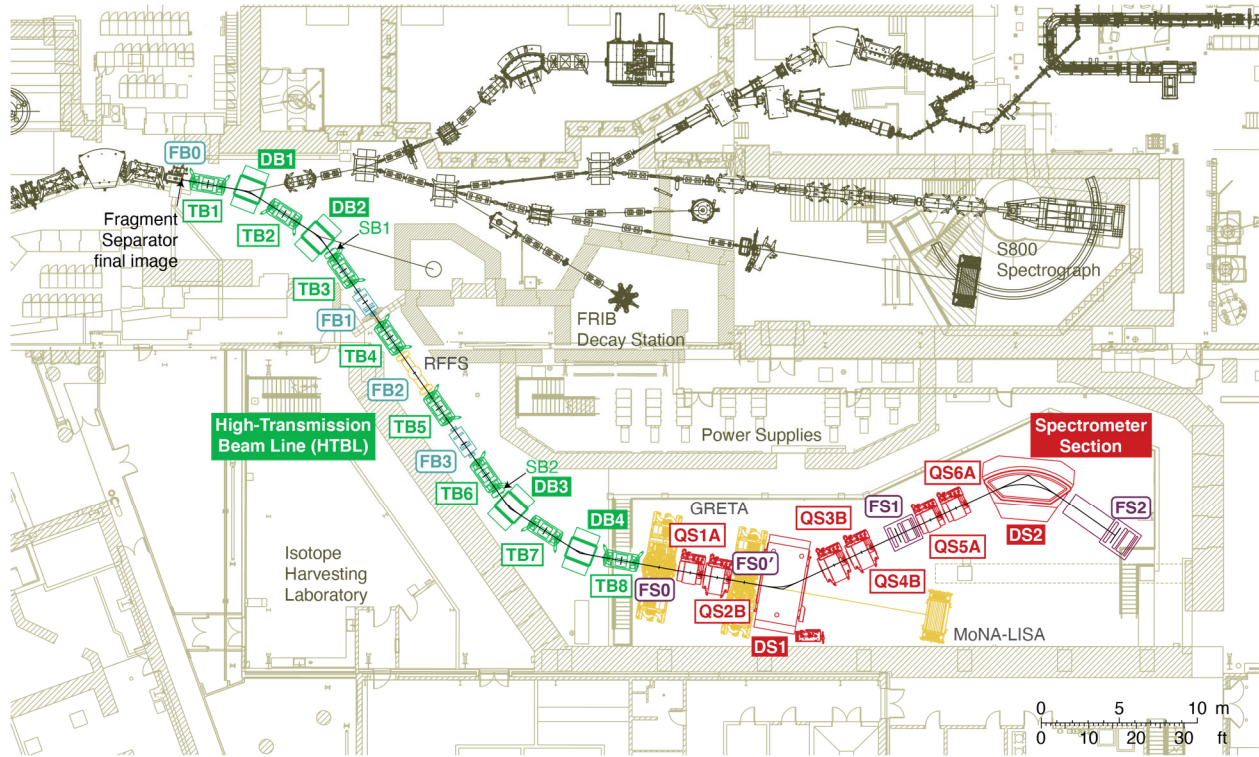


Figure 9-1 (Top) Overview of the magnetic elements of the HRS, with the nomenclature as shown on the left. The HTBL magnetic elements include triplets (TB<sub>x</sub>, x=1..8), dipoles (DB<sub>x</sub>, x=1..4), and steerer magnets (SB1, SB2). The Spectrometer Section magnets include six single quadrupoles (type A = QS1A, QS5A, QS6A; type B = QS2B, QS3B, QS4B) and two dipoles (DS1, DS2).



Table 9-2. High-Transmission Beam Line (HTBL) quadrupole magnet requirements for 8 triplets labeled TB1-TB8 in Figure 9-1. Each triplet has three quadrupole magnet elements: FSQB, FSQC, and FSQB. Each quadrupole segment includes sextupole and octupole windings.

Label	FSQB	FSQC
Quantity (in 8 quadrupole triplets)	16	8
Effective field length (nominal) (m)	0.40	0.79
Pole-tip radius (m)	0.15	0.15
Warm-bore radius (m)	0.10	0.10
Quadrupole maximum field strength (T@poletip, base requirement)†	2.34	2.48
Quadrupole maximum field strength (T@poletip, with 10% tuning margin)†	2.57	2.73
Quadrupole field integral (T, base requirement)†	6.24	13.06
Quadrupole field integral (T, with 10% tuning margin)†	6.86	14.37
Quadrupole good-field region radius (m)	0.10	0.10
Sextupole maximum field strength (T/m <sup>2</sup> , base requirement)	10	10
Sextupole maximum field strength (T/m <sup>2</sup> , with 10% tuning margin)†	11	11
Octupole maximum field strength (T/m <sup>3</sup> , base requirement)	50	50
Octupole maximum field strength (T/m <sup>3</sup> , with 10% tuning margin)†	55	55
Octupole maximum field strength (T/m <sup>3</sup> , with 10% tuning margin)†	55	55

†: This table includes the base magnetic field requirements as determined from ion-optical calculations, needed to achieve the design beam transport in both operations modes at the maximum magnetic rigidities of 8 Tm. Additionally this table includes magnetic field requirements with tuning margin to ensure project specifications are met. The magnet designs are based on the magnetic field requirements with tuning margin, and therefore the power supply voltage and currents include tuning margin.





Table 9-3 High-Transmission Beam Line (HTBL) dipole magnet requirements for dipoles labeled DBx in Figure 9-1 compared to extant NSCL XFP dipole magnets.

Label	NSCL XFP	DBx (x = 1, 2, 3, 4)
Quantity	N/A	4
Bending radius (m)	3.1	4.10
Maximum rigidity (Tm)	5.3	8.0
Maximum field (T, base requirement)†	1.7	1.95
Maximum field (T, with 5% tuning margin)†		2.05
Bending angle (deg)	±22.5	22.5
Arc length for central ray (m)		1.61
Field integral (Tm, base requirement)†		3.15
Field integral (Tm, with 5% tuning margin)†		3.30
Vertical gap size (m)	±0.035	±0.05
Good field region (m)		±0.10
Pole-face rotation entrance (deg)		11.25
Pole-face rotation exit (deg)		11.25

†: This table includes the base magnetic field requirements as determined from ion-optical calculations, needed to achieve the design beam transport at the maximum magnetic rigidities of 8 Tm. Additionally this table includes magnetic field requirements with tuning margin to ensure project specifications are met. The magnet designs are based on the magnetic field requirements with tuning margin, and therefore the power supply voltage and currents include tuning margin.

Table 9-4. High-Transmission Beam Line (HTBL) steerer dipole magnet requirements for steerers labeled SB1, SB2 in Figure 9-1.

Label	SBx (x = 1, 2)
Quantity	2
Length	0.40
Gap size (m)	±0.10
Maximum rigidity (Tm)	8
Maximum deflection angle (mrad)	10
Maximum field (T)	0.20
Maximum field (T, with 10% margin)	0.22

### 9.2.2 Spectrometer Section magnets requirements

The Spectrometer Section magnets include six quadrupole singlet magnets and two dipoles. Each quadrupole has sextupole and octupole coils superimposed to correct for higher-order aberrations. There are 2 different types, labelled with A and B. There are magnets of each type: QS1A, QS5A, QS6A of type A and QS2B, QS3B, QS4B of type B. The quadrupole magnet specifications





for each type are given in Table 9-5. The Spectrometer Section of the HRS contains two large dipoles, the Sweeper Dipole (DS1) and the Spectrometer Dipole (DS2), with specifications provided in Table 9-6.

Table 9-5 Quadrupole magnet requirements for the Spectrometer section of the HRS.

Label	A	B
Quantity	3	3
Location	QS1,5,6	QS2, 3, 4
Effective field length (m)	1.00	1.00
Warm-bore (WB) radius (m)	0.20	0.40
Quadrupole maximum field strength (T@WB, base requirement)†	1.46	2.03
Quadrupole maximum field strength (T@WB, with 10% tuning margin)†	1.61	2.23
Quadrupole field integral (T, base requirement)†	7.30	5.08
Quadrupole field integral (T, with 10% tuning margin)†	8.03	5.59
Quadrupole good-field region radius (m)	0.16	0.32
Sextupole maximum field gradient (T/m <sup>2</sup> , base requirement)†	4.5	2.4
Sextupole maximum field gradient (T/m <sup>2</sup> , with 10% tuning margin)†	5.0	2.6
Octupole maximum field gradient (T/m <sup>3</sup> , base requirement)†	8.2	2.5
Octupole maximum field gradient (T/m <sup>3</sup> , with 10% tuning margin)†	9.0	2.8
Octupole maximum field gradient (T/m <sup>3</sup> , base requirement)†	8.2	2.5
Octupole maximum field gradient (T/m <sup>3</sup> , with 10% tuning margin)†	9.0	2.8

†: This table includes the base magnetic field requirements as determined from ion-optical calculations, needed to achieve the design beam transport in both operations modes at the maximum magnetic rigidities of 8 Tm. Additionally this table includes magnetic field requirements with tuning margin to ensure project specifications are met. The magnet designs are based on the magnetic field requirements with tuning margin, and therefore the power supply voltage and currents include tuning margin.



Table 9-6 Dipole magnet requirements for Spectrometer Section of the HRS.

Label	DS1	DS2
Quantity	1	1
Bending radius (m)	3.2	4.0
Maximum rigidity (Tm)	8.0	8.0
Bending angle (deg)	-35	60
Arc length for central ray (m)	1.95	4.19
Field integral (Tm, base requirement)†	4.89	8.38
Field integral (Tm, with 5% tuning margin)†	5.13	8.80
Vertical gap size (m)	±0.30	±0.10
Good field region width (m)	±0.30	±0.50
Pole-face rotation entrance (deg)	0	-20
Pole-face rotation exit (deg)	35	-20
Pole-face rotation entrance (deg)	0	-20
Pole-face rotation exit (deg)	35	-20

†: This table includes the base magnetic field requirements as determined from ion-optical calculations, needed to achieve the design beam transport at the maximum magnetic rigidities of 8 Tm. Additionally this table includes magnetic field requirements with tuning margin to ensure project specifications are met. The magnet designs are based on the magnetic field requirements with tuning margin, and therefore the power supply voltage and currents include tuning margin.

### 9.3 Design approach

The requirements for the HTBL (Section 5) and Spectrometer Section (Section 6) that are derived from the HRS experimental program (Section 4) includes the use of ion beams of relatively high rigidity (up to 8 Tm) and the necessity to transport beams of large three-dimensional phase space, which requires that the magnets have substantial apertures, especially in the Spectrometer Section. Iron-dominated magnetic elements using superconducting coils have been used at the NSCL for decades for similar purposes and have been chosen as preferred designs for the HTBL quadrupoles and dipoles as well as the spectrometer dipoles. Current dominated, warm iron quadrupole designs were chosen for the spectrometer quadrupoles, which provide a more compact design as well as cryostats that do not have to take into account the shape of steel poles which would complicate coil constraint and cryostat design. A design and costing study on a current dominated design for the large gap DS1 spectrometer dipole was done but proved to be of higher risk and cost. The steering dipoles only need to bend the beams with an angle of  $\pm 10$  mrad. Consequently, for these magnets, iron-dominated, normal-conducting designs will be pursued.



## 9.4 Preferred alternative

As described below, a preliminary design for each magnetic element has been developed. Though not discussed in detail, magnet stand preliminary designs and costs have been developed and are shown in some of the magnet figures following with most typical of extant NSCL systems. The design model magnetic fields from MAXWELL [ANS18] were used in ion-optical simulations (Sections 5 and 6) to verify that the preliminary design provides appropriate performance. In addition, these designs provided a good basis for estimating the cost. Further detailed analyses will be used to optimize the designs relative to cost, risk, and performance, including the usual iterations with concomitant ion optical performance compared to science-driven requirements.

### 9.4.1 HTBL quadrupole magnets

The quadrupole triplet design meeting the magnet requirements provided in Table 9-2 is the NSCL T2 triplet with a FSQB-FSQC-FSQB configuration presently used in the A1900 Fragment Separator (See Figure 9-2) with each quadrupole having sextupole and octupole coils to correct for higher-order aberrations. The design values for the quadrupole triples are provided in Table 9-7.

The field quality from magnetic measurements of these magnets was included in the ion-optical simulations and found to be appropriate. In the detail design phase, lessons learned from the A1900 magnet fabrication as well as the more recent FRIB magnet experience will be incorporated.

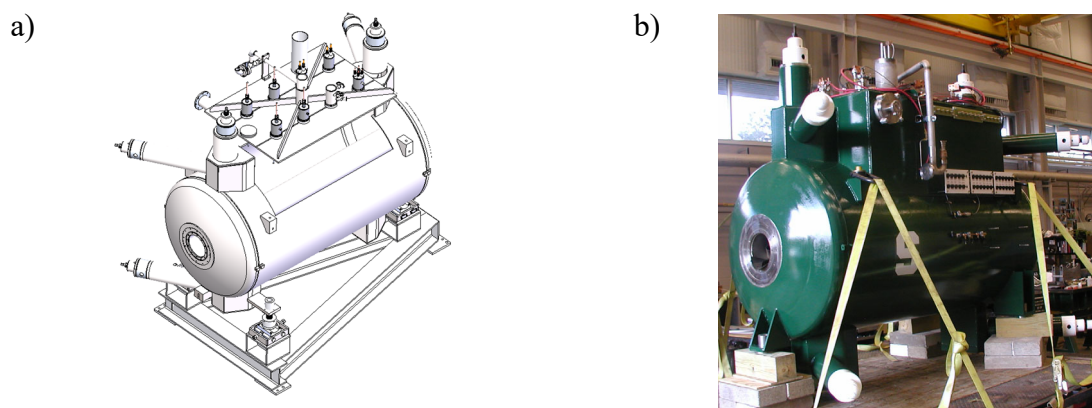


Figure 9-2 a) Mechanical layout and b) picture of the Quadrupole Triplet used for TBx in the HTBL. The same quadrupole design is used in the NSCL A1900 Fragment Separator.

Table 9-7 Design values for the quadrupole triples that meet the requirements of Table 9-2 are provided.

Label	FSQB	FSQC
Quantity (in 8 quadrupole triplets)	16	8
<b>Quadrupole Specifications</b>		
Steel length / quadrupole effective length (m)	0.325 / 0.400	0.715 / 0.790
Steel mass (kg)	821	1806
Steel pole radius (cm)	15	15
Wire diameter bare / insulated (mm)	0.80 / 0.86	0.87 / 0.93
Length of wire per coil (m, approximate)	3658	4258
Coil cross section (mm <sup>2</sup> )	2710	2710
Coil type:	potted – random wound – self protecting	
Peak gradient integral (T) / peak I (A)	6.93 / 76	14.46 / 98
Stored energy at peak field (kJ)	87.7	196.6
kA-turns	217	236
Inductance (H)	30.4	41.0
Power supply A / V bipolar	76 / 6	98 / 6
<b>Sextupole Specifications</b>		
Wire diameter bare / insulated (mm)	0.648 / 0.698	0.648 / 0.698
Peak gradient integral (T/m) / Peak I (A)	4.67 / 38.6	9.14 / 38.6
kA-turns	11.2	11.2
Inductance (H)	0.37	0.71
Power supply A / V bipolar	40 / 6	40 / 6
<b>Octupole</b>		
Wire diameter bare / insulated (mm)	0.50 / 0.55	0.50 / 0.55
Peak gradient integral (T/m <sup>2</sup> ) / peak I (A)	22.1 / 18.4	44.1 / 15.5
kA-turns	8.3	7.0
Inductance (H)	0.59	1.38
Power supply A / V bipolar	20 / 6	20 / 6
<b>Cryostat Specifications</b>		
Cryogenic load	See Section 11	
Warm bore radius (cm)	10	
Magnet steel separation distance (m)	0.237	
Flange-to-flange overall length (m)	2.267	
Assembled mass (kg)	5610	



### 9.4.2 HTBL dipole magnets

The four dipole (DB1-DB4) magnets are a larger version of an existing NSCL XPF 6-Tm dipole, shown in Figure 9-3. A preliminary design of DBx meeting the requirements of Table 9-3 is shown next to the NSCL XPF dipole in Figure 9-4 with design values as specified in Table 9-8. The magnetic field analysis is shown in Figure 9-5. These magnets are comparable in size, field magnitude and stored energy to other NSCL dipoles, so there are no concerns with respect to the design (forces, critical current, quench protection, etc.). As shown in the bottom panel of Figure 9-5, the magnetic field at the outside of the steel does not exceed the saturation level. This ensures that the fringe fields will not be excessive.

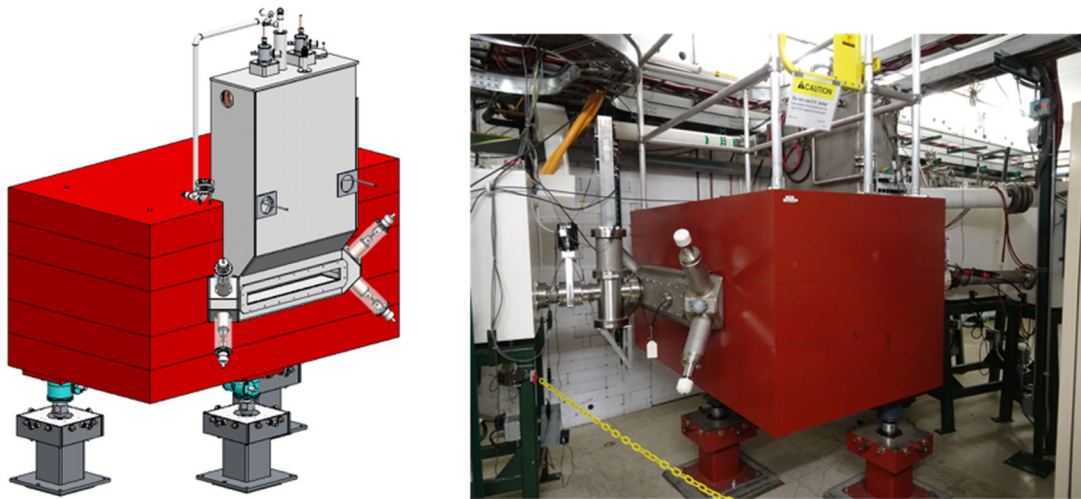


Figure 9-3 Mechanical design layout (left) and image (right) of an existing XPF 6-Tm dipole magnet used in the NSCL A1900 Fragment Separator. This magnet forms the basis of the dipole magnets used in the HTBL, which are scaled up to accommodate operation at rigidities of up to 8 Tm.

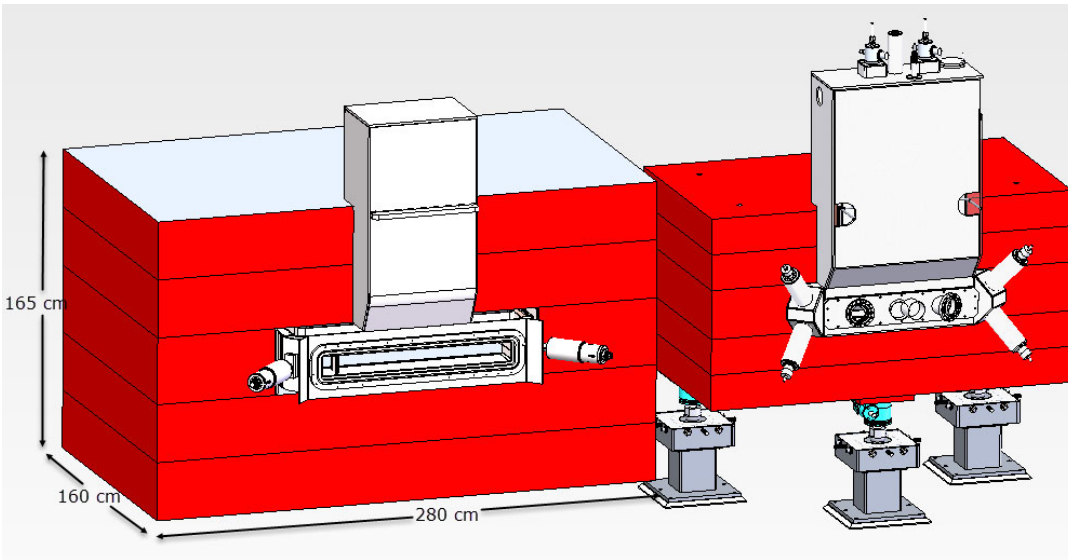


Figure 9-4 HTBL dipole magnet (DB1-DB4) layout with a length of 160 cm, a width of 280 cm, a height of 165 cm, a gap size of 10 cm, a gap width of 148 cm, necessary to accommodate a pole width of 118.4 cm. The magnet is shown next to an NSCL XFP dipole for comparison.

Table 9-8 HTBL DBx dipole design values meeting the requirements of Table 9-3.

Parameter	Value
Quantity	4
Steel length/width/height/gap (m)	1.60,2.80,1.65,0.10
Steel mass (metric tons)	55.28
SC wire cross section (mm <sup>2</sup> )/kA-turns	34x34, 100.0
$B_{max}$ (T) gap	2.02
Integrated field non-uniformity (%)	0.20
$B_{max}$ on outside of yoke (T)	1.92
$B_{max}$ in coil (T)	1.53
Stored energy (kJ)	339.5
Effective magnetic length (m)	1.66
$\int B \cdot dl$ (T m)	3.35
$J_c$ with 1.77T & 4.2K (A/mm <sup>2</sup> ) for 2 mm x 1 mm wire with Cu:SC=10	466
$J_{op}$ - operating current density (A/mm <sup>2</sup> )	91.1
$J_{op}/J_c$	0.20
Power supply A,V, uni or bipolar	182, 6, 2 quadrant (+I, ±V)



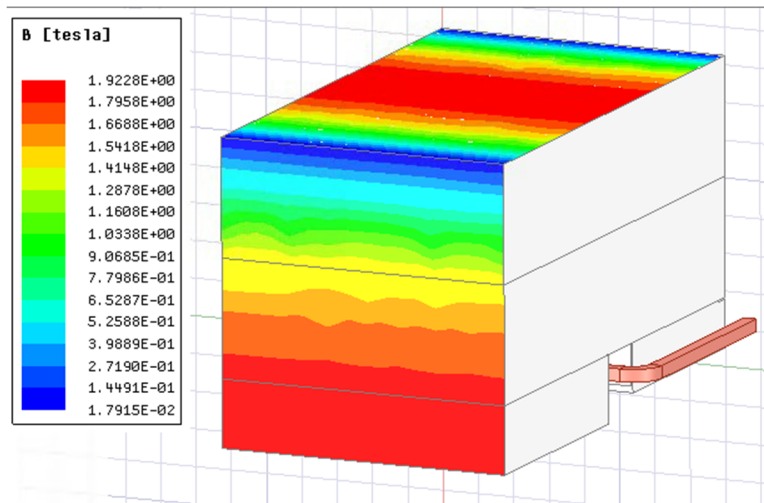
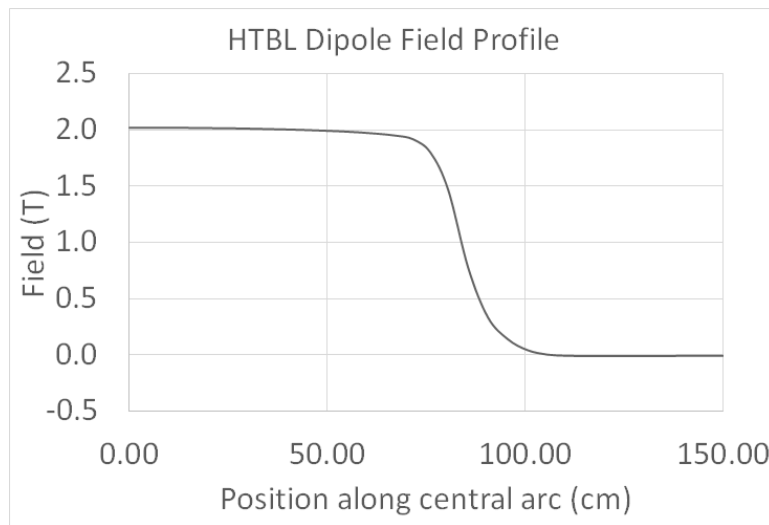


Figure 9-5 Magnetic field analysis of the DBx dipole magnets of the HTBL. (top) HTBL dipole field profile as a function of position along the central arc. (bottom) Analysis of the magnetic field outside of the steel, which is below the saturation level. This ensures that the fringe fields will not be excessive.

The structural analysis of two preliminary designs of the coil bobbin for the HTBL dipole magnet has been performed. One design has an additional compression link added to the long straight section of the coil. The resulting stress and deformations are shown in Figure 9-6. The addition of the compression link reduces the displacement of the long straight section from 1.76 mm to 0.95 mm, which will help ensure the bobbin fits within the cryostat.

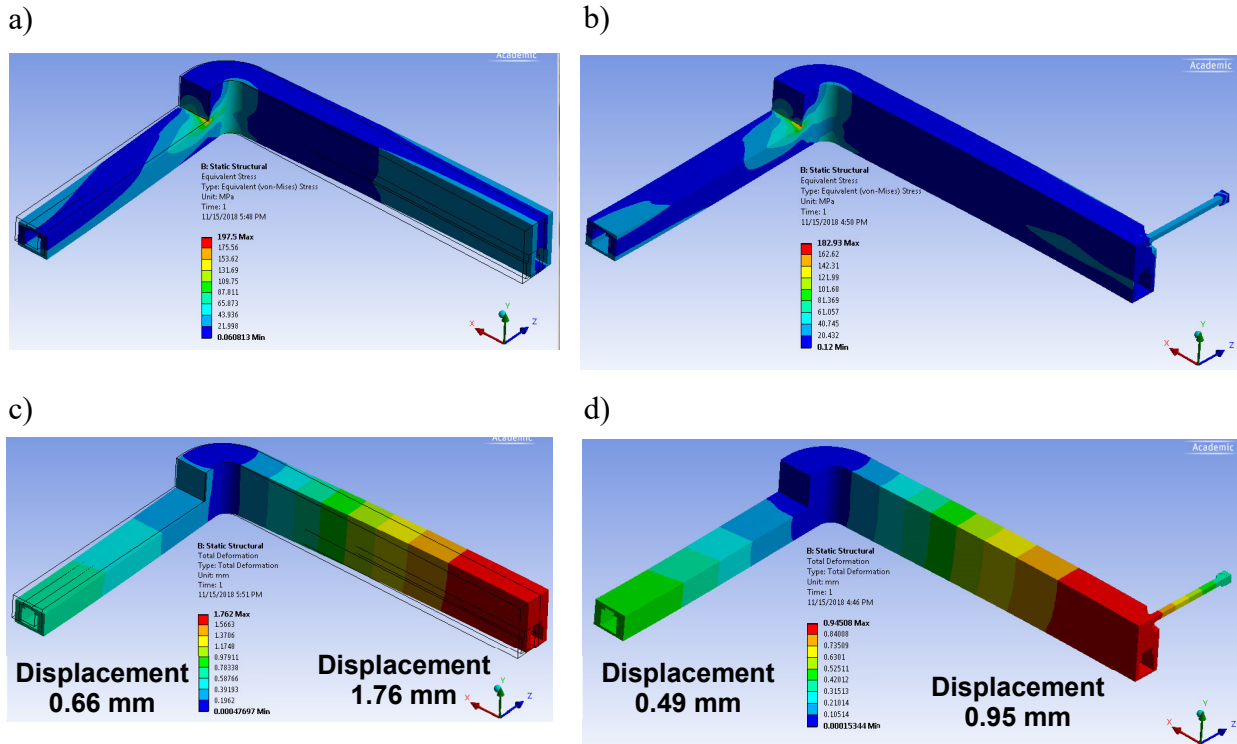


Figure 9-6 Stress (a and b) and deformation (c and d) calculations for the coil bobbin of the HTBL dipoles before (a and c) and after (b and d) the inclusion of an additional compression link. The displacement along the long straight section has been reduced from 1.76 mm to 0.95 mm.

### 9.4.3 HTBL steering magnets

A preliminary design of the steering magnets (SB1,SB2) that meets the requirements of Table 9-4 is shown in Figure 9-7(a). The design values are shown in Table 9-9 and the derived magnetic-field analysis, calculated in MAXWELL, is shown Figure 9-7(b).

The copper conductor of the steerer magnets will be Luvata #8581 (with a 1/4"×1/4" cross section and with a 0.143" cooling channel) in 7 double pancakes with 24 turns per double-pancake giving 168 turns per coil (7x24) or 37.0 kA-turns per coil with a current of 220.2 A. Given the voltage of 77 V, the power is about 16.9 kW. These magnets are comparable in size and field magnitude to common accelerator-based steering magnets, so there are no concerns with respect to the design challenges.

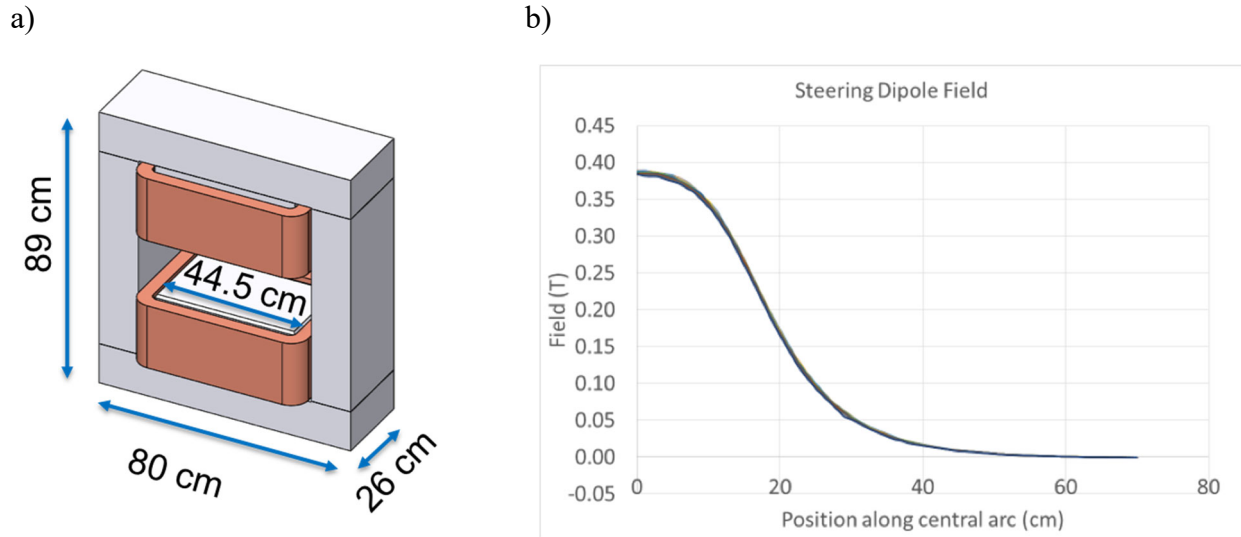


Figure 9-7 (a) HTBL steerer (SB1-SB2) layout with a length of 26 cm, a width of 80 cm, a height of 89 cm, a gap of 21 cm, and a pole width of 44.5 cm. (b) SBx magnetic dipole field as a function of the position along the central arc, as calculated in MAXWELL.

Table 9-9. HTBL SBx steerer design values that meet the requirements of Table 9-4.

Parameter	Value
Quantity	2
Steel length/width/height/gap (m)	0.26,0.80,0.89,0.21
Pole width (m)	0.445
Steel mass (kg)	1400
SC wire cross section(cm <sup>2</sup> )/kA-turns	0.25×0.25,37.0
$B_{max}$ (T) gap	0.39
Integrated field non-uniformity (%)	±1.5
Effective magnetic length (m)	0.21
$\int B \cdot dl$ (T m)	0.081
Power supply A,V, uni or bipolar	250,100,bipolar

### 9.4.4 Spectrometer Section quadrupoles

The quadrupoles in the spectrometer section are all ‘warm-iron’ quadrupoles, i.e., only the superconducting coils are in liquid helium (“cold”) and the yokes are at room-temperature (“warm”). These quadrupoles benefit using lessons learned from the design and construction of the warm-iron quadrupoles of the new ARIS Fragment Separator. In those magnets, the

complicated cryostat shape to accommodate the warm iron poles, and the trapezoidal cross section of the random wound coils proved complicated to build. A second design was considered using poles attached to a thin yoke annulus within the helium vessel, racetrack coils with rectangular cross section, and larger warm yoke around the cryostat. Finally a third design was considered and has been chosen for the HRS. Design optimizations of bore size and effective lengths from ion-optical simulations helped to reduce the different sizes from three to only two. The present design utilizes stacked annular double pancake coils to form each pole. The coils are contained by collars within the helium vessel and a warm iron yoke outside the cryostat is used. The design is similar to that used by Jefferson Lab in their Hall C spectrometers. This design has the advantage of cylindrical vessels, minimizes cold mass, and gives a more compact cryostat. The multipole components within the bore of the quadrupole have also been engineered with an improved assembly process. The cryostat design utilizes modified designs of the cryogenic service vessels presently being used on FRIB ARIS spectrometer dipoles.

These warm-iron quadrupole designs meet the magnet requirements provided in Table 9-5, and are shown in Figure 9-9(a-c), accompanied by the magnetic fields calculated in MAXWELL. These fields were used in the ion-optical simulations of Section 6 and the field quality was found to be acceptable. The parameters for the quadrupole magnets are given in Table 9-10 and for the sextupole and octupole coils in Table 9-11.

These warm iron quadrupoles have forces and stored energy that are considerably larger than the FRIB quadrupoles, with the QB size having close to the same stored energy as the FRIB ARIS dipoles. The coil forces are very effectively contained using the collared type of design. The cryogenic service vessel designs also incorporate safety vent piping of size to handle the larger stored energy. The cylindrical cryostat provides for symmetric support of the cold mass. For these quadrupoles, the field at the pole tip is comparable to FRIB quadrupoles, 1.61 T for QA and 2.23 T for QB vs. 2.0 T for FRIB FSQ5. Since the design does not use steel poles, the gradient is approximately linear with current throughout the operating range. Since the collaring contains coil forces and the LHe vessel uses cylindrical components, approximate sizing of components in the preliminary design are straight forward and displacements under loads will be small. Detailed stress analysis on the design will be done as the design progresses. Some detailed design was needed when evaluating the other two designs considered. Solid models of this design are shown in Figure 9-8. Also, preliminary quench analysis has been performed to ensure that the quench protection of the magnets is achievable and both types are self-protecting as mentioned later in Section 9.5. Similarly, the sextupole and octupole packages (Table 9-11) have been evaluated following experience with similar implementations in the A1900 T2 quadrupoles and the FRIB warm-iron quadrupoles. The resulting magnetic fields, coil package evaluations for clearances, forces, critical currents, and stored energy were found to meet requirements.

a)

b)



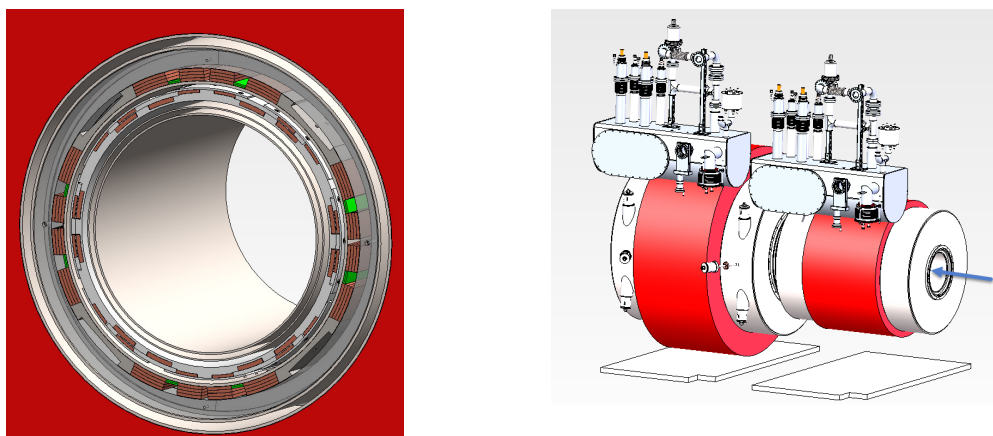
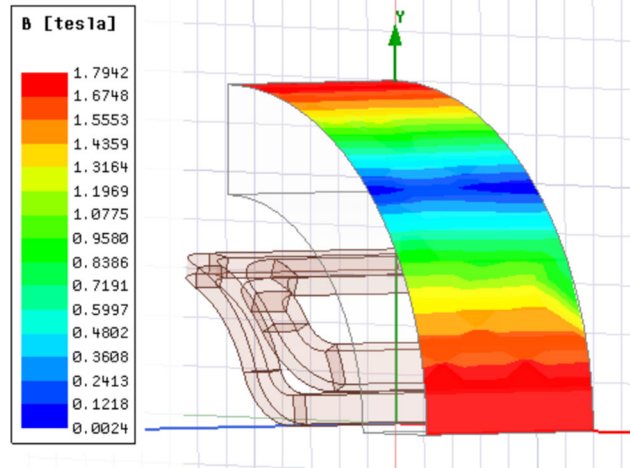
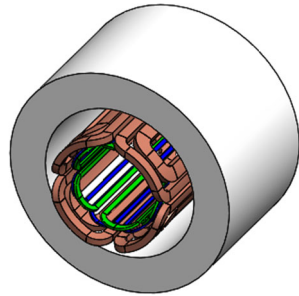


Figure 9-8 Spectrometer warm iron quadrupoles section view and layout of QSA (smaller) and QSB with cryogenic service vessels as modeled in relative position before the DSI spectrometer dipole.

Table 9-10 Spectrometer Section quadrupole design values that meet the requirements of Table 9-5. Note that the initial ion-optical simulations have found the integrated field non-uniformities to be acceptable. The non-uniformity values shown are the values calculated from the magnetostatic models and are similar to the preliminary estimates (1%). The field values from the MAXWELL model were found to achieve acceptable performance providing a sound basis for detailed design and optimization.

Label	QSA	QSB
Quantity	3	3
Steel length (cm)	85	85
Steel mass (metric tons)	6.28	19.25
Quadrupole SC coil cross section(mm <sup>2</sup> )/ kA-turns	Outer: 63×42, 240 Inner: 88×42, 336	Outer: 85×42, 354 Inner: 121×42, 499
Quadrupole power supply A,V, uni or bipolar	1100 A, 6 V, 4 quad. (±I, ±V)	1050 A, 6 V, 4 quad. (±I, ±V)
Integrated field non-uniformity	0.43%	0.22%
$B_{max}$ on outside of yoke (T)	1.79	1.80
$B_{max}$ in quadrupole coils (T)	Outer: 2.58 Inner: 4.13	Outer: 3.15 Inner: 4.89
Stored energy in quadrupole (kJ)	824	2294
$L_{eff}$ of quadrupole (m)	1.01	1.08
$\int G \cdot dl$ (T)	8.30	5.73
$J_c$ ( $B_{max}$ in quad, 4.2 K) (A/mm <sup>2</sup> )	Outer: 514 Inner: 404	Outer: 377 Inner: 279
$J_{op}$ (A/mm <sup>2</sup> )	102	106.0
$J_{op}/J_c$	Outer: 20% Inner: 25%	Outer: 28% Inner: 38%

a)



b)

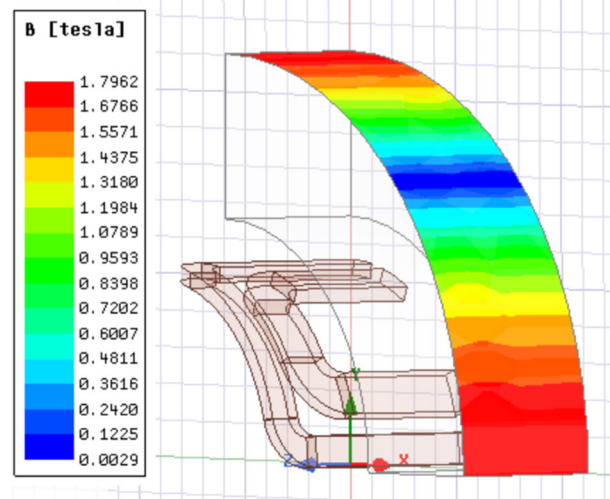
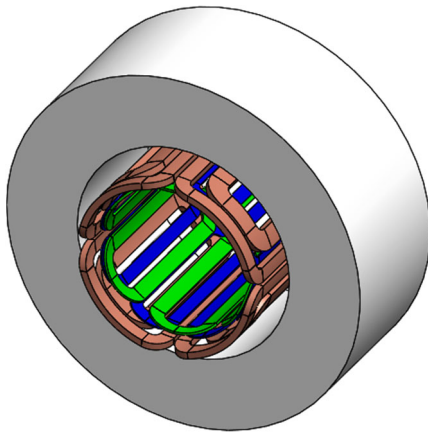


Figure 9-9 Layout and magnetic-field analysis of the quadrupole magnet types of the Spectrometer Section. (a) Type A; (b) Type B.



Table 9-11 Spectrometer Section sextupole and octupole design values that meet the requirements of Table 9-5.

Label	QSA	QSB
<b>Sextupole</b>		
Sextupole SC coil cross section(mm <sup>2</sup> )/ kA-turns	451, 46	1418, 120
Sextupole power supply A,V, uni or bipolar	65 A, 6 V 4 quadrant ( $\pm I, \pm V$ )	151 A, 6 V 4 quadrant ( $\pm I, \pm V$ )
B <sub>max</sub> in sextupole coils (T)	3.17	4.18
Stored energy in sextupole (kJ)	7.85	65.1
L <sub>eff</sub> of sextupole (m)	0.924	0.980
$\int G \cdot dl$ (T/m)	5.01	2.74
<b>Octupole</b>		
Octupole SC coil cross section (mm <sup>2</sup> ) / kA-turns	247, 20	770, 55
Octupole power supply A,V, uni or bipolar	52 A, 6 V 4 quadrant ( $\pm I, \pm V$ )	55 A, 6 V 4 quadrant ( $\pm I, \pm V$ )
B <sub>max</sub> in octupole coils (T)	3.33	4.32
Stored energy in octupole (kJ)	2.37	15.8
L <sub>eff</sub> of octupole (m)	0.944	0.972
$\int G \cdot dl$ (T/m <sup>2</sup> )	9.03	2.89

#### 9.4.5 Spectrometer Section dipole magnets

As discussed in Section 6, the Spectrometer Section contains two large dipole magnets. Spectrometer warm iron quadrupoles section view and layout of QSA (smaller) and QSB with cryogenic service vessels as modeled in relative position before the DS1 spectrometer dipole. The preliminary design for DS1 is shown in Figure 9-10. An analysis of the magnetic field for DS1 was performed in MAWELL. The magnetic field at the highest operating current on the outside of the magnet yoke is shown in Figure 9-11. The magnetic fields are below the saturation level, which ensures that the fringe fields do not become excessively large. In Figure 9-12, the dipole field uniformity as a function of radial position is shown for different operating currents. The non-uniformity ranges from +0.0% to -1.7% in the good field region, but is almost independent of the operating current. Since the MAXWELL fields from this design were used in the ion-optical simulations presented in Section 6 and the required ion-optical properties of the Spectrometer Section were achieved, these levels of non-uniformity are acceptable for DS1. During the detailed design of DS1 optimization with respect to the cost, risk, and performance will be done in conjunction with further evaluation of the ion-optical performance under DS1 design assumptions.

Initial modeling and engineering studies have been done to give a preliminary cryostat design that fits into the HRS lattice within space requirements needed for closely positioned detector arrays such as GRETA, have a gap space accommodating the TPC, and downstream window opening



that does not interfere with the maximum bend angle of the beam. The design now uses flat plates for yoke steel instead of the previous vertical sections required for the 50 ton crane capacity requirements before optimizing the design. Steel support studies have verified support for pole gap precision. The displacement uniformity across the pole being 0.011 mm (0.0004”) as shown in Figure 9-13. These are very small and coupled with manufacturing tolerances should easily meet requirements as needed for field uniformity. Note that the vault floor is recessed by 6 feet allowing for the steel to extend below the working floor level. A preliminary design of the helium vessel has been analyzed to ensure that the large Lorentz forces in the coils are manageable. The forces on the coils, both along the straight section in the yoke and along the ends, have been studied and sufficient space between the coils and yoke pole tips exists. The results of initial structural analysis for the coil bobbin structure are shown in Figure 9-14. Both the stress and deformation are within tolerable limits. The present cryogenic service vessel is of a design adopted from the FRIB ARIS dipoles. This has the current leads and overpressure safety piping and couples to the cryogenic transfer line and associated valve box. The total magnet mass including the cryostat and cryogenic service vessel is 427 metric tons. A view of the DS1 magnet assembly with cryogenic service vessel is shown in Figure 9-15.

The stored energy in this magnet is significantly larger than other magnets at FRIB/NSCL being around 9.3 MJ. The wire size has been adjusted to make the magnet self-protecting during a quench. As shown, the present design has ducts from each coil that will couple to a single large duct into the cryogenic service vessel to handle current leads, helium piping, and nitrogen shield piping as to not interfere with beam window requirements.

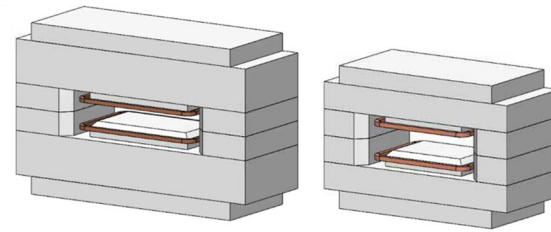
During the detailed design phase, the magnet design will be optimized to minimize cost and to reduce risk while meeting the ion optical performance requirements.

Table 9-12 is a summary of the preliminary design for DS1.



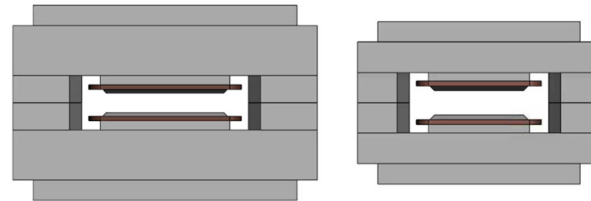
▪ **Original DS1**

- Steel mass = 649 tons
- Coil mass (each) = 1240 kg
  - » Cross-section = 11 cm × 11 cm
- Stored energy = 7.7 MJ
- $I_{op} = 364$  A
- Samurai style quench protection needed



▪ **Optimized DS1**

- Steel mass = 400 tons
  - » Reduced pole width → reduced steel
- Coil mass (each) = 1306 kg
  - » Cross-section = 12 cm × 12 cm
- Stored energy = 9.3 MJ
- $I_{op} = 457$  A
- Magnet is self-protected during quench



DS1 Original

DS1 Optimized

Figure 9-10 Optimized DS1 magnet design vs. initial design.

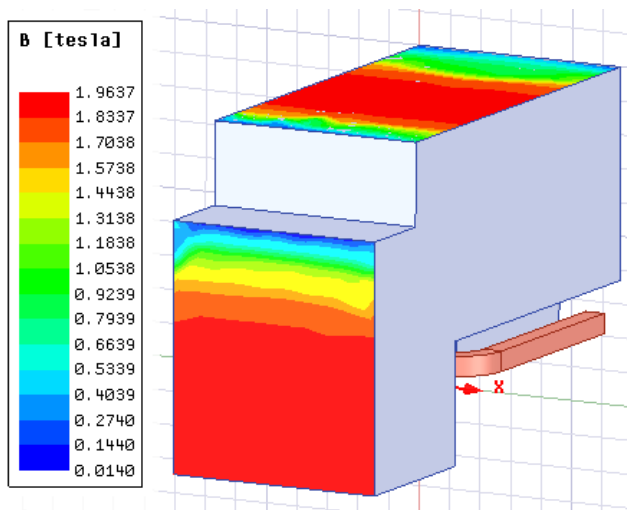


Figure 9-11 Magnetic field on the outside of the yoke for the DS1 magnet.

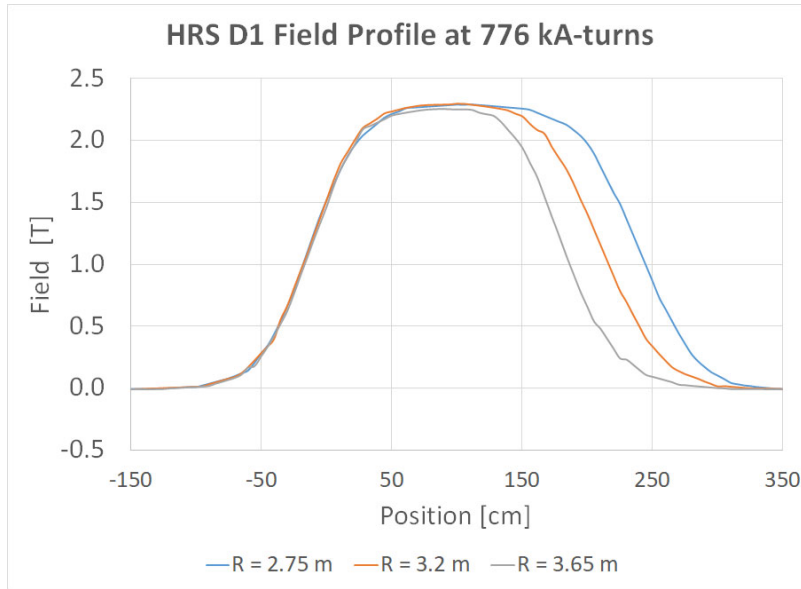


Figure 9-12 Field profile of spectrometer section DS1 dipole at 3 different radii.

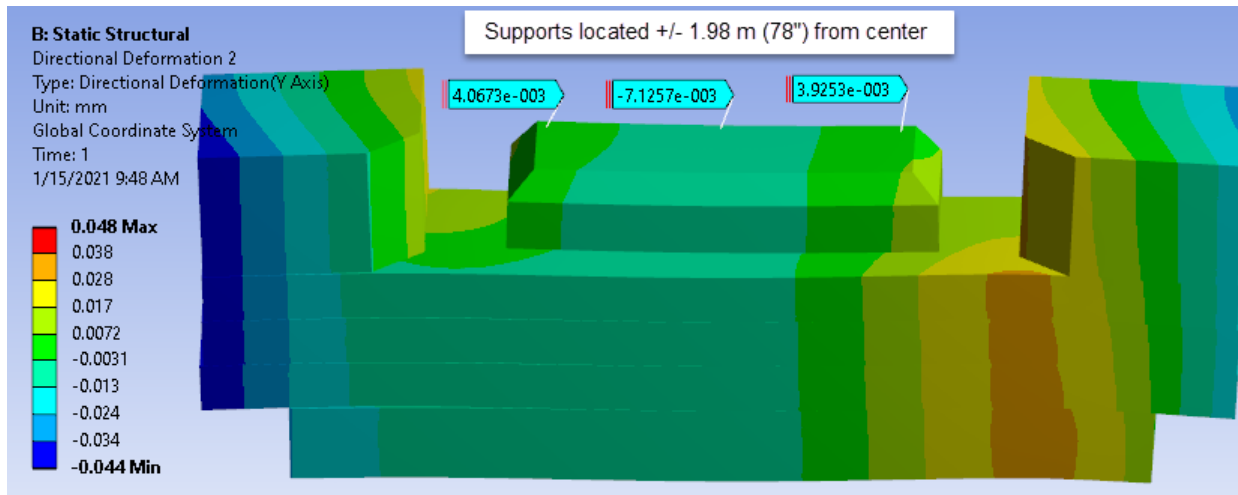
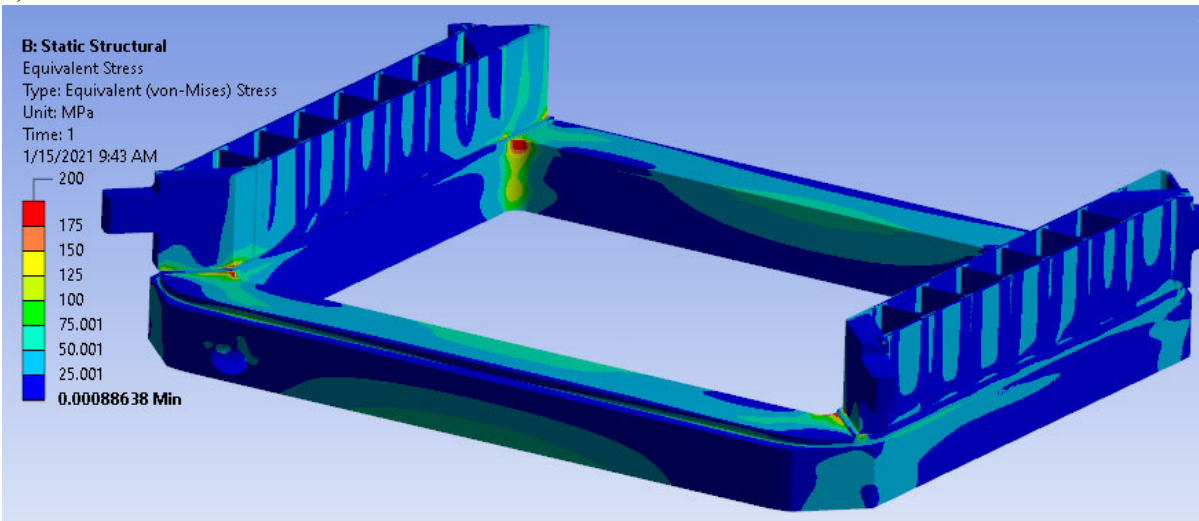


Figure 9-13 Steel support using three jacks at optimal locations. Upper steel weight applied as load on side yoke surfaces. Assumes frictionless slab to slab contact. Support areas below steel compensated in calculation to keep median plane level.

a)



b)

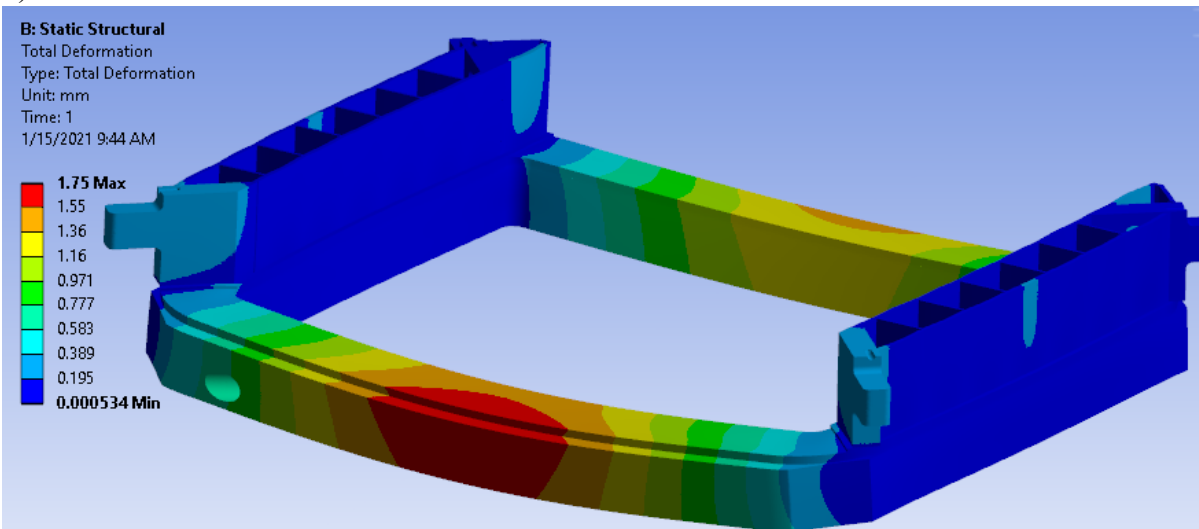


Figure 9-14 Bobbin stresses (a) and displacements (b) from helium pressure and Lorentz forces

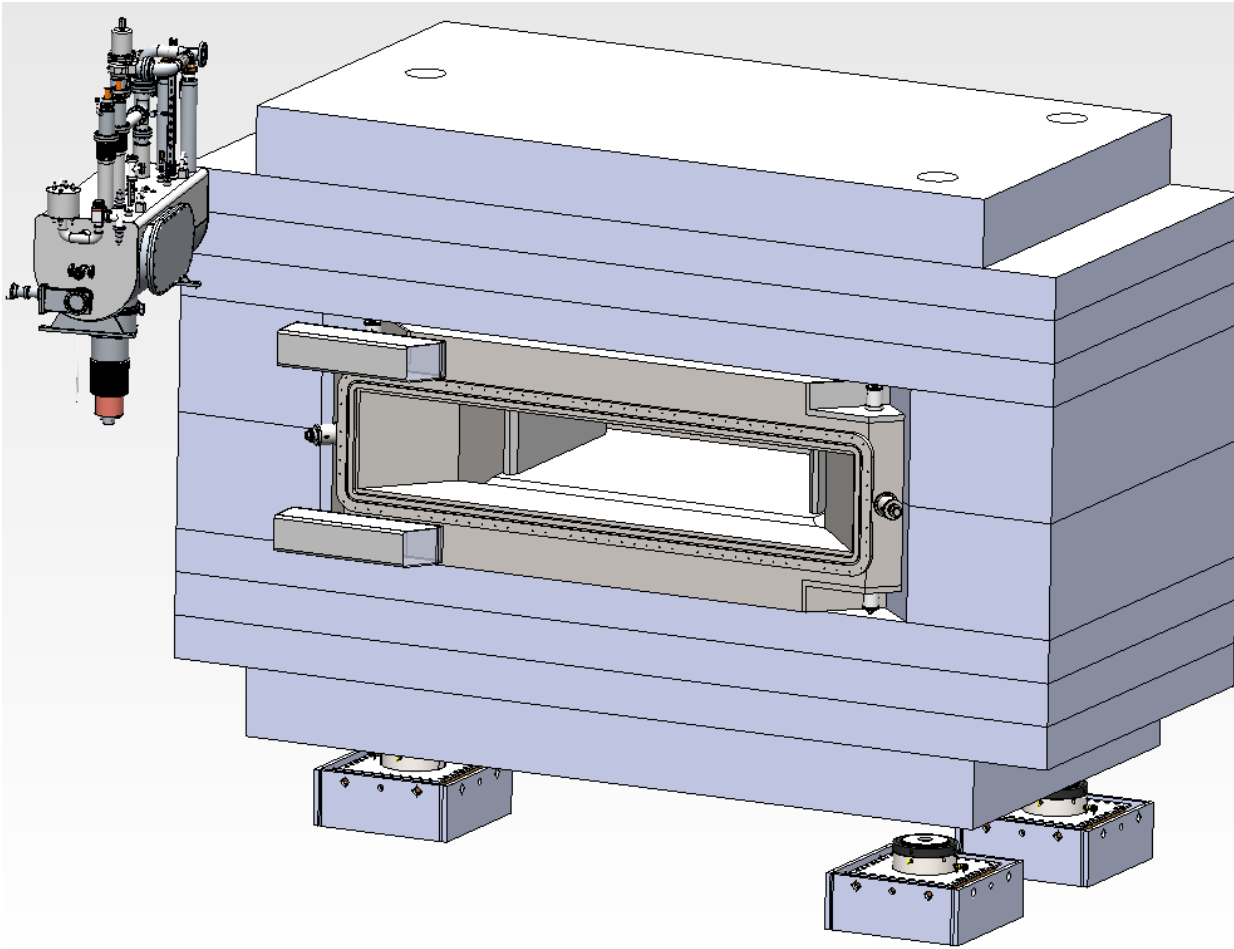


Figure 9-15 Spectrometer dipole DS1 assembly with coil cryostat and cryogenic service vessel.



Table 9-12 Spectrometer section DS1 dipole design values that meet the requirements of Table 9-6.

Parameter	Value
Quantity	1
Steel length/width/height/gap (m)	2.635 / 6.00 / 4.00 / 0.60
Steel mass (metric tons)	399.6
SC wire cross section (mm <sup>2</sup> )/kA-turns	120×120, 776
$B_{max}$ (T) gap	2.26
Integrated field non-uniformity (%)	+0.0 / -1.7
$B_{max}$ on outside of yoke (T)	1.96
$B_{max}$ in coil (T)	3.71
Stored energy @ 776 kA-turns (kJ)	9307
$L_{eff}$ @ 770 kA-turns (m)	2.235
$\int B \cdot dl$ (T-m) with 5% tuning margin	5.135
$J_c$ ( $B_{max}$ in quad, 4.2 K) (A/mm <sup>2</sup> )*	153.8
$J_{op}$ - operating current density (A/mm <sup>2</sup> )	56.7
$J_{op}/J_c$	37%
Power supply A,V, uni or bipolar	457 A, 40 V 2 quadrant (+I, ±V)

\* Based on FRIB FSD1 wire

The preliminary design for DS2 is shown in Figure 9-16. In Figure 9-17, the dipole field non uniformity is shown as a function of the radial position, with levels ranging from -1.0% to +0.0% within the good field region. Since the MAXWELL fields from this design were used in the ion-optical simulations presented in Section 6 and the required ion-optical properties of the Spectrometer Section were achieved, these levels of non-uniformity are acceptable for DS2. During the detailed design of DS2 optimization with respect to the cost, risk, and performance will done in conjunction to further evaluation of the ion-optical performance under DS1 design assumptions. Table 9-13 is a summary of the design details.

Engineering analyses for DS2 has not progressed to the level of that for DS1. However, the DS2 design follows design approaches based on NSCL/FRIB experience and engineering evaluations of the DS1 dipole. As a consequence, the preliminary design provides a sound basis for costing and further detailed analyses.



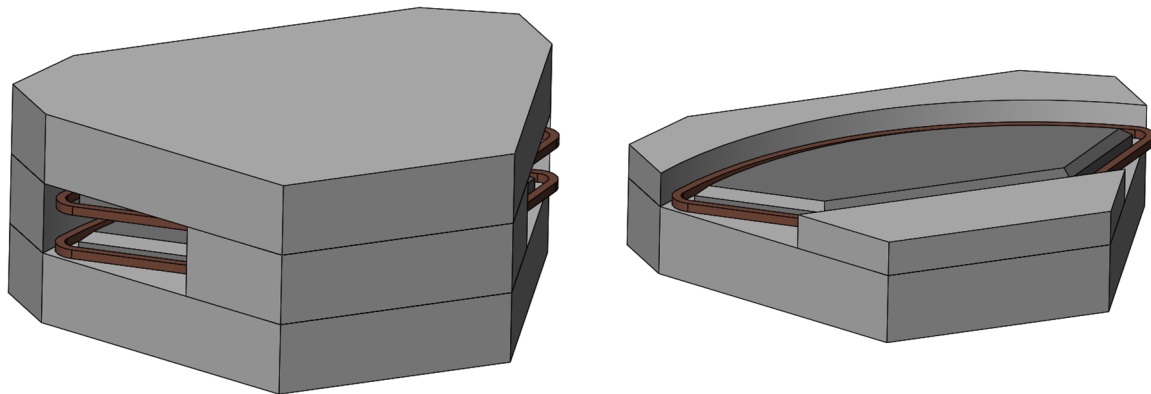


Figure 9-16 DS2 dipole layout, including a cut-away view showing the pole-tip and coil details. The length of DS2 is 5.87 m, the width is 4.21 m, and the height is 2.40 m.

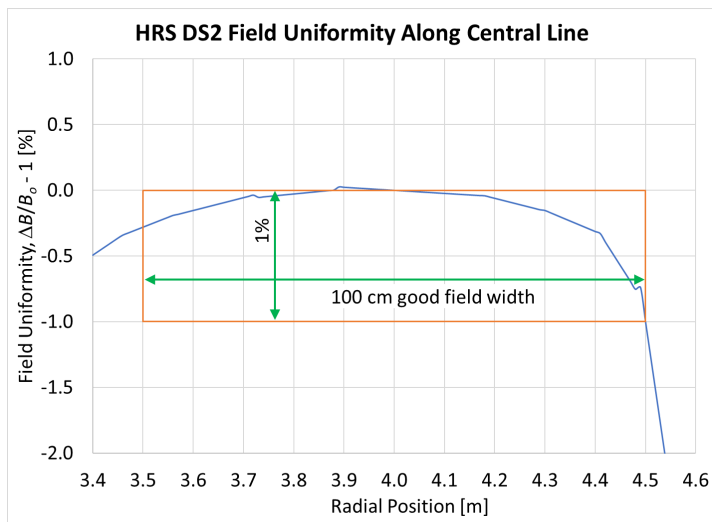


Figure 9-17 DS2 field non-uniformity as a function of the radial position. A non-uniformity ranging from +0.03% to -1.0% is achieved over the good field region in the preliminary design. Note that the ion-optical simulations have found this level of non-uniformity to be acceptable and close to a preliminary specification of 1% non-uniformity.

Table 9-13 Spectrometer section DS2 dipole design values that meet the requirements of Table 9-6.

Parameter	Value
Quantity	1
Steel length/width/height/gap (m)	5.87 / 3.99 / 2.30 / 0.20
Steel mass (metric tons)	305.7
SC wire cross section (mm <sup>2</sup> )/kA-turns	55×50 / 200
$B_{\max}$ (T) gap	1.96
Integrated field non-uniformity (%)	-1.0 / +0.0
$B_{\max}$ on outside of yoke (T)	1.80
$B_{\max}$ in coil (T)	1.84
Stored energy (kJ)	2696
Effective magnetic length at $R = 4$ m (m)	4.28
$\int B \cdot dl$ (T m)	8.99
$J_c$ with 1.84T & 4.2K (A/mm <sup>2</sup> ) - for FRIB FSD1 wire	4538
$J_{op}$ - operating current density (A/mm <sup>2</sup> )	1527
$J_{op}/J_c$	34%
Power supply A,V, uni or bipolar	393 A, 40 V 2 quadrant (+I, ±V)

## 9.5 Quench protection

A quench analysis has been performed for the HTBL dipole and all magnets in the Spectrometer Section. All magnets are self-protecting and do not require quench detection or fast energy dump circuits. In the event of a quench, the PLC will detect the quench via the lead drop voltage, helium level, or helium pressure measurement and ramp the power supply to 0 A or interlock the power supply off as required by the thresholds documented in an HRS alarms and interlock document. The PLC shall respond within 50 ms of the threshold being exceeded, and the power supply shall interlock off within 50 ms of receiving the interlock command from the PLC (100 ms total). Once interlocked off the magnet current will then decay through the slow dump resistor. The corresponding circuit diagram is shown in Figure 9-18.

In Table 9-14, the quenching-protecting method for each of the magnets is identified. The preliminary estimated peak voltage and temperature during the quench are also provided.



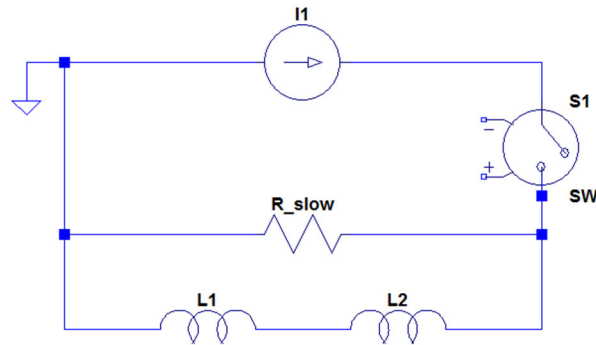


Figure 9-18 Circuit diagram for self-protecting magnets.

Table 9-14 Quench protection methods used for each magnet and preliminary estimated quench results.

Magnet	Quench Protection Method	Peak Voltage (V)	Peak Temperature (K)
HTBL QB quadrupole	Self-protecting	315	89
HTBL QB sextupole	Self-protecting	5.6	34
HTBL QB octupole	Self-protecting	4.5	28
HTBL QC quadrupole	Self-protecting	630	108
HTBL QC sextupole	Self-protecting	9.3	36
HTBL QC octupole	Self-protecting	6.8	28
QSA quadrupole	Self-protecting	Outer coil: 118 Inner coil: 125	Outer coil: 171 Inner coil: 129
QSA sextupole	Self-protecting	86	64
QSA octupole	Self-protecting	31	48
QSB quadrupole	Self-protecting	Outer coil: 250 Inner coil: 258	Outer coil: 211 Inner coil: 164
QSB sextupole	Self-protecting	141	81
QSB octupole	Self-protecting	83	58
DS1 dipole	Self-protecting	505	143
DS2 dipole	Self-protecting	281	262
HTBL dipole	Self-protecting	161	186

## 9.6 References

[ANS18] ANSYS® MAXWELL, Release 19.1, ANSYS, Inc.



## 10 Power Supplies

### 10.1 Introduction and overview

The Power Supplies (PS) scope includes the materials and manpower needed for designing, acquiring, bench testing, installing, in-situ testing, and final integrated testing without beam of the power supplies, power connection to the loads, and technical utilities, as specified by the WBS provided in Table 10-1.

Table 10-1 Power Supply WBS

<b>Experimental Systems - High Rigidity Spectrometer</b>	<b>HRS.3</b>
<b>High Transmission Beamline (HTBL)</b>	<b>HRS.3.01</b>
<b>High Transmission Beamline Power Supplies</b>	<b>HRS.3.01.05</b>
<b>Spectrometer Section</b>	<b>HRS.3.02</b>
<b>Spectrometer Section Power Supplies</b>	<b>HRS.3.02.07</b>
<b>Central Systems</b>	<b>HRS.3.03</b>
<b>Technical Utilities and Infrastructure</b>	<b>HRS.3.03.04</b>

### 10.2 Requirements

The requirements of the power supplies (PS) originate from the lattice design meeting the physics requirements (See Section 4) for the HTBL (See Section 5) and for the Spectrometer section (See Section 6) with concomitant hardware for the magnets (See Section 9). These requirements are summarized in Table 10-2 and Table 10-3 in Section 10.3.1. The general power supply requirements are as follows:

- All superconducting magnet (SCM) PS will operate continuously in DC mode, i.e., there are no superconducting persistent switches.
- All PS are remotely programmable.
- In order to ramp the magnet current up (source) and down (sink), the dipole magnets require 2 quadrant (+I,  $\pm V$ ) SCM PS, and the multipoles require 4 quadrant ( $\pm I$ ,  $\pm V$ ) SCM PS. Most magnets require the SCM PS to source and sink at  $\pm 6$  V (or at a lower programmable voltage limits). However the QSB quadrupole and DS1 dipole magnets require the power supplies to source and sink at  $\pm 40$  V in order to minimize the time required to ramp the magnets to field.
- During ramp up and ramp down, the PS ramps at the programmable voltage limit. Once the current set point is reached, the voltage will drop (to the voltage drop on the resistive DC leads) and the PS will regulate current.



- The SCM PS will supply power to a superconducting magnet, which is a purely inductive load, through a series DC lead resistance. Every SC magnet will have a dump resistor in parallel, located at the PS, to protect the magnet and PS from open circuit and to provide a safe path to discharge stored energy in the magnet. The dump resistor must be rated to dissipate the stored energy in the magnet plus margin, after a ramp at full voltage to full current. The current feedback measurement must be taken after the dump resistor (shown in Figure 10-2), so that the magnet current is the regulated parameter. The dump resistor is included in the PS scope. If the current measurement device fails or becomes disconnected, the PS shall interlock off.
- The dump resistors shall be air cooled as a loss of building power would cause all magnets to dump their stored energy in the dump resistors while the cooling water ceases to flow.
- The dump resistors shall have an energy rating of at least 20% above the stored energy of the magnet.
- The PS shall include methods to prevent repetitive energy dumps which could potentially overheat and damage the resistors. For example a delay that prevents re-energizing the magnet until the resistor has cooled.
  - This delay is function of the output current when the interlock occurred and a maximal delay set by the user:
    - 0-20% 0s
    - 20-30% 0.10\*max
    - 30-40% 0.15\*max
    - 40-50% 0.25\*max
    - 50-60% 0.35\*max
    - 60-70% 0.50\*max
    - 70-80% 0.65\*max
    - 80-90% 0.80\*max
    - 90-100% max
- If the PS shuts off (for any reason, AC power, operator command, PS failure, external interlock, etc.), most magnets will slow dump at a maximum of 80 V. The dump resistance is based on 80V at maximum supply current. For example, a 0.8-Ohm dump resistor is used for a 100-A maximum-current supply). The DS1 and DS2 dipole magnets will slow dump at 200V. All of the HTBL and Spectrometer Section magnets are self-protecting and no special circuits are needed other than the dump resistors.
- All Magnet and PS connections will be covered. The PS racks will have global covers such that all exposed conductors within the rack are guarded. Additionally the PS racks will be locked, and hazard / safety instruction signs will be posted. Before the racks can be unlocked and covers removed, the safety instruction signs will include the necessary information to mitigate the hazards including Lock-Out Tag-Out (LOTO) procedure number, circuit breaker information, and the time to wait for magnet energy to be safely discharged. The magnets will include covers over any conductors such as the superconducting magnet lead cans and terminal





blocks, or the room temperature magnet terminals, interconnects, water fittings, etc. The magnet covers will include hazard / safety instruction signage to follow prior to cover removal. A tool will be required to remove the covers.

- All PS will have sufficient internal and hardwired external PLC (controls scope) interlocks to prevent damage to either the PS or magnet due to changes in cooling conditions, AC power disturbances, and out-of-range set-points. Room-temperature corrector magnet (RTM) coils will have a water-flow interlock, and an over-temperature interlock to provide redundant protection against damage from overheating. All superconducting magnets (SCM) will be protected by having helium-level, helium-pressure, and lead-voltage interlocks.
- In addition, the current leads are protected against excessive temperatures by continuously monitoring lead voltage drops. The measurements are taken across the leads (not across the magnet) inside of the cryo-vessel, from the room temperature feedthrough to the superconducting magnet connections. The leads typically are set to have a voltage drop of 70 mV at maximum current. If the lead voltage increases to 100 mV the PS is interlocked off. The power supply shall shut off its output within 50 ms, measured from the time the external interlock signal is received to the time the supply switches off.
- SCM PS operates in either two or four quadrants. A two quadrant SCM PS sources or sinks power with one polarity of current [(+V, +I), (-V, +I)]. A four quadrant (or bipolar) SCM PS, sources or sinks power in any polarity [(+V, +I), (+V, -I), (-V, +I), (-V, -I)], and cross through zero current smoothly. Dipole PS require two-quadrant operation, all others require four-quadrant operation. However, it may be advantageous to use a four-quadrant SCM PS, even if only two quadrants are required. This would simplify the overall system, and reduce the types of spares required.
- All PS will use Ethernet Digital control with EPICS interface capability, by using the Modbus TCP communication protocol. The current and/or voltage set points, read backs, limits, and digital commands, and statuses (other than external interlock and on/off status) shall be made over the network. All PS shall have a hardwired on/off status output. The response time of this output shall be 50 ms or less. The on/off status output shall be a 24-V signal, with 24 V signifies “on”, and 0 V or disconnected signifies “off”. The external interlock and fast dump-switch control signals shall always be hardwired, and designed to be fail-safe. Hence, if the signal becomes disconnected, the PS shall shut off, or the switch shall open. These signals shall operate using an isolated 24-V signal: a 24-V level allows operation while 0-V or a disconnected status disables the PS or opens the switch.
- The long-term current stability requirements (defined as parts per full scale current, over 8 hours with fixed line, load, and ambient temperature) and temperature coefficient match those from the FRIB Experimental Systems Division [FRIB-T31209-SP-000152] pre-separator:  $\pm 20$  ppm (long term stability and temperature coefficient) class for the dipoles,  $\pm 300$  ppm class for quadrupoles, and  $\pm 500$  ppm for the multipoles. The dipole PS will be located in the lower level of the PS area, where the air-temperature stability will be tightest at  $24\text{ }^{\circ}\text{C} \pm 2.8\text{ }^{\circ}\text{C}$ . The



calculated worst-case long-term dipole PS current stability equals  $\pm 130$  ppm full scale (20 ppm/ $^{\circ}\text{C}$  temperature coefficient, assuming constant line and load, and worst case air temperature stability). The worst-case air-temperature stability on the mezzanine will be  $24^{\circ}\text{C} \pm 5.6^{\circ}\text{C}$ . Therefore, the calculated worst-case long-term quadrupole-current stability equals  $\pm 1850$  ppm (140 ppm/ $^{\circ}\text{C}$  temperature coefficient), and the calculated worst-case long-term multipole current stability equals  $\pm 2740$  ppm (200 ppm/ $^{\circ}\text{C}$  temperature coefficient). These calculated worst-case long-term current stabilities meet the required PS stability in Table 10-2 and Table 10-3.

- Testing of similar systems at FRIB and NSCL have shown the measured long-term current stability to be well within the calculated values.
- All power supplies and beamline stands are tied to the facility ground by a grounding conductor sized by NEC 2017 Table 250.122. Additionally all power supplies are tied to ground by a low impedance path to shunt high frequency currents to ground as shown in figure 10.1.
- Power supply response to network failure / restore
  - PS will stay at last commanded set point, interlocks by PLC, will remain functional.
- Power supply response to AC power failure
  - Typical SCM PS; bulk PS hold up time 20 ms, after which the PS may latch off on DC bus under voltage. Additionally the DC bus capacitors may extend the hold-up time depending on the operating mode, i.e no significant extended hold-up time while sourcing full power, to an additional  $\sim 1$  cycle hold-up while sourcing 10% power, also during sink mode the magnet sources the energy to hold-up the DC bus.
  - If latched off, magnet stored energy will safely dissipate in PS dump resistor. PS will be functional after power restore, and reset if latched off.
  - Typical RTM PS;  $\frac{1}{2}$  cycle ride-through, typical, on all three phases, 3 cycle ride through on single phase; missing phase shutdown. PS may latch off.
- Power supply response to Controls failure: 24 V I/O drop or PLC failure
  - PS interlock signal will be removed and PS will shut off
  - Magnet stored energy will safely dissipate in PS dump resistor. PS will be latched off and functional after controls restore.
- Power supply response to cooling water out of range;
  - Temperature or flow rate may effect output stability, at worst case the PS would be interlocked off by either an external flow meter or internal temperature protection. Long term high temperature may reduce MTBF.
- Magnet stored energy will safely dissipate in PS dump resistor. PS will be latched off and functional after water restore.
- DC leads are cables required to connect the PS to the magnets. The DC leads from the PS to the magnet will be approximately 150 ft. each. Extra flex UL tray-rated cable will be used because of its flexibility and durability. The number of conduits to exit the rack area and route to the magnets has been calculated and incorporated into the building design. The conduits are



based on the number of DC leads, lead gauge, and lead length of the HRS DC leads, with additional conduits for all other signal types and spare conduits. The DC leads will be routed between the racks and beamline vault, will be routed in cable trays, and through conduits between the areas. The DC leads are required to be UL listed for use in cable tray, and follow NEC guidelines for use in conduits, terminations, connections, etc. The DC leads are also sized to minimize the voltage drop to  $\sim 1$  V, in order to minimize the time to ramp the magnet to field. The single conductor DC leads are run adjacent in pairs and interleaved (+,-,+,-) in the cable tray to minimize any magnetic loops.

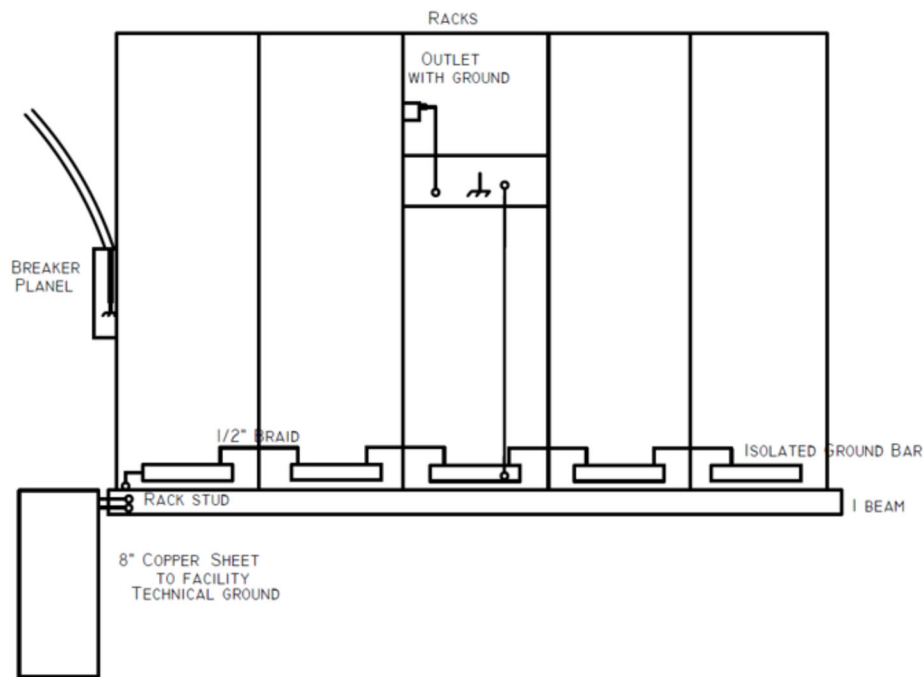


Figure 10-1 Typical rack row and device grounding block diagram.

### 10.3 Preliminary Design

The hardware including power supplies and associated infrastructure will be similar to recent FRIB procurements. Technical utilities use off-the-shelf equipment and follow standard industrial practices.

Switch-mode regulated PS technology is selected over linearly-regulated PS technology because of the higher efficiency and the smaller physical size. Switch-mode technology is a proven technology at NSCL and FRIB. One drawback of the switch-mode topology is the presence of high-frequency noise, which can be mitigated by high-frequency grounding. Like most electrical equipment, the FRIB Power Supply (PS) systems must be grounded to a facility ground to comply with electrical codes. This is typically achieved through the main electrical ground from the 60-

Hz supply. But while this type of grounding is sufficient for safety purposes, it is inadequate for high-frequency currents, which require a very low impedance path. The high-frequency grounding of HRS power supplies will follow standard practices and suggestions [FRIB-T31209-PR-000444, FRIB-T10503-VS-000001], and as shown in Figure 10-1. The magnet steel and magnet stands are tied to facility ground with a code grounding conductor sized by NEC 2017 Table 250.122. The facility ground provides a low impedance ground from the supply to the magnet.

Standard “off-the-shelf” single-quadrant PS with external polarity reversal will be used for the Room-Temperature (RT) steerer magnet PS. The polarity reversal will have a zero-crossing delay of around 2 seconds. The SCM PS will utilize FRIB type PS or similar custom build-to-specification PS. Build-in-house, and build-to-print procurement strategies have been considered but are not practical as the SCM PS use standard technology available at several specialty power-supply suppliers. Technical utilities use off-the-shelf equipment and standard industrial practices. SCM PS interfaces have been documented [FRIB-T31209-CM-000111] and are depicted in Figure 10-2.

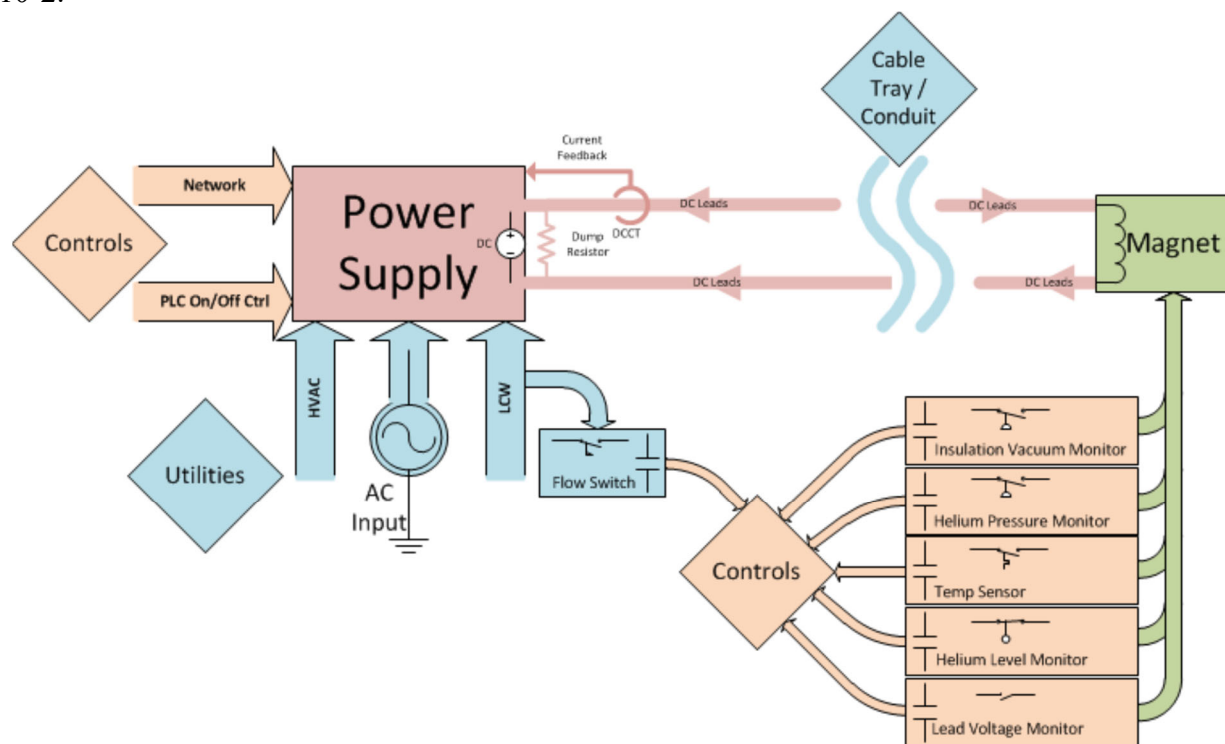


Figure 10-2 Typical SCM PS block diagram

### 10.3.1 Power supplies

#### 10.3.1.1 HTBL power supplies

Table 10-2 contains the HTBL magnet name, quantity, maximum magnet current required, PS current, PS voltage, stability requirement, and PS stability. These requirements originate from the lattice design meeting the physics requirements (See Section 4) for the HTBL (See Section 5) with concomitant magnet hardware (See Section 9).

Table 10-2 HTBL PS requirements.

Magnet type	Magnet Description	Current (A) †	PS stability ppm_fs*	Required PS stability ppm_fs**	Voltage (V)	Number of Quadrants	E_stored (kJ)	L (H)	Total PS needed	80 V Slow Dump Circuit Required	200V Fast Dump Circuit Required	Delta V Circuit Required	Quench Protection Topology
HTBL-D	Dipole	182	20	150	6	2 (or 4)	356	21.5	4	yes	no	no	Self-protecting
HTBL-QB(Q)	Quad	76	300	2000	6	4	87.7	30.4	16	yes	no	no	Self-protecting
HTBL-QB(S)	Sextupole	40	300	2000	6	4	0.3	0.37	16	yes	no	no	Self-protecting
HTBL-QB(O)	Octupole	20	500	3000	6	4	0.08	0.38	16	yes	no	no	Self-protecting
HTBL-QC(Q)	Quad	98	300	2000	6	4	196.6	41	8	yes	no	no	Self-protecting
HTBL-QC(S)	Sextupole	40	300	2000	6	4	0.57	0.71	8	yes	no	no	Self-protecting
HTBL-QC(O)	Octupole	20	500	3000	6	4	0.08	0.38	8	yes	no	no	Self-protecting
C1***	RT Corrector	250	500	3000	100	2	5	0.16	2	NA	NA	NA	NA

\* Parts per million of full scale (ppm\_fs) assuming constant line, load, and ambient temperature

\*\* ppm fs assuming constant line, load, and worst case ambient temperature change

\*\*\* Magnet / PS optimization in process

†: This table includes current (amps) requirements with tuning margin to ensure project specifications are met. The current requirements are based on the magnetic designs which include magnetic field requirements with tuning margin, therefore the power supply voltage and currents include tuning margin.

#### 10.3.1.2 Spectrometer Section power supplies

Table 10-3 contains the HTBL magnet name, quantity, maximum magnet current required, PS current, PS voltage, stability requirement, and PS stability. These requirements originate from



the lattice design meeting the physics requirements (See Section 4) for the Spectrometer Section (See Section 6) with concomitant magnet hardware (See Section 9).

Table 10-3 Spectrometer Section PS requirements

Magnet type	Magnet Description	Current (A) †	PS stability ppm_fs*	Required PS stability ppm_fs**	Voltage (V)	Number of Quadrants	E_stored (kJ)	L (H)	Total PS needed	80 V Slow Dump Circuit Required	200V Fast Dump Circuit Required	Delta V Circuit Required	Quench Protection Topology
QSA	Quad	1100	300	2000	6	4	824	1.4	3	yes	no	no	Self-protecting
	Sextupole	65	300	2000	6	4	7.9	3.7	3	yes	no	no	Self-protecting
	Octupole	52	300	2000	6	4	2.4	1.8	3	yes	no	no	Self-protecting
QSB	Quad	1300***	300	2000	6	4	2294	2.7	3	yes	no	no	Self-protecting
	Sextupole	151	300	2000	6	4	65.1	5.7	3	yes	no	no	Self-protecting
	Octupole	65	300	2000	6	4	15.8	7.5	3	yes	no	no	Self-protecting
DS1	Dipole	457	20	150	40	2 (or 4)	9010.1	86.3	1	no	yes	no	Self-protecting
		393	20	150	40	2 (or 4)	2326	30.1	1	no	yes	no	Self-protecting

\* ppm\_fs assuming constant line, load, and ambient temperature

\*\* ppm\_fs assuming constant line, load, and worst case ambient temperature change

\*\*\* Magnet / PS optimization in process

†: This table includes current (amps) requirements with tuning margin to ensure project specifications are met. The current requirements are based on the magnetic designs which include magnetic field requirements with tuning margin, therefore the power supply voltage and currents include tuning margin.

### 10.3.2 Technical utilities and infrastructure

HRS technical-equipment racks are part of the technical utilities. A preliminary rack layout spreadsheet has been made, which includes the following specifications. To keep the temperature of the PS well below the maximum operating temperature, the use of exhaust fans may be incorporated in racks that contain air-cooled PS. One rack unit (1.75 in) is the recommended spacing between power supplies and is accounted for in the calculations. Blank panels will be installed in the 1 U spaces between power supplies to help prevent dust from settling inside the PS. Water cooled PS (SCM PS) will be located in the bottom of the rack to keep them out of the exhaust path, to help prevent equipment damage in case of a water leak, and to keep them from heating unnecessarily. Hoffman boxes will be used where possible to make better use of the





available rack space, i.e. non 19-inch rack mount equipment should be housed in Hoffman boxes to reserve racks for rack mount equipment. Physical space is available for additional and upgrade racks if necessary. Forty-two racks are reserved for HRS PS (35) and controls (7). Five racks are foreseen and reserved for the future 120 kW RF separator electronics. Space for 56 racks is available on the mezzanine and ground levels of the PS area as shown in Figure 10-3.

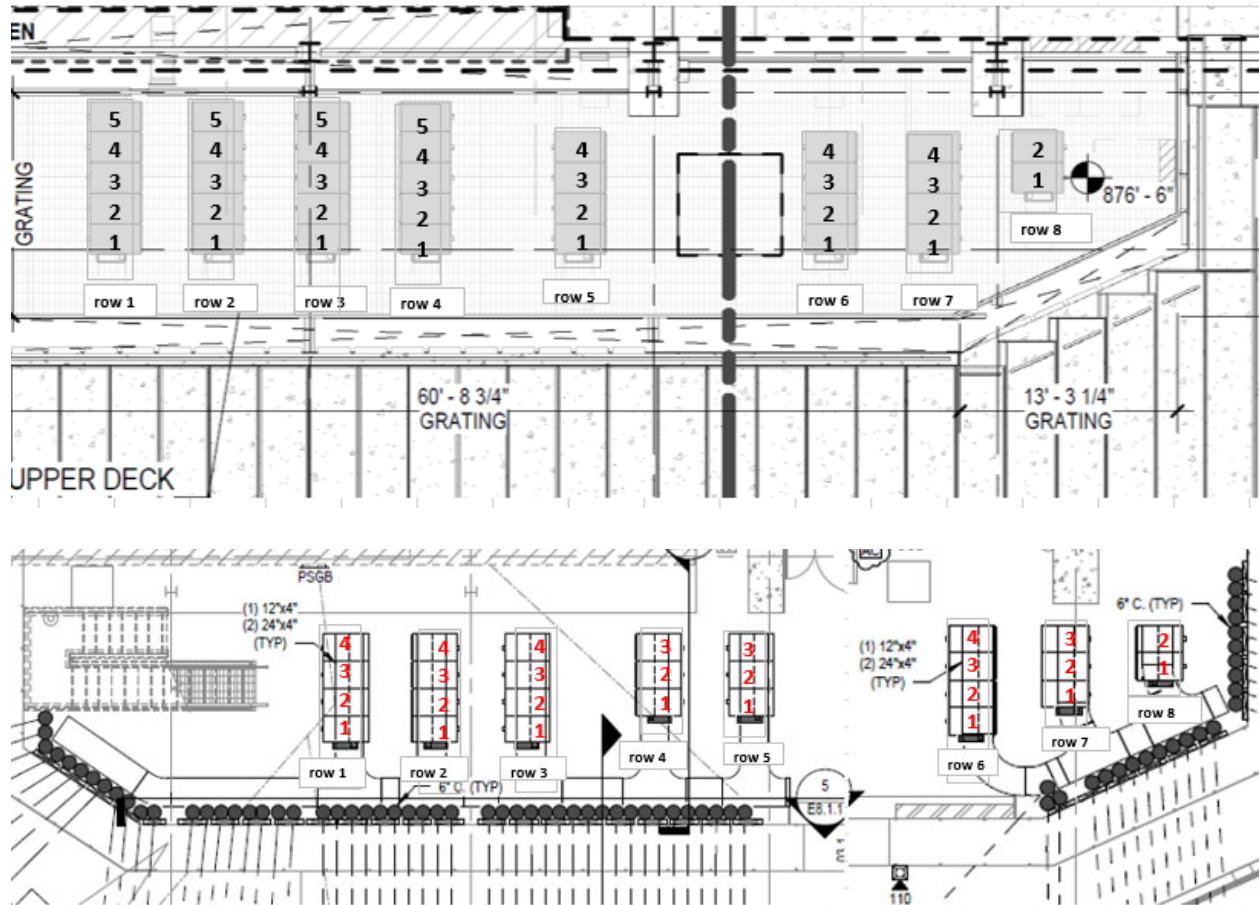


Figure 10-3 (top) Rack layout at the mezzanine level, providing space for 38 racks. (bottom) Rack layout at the ground floor level, providing space for 25 racks.

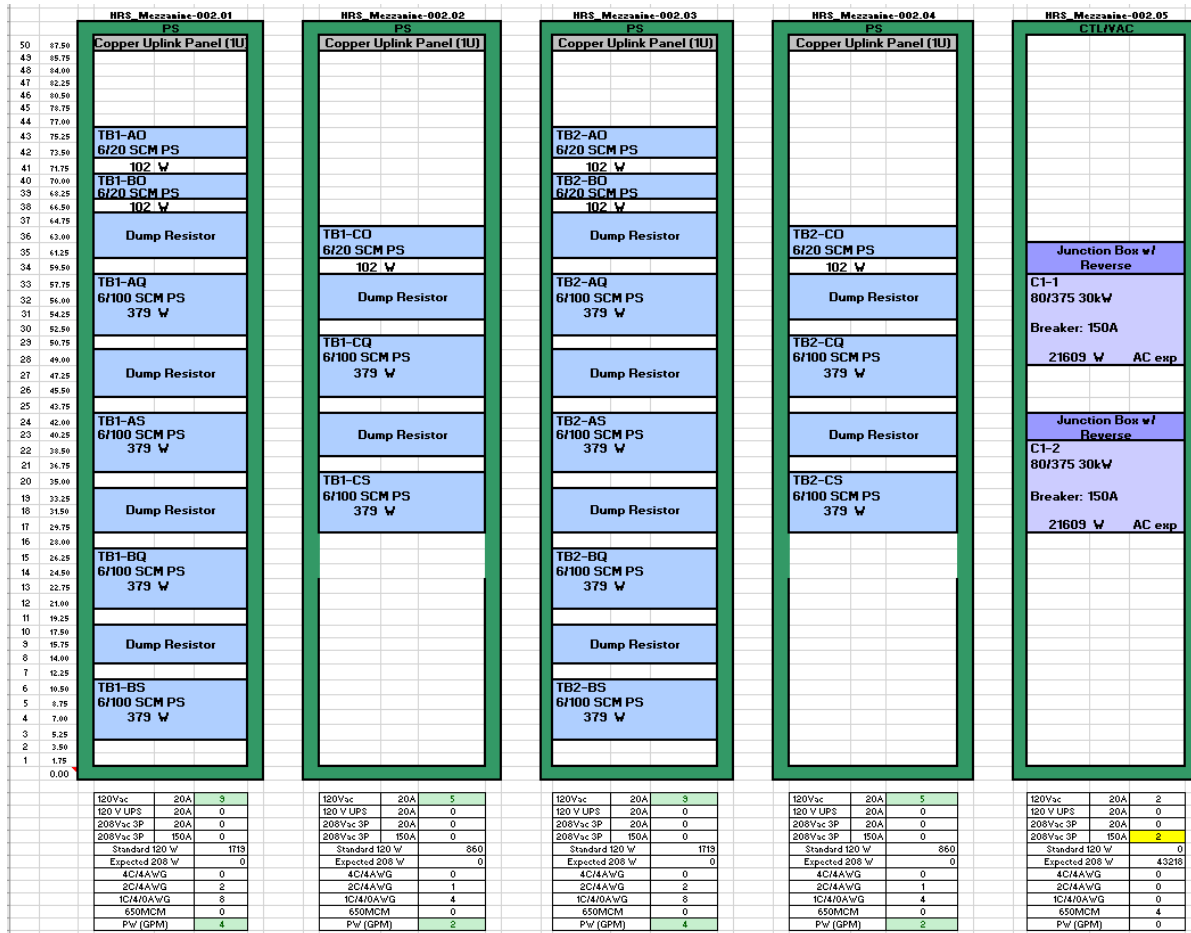


Figure 10-4 Example of a Rack layout spreadsheet

- Utilities for PS include AC power (330 kW total with upgrades), treated filtered Process Water (PW) for SCM PS (360 GPM total with upgrades), and HVAC (7.8 tons total with upgrades). The capacities have been calculated and provided through the conventional facilities scope (outside of the HRS scope). The final distribution of AC power (from the AC panels to the racks) and PW (from main header to devices in the racks) is part of technical utilities. The final distribution requirements are documented in the preliminary rack spreadsheet, as shown in Figure 10-4.
- All SCM PS will be fed from 208 VAC 3-phase AC power, or standard 120 VAC. RT corrector magnets will use standard 208 VAC 3-phase AC power. Each rack row will have a 400-A panelboard mounted on the end of the row. A 480 VAC 3-phase power for a future 120-kW



RF separator has been provided by conventional facilities. A UPS panel has been provided by conventional facilities and the technical utilities scope will cover the distribution from the UPS panel to the controls racks where UPS is required for cryogenic PLCs. Six clean-power AC panels, clean-power transformers, and related equipment has been provided by conventional facilities. Technical utilities scope will cover the clean-power distribution from the 6 panels in the vault to the diagnostics and detectors on the HTBL and Spectrometer Section.

- All HRS PS with hardwired AC power will have lockable disconnecting means and Zero voltage indicators with safe test points installed.
- The rack spreadsheet includes PW flow requirements for water-cooled SCM PS. Conventional facilities has provided the Process Water (PW) system used to cool the power supplies, and technical utilities will provide the final rack PW distribution. The PW system is cooled with a dedicated cooling-tower water system. The PW system is a 150-lb. rated system. Process Water temperature rise through equipment will be similar to the RF rack facility at FRIB, an average temperature rise through the equipment of approximately 7 °F. The Process water loop is designed to provide water with a temperature of 90 °F ± 2 °F to the technical equipment. PW systems are normal-quality cooling water, not Low Conductivity Water (LCW). There are no special quality requirements. A 5-Micron Side-Stream filter is included for the closed loop PW system. The process-water pressure drop across each Power Supply has been measured to be approximately 80 psig.
- Low-conductivity water is required for the RT steerer magnets, and several vacuum pumps in the vault. The two magnets require 5 GPM each, and 5 GPM has been reserved for 5 large roughing pumps. LCW capacity is reserved for the future RF separator, which will require 28 GPM of PW on the rack mezzanine, 120 GPM of LCW to the transmitter (72 GPM) and cavity (48 GPM), and 5 GPM each for the RT kicker magnets. Conventional facilities has provided the LCW supply into the HRS vault, technical utilities will provide the distribution along the beamline.
- Waste heat from DC cables and air-cooled RT steerer magnet PS are included in the HVAC requirements that have been provided to Conventional Facilities. Conventional facilities has provided the HVAC systems. The High bay Air Handling Unit will maintain the air temperature at 75 °F ± 10 °F throughout the high bay, but will control to the thermostat furthest from set point. The thermostats will be located near the mezzanine. The lower level of the rack area will be controlled to a space temperature of 75 °F ± 5 °F. Space relative humidity will vary from 10% to 60 %. The dipole PS will be located in the lower level rack area due to the tighter air temperature stability.
- The DC leads from the PS to the magnet will be routed between the equipment racks and the magnets in the vaults. The DC cables will be routed in cable trays, and through conduit between the areas. The conduits are part of the conventional facilities scope (outside of the HRS scope). The cable trays from the racks to the conduits and cable trays along the beamline are part of technical utilities scope. The number of conduits has been calculated, and the calculations of



the number of conduits include a 50% fill factor versus the National Electric Code. The voltage drop on the cables have been calculated to be approximately 1 V for the superconducting magnet PS and is well within the acceptable range. Sixty-one six-inch conduits for DC and controls are foreseen. The building design includes 71 six-inch conduits, as shown in Figure 10-5, plus an alternate route with 16 four-inch conduits. Additionally, an alternate route through the existing NSCL wall and through conduits in a future roof-beam ledge has been identified.

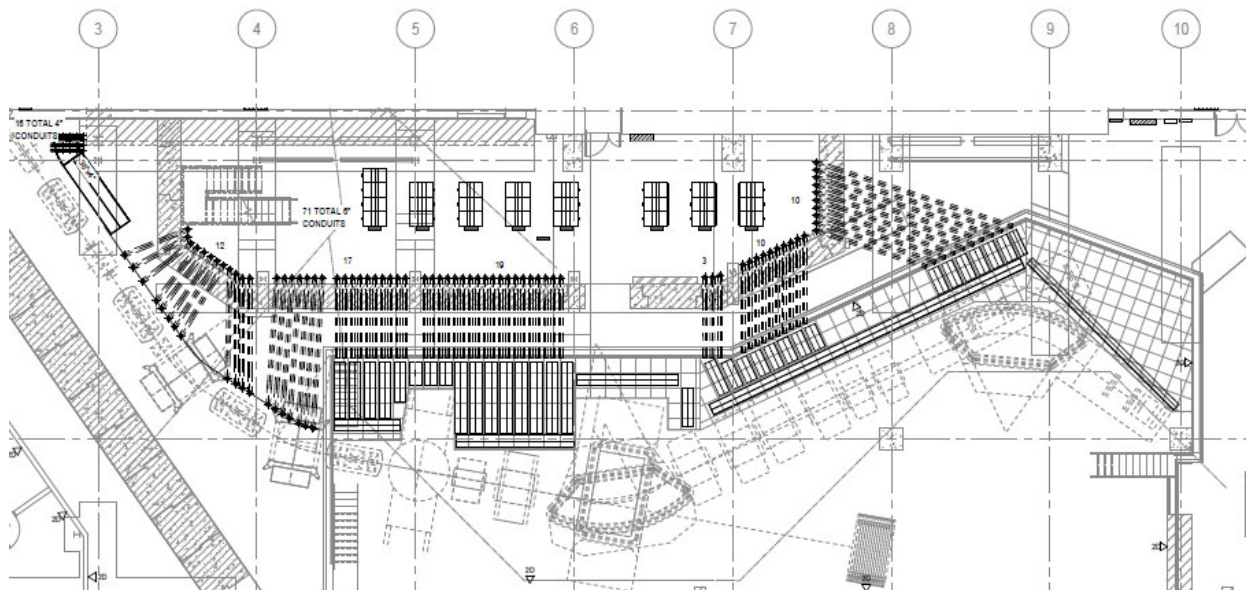


Figure 10-5 Layout of conduits from equipment racks to the HTBL and Spectrometer Section of the HRS.

Compressed-air and dry-nitrogen distribution along the HRS beamlines are part of technical utilities scope. Conventional facilities will provide the compressed air capacity and main distribution, technical utilities provides the final distribution along the beam line. The existing NSCL dry-nitrogen supply will be the primary source for HRS, along with N<sub>2</sub> bottles and/or boil-off Dewars, if additional capacity is required.

Possible future upgrades have been considered for the worst-case upgrade as far as rack space, conduit, and utilities are concerned. Physical room for racks will be available, conduits will be in place, and utilities will have adequate infrastructure in place for future upgrades. Future upgrades include an RF Separator along with 2 kicker magnets (identical to the RT corrector magnets), and some rack space is reserved for other future possibilities.

## 10.4 References

- [FRIB-T31209-SP-000152] Superconducting Magnet Power Supplies Specifications
- [FRIB-T31209-PR-000444] FRIB Power Supplies High Frequency Grounding Installation Procedure
- [FRIB-T10503-VS-000001] Using the FRIB Facility Grounding Mesh System Effectively
- [HRS-M41800-CM-000308-R001] HRS Power Supply Interface Control Document





## 11 Cryogenic Systems

### 11.1 Introduction and overview

The HRS requires cryogenic capacity in the form of liquid helium and liquid nitrogen for cooling of the superconducting magnets. The Work Breakdown Structure (WBS) is given in Table 11-1. The cryogenic mode of operation is patterned after the existing refrigeration system presently supplying the magnets of the NSCL A1900 fragment separator. The system design assumes the magnetic coils are bath cooled with helium supplied directly as liquid from a pressurized Dewar. The thermal shield is assumed to be cooled with liquid nitrogen.

Table 11-1. Work Breakdown Structure (WBS) for HRS cryogenic system.

<b>Experimental Systems - High Rigidity Spectrometer</b>	<b>HRS.3</b>
<b>High Transmission Beamline (HTBL)</b>	<b>HRS.3.01</b>
<b>High Transmission Beamline Power Cryogenics</b>	<b>HRS.3.01.06</b>
<b>Spectrometer Section</b>	<b>HRS.3.02</b>
<b>Spectrometer Section Cryogenics</b>	<b>HRS.3.02.08</b>

There are several possible cryogenic plants that may be used to supply cryogenics to the HRS, including the existing NSCL plant, the existing FRIB plant, or a new cryogenic plant. It is not foreseen that the costs incurred in providing service to the HRS system will change significantly as long as a welded and flanged line type (not U-tube) design for local magnet connections is used.

All new magnet designs will comply with FRIB cryogenic plant requirements. Since the HTBL quadrupole triplet is based on the existing design of the A1900 triplet, its design will be reviewed and any necessary modifications made to comply with these requirements. For example, the FRIB system returns cold helium to the refrigerator at a lower pressure than in the NSCL system. This results in a smaller pressure difference to drive lead flow since the cold return pressure defines helium pressure in the cryostat and the current leads return their gas flow to compressor suction pressure. Review of current lead designs will be done to assure adequate flow of gas through the lead given the flow resistance inherent in the design, with margin for dynamic conditions of operation. Electronic flow controls have also been costed in for each lead assembly whereas the A1900 triplets and dipoles have traditionally used manual set flow control valves on their leads.

### 11.2 Requirements

Requirements for cryogenic capacity of the HTBL and Spectrometer Section are as shown in





Table 11-2. The cryogenic loads are based on known loads of similar operational equipment. For example, the existing A1900 system loads are known and almost identical to the HTBL system design. NSCL and FRIB have many large superconducting magnets of unique types in operation providing a good basis for accurate estimates of the spectrometer magnets cryogenic loads. Refrigeration loads due to current-lead mass-flow requirements that return gas to compressor suction at 295K require additional refrigeration capacity to remove heat between 80 K and 4.5 K. The refrigeration loads due to both static loads returned cold and those for lead flow requirement (at maximum current requirement) of these devices are shown in Table 11-2. Loads above the 80K temperature are removed by heat exchange with liquid nitrogen and so nominally do not effect helium refrigeration capacity.

Cool down requirements for each magnet type is given in Table 11-3 assuming a four stage process using a maximum temperature difference of 50K between device temperature and the gas or liquid helium supply as the process dictates.

For present operation of the NSCL coupled cyclotron accelerator system, most of the cryogenic capacity of the existing plant is required. Upon commissioning of the new FRIB accelerator, however, some devices will be removed from the system and that capacity as given in Table 11-4 becomes available. There is a shortfall of about 208W between the new cryogenic loads and those decommissioned, much of that being due to the increased current lead requirement due to larger total current requirement from an increased number of magnets. One possible option being explored is the operation of the reconfigured A1900 off the FRIB cryogenic plant. The loads of the A1900 are equivalent to that shown for the HTBL magnets, close to being equal to the shortfall. This would therefore leave enough capacity in the present NSCL plant to fully handle the HRS total cryogenic load in addition to its other remaining loads. Importantly, no additional cryogenic plant capacity will be required. The cryogenic capacity necessary for the HRS will be available from a combination of extant FRIB and NSCL cryogenic plants.



Table 11-2. HTBL, Spectrometer Section, and distribution cryogenic loads at 4.5K.

HTBL and HRS Cryogenic Loads		Load/ unit @ 4.5 K (W)	Total load @ 4.5 K (W)	Total load for leads (80 K-4.5 K) (W)	Total (W)
Device	Quantity				
HTBL Valve Boxes	12	6.5	78		
HTBL Magnets	12	5	60	151	
Spectrometer Valve Boxes	8	6.5	52		
Spectrometer Dipoles	2	20	40	32	
QS1A Quad	1	11	11	21	
QS2B-QS4B Quads	3	16	48	104	
QS5C - QS6C Quads	2	13	26	37	
Branch Box 1 System	1	16	16		
Branch Box 2	1	16	16		
Transfer Line, 300 ft	300	0.1	30		
<b>Total</b>			<b>377</b>	<b>345</b>	<b>722</b>

Table 11-3 Cool-down parameters for each magnet type.

Device type	Units	HTBL Triplet	HTBL Dipole	QSA Type Quad	QSB Type Quad	DS1 Dipole	DS2 Dipole
Cold mass weight	kg	4500	900	2293	4052	16400	7300
Shield weight	kg	350	110	190	370	1200	680
Helium Volume	liters	600	160	175	240	350	270
Cold mass cool-down load							
Phase 1: 300 K–100 K	MJ	348	70.0	177	314	1279	570
Phase 2: 100 K–50 K	MJ	64.5	13.5	33	58	236	105
Phase 3: 50 K–4.5 K	MJ	11.8	2	6	10	44	19.4
<b>Total</b>	MJ	424.3	85.5	216	382	1559	694.4
Shield cool-down load							
Phase 1: 300 K–80 K	MJ	29	9.3	15.7	30.7	102	57
Cold mass and shield cooldown max. ΔT	K	120	120	120	120	120	120
Cool-down time	Hrs.	96	72	72	72	144	144
Cool-down control ΔT	K	50	50	50	50	50	50
Cool-down Helium flow							
Phase 1: Cold mass	g/s	7	7	7	7	10.0	10
Phase 2: Cold mass	g/s	2	2	2	2	3	2
Phase 3: Cold mass	g/s	1	1	1	1	1.5	1
Phase 4: Final cool-down & filling, 1-2 days	g/s	0.70	0.15	0.3	0.6	.20	0.15
Warm up time	Hrs.	84	20	43	75	260	140



Table 11-4 Cryogenic load reduction from decommissioned coupled cyclotron elements.

	Loads Removed Upon FRIB Operation (W)	Total load for leads (80 K-4.5 K) (W)	Total (W)
K1200 Coil	144	61.8	
K1200 Cryopanel	45		
K500 Coil	62	38.6	
K500 Cryopanel	40		
SC ECR	48	52.1	
Coupling Line	15	7.3	
<b>Total</b>	<b>354</b>	<b>160</b>	<b>514</b>

### 11.3 Design approach

The design approach for the cryogenic system is based on a system similar to the cryogenics of the current A1900 and assumes branching from an existing cryogenic transfer line as is shown in Figure 11-1. This line has proven cryogenic capacity since it is part of the system supplying equipment of similar loads to be later decommissioned. If another cryogenic plant is used as the source, the existing cryogenic header of Figure 11-1 will be appropriately modified.

A branch box (HRS Branch Box 1 in Figure 11-1) from the existing main transfer line serviced by U-Tube connections is included in the design. Its location after cryogenics design may be changed from the one shown in the figure. A directional control box (HRS Branch Box 2 in Figure 11-1) separating upstream and downstream section sections of the HTBL is included and has valves to isolate one direction of the transfer line. HRS Branch Box 2 is assumed to be a welded-line construction without U-tube disconnects, similar to the extant NSCL cryogenic Box 23 shown in Figure 11-2(a).



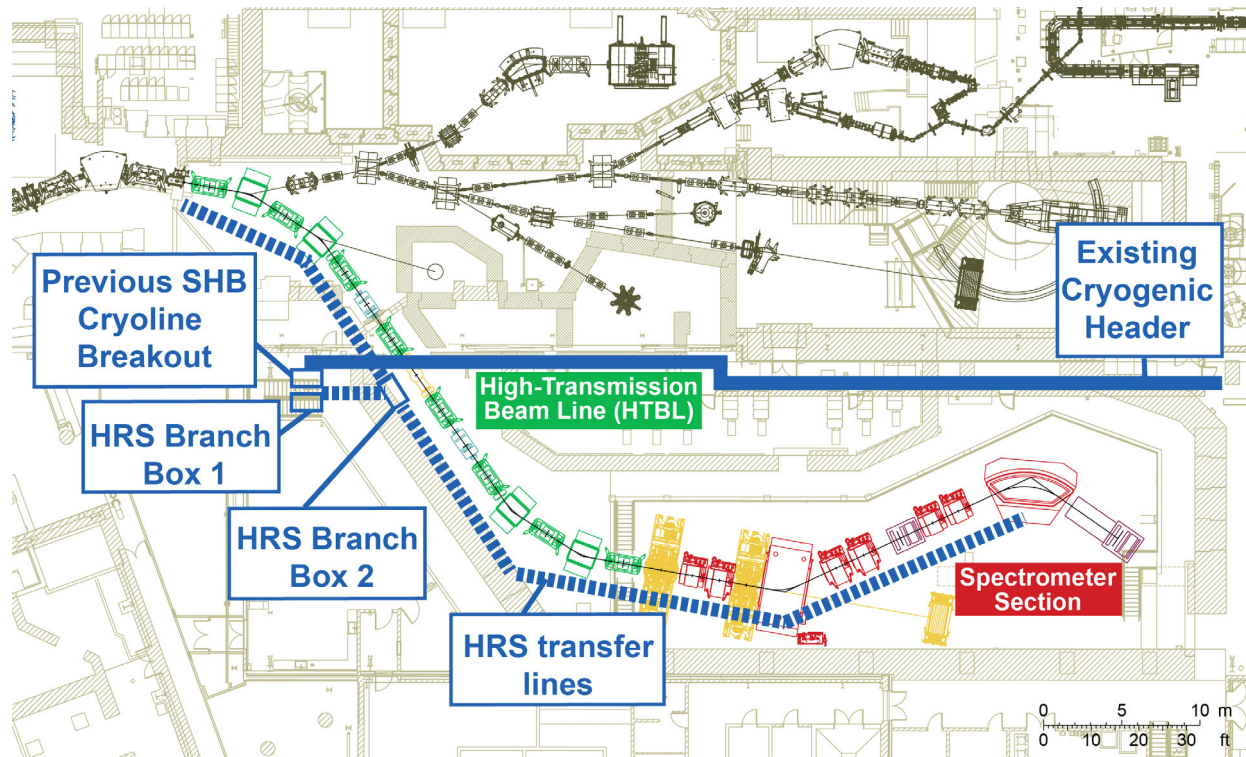


Figure 11-1 Cryogenic system layout preliminary design.

For each of the 20 cryostats (12 in the HTBL and 8 in the Spectrometer Section), there will be local valve boxes of the same design as those used for the A1900 magnets. Each valve box will have the capability of switching return helium to a warm (>20K) or cold return with the capability of supplying cold gas or LHe during cooling down. Liquid nitrogen supply and return switching for the thermal shield is also present in the local box. Similar to NSCL local distribution shown in Figure 11-2(b), welded connections to the magnets are assumed with no U-Tubes at the magnets. See references [NSCL09], [VIN09], and [LAU98].



Figure 11-2 (a) NSCL Box 23 similar to proposed HRS Branch Box 2; (b) NSCL local valve box and transfer line section similar to proposed local HRS cryogenic boxes and transfer line

The initial implementation will include a cryogenic line from the main transfer line, all branch boxes and the entire section of the transfer line including local valve boxes for 1<sup>st</sup> half of the HTBL. The further implementation will include the extension of the cryogenic head and local valve boxes needed to service the additional devices.

The new FRIB cryogenic plant is being coupled to the NSCL plant through a distribution system independent of cost to the HRS project as shown in Figure 11-3. Loads may be shared by isolating specific line sections supplied either from the east HTBL side or the west side in the HRS building through the coupled distribution box area. The HRS Branch box 2 allows for east and west side isolation and its specific location in the system may be changed as cryogenic system design dictates. This also allows for sharing extra cryogenic loads due to temporary load increases such as cool down.



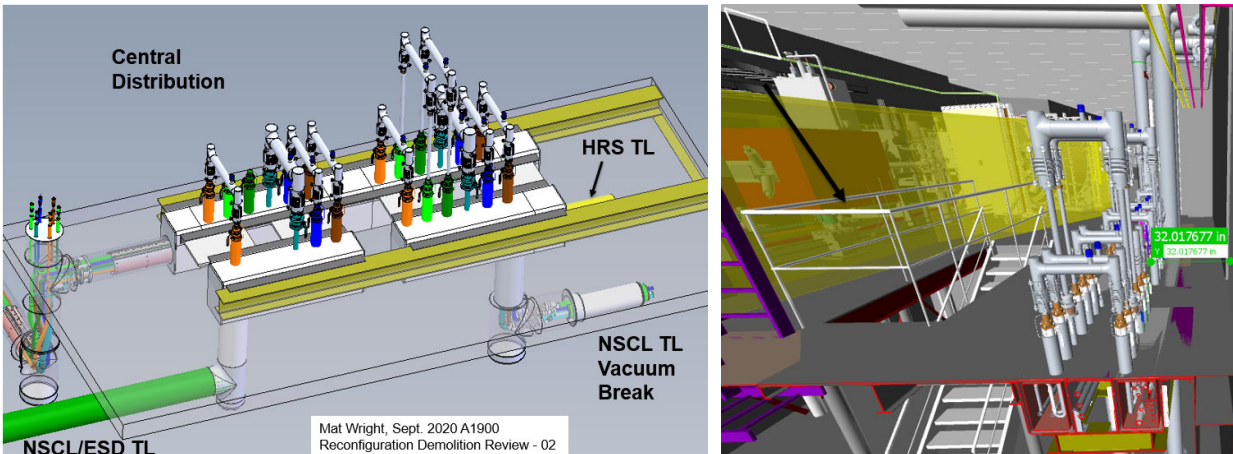


Figure 11-3 FRIB ESD-NSCL coupling and east-end distribution area. The HRS transfer line will supply the west-end distribution area.

In the future, there may also be plans to incorporate a new, more modern helium plant. Besides having higher efficiency, this may increase cryogenic capacity. Even though the existing system and possibly the existing main cryogenic header may be replaced, it is not foreseen that the costs incurred in providing service to the HRS system will change significantly as long as a welded line type design for local magnet connections is used.

## 11.4 References

- [NSCL09] NSCL Cryoplant Upgrade Recommendation Report, NSCL Meeting, 6/26/2009
- [VIN09] Cryoplant Options and Operation Report, John Vincent, 6/2/2009
- [LAU98] Review of Liquid Helium Production System, H. Laumer, 1/29/1998



## 12 Control Systems

### 12.1 Introduction and overview

The Controls scope includes the materials and labor needed to design, procure, assemble, bench test, install, test in situ, and to perform final integrated testing without beam as specified by the WBS provided in Table 12-1. The main areas of scope include Low Level Controls, Protection Systems, Network & IT, and High Level Controls.

Low Level Control Systems include Low level controls for both the High Transmission Beamline and Spectrometer Section and is based on Experimental Physics and Industrial Control (EPICS) framework.

Protection systems include both Personnel Protection Systems (PPS), and Machine Protection Systems (MPS). The PPS provides protection to personnel from radiation hazards through access control and radiation monitoring. It also provides monitoring and alarming for low oxygen or flammable gas conditions. The MPS monitors relevant beam parameters and stops beam when conditions are no longer satisfied.

The Network and IT systems provide a high-bandwidth, high reliability network and computing platform to support control system operation.

High Level controls provide CS-Studio Operation screens, and applications such as Chart recorders, Save/Restore Utility, Archiver, alarm server, logging applications, high level EPICS Input, Output Controllers (IOC)s, and controls for the beamline commissioning.

Table 12-1 WBS for the control systems of the HRS

<b>Experimental Systems - High Rigidity Spectrometer</b>	<b>HRS.3</b>
<b>High Transmission Beamline (HTBL)</b>	<b>HRS.3.01</b>
<b>High Transmission Beamline Low Level Controls</b>	<b>HRS.3.01.07</b>
<b>Spectrometer Section</b>	<b>HRS.3.02</b>
<b>Spectrometer Section Low Level Controls</b>	<b>HRS.3.02.09</b>
<b>Central Systems</b>	<b>HRS.3.03</b>
<b>Protection Systems</b>	<b>HRS.3.03.01</b>
<i>Personnel Protection Systems</i>	<i>HRS.3.03.01.01</i>
<i>Machine Protection Systems</i>	<i>HRS.3.03.01.02</i>
<b>Network &amp; IT</b>	<b>HRS.3.03.02</b>
<b>High Level Controls</b>	<b>HRS.3.03.03</b>



## 12.2 Requirements

The requirements for controls originate from the lattice design meeting the physics requirements (see Section 4) for the HTBL (see Section 5) and for the Spectrometer section (see Section 6) with concomitant hardware (see Sections 7, 9, 10, 11, and 13).

### 12.2.1 Controls requirements

The resulting hardware to support the design used for magnets, power supplies, diagnostic systems, vacuum systems and cryogenics drive the signal requirements for control systems. These requirements are captured in tables for each device. An example is given for the HTBL quadrupole triplets in Table 12-2. These tables are used to determine the number of analog inputs (AI), analog outputs (AO), digital inputs (DI), digital output (DO) points, and instrumentation such as temperature controller points (Temp), 5B style signal conditioning modules, serial/ethernet connections, and motor controls (Motor Ctrl).



Table 12-2 Signal list for the HTBL quadrupole triplets used to determine the controls I/O requirements.

TBn Quad Triplet - Cryoload PLC									
Signal	AI	AO	DI	DO	Temp	5B	Serial	Ethernet	Motor Ctrl
Helium Vessel Pressure Transducer	1					1			
Helium Level Sensor	1								
Helium Vessel Temperature Sensor 1			1		1		0.125		
Helium Vessel Temperature Sensor 2			1		1		0.125		
Heat Shield Temperature Sensor 1			1		1		0.125		
Heat Shield Temperature Sensor 2			1		1		0.125		
Cryostat Vacuum Indicator	1		2				1		
Helium Vessel Rupture Disc/Popoff	1					1			
4-20 mA I to P	1	1							
4-20 mA I to P	1	1							
Solenoid Valve				1					
Solenoid Valve				1					
Solenoid Valve				1					
Insulating Vacuum Turbo Gate Valve			2	1					
Insulating Vacuum Foreline Pirani	1		2						
Insulating Vacuum Roughing Pirani	1		2						
Insulating Vacuum Pirani	1		2						
Insulating Vacuum Cold Cathode	1		2				1		
Insulating Vacuum Turbo Pump	1		2	2			1		
PLC Interconnect			3	3					
TBn Quad Triplet Cryoload PLC Total:	11	2	21	9	4	2	3.5	0	0

Based on these tables, the device requirements are then summarized by portions of the project as shown in Table 12-3 for the HTBL and in Table 12-4 for the Spectrometer Section.

Tables 12-3 & 12-4 add an additional column estimating low level EPICS signals or process variables (PVs) based on FRIB’s PV’s per device type.

High-level controls requirements flow from higher-level systems requirements and will utilize systems similar to those used at the FRIB Laboratory at present. High level control screens for use by Operations will be required, driven by CS-Studio. Applications already utilized by the FRIB Laboratory will be extended for use for the HRS, such as EPICS archivers, alarm servers, CS-Studio for screen creation and an Electronic Logbook.



Table 12-3 Device I/O Summary for the HTBL, separated into beamline, vacuum and cryoload control systems used to determine the controls I/O requirements.

System	Device	AI	AO	DI	DO	TEMP	5B	Serial	Ethernet	Motor Ctrl	EPICS Signals
HTBL – Beam line	TB1	27	9	12	21	0	27	0	9	0	540
	DB1	4	2	4	6	0	4	0	1	0	91
	TB2	27	9	12	21	0	27	0	9	0	540
	DB2	4	2	4	6	0	4	0	1	0	91
	SB1	1	0	4	2	0	0	0	2	0	74
	TB3	27	9	12	21	0	27	0	9	0	540
	FB1	10	2	14	29	0	0	0	4	1	326
	TB4	27	9	12	21	0	27	0	9	0	540
	FB2	1	0	2	3	0	0	0	1	0	46
	TB5	27	9	12	21	0	27	0	9	0	540
	FB3	12	2	16	36	0	0	0	4	3	415
	Mobile	0	0	4	3	0	0	0	0	0	21
	TB6	27	9	12	21	0	27	0	9	0	540
	SB2	1	0	4	2	0	0	0	2	0	74
	DB3	4	2	4	6	0	4	0	1	0	91
	TB7	27	9	12	21	0	27	0	9	0	540
	DB4	4	2	4	6	0	4	0	1	0	91
	TB8	27	9	12	21	0	27	0	9	0	540
<b>Total</b>	<b>257</b>	<b>84</b>	<b>156</b>	<b>267</b>	<b>0</b>	<b>232</b>	<b>0</b>	<b>89</b>	<b>4</b>	<b>5640</b>	
HTBL - Vacuum	Vacuum	34	0	113	35	0	0	17	0	0	1073
	<b>Total</b>	<b>34</b>	<b>0</b>	<b>113</b>	<b>35</b>	<b>0</b>	<b>0</b>	<b>17</b>	<b>0</b>	<b>0</b>	<b>1073</b>
HTBL - Cryoload	TB1	11	2	21	9	4	2	3.5	0	0	280
	DB1	11	2	22	9	5	2	3.625	0	0	292
	TB2	11	2	21	9	4	2	3.5	0	0	280
	DB2	11	2	22	9	5	2	3.625	0	0	292
	TB3	11	2	21	9	4	2	3.5	0	0	280
	TB4	11	2	21	9	4	2	3.5	0	0	280
	TB5	11	2	21	9	4	2	3.5	0	0	280
	FB3	0	0	0	0	0	0	0	0	0	0
	TB6	11	2	21	9	4	2	3.5	0	0	280
	DB3	11	2	22	9	5	2	3.625	0	0	292
	TB7	11	2	21	9	4	2	3.5	0	0	280
	DB4	11	2	22	9	5	2	3.625	0	0	292
	TB8	11	2	21	9	4	2	3.5	0	0	280
<b>Total</b>	<b>132</b>	<b>24</b>	<b>256</b>	<b>108</b>	<b>52</b>	<b>24</b>	<b>42.5</b>	<b>0</b>	<b>0</b>	<b>3403</b>	



Table 12-4 Device I/O Summary for the Spectrometer Section, separated into beamline and cryoload control systems used to determine I/O requirements.

Beamline Section	Device	AI	AO	DI	DO	TEMP	5B	Serial	Ethernet	Motor Ctrl	EPICS Signals
Spectrometer Section - Beamline	FS0	10	2	10	27	0	0	0	4	1	308
	QS1A	11	5	6	11	0	11	0	3	0	222
	QS2B	11	5	6	11	0	11	0	3	0	222
	DS1	18	2	6	9	0	2	0	1	0	190
	FS1	13	2	18	41	0	0	0	2	2	367
	QS3B	11	5	6	11	0	11	0	3	0	222
	QS4B	11	5	6	11	0	11	0	3	0	222
	QS5A	11	5	6	11	0	11	0	3	0	222
	QS6A	11	5	6	11	0	11	0	3	0	222
	DS2	18	2	6	9	0	2	0	1	0	190
	FS2	11	2	14	39	0	0	0	2	2	337
<b>Total</b>	<b>136</b>	<b>40</b>	<b>90</b>	<b>191</b>	<b>0</b>	<b>70</b>	<b>0</b>	<b>28</b>	<b>5</b>	<b>2724</b>	
Spectrometer Section - Vacuum	Vacuum	24	0	94	36	0	0	12	0	0	834
	<b>Total</b>	<b>24</b>	<b>0</b>	<b>94</b>	<b>36</b>	<b>0</b>	<b>0</b>	<b>12</b>	<b>0</b>	<b>0</b>	<b>834</b>
Spectrometer Section - Cryoload	QS1A	11	2	22	9	5	2	3.625	0	0	292
	QS2B	11	2	22	9	5	2	3.625	0	0	292
	DS1	10	2	29	10	14	0	3.625	0	0	364
	QS3B	11	2	22	9	5	2	3.625	0	0	292
	QS4B	11	2	22	9	5	2	3.625	0	0	292
	QS5A	11	2	22	9	5	2	3.625	0	0	292
	QS6A	11	2	22	9	5	2	3.625	0	0	292
	DS2	10	2	29	10	14	0	3.625	0	0	364
<b>Total</b>	<b>86</b>	<b>16</b>	<b>190</b>	<b>74</b>	<b>58</b>	<b>12</b>	<b>29</b>	<b>0</b>	<b>0</b>	<b>2478</b>	

### 12.2.2 Protection systems requirements

The requirements for protection systems are derived from the hardware used to support the design of the HRS and fall into two categories, personnel protection and machine protection. The use of superconducting magnets requires an oxygen deficiency hazard monitoring system. Prompt radiation produced by the beam requires a radiation safety system. Possible damage from the beam to equipment and detectors in the vault determine the requirement for a machine protection system.

The requirements for Personnel Protection Systems (PPS) include monitoring radiation levels, providing warnings and triggering beam shutdown when levels exceed thresholds. It also includes providing access control to the vault to prevent personnel from being present when beam is present



in the vault. PPS will also use a Fast Beam Containment System being extended from FRIB to monitor for unexpected beam loss and will shut down the beam in less than 0.5 ms.

PPS also provides low-oxygen monitoring and flammable-gas detection and alarming using both visual and audio systems upon detection. If oxygen concentration levels below 19.5% are detected, both audible and visual alarms will be triggered signaling for evacuation from the vault. Additionally, flammable gasses will be used in some detector systems used with the HRS, requiring monitoring for such flammable gases in the vault. If unsafe levels are detected this system will also signal evacuations using both audible and visual alarms.

The PPS is to be compatible with existing Laboratory personnel protection systems, using similar hardware for both the PLCs, monitoring, and miscellaneous hardware to minimize the total cost of ownership across the Laboratory.

The Machine Protection Systems (MPS) are to provide a hardware interface for diagnostics which will shut down beam delivery within 500 ms if an unsafe beam condition is detected for the hardware based on the current diagnostics.

In Table 12-5, an example of safety devices for the proposed design for the Radiation Safety portion of PPS is provided as an example of how I/O requirements for the personnel protection system are determined, adding up digital inputs (DI) and digital output (DO) points.

*Table 12-5 Radiation Safety System Hardware and I/O List used to determine I/O requirements*

Device	Qty	DI	DO
Door Switch	4	8	4
Gate Switch	5	10	5
E-Stop	5	10	5
Light Stack	7		21
Gamma Detector	2	6	
Neutron Detector	4	12	
Rad Monitor	3	3	
Wall Plug	1	2	1
Arm Button	7	14	7
Fast Containment Det	8	8	8
Interface Relays to upstream PPS	6	2	4
I/O Count Totals		75	55





### 12.2.3 Network and IT requirements

The requirements for network and IT flow from the hardware used in the beamline, vacuum & cryoload controls design. The Ethernet, serial connections, and EPICS signals are totaled from individual device requirements

The overall design is an extension of existing Laboratory design, utilizing standardized hardware and providing similar bandwidth to existing systems. IT will utilize existing servers, including NetApp for file storage, Backup Server, IT Management Server, Active Directory Domain Server, archivers, and Hypervisor clusters which include VMs for EPICS IOCs, and will expand capabilities for the additional signals being added to the control system.

### 12.3 Design approach

The requirements are readily achieved using systems that are the same or similar as those that have been in use at NSCL and/or were more recently implemented at FRIB. This approach minimizes both cost and performance risk and does not require an R&D program. This also reduces the overall cost of ownership in expertise required to support similar systems and in spare parts costs.

The design process will be based on the multiple documentation elements defining the processes for hardware and software design, including PLC code development, version control, testing, verification and deployment based on experience at both NSCL and FRIB.

HRS controls will utilize the robust formalized configuration management system and work control planning system which helps identify and reduce potential risks and impacts as installations progress. HRS controls will also utilize version control systems currently in use by FRIB which allows for rolling back a change if it is not successful.

The existing FRIB control system architecture was designed in a modular fashion to be able to be expanded upon with minimal impact to existing controls. The segmented network between device types and IOCs, and appropriate sizing of file servers, and network architecture has ensured the system continues to operate reliably.

#### 12.3.1 Low-level control systems design approach

While the control system is based on EPICS, hardwired inputs will be wired into separate PLCs for beamline, vacuum, and cryogenic signals. Requirements from assessments in Table 12-3 and Table 12-4 are used to determine the PLC I/O modules required and associated hardware to support the system. The I/O modules and PLC drops are tallied in Table 12-6 for the HTBL and Table 12-7 for the Spectrometer Section.



Cryogenic and vacuum control systems require a higher level of reliability and will use redundant power supplies or transfer switches tied to both the house power and the centralized UPS system.

Table 12-6 PLC hardware design summary for the HTBL.

		AI	AO	DI	DO	TEMP	5B	Serial	Ethernet	Motor Ctrl	EPICS Signals	
<b>Beamline PLC</b>	Signals	257	84	156	267	0	232	0	90	4	5640	
	I/O Modules	17	11	10	17	0	15	0		1		
	Module Total	55										
	Drops Required	7										
<b>Vacuum PLC</b>	Signals	34	0	113	35	0	0	17	3	0	1073	
	I/O Modules	3	0	8	3	0	0	2		0		
	Module Total	14										
	Drops Required	2										
<b>Cryoload PLC</b>	Signals	132	24	256	108	52	24	42.5	4	0	3403	
	I/O Modules	9	3	16	7	7	2	3		0		
	Module Total	35										
	Drops Required	4										

Table 12-7 PLC hardware design summary for the Spectrometer Section.

		AI	AO	DI	DO	TEMP	5B	Serial	Ethernet	Motor Ctrl	EPICS Signals	
<b>Beamline PLC</b>	Signals	136	40	90	191	0	70	0	28	5	2724	
	I/O Modules	9	5	6	12	0	5	0		1		
	Module Total	32										
	Drops Required	4										
<b>Vacuum PLC</b>	Signals	18	0	94	36	0	0	12	2	0	834	
	I/O Modules	2	0	6	3	0	0	1		0		
	Module Total	11										
	Drops Required	2										
<b>Cryoload PLC</b>	Signals	86	16	190	74	58	12	29	3	0	2478	
	I/O Modules	6	2	12	5	8	1	2		0		
	Module Total	25										
	Drops Required	3										



## 12.4 Design

### 12.4.1 Controls systems design

The PLC proposed for the HRS is based on the Allen Bradley ControlLogix Family. This was originally selected for NSCL and FRIB due to several factors. It has the largest installed market share in industrial settings in North America and is used at other national laboratories. There is existing in-house expertise and the manufacturer provides excellent local support. The I/O cards provide the direct interface to the process devices via modular I/O. Digital I/O interfaces with discrete logic signals via 24 VDC. Analog I/O interfaces for devices will use 4-20 mA current loops or  $\pm 10$  VDC signal levels. Other signaling levels can be translated through appropriate signal conditioning. An example of a PLC system is shown in Figure 12-1(a) and I/O wiring installation in racks is shown in Figure 12-1(d).

Interface modules (IFMs) will be used as the connection point between the 1756 ControlLogix PLC Input and Output modules and the signals from the operational devices. This significantly reduces the amount of labor and possible errors involved in wiring terminal blocks to the PLC I/O modules.

The IFMs were designed in house (see Figure 12-1(c)) to interface with specific Allen Bradley I/O modules. Unlike commercial versions, they have added 24VDC or Com connections for every signal (module-type dependent) through the use of multi-level terminal. The IFMs use one module for each IO type, analog input and output, digital inputs and outputs, and utilize a commercial pre-wired cable (see Figure 12-1(b)) from the I/O module to the IFM to reduce the amount of customized wiring.

While many devices such as power supplies, vacuum controllers, and motor controllers have intelligent Ethernet interfaces where signals can be read directly into EPICS, any signals that will use interlocks will be hardwired from the devices to a PLC.

All of the PLCs will have the ability to interface directly with EPICS IOCs. The EPICS IOCs convert PLC tag names into EPICS control system names that can be accessed across the control system network and allows users the ability to control and monitor devices connected through the PLCs. Low Level EPICS IOC PVs will be split across several IOCs covering, Cryoload, Beamline, Vacuum, Diagnostics, and PLC IOCs similar to FRIB. These will also be further divided across several soft IOCs for each section of the HRS, the High Transmission Beamline (HTBL), & the Spectrometer segments. The EPICS soft IOCs will reside on virtual machines (VM) expanding the current FRIB pool.



a)



b)



c)



d)

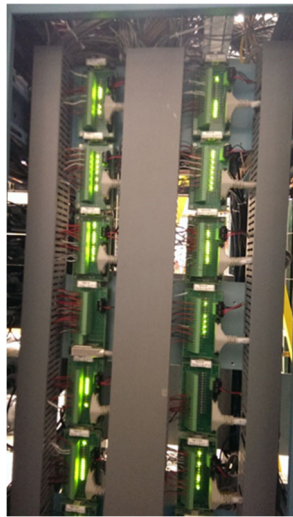


Figure 12-1 a) PLC installed in rack; b) Commercial cable; c) Sample IFM; d) 19" racks installed at the Laboratory

The number of EPICS PV's estimated in Tables 12-3 and 12-4 represent the Low Level controls EPICS PVs totaling ~16K and are based on FRIB low level PVs per device. If High Level EPICS PVs were 10x more, totaling 160K PVs, it would be ~1/5 of FRIB's 750K archived PV's, and an even smaller fraction of FRIB's unarchived PV's numbering in the millions. Additionally, a new archiver would likely be setup for Experimental Beamlines on the hypervisor nodes.

High level controls design will include CS-Studio for operations screens, high level EPICS IOCs, channel archivers, logbooks, alarm servers, and channel access security similar to the existing facility.

Instrumentation signals requiring a transducer or signal-level conditioning will use a subset of commercially available hardware utilized in NSCL and FRIB. All controls instrumentation is located in racks placed outside of the experimental vault to protect against any radiation damage.

In addition, this provides access to the instrumentation without the need for entering the vault during experiments.

All of the HTBL and Spectrometer Section magnets are self-protecting and require lead-voltage, helium-level, and helium-pressure monitors for quench detection.

Cryogenic temperatures will be read utilizing Lakeshore Monitors hardware as is used for FRIB. This provides the advantage of utilizing the same manufacturer for sensor and instrumentation interfaces, reducing possible future incompatibilities between equipment obtained from different vendors. Most temperature readings will be read over the serial interface by the EPICS control system. When temperatures are needed in a control loop within the PLC, they will be wired directly to the PLC as an analog input from the Lakeshore Monitor.

Cryogenic helium levels will be read through American Magnetics level monitors which also provide burnout protection to the sensor. Lakeshore temperature monitors and the American Magnetics level monitors provide digital outputs for use with interlocks, and provide local displays independent of the control system. Analog readings are also provided and hardwired into the PLC.

Lead drops and pressure sensors will utilize a commercially available Isolated Signal conditioning Module called a 5B module to convert from low-level signals to standard analog input values of  $\pm 5$  V wired to the PLC.

#### 12.4.2 Protection systems design

Personnel Protection Systems (PPS) are separated into two systems: Radiation Safety System (RSS) and Oxygen Deficiency Hazard (ODH), as shown in Figure 12-2.

Radiation Safety PPS includes radiation control and monitoring, access control, and beam intercepting devices. Oxygen Deficiency PPS includes monitoring and alarming functions.

The personnel protection system will be an extension of the Laboratory's existing experimental radiation safety system and Oxygen Deficiency Hazard Control System (ODHCS). It will utilize a safety rated Allen Bradley GuardLogix PLC. The PPS system will also utilize transfer switches and/or redundant power supplies connected to both house power and the centralized UPS system.

The safety PLC monitors inputs from door switches, E-stops, arm buttons, radiation monitors, and oxygen monitors to either trigger the interruption of beam, or to trigger warning alarms using both lights, and audible systems. A preliminary layout of the PPS for the HRS is shown in Figure 12-3. It illustrates the placement of safety hardware, monitors and detectors. The system also includes a wall plug, beam stop and faraday cup.





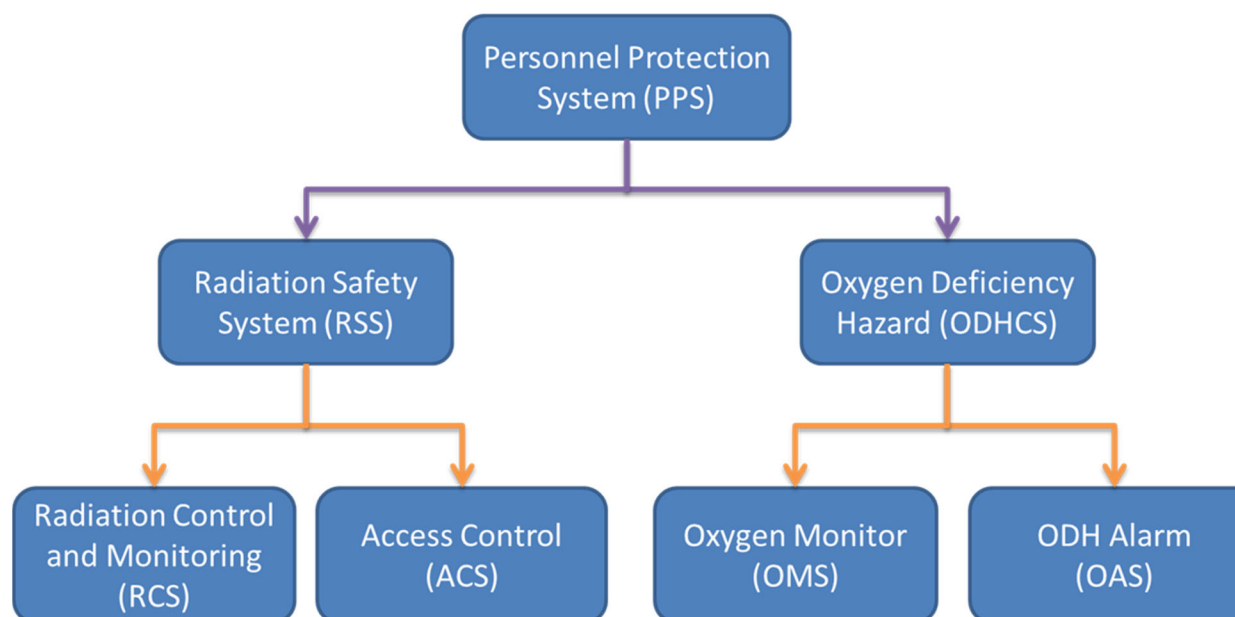


Figure 12-2 Personnel Protection System Architecture

While experiments in the HRS vault are ongoing, the vault is secured by using an access control system. Radiation levels are monitored in and around the experimental areas as seen in Figure 12-3. Neutron Radiation levels above an initial threshold of 0.5 mR/hr for public areas, and 2 mR/hr within the radiation level 2 areas of the lab, will trigger the yellow portion of the stack light to flash. Higher radiation levels (2 mR/hr for public areas, 5 mR/hr within the radiation level 2 areas in the lab) will shut off the beam. The Fast Beam Containment System detectors will be used to sense high radiation (current) above a fixed threshold, latch a fault, and turn off the RFQ in the FRIB Front End within 0.5 ms. Access control violations into the HRS Vault while running beam into the vault will also terminate the beam. The ODH system will have sensors that measure oxygen concentrations and the presence of flammable/explosive gases. Appropriate warning lights and audible systems will be utilized for both radiation safety and ODH safety systems, posted within the vault and at entrances as seen in Figure 12-3.

MPS will provide a Fast Protection System slave node in the HRS rack room. This will interface to the FRIB machine protection system Fast Protection System Master via a fiber connection. The overall architecture is shown in Figure 12-4. Diagnostic devices requiring a beam shut off can be hardwired to the HRS MPS slave using either a fiber or copper connection and will provide one of two signals (“Not OK” and “Not OK latch”) to the MPS slave. If the “Not OK” signal is detected by the MPS slave from the diagnostic electronics, the signal will be relayed to the FRIB MPS master, which in turn will terminate the beam through mitigation devices in the FRIB Front End.



Beamline and vacuum PLCs will also have an input into the MPS slave node. Signals that do not require as fast of response (10s of ms) can be wired to the PLC which will summarize a number of conditions into one signal to the MPS system that will in turn shutdown beam if “Not OK”

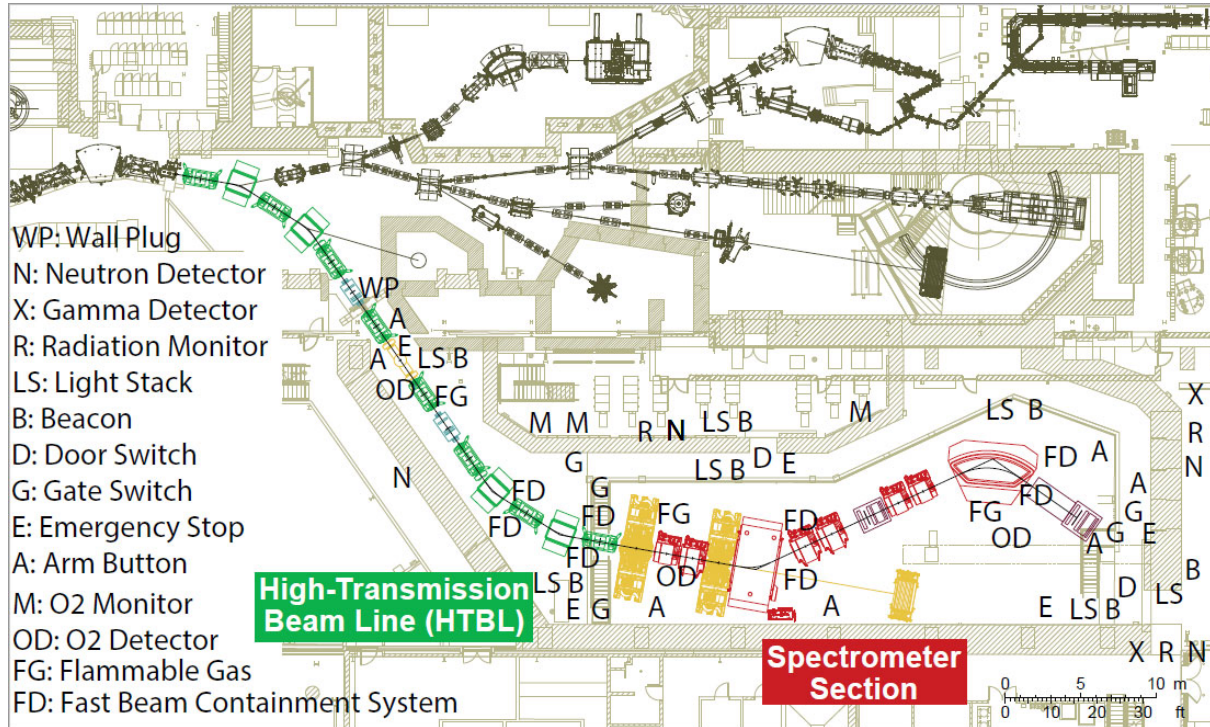


Figure 12-3 Preliminary layout of the Personnel Protection Systems for the HRS.

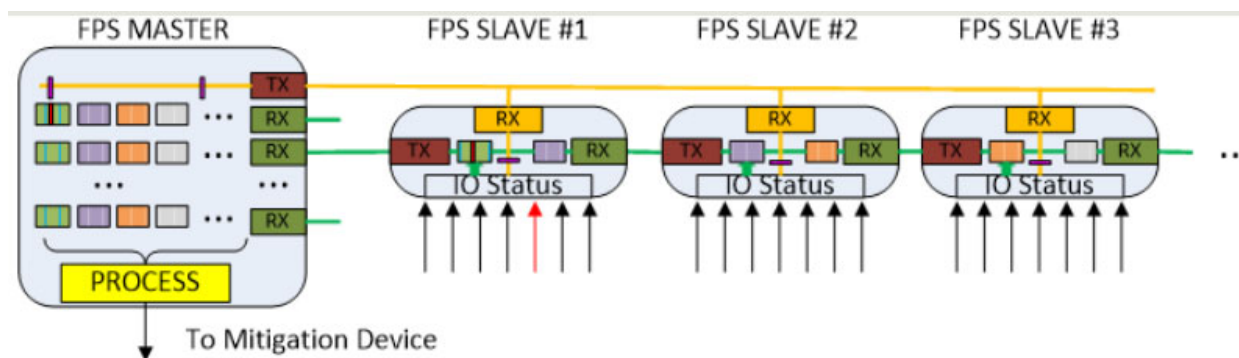


Figure 12-4 MPS Fast Protection System architecture

### 12.4.3 Network and IT design

The Network design will extend the existing experimental controls network utilizing Juniper series smart switches. Juniper switches are an MSU/FRIB/NSCL standard and provide the best

performance/price ratio. The expected number of ports based on the requirements demonstrated in the Table 12-3 and Table 12-4. The total number of connections for the project will be covered by approximately six edge switches connected either through aggregations switches or directly to the core switches. The controls network architecture is shown in Figure 12-5. All core and edge switches will have dual redundant power supplies installed. One power supply will be connected to house power and the other to power delivered using a centralized UPS system backed by a generator. In the event of a power outage, network infrastructure devices and systems will remain operational.

Cryogenic controls will also be tied into cryo-plant control controls network. Cameras will be segmented onto their own separate network so controls network throughput is not affected. Current design requirements call for five 1 Gb/s cameras which will use one edge switch. This will be tied to an independent IOC running on a local PC to serve data onto the controls network.

The increased load on the network would also be fractional as compared to FRIB. All switches will have a 10Gb/s uplink to the network core. The Juniper EX4600 can handle up to 72 ports at 10 Gb/s for a total of 720 Gb/s at line-rate speed. FRIB is currently using far less than 10 Gb/s in total. If HRS uses up to 20% of FRIB, total usage would be ~12 Gb/s total on a network capable of 720 Gb/s.

The network architecture will be segmented into several VLANs as is done for FRIB to better manage traffic to the many types of devices, as shown in Figure 12-6. Each device type will be on its own VLAN, such as PLCs, power supplies, vacuum devices, motor controllers and IOCs to illustrate a few example VLANs. This separates the broadcast traffic from EPICS from the various devices.

The HRS IT design includes a 25% expansion of the FRIB hypervisor cluster. The FRIB hypervisor cluster currently consists 4 hypervisor nodes with 24 CPUs/node (96 total cluster CPU cores). It has a total of 133 virtual machines which satisfies the current FRIB load for the FRIB accelerator and into the target area. Due to age, FRIB's hypervisor cluster will soon be upgraded to 4 hypervisor nodes of 128 CPU cores/node totaling 512 total CPUs cores in the cluster which should support up to an equivalent of 665 VMs on the new cluster. This will easily support the addition of HRS virtual machines which would number in the tens of VMs.

The new hypervisor platform will consist of Dell PowerEdge R7525's, or equivalent. There will be 5 hypervisor nodes (including HRS contribution) consisting of 128 CPU cores/node, 1 TB RAM/node, 30 TB of SSD cluster storage for virtual machine images (data will be stored on NetApp). The current storage space consists of a NetApp FAS2750 with a 100TB capacity.



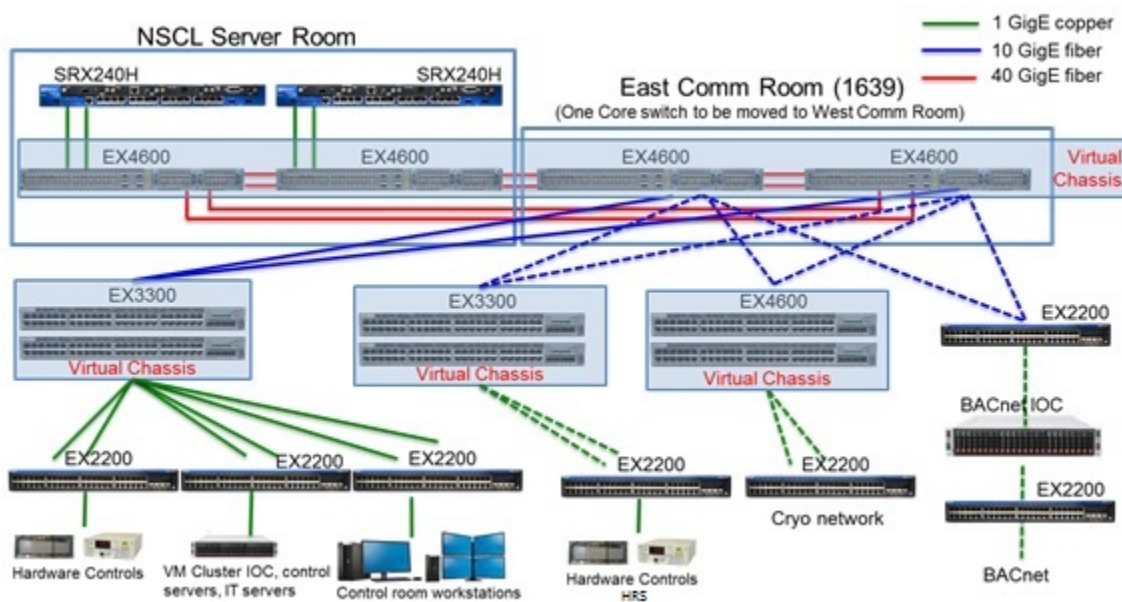


Figure 12-5 Controls Network Architecture

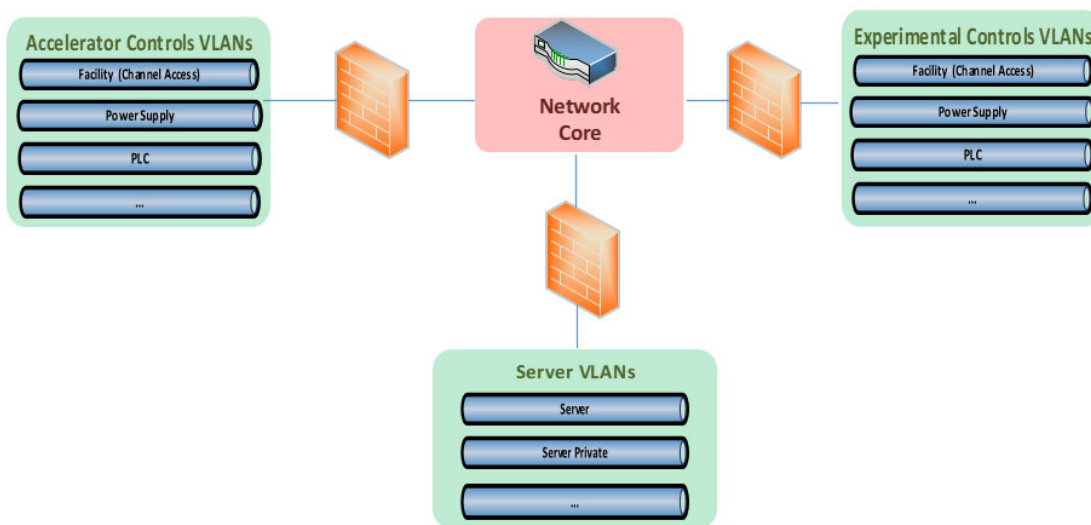


Figure 12-6 Controls Network VLAN Segmentation

Though FRIB’s current capabilities may support the fractional increase from HRS Network & IT requirements, the HRS Network & IT design & budget includes funding for an additional Hypervisor, and 1/8 to 1/4 of the current FRIB capability for the NetApp, Backup Server, IT Management Server, and Active Directory Domain Server.

HRS IT design will utilize existing servers, including NetApp for file storage, Backup Server, IT Management Server, Active Directory Domain Server, archivers, and Hypervisor clusters which include VMs for EPICS IOCs, and will expand capabilities for the additional signals being added to the control system.





## 13 Vacuum Systems

### 13.1 Introduction and overview

In Table 13-1, the WBS entries of relevance for the vacuum systems of the HRS are provided, which include the vacuum systems for the HTBL and the Spectrometer Section. In Figure 13-1, the scope of the vacuum systems is shown. It includes the diagnostic and detector boxes, gate valves, bellows, flanges, and beam-line chambers that connect the ion-optical elements. However, the vacuum chambers inside the magnetic elements (e.g. dipoles, quadrupoles) are not included, as they are included as part of the scope of the magnets.

Table 13-1 WBS for the vacuum systems for the HRS

Experimental Systems - High Rigidity Spectrometer	HRS.3
High Transmission Beamline (HTBL)	HRS.3.01
High Transmission Beamline Vacuum	HRS.3.01.04
Spectrometer Section	HRS.3.02
Spectrometer Section Vacuum	HRS.3.02.06

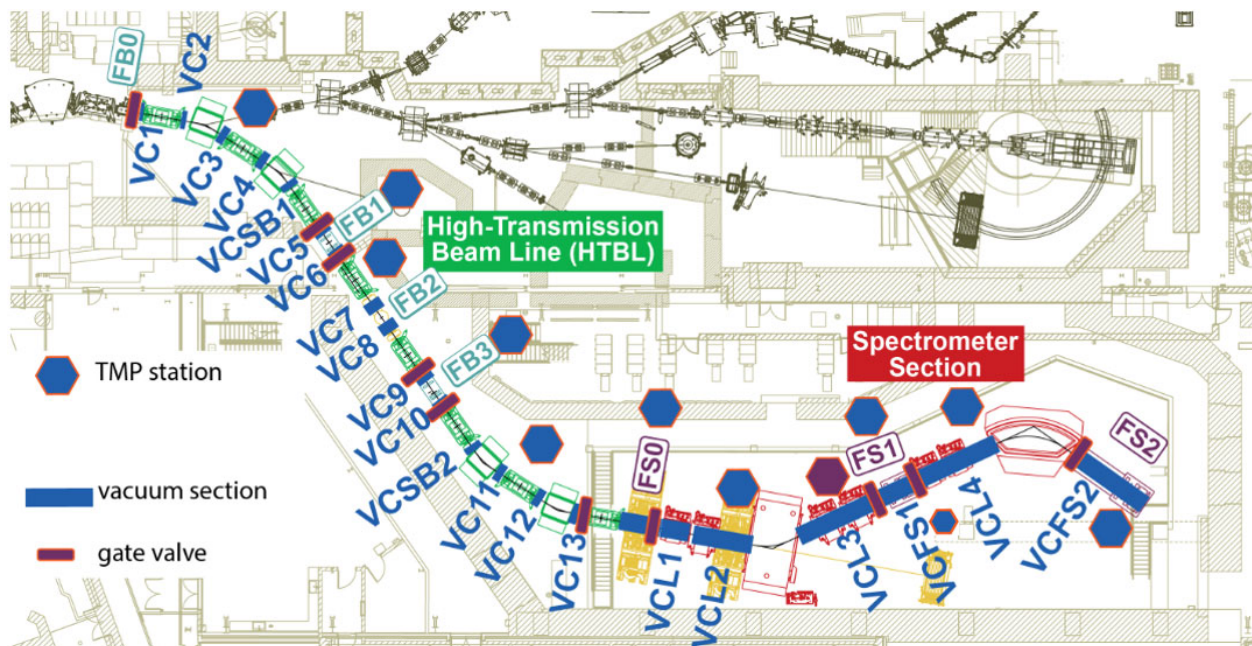


Figure 13-1 Overview of the vacuum elements and pumping systems of the HRS.

## 13.2 Requirements

The requirements for the vacuum system originate from the lattice design that meets the scientific requirements (see Section 4) for the HTBL (See Section 5.8.3), the Spectrometer Section (See Section 6.5.3), and their detector and diagnostic systems (See Section 7). The required pressures for the HTBL and the Spectrometer Section of the HRS are  $1.0 \times 10^{-5}$  Torr, based on experience with running experiments with fast beams in the S800 Spectrograph and the sweeper magnet system. This level of vacuum is sufficient to operate all detector systems except for the Multi-Channel Plates (MCPs; see Section 7.3.1.5), which requires a pressure of  $\sim 1.0 \times 10^{-6}$  Torr. When this system is used, that pressure will be achieved by adding pumping capacity locally, as is presently done for the operation of MCP detectors in the beam line to the S800 Spectrograph.

Gate valves are included in the design of the vacuum system to enable the isolation of beam line sections and diagnostic chambers for servicing specific items without the need for venting the entire beam line. The beam chambers have sufficient diameters to allow for the transmission of the rare isotope beams from the ARIS Fragment Separator to the target station of the HRS and for the transport of reaction products to the focal planes of the Spectrometer Section.

Turbo-molecular pumping systems must be placed outside of magnetic fields in excess of 50 Gauss or will be shielded as required. This limits the location where they can be placed, especially for the large sweeper dipole DS1, as shown in Figure 13-1. The HRS uses 10 Turbo-Molecular pumps (TMP) that must be located as close to the beamline as possible while avoiding magnetic fields in excess of 50 Gauss. The choice of location for the 10 TMP's will be confirmed by performing magnetic field plots around each HRS dipole magnet and the large QSA and QSB quads in the HRS. This will ensure that the 5 Gauss boundary for personnel exposure and 50 Gauss boundary for TMP's can be accurately determined. Extra care shall be taken in evaluation of the fields around detectors such as Greta and for other potentially magnetic field sensitive instruments. Similar consideration will also be given to vacuum gauging, some of which has maximum magnetic field limits specified by the supplier.

## 13.3 Preferred alternative

As shown in Figure 13-1, the HRS vacuum system contains twenty-five vacuum chambers, six of which contain diagnostic devices and detectors along the beamline (FB1, FB2, FB3, FS0, FS1, and FS2). The beam pipes in the HTBL section have a nominal diameter of 0.2 meters. In the Spectrometer Section (downstream of FS0), larger beam profiles require chambers and beam pipes with apertures of more than one meter in diameter. The vacuum elements for the HTBL are provided in Table 13-2 and for the Spectrometer Section in Table 13-3. They include the dimensions of each section, which are designed to accommodate the trajectories of rare isotope





beams based on the ion-optical studies presented in Section 5 for the HTBL and Section 6 for the Spectrometer Section.

Ten in-line gate valves are included to allow independent pump-down of beamline segments, and removal of diagnostic chambers without the need to vent the entire beamline. Additionally, gate valves are located on each of the ten turbo-molecular pumping stations installed along the beamline for machine protection and ease of maintenance. The HTBL section of the HRS beamline is very similar in design to the existing A1900 beamline, currently in operation at NSCL. Due to their design similarities, five turbo pumping stations with similar capacity to those used in A1900 (~500 l/s nominal pumping speed) were selected for the HTBL. The significantly larger chamber volumes in the spectrometer section require higher-capacity pumps. Therefore, five 2000 l/s turbo pumping stations were selected. To supplement these pumping stations, a large secondary roughing system was specified to aid in the initial evacuation of the large volume spectrometer section vacuum vessels.



Table 13-2 Vacuum elements of the HTBL.

Item	Description	Flange Size
GV10	Gate Valve 10" CFF	ISO 250
VC1	Vacuum chamber ~0.47m long, 0.2m bore, 10" CFF; 2.75" CFF ports for gauges	ISO 250
TB1	Magnetic element	
VC2	Vacuum chamber ~0.46m long, 0.2m bore, 10" CFF ends; 2.75" CFF ports for gauges	ISO 250
DB1	Magnetic element	
VC3	Vacuum chamber ~0.45m long, 0.2m bore, 10" CFF ends; 10" CFF side port for pumping; 2.75" CFF ports for gauges	ISO 250
TB2	Magnetic element	
VC4	Vacuum chamber ~0.45m long, 0.2m bore, 10" CFF ends; 2.75" CFF ports for gauges	ISO 250
DB2	Magnetic element	
VCSB1	Vacuum chamber ~0.46m long, 0.2m bore, 10" CFF ends; 2.75" CFF ports for gauges	ISO 250
TB3	Magnetic element	
GV10	Gate Valve 10" CFF	ISO 250
VC5	Vacuum chamber ~0.49m long, 0.2m bore, 10" CFF ends; 10" CFF side port for pumping; 2.75" CFF ports for gauges	ISO 250
FB1	Diagnostic Chamber (Viewer system, position detector x2, timing detector)	ISO 250
VC6	Vacuum chamber ~0.49m long, 0.2m bore, 10" CFF ends; 2.75" CFF ports for gauges	ISO 250
GV10	Gate Valve 10" CFF	ISO 250
TB4	Magnetic element	
VC7	Vacuum chamber ~1.32m long, 0.2m bore, 10" CFF ends; 10" CFF side port for pumping; 2.75" CFF ports for gauges	ISO 250
FB2	Diagnostic Chamber - 6 way cross (retractable viewer system)	ISO 250
VC8	Vacuum chamber ~1.32m long, 0.2m bore, 10" CFF ends; 2.75" CFF ports for gauges	ISO 250
TB5	Magnetic element	
GV10	Gate Valve 10" CFF	ISO 250
VC9	Vacuum chamber ~0.9m long, 0.2m bore, 10" CFF ends; 10" CFF side port for pumping; 2.75" CFF ports for gauges	ISO 250
FB3	Diagnostic Chamber (Viewer system, position detector, timing detector, energy-loss detector & slit system)	ISO 250
VC10	Vacuum chamber ~0.9m long, 0.2m bore, 10" CFF ends; 2.75" CFF ports for gauges	ISO 250
GV10	Gate Valve 10" CFF	ISO 250
TB6	Magnetic element	
VCSB2	Vacuum chamber ~0.46m long, 0.2m bore, 10" CFF ends; 2.75" CFF ports for gauges	ISO 250
DB3	Magnetic element	
VC11	Vacuum chamber ~0.45m long, 0.2m bore, 10" CFF ends; 2.75" CFF ports for gauges	ISO 250
TB7	Magnetic element	
VC12	Vacuum chamber ~0.45m long, 0.2m bore, 10" CFF ends; 10" CFF side port for pumping; 2.75" CFF ports for gauges	ISO 250
DB4	Magnetic element	
GV10	Gate Valve 10" CFF	ISO 250
VC13	Vacuum chamber ~0.45m long, 0.2m bore, 10" CFF ends; 2.75" CFF ports for gauges	ISO 250
TB8	Magnetic element	



Table 13-3 Vacuum elements of the Spectrometer Section

Item	Description	Flange Size
GV10	Gate Valve	ISO 250
FS0	HRS Target (Viewer system, position detector, timing detector)	ISO 250
GVL	Gate Valve 1.1m diameter	O-ring seal
VCL1	Vacuum chamber ~2m long, 0.5m bore, 12" CFF port for pumping, 2x 2.75" CFF ports for gauges	O-ring seal
VCL2	Vacuum chamber ~3m long, 1.1m bore; 12" CFF port for pumping, 2x 2.75" CFF ports for gauges	O-ring seal
DS1	SWEEPER MAGNET	
VCL3	Vacuum chamber ~6m long, 1.1m bore; 12" CFF port for pumping, 2x 2.75" CFF ports for gauges	O-ring seal
GVL	Gate Valve 1.1m diameter	O-ring seal
FS1	Vacuum chamber 1.5m x 1.5m x 3.0m	O-ring seal
GVL	Gate Valve 0.7m diameter	O-ring seal
VCL4	Vacuum chamber ~6m long, 0.7m bore; 12" CFF port for pumping, 2x 2.75" CFF ports for gauges	O-ring seal
DS2	SPECTROMETER DIPOLE MAGNET	
GVR	Gate Valve 1.1m x 0.22m rectangular	Custom O-ring
FS2	Vacuum chamber 1.5m x 1.5m x 5.0m	O-ring seal



## 14 Conventional Facilities

### 14.1 Introduction

The Conventional Facilities was provided by Michigan State University at a cost of ~\$23M. The construction of the 31000-square-foot High Rigidity Spectrometer and Isotope Harvesting vault began mid-calendar year 2018 with beneficial occupancy provided at the beginning of calendar year 2020. The new vault is located in the center of the FRIB complex as shown in Figure 14-1.

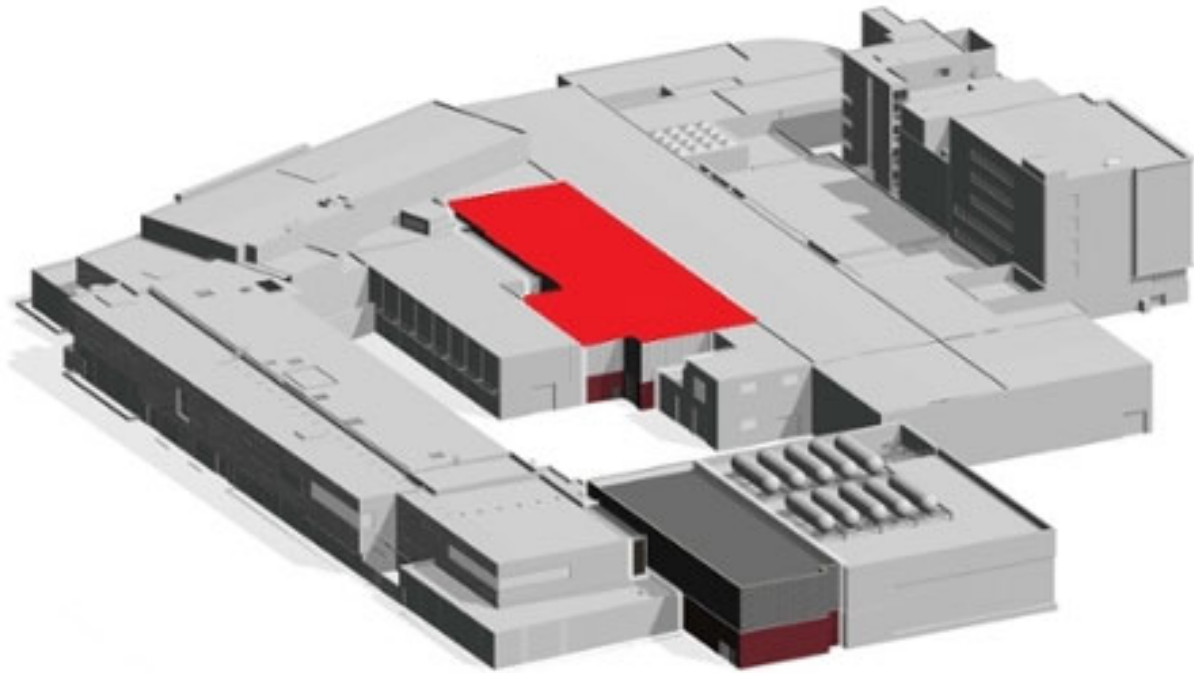


*Figure 14-1 The location of the High Rigidity Spectrometer and Isotope Harvesting vault (indicated in red) within the FRIB complex on the campus of Michigan State University.*

The layout of the HRS, consisting of the HTBL and the Spectrometer Section are provided in Figure 14-2. Note that the initial section of the HTBL, from FB0 (the final focal plane of the ARIS fragment separator) to FB2 will be situated inside the existing building infrastructure. An internal wall between FB1 and quadrupole triplet TB4 separates the FRIB Laboratory beam delivery system from the experiment area that houses the HRS. The high bay that houses the HRS also houses the Isotope Harvesting Laboratory (on the west side), which will be separated from the HRS area by a radiation shielding wall.

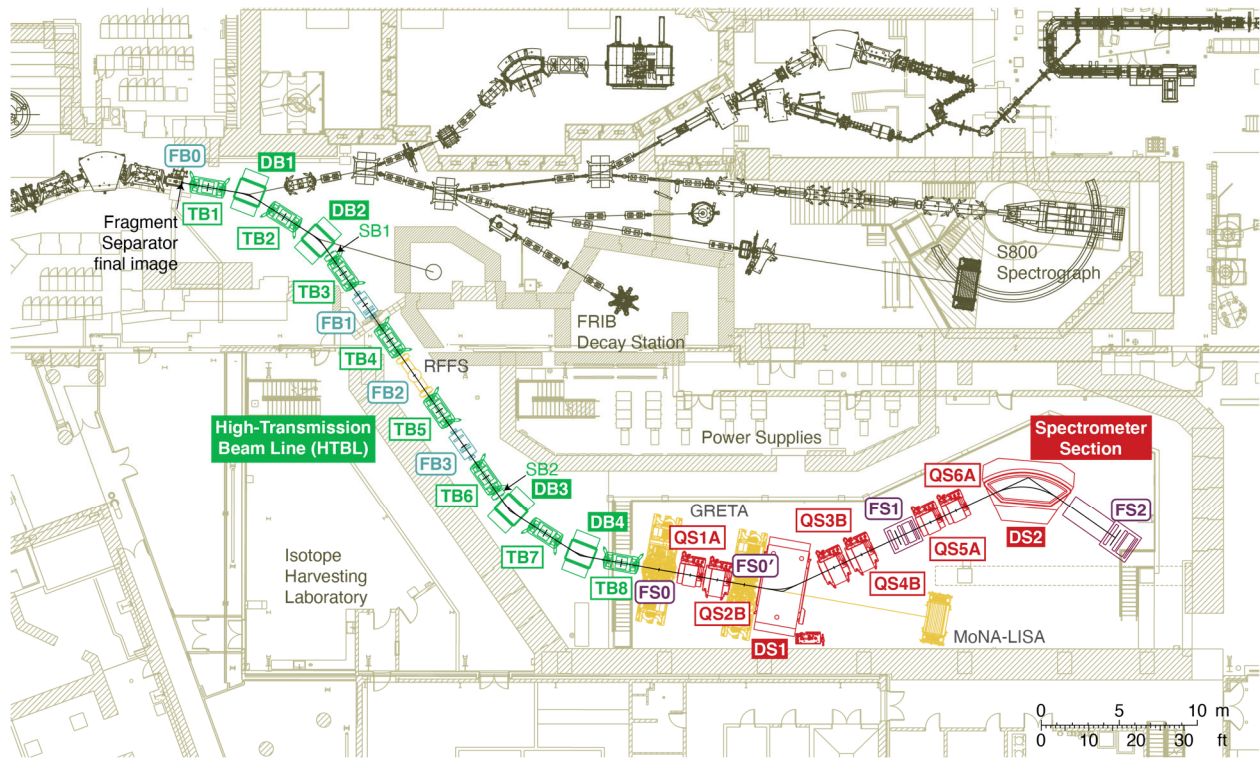


Figure 14-2 Layout of the High-Transmission Beam Line (HTBL) and the Spectrometer Section of the HRS

## 14.2 Radiation transport and safety

### 14.2.1 Requirements

The radiation shielding for the High Rigidity Spectrometer (HRS) experimental area has been analyzed [GEO18] to ensure that it will achieve radiation dose levels external to the shielding compatible with requirements for controlled areas ( $<2$  mrem/h) and for public areas ( $<2$  mrem in any hour and  $<100$  mrem in a year) [GRI18].

### 14.2.2 Radiation transport analysis

A Monte-Carlo radiation transport code PHITS [SAT13] was used to evaluate radiation environment in the HRS experimental area to ensure the adequacy of the proposed shielding. The effect of penetrations in the shielding was evaluated using PHITS and a labyrinth formalism using a semi-empirical method outlined in [COS14]. To cover the range of possible conditions, a light ( $^{18}\text{O}$ ), a medium ( $^{132}\text{Sn}$ ), or a heavy ( $^{238}\text{U}$ ) beam with an energy of 250 MeV/u and an intensity of  $10^7$  particles per second (pps) was stopped in a beryllium target at one of three possible locations labeled S1, S2, and S3 (see Figure 14-3). To perform failure mode analysis, another set of points labeled F1, F2, and F3 was identified as failure locations to mimic scenarios where a dipole fails





and a beam goes straight into concrete walls instead of being bent by a dipole (see also Figure 14-3). The resulting radiation fields are linearly proportional to beam intensity; maximum beam intensities compatible with radiation requirements were determined. A simplified radiation transport geometry was used that has a realistic shielding layout and includes beamline magnet iron parts, but not other items in the vault inconsequential to radiation shielding such as vacuum chambers, detectors etc.

The radiation outside the vault at locations where personnel can be present, labelled L3, L4, L6-9, and above the roof beams, as well as sky shine and at the closest public area was evaluated (see Figure 14-3). Dose equivalent rates were estimated 30 cm away from nearest walls. Vertical integration was performed according to NASA “human torso” definition, approximately 61 cm to 190 cm above the ground surface [NAS95]. The radiation levels at L6, the exhaust air labyrinth used to mitigate oxygen deficiency hazard conditions, were evaluated by using PHITS and by using the above-mentioned semi-empirical method [COS14]. The latter method was found to overestimate radiation levels several times compared to PHITS. Other penetrations were evaluated by using the semi-empirical method.

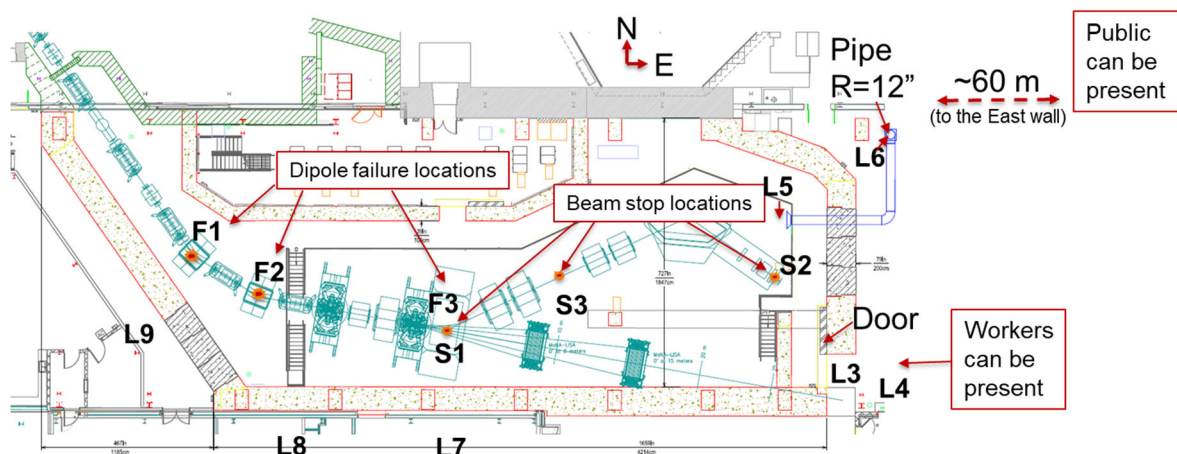


Figure 14-3 HRS layout showing three possible beam loss locations (S1, S2, and S3), dipole failure locations (F1, F2, and F3) and radiation dose evaluation points (tallies) L3 (30 cm from door), L4 (30 cm from wall), L6 (60 cm cube at exit of 12" pipe), L7, L8, and L9 (30 cm from nearest walls). Labeled “Door”, the main vault entrance door consists of 18-inch thick steel backed by 6 inches of polyethylene. The closest public area is also shown.

### 14.2.3 Radiation analysis results

The dose equivalent rates (in mrem/h) calculated for tally points L3, L4, L6, L7, L8, and L9 for  $^{18}\text{O}$ ,  $^{132}\text{Sn}$ , and  $^{238}\text{U}$  beams at 250 MeV/u stopped at loss points S1, S2, and S3, or passing through



a failed dipole magnet at F1, F2, and F3, were converted to beam intensities (in particles per second, or pps) meeting the 2 mrem/h requirement are presented in Table 14-1 and Table 14-2. These beam intensities are compatible with the HRS Science program. Experiments with beam intensities of  $10^6$  pps are possible across the chart of nuclei and for many beams intensities of  $10^7$  pps or higher are feasible, especially if shielding is added locally to further reduce dose rates.

Dose rates in other key areas were estimated, including direct dose rates in the area accessible by general public and closest to the HRS facility (see Figure 14-3). For a 250-MeV/u  $^{238}\text{U}$  beam at an intensity of  $10^7$  pps and stopped at S3, the dose rate was found to be 0.1 mrem/h. Lighter beams stopped at S3 produce lower doses. All beams stopped at S1 and S2 loss points produce significantly lower doses.

Dose rates from sky shine are very low; the highest dose rate is  $2 \times 10^{-4}$  mrem/h. Dose rates above the HRS vault roof could be as high as 0.25 mrem/h (for the  $^{238}\text{U}$  beam stopped at S1 loss point). Other beams stopped at S1, and all beams stopped at other loss points, produce significantly lower doses.

Radiation levels produced by penetrations in the HRS experimental area shielding walls were also assessed. Radiation levels in the tally location L6, an area above the outer end of the 24" ventilation pipe, were analyzed (see Figure 14-3, "Pipe" in the NE corner). Among several HRS penetrations, this is by far the largest. PHITS Monte-Carlo analysis shows that dose rates at L6 exit are below the limits. This penetration was also analyzed by using the "labyrinth" method of reference [COS14]. This method is conservative and overestimates radiation levels by ~5 to 30 times compared to the calculations with PHITS. The semi-analytical "labyrinth" method was used on the other vault penetrations; the analysis showed that these penetrations do not affect radiation levels outside of the walls.



Table 14-1. Beam intensities in particles per second (pps) that satisfy the 2 mrem/h requirement for 250 MeV/u <sup>18</sup>O, <sup>132</sup>Sn, and <sup>238</sup>U stopped at beam loss locations S1, S2, and S3 and tally locations L3, L4, L6, L7, L8, and L9. (see Figure 14-3).

Beam Loss Point	S1			S2			S3		
Beam	<sup>18</sup> O	<sup>132</sup> Sn	<sup>238</sup> U	<sup>18</sup> O	<sup>132</sup> Sn	<sup>238</sup> U	<sup>18</sup> O	<sup>132</sup> Sn	<sup>238</sup> U
Tally Location	Beam intensity (pps) for which the dose rate is less than 2 mrem/h								
L3	2.3E+08	5.2E+07	4.7E+07	1.3E+07	4.9E+06	4.6E+06	7.7E+09	4.1E+09	3.7E+09
L4	6.7E+08	1.5E+08	1.4E+08	3.5E+07	1.1E+07	9.8E+06	1.7E+10	5.7E+09	7.3E+09
L6	1.4E+11	6.7E+10	1.8E+10	1.7E+10	7.6E+09	1.1E+10	5.1E+09	3.5E+09	1.5E+09
L7	2.5E+11	7.7E+11	3.0E+12	4.5E+11	2.0E+12	4.8E+10	4.0E+13	3.3E+12	3.4E+12
L8	4.2E+11	4.7E+11	5.5E+12	7.1E+11	6.0E+11	9.4E+10	3.2E+12	3.6E+11	3.1E+12
L9	1.3E+12	3.4E+11	3.0E+13	1.7E+12	3.6E+11	2.0E+12	1.7E+12	1.9E+11	2.8E+12

Table 14-2 Beam intensities in particles per second (pps) that satisfy the 2 mrem/h requirement for 250 MeV/u <sup>18</sup>O, <sup>132</sup>Sn, and <sup>238</sup>U passing through dipole failure locations F1, F2, and F3 and tally locations L3, L4, L6, L7, L8, L9 (see Figure 14-3).

Dipole Failure Point	F1			F2			F3		
Beam	<sup>18</sup> O	<sup>132</sup> Sn	<sup>238</sup> U	<sup>18</sup> O	<sup>132</sup> Sn	<sup>238</sup> U	<sup>18</sup> O	<sup>132</sup> Sn	<sup>238</sup> U
Tally Location	Beam intensity (pps) for which the dose rate is less than 2 mrem/h								
L3	4.1E+11	1.1E+11	9.1E+10	1.9E+10	5.3E+09	4.2E+09	4.9E+07	1.4E+07	1.1E+07
L4	1.1E+12	3.2E+11	2.5E+11	6.8E+10	1.9E+10	1.5E+10	2.2E+08	6.2E+07	4.9E+07
L6	5.4E+13	1.5E+13	1.2E+13	2.1E+11	5.8E+10	4.6E+10	6.0E+10	1.7E+10	1.3E+10
L7	1.2E+10	3.4E+09	2.7E+09	9.6E+07	2.7E+07	2.1E+07	2.9E+11	8.1E+10	6.4E+10
L8	2.3E+07	6.3E+06	5.0E+06	1.7E+09	4.8E+08	3.8E+08	7.2E+11	2.0E+11	1.6E+11
L9	2.3E+12	6.4E+11	5.1E+11	1.1E+12	3.2E+11	2.5E+11	3.4E+12	9.4E+11	7.4E+11

### 14.2.4 Magnet power-supply interlocks

Rare isotope beams are guided from the fragment separator through the HTBL and the Spectrometer Section. A failure or incorrect setting of the magnets in the HTBL and Spectrometer setting could result in beams going in an unintended direction or have uncontrolled properties. To prevent such occurrences, the beam delivery to the HRS will be stopped if read currents deviate from their set values by more than 1% for dipole magnets and 10% for quadrupole magnets. This interlock will trigger in about ~1 s, which reduces the amount of beam directed in an unintended direction to negligible level.



### 14.2.5 Summary

A radiation transport analysis was performed to assess the adequacy of the High Rigidity Spectrometer (HRS) experimental area shielding. To encompass the range of possible scenarios, representative beams  $^{18}\text{O}$  (light),  $^{132}\text{Sn}$  (medium), and  $^{238}\text{U}$  (heavy) at 250 MeV/u and  $10^7$  particles per second (pps) were stopped in beryllium at three beam loss points S1, S2, and S3. Also, to mimic dipole failure scenarios that would result in a beam hitting a concrete wall, three locations, F1, F2, and F3, were identified as source locations. The resulting dose rates in key locations around the facility were scaled to determine the maximum beam intensities (in pps) necessary to meet the maximum dose criterion of 2 mrem/h. For a very large fraction of experiments, the beam intensities will be less than  $10^6$  pps and these can be performed without additional shielding, as the simulations indicate that the 2 mrem/h criterion is not exceeded for any beams with intensities below  $4 \times 10^6$  pps. By adding shielding locally near locations where beams are stopped, it will be possible to perform experiments at higher intensities than  $10^6$  pps. The analysis also showed that penetrations maintain shielding integrity and do not produce significant local dose enhancements. Public exposure due to direct radiation and skyshine are below limits without additional shielding for all beams with intensities of up to  $10^7$  pps. Note that radiation monitors will be used to continuously monitor these doses. The beam will be stopped with PPS Beam Inhibit Devices (BIDs) in the front end in the event that the dose rates exceed 2 mrem/h external to the experimental vault.

### 14.3 References

- [COS14] J.D. Cossairt, *Radiation Physics for Personnel and Environmental Protection*, Fermilab report TM-1834, Rev 13, March 2014
- [GEO18] Dali Georgobiani, HRS Radiation Shielding Analysis, FRIB-T40204-CA-000217, 2018
- [GRI18] Peter Grivins, Laboratory Radiation Safety Manual, FRIB-S10300-MA-004597-R001 (Nov. 2018).
- [NAS95] NASA Man-Systems Integration Standards, NASA-STD-3000, Volume I, section 3
- [SAT13] T. Sato, K. Niita, N. Matsuda, S. Hashimoto, Y. Iwamoto, S. Noda, T. Ogawa, H. Iwase, H. Nakashima, T. Fukahori, K. Okumura, T. Kai, S. Chiba, T. Furuta and L. Sihver, Particle and Heavy Ion Transport Code System PHITS, Version 2.52, J. Nucl. Sci. Technol. 50:9, 913, 2013



## 15 EHS and Quality assurance

### 15.1 Introduction

FRIB operates under an established regulatory framework that includes the US Nuclear Regulatory Commission, the State of Michigan, and Michigan State University. The various regulatory agencies establish requirements for HRS design, and operation and provide oversight and inspection of the project's implementation of the requirements. The applicable ESH and Quality regulatory requirements can be found in the FRIB Regulatory Requirements document [FRIB-T10400-TD-000363].

The Laboratory has committed to maintaining ISO 45001, ISO 14001, and ISO 9001 registered programs. These self-imposed and third-party registered management systems assure that FRIB maintains the current high standards for Occupational Health and Safety, Environmental Management and Quality Management required to maintain these certifications.

A risk-based approach is used to determine the need for controls on facilities, systems, or components to protect the public, workers, the environment and the Laboratory's mission. Controls that prevent or mitigate serious events will be formally credited as part of the approved safety envelope.

As used in this document, controls and hazard controls mean those engineered or administrative protective elements that are used to protect against a hazard. Normal process or operational controls are not included in these requirements except to the extent that their use is directly tied to hazard protection.

The concept of credited control is well established in the accelerator safety community. A credited control is defined in DOE Order 420.2C "Safety of Accelerator Facilities" [DOE420], as "controls determined through safety analysis to be essential for safe operation directly related to the protection of personnel or the environment."

FRIB extends the robust principles of credited control management to the management of controls for non-safety hazards of similar risk, such as investment and facility protection. FRIB credited controls consist of credited controls with Environment, Safety and Health (ESH) impact and credited controls without ESH impact. The intent is to manage like risks and hazards in a consistent, rigorous fashion.

The following are guiding principles for hazard controls:

- Controls shall be implemented as interventions that mitigate risk.



- Controls shall be selected using a risk-based approach.
- Controls management shall rely on certain key attributes.

Since the HRS Project is following consensus codes and standards, standard industrial hazards are addressed and the risks minimized by adherence to established policies of Michigan State University applicable to activities of the HRS and by implementing integrated safety management (ISM) practices through its certified ISO programs (ISO 14001, ISO 45001, and ISO 9001).

## 15.2 Hazard analysis and controls

The current FRIB Laboratory Hazard Analysis (HA) [FRIB-T10101-TD-001075] is a comprehensive hazard analysis that covers all aspects of the FRIB project and accelerator facility. The HRS project follows the same approach to assure that hazards have been successfully captured and mitigated. The HRS has developed a Hazard Analysis (HA) report [FRIB-M41800-TD-001608].

## 15.3 Hazard control implementation and management

Controls must be specified using a risk-based approach in which ongoing operations and credible upsets are listed, the probability and consequences are predicted, and a resulting risk is qualified. Controls are used as interventions to mitigate risks. Risks may be personal (for example, injury or illness), environmental (for example, spill, contamination, release to the environment), regulatory (for example, exceedance of a published standard), programmatic (for example, interruption of a user experiment), financial, reputational, or a number of other potential negative consequences.

The FRIB HA examines risks to personnel and the environment and provides a matrix appropriate for the qualification of risks. The selection of engineered and administrative controls depends upon the risk to workers, the public or the environment from the unmitigated hazard (that is, without controls in place). Controls must be assigned to reduce risk to a level that is “as low as reasonably practicable” (ALARP). In general, unacceptable risks (for example, high risks as outlined in the FRIB HA) require the use of credited controls to reduce risks to an acceptable level, while acceptable risks (for example, medium, low, and extremely low) use non-credited controls per the ALARP principle.

Categorization of risk (for example, as high, medium, low, or extremely low) is made through a hazard analysis process.

- High risks require at a minimum a credited control to protect workers or the public from the risk. Residual mitigated risks are further reduced with non-credited controls.



- Medium risks should be mitigated using at least one non-credited (engineered and/or administrative) control, supplemented by basic safety management programs and inherent robust design.
- Low risks may be further reduced using a combination of engineered and administrative non-credited controls.
- If the unmitigated risk is extremely low then no additional controls are required, but may be applied as best practice.

## 15.4 Credited engineered controls with ESH impact

Credited Engineered Controls assure high risk hazards are mitigated. Nine attributes are associated with Credited Engineered Controls (CEC): competence; specificity; monitoring; fail-safe; responsibility; configuration management; initial verification and periodic testing; record keeping, and independence. Personnel Protection System (PPS) controls are a special class of Credited Engineered Controls that protect against radiation and oxygen deficiency hazards.

CECs with ES&H impact are selected according to the FRIB Functional Safety Program [FRIB-S10206-PL-000313]. The IEC 61511 (Safety instrumented systems for the process industry sector) Safety Integrity Level (SIL) determination process shall be followed for active engineered controls with ESH impact. The operation creating the hazard must stop, or space must be evacuated, when a required CEC with ESH impact is unable to fulfil its safety function.

## 15.5 Non-credited controls with ESH impact

Non-credited controls with ESH impact are used to 1) mitigate medium level hazards, or 2) mitigate residual risks, e.g., due to the possibility of human error associated with a credited administrative control, or reliance upon a simulation only for a credited engineered control. While “standard industrial hazards” still have high consequence, the risk is reduced by prescriptive legal requirements (i.e. lockout/tagout in occupational safety acts) and extensive engineering code and practice (i.e. National Electrical and American Society of Mechanical Engineers Codes).

## 15.6 Selection of credited controls

Once the need for a credited control is determined, a disciplined process has been established to select the set of equipment items (credited engineered controls), and/or administrative items (credited administrative controls) needed to accomplish the required safety function. The selection of credited controls often involves choices between multiple items that could function to control a particular hazard:





1. When either an active or passive control can be credited to ensure the safety function, the passive control should be selected over the active. This selection is based on the inherently higher reliability of passive devices.
2. If either engineered control(s) or administrative control(s) could perform the needed safety function, the engineered control should be selected over the administrative control. This selection is based on the generally higher reliability of engineered controls versus human actions.
3. When a choice exists between controls that would prevent an event and controls that could mitigate the consequences of the event, the preventive controls should be selected over mitigating controls. This selection is based on the inherent value of preventing accidents as opposed to mitigating their effects.
4. Only those items essential for safe operation directly related to the protection of workers, the public, and the environment should be selected as Credited Controls. The number of Credited Controls should, in general, be minimized and include only a limited subset of the total number of controls employed for overall facility operation. This guidance allows a high degree of operational attention (e.g., monitoring, surveillance, maintenance, control of documentation, etc.) to be devoted to the Credited Controls. To support this selection criterion, Credited Controls that protect against multiple events or receptors are preferred.
5. Where two levels of control are selected, the controls are to be independent such that the failure of one level of control does not cause failure of the other. This criterion ensures that multiple levels of control are not compromised by a single failure.
6. When choosing between a single CEC to address each safety function or a common CEC to address multiple safety functions, the overall risk reduction shall be analyzed and reviewed, taking into consideration common points of failure and configuration management. The default project position is to avoid CECs that fulfill more than one safety function. This guidance prioritizes removing common failure modes.

## 15.7 Selection of non-credited controls

Non-credited engineered and administrative controls are selected based upon the specific hazards being protected against. Engineered controls are preferred and shall be implemented unless infeasible.

## 15.8 Management of controls

Credited and non-credited engineered and administrative controls shall be managed per best practice (for example, manufacturer recommendations) and in accordance with this plan and the Functional Safety Program [FRIB-S10206-PL-000313]. The hazard owner is responsible for the integrity of hazard controls necessary to safely operate the system. Changes to controls shall follow the Laboratory Configuration Management Plan and Functional Safety Program.



## 15.9 Management of credited controls

The system owner must ensure that the credited control, whether engineered or administrative, or a combination, is managed to include the following attributes. To accomplish this, a credited control system management plan specifying procedures for fulfilling these elements shall be established by the system owner.

1. **Competence.** Individuals who analyze, specify, design, operate, and maintain credited control systems must be competent in the tasks they perform.
2. **Specificity.** The elements that collectively make up the credited control system must be specified.
3. **Monitoring.** When credited controls provide feedback (for example, alarm status) indicating that the specified protection is being provided, the status of that feedback must be monitored to detect out-of-tolerance conditions and to direct appropriate responses.
4. **Fail-safe.** Credited controls must be configured, when practical, so that in the event of component failure due to internal or external events (including loss of power), the action is to maintain the protective nature of the control. Some credited controls may not be configured to be fail-safe. In these cases there must be sufficient redundancy of protection (“defense in depth”) that a single failure will not lead to unacceptable risk.
5. **Responsibility.** Each credited control system must have a specified responsible owner who has the authority and responsibility for assuring that the system is managed per these requirements.
6. **Configuration management.** Before being placed into service, each new credited control system must be reviewed per the FRIB Device Readiness Review (DRR) process. Changes to a credited control system may only be made after a thorough review process to ensure that the level of safety required is maintained by the change. Changes may only be made after approval by the responsible owner or designee. There may be separate configuration management processes for permanent changes and for temporary changes.
7. **Testing and Verification.** Credited control systems must be initially, and periodically thereafter, tested and verified to be operating properly. Testing intervals are specified in the credited controls system management plan. Procedures for the initial and periodic test and verification procedures must be specified and managed through a formal change control process.
8. **Recordkeeping.** Records of design and approval, as well as procedures for acceptance, testing and verification shall be maintained in a retrievable fashion. The hazard control system owner ensures that these records are maintained.
9. **Independence.** The functional requirements, configuration, and validation of these controls is approved by the Radiation Safety Officer for radiation safety related credited controls; and by the Chief Engineer and/or Functional Safety Manager for other credited controls.



## 15.10 Compensatory measures

“Compensatory Measures” are temporary actions designed to afford equivalent protection when a CEC has failed or a new requirement arises. Compensatory measures can replace a CEC with an equivalent CEC, or compensatory measures may control a lesser hazard when additional Credited Administrative Controls are put in place to reduce risk.

Compensatory Measures need the same approvals as the originally approved CEC.

## 15.11 Management of non-credited controls

Non-credited controls shall be managed to include the following attributes:

1. **Competence.** Individuals who analyze, specify, design, operate, and maintain non-credited controls must be competent in the tasks they perform.
2. **Configuration management.** Changes to non-credited controls may only be made after assurance that the level of safety required is maintained by the change. Whenever a non-credited control system interacts (for example, signals, dependencies) with a credited control system, or interacts with any system such that the interaction crosses system boundaries or technical system ownership, that interaction must be documented. The documentation must specify the information that each system is receiving from the other, what the expected actions of each system in relation to that information are, and who is responsible for maintaining each side of that interface. The documentation is approved by the owner of the technical system having the hazards being controlled and contains concurring signatures of the hazard control system owners of the systems on all sides of that interface. That interface becomes a configuration controlled element.
3. **Verification.** Non-credited controls must be periodically evaluated to ensure that they continue to be effective. This evaluation may be through inspection, measurement, or other means.
4. **Recordkeeping.** Records of design, approval, acceptance, testing, and verification of non-credited controls must be maintained in a retrievable fashion. Who maintains these records is generally specified in the institutional program managing the specific hazard for which the non-credited control is used.

## 15.12 Control identification and maintenance

CECs with ESH impact will be labeled. Workers will be trained to the specific requirements and attributes: competence, configuration management, testing and verification, and record keeping. Functional safety manager will verify color and label scheme for CECs with ESH impact at initial implementation and periodic testing.



Workers will be trained to specific requirements and attributes for Non-credited Controls with ESH impact: competence, configuration management, verification and record keeping.

### 15.13 Quality assurance

HRS will be designed and built with the assistance of a fully involved Quality Assurance (QA) Program. A Quality Assurance Plan [FRIB-S10300-PL-000148] has been developed and is in use throughout the Laboratory. This plan specifies the program requirements that apply to all Laboratory work through a graded approach to ensure appropriate quality measures are applied in a manner commensurate with the scope.

### 15.14 References

[DOE420] DOE O 420.2C, [Safety of Accelerator Facilities](#)

[FRIB-T10400-TD-000363] FRIB Regulatory Requirements with ESH&Q inputs

[FRIB-S10300-PL-000148] FRIB Laboratory Quality Assurance Plan

[FRIB-T10101-TD-001075] FRIB Hazard Analysis

[FRIB-T10401-AD-000353] FRIB Requirements for Selecting Safety Related Credited Controls

